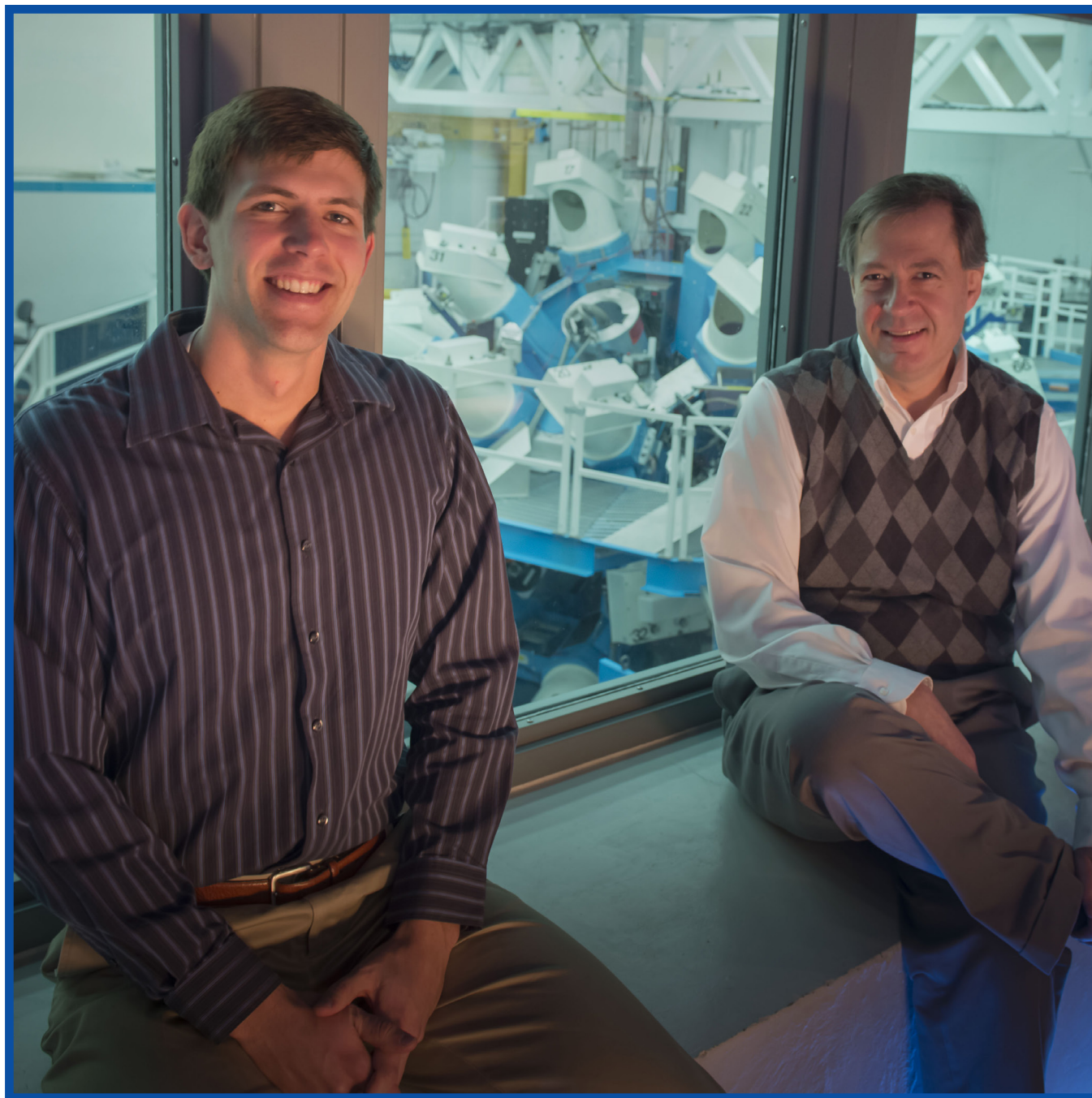


LLE Review

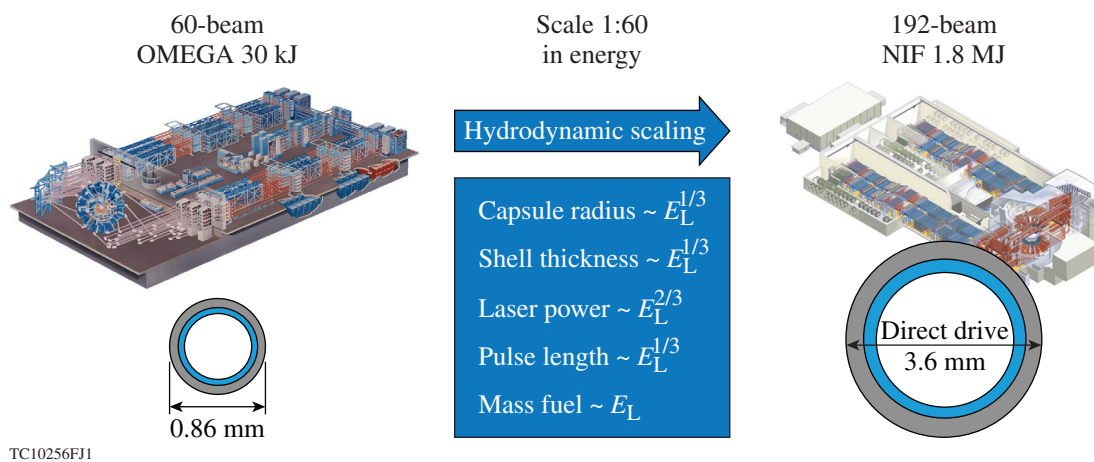
Quarterly Report



About the Cover:

The photograph on the cover features Ryan Nora, Department of Physics doctoral student, and his advisor Professor Riccardo Betti, LLE Scientist and Professor of Mechanical Engineering and Physics, sitting in the OMEGA viewing gallery with the target chamber visible behind the windows. Nora is the lead author of the featured article in this volume, which proposes a theory of hydrodynamic similarity that will guide LLE's design of direct-drive-implosion experiments on OMEGA. According to the theory presented, these experiments are hydrodynamically equivalent to implosions that would result in ignition if carried out on the National Ignition Facility (NIF).

The figure below illustrates the size difference between hydrodynamically equivalent implosion targets on OMEGA and the NIF. The size increase for the NIF target is based on the scaling relations shown in the figure. The particular extrapolation between the facilities shown in this figure applies to the case of a symmetric direct-drive-ignition implosion on the NIF. E_L is the total laser energy delivered to the target.



This report was prepared as an account of work conducted by the Laboratory for Laser Energetics and sponsored by New York State Energy Research and Development Authority, the University of Rochester, the U.S. Department of Energy, and other agencies. Neither the above-named sponsors nor any of their employees makes any warranty, expressed or implied, or assumes any legal liability or responsibility for the accuracy, completeness, or usefulness of any information, apparatus, product, or process disclosed, or represents that its use would not infringe privately owned rights. Reference herein to any specific commercial product, process, or service by trade name, mark, manufacturer, or otherwise, does not necessarily constitute or imply its endorsement, recommendation, or favoring

by the United States Government or any agency thereof or any other sponsor. Results reported in the LLE Review should not be taken as necessarily final results as they represent active research. The views and opinions of authors expressed herein do not necessarily state or reflect those of any of the above sponsoring entities.

The work described in this volume includes current research at the Laboratory for Laser Energetics, which is supported by New York State Energy Research and Development Authority, the University of Rochester, the U.S. Department of Energy Office of Inertial Confinement Fusion under Cooperative Agreement No. DE-NA0001944, and other agencies.

Printed in the United States of America

Available from

National Technical Information Services
U.S. Department of Commerce
5285 Port Royal Road
Springfield, VA 22161
www.ntis.gov

For questions or comments, contact Matthew Barczys, Editor, Laboratory for Laser Energetics, 250 East River Road, Rochester, NY 14623-1299, (585) 273-3732.

Worldwide-Web Home Page: <http://www.lle.rochester.edu/>
(Color online)

LLE Review

Quarterly Report



Contents

In Brief	iii
Theory of Hydro-Equivalent Ignition for Inertial Fusion and Its Applications to OMEGA and the National Ignition Facility	1
Improving the Hot-Spot Pressure and Demonstrating Ignition Hydrodynamic Equivalence in Cryogenic Deuterium–Tritium Implosions on OMEGA	18
Measurements of Electron Density Profiles Using an Angular Filter Refractometer	50
Multibeam Laser–Plasma Interactions in Inertial Confinement Fusion	58
First-Principles Thermal Conductivity of Deuterium for Inertial Confinement Fusion Applications	81
Self-Phase Modulation Compensation in a Regenerative Amplifier Using Cascaded Second-Order Nonlinearities	97
Publications and Conference Presentations	

In Brief

This volume of the LLE Review, covering October–December 2013, features “Theory of Hydro-Equivalent Ignition for Inertial Fusion and Its Applications to OMEGA and the National Ignition Facility” by R. Nora, A. Bose, and K. M. Woo (LLE, Fusion Science Center, and the Department of Physics and Astronomy, University of Rochester); R. Betti, (LLE, Fusion Science Center, and the Departments of Mechanical Engineering and Physics and Astronomy, University of Rochester); A. R. Christopherson (LLE, Fusion Science Center, and the Department of Mechanical Engineering, University of Rochester); R. L. McCrory, D. D. Meyerhofer (LLE and Departments of Mechanical Engineering and Physics and Astronomy, University of Rochester); and K. S. Anderson, A. Shvydky, J. A. Marozas, T. J. B. Collins, P. B. Radha, S. X. Hu, R. Epstein, F. J. Marshall, and T. C. Sangster (LLE). This article (p. 1) reports on the development of the theory of hydrodynamic similarity, which is used to scale the performance of direct-drive cryogenic implosions conducted at the Omega Laser Facility to National Ignition Facility (NIF) energy scales. The theory of hydrodynamic similarity is developed in both one and two dimensions, tested with hydrodynamic simulations, and then used to determine the requirements for demonstrating hydro-equivalent ignition (implosions with the same implosion velocity, adiabat, and laser intensity) on OMEGA. Hydro-equivalent ignition on OMEGA is represented by a cryogenic implosion that would scale to ignition on the NIF at 1.8 MJ of laser energy symmetrically illuminating the target. It is found that a reasonable combination of neutron yield and areal density for OMEGA hydro-equivalent ignition is 3 to 6×10^{13} and ~ 0.3 g/cm², respectively, depending on the level of laser imprinting, although this performance has yet to be achieved on OMEGA.

Additional highlights of research presented in this issue include the following:

- V. N. Goncharov (LLE and Department of Mechanical Engineering, University of Rochester); T. C. Sangster, T. R. Boehly, M. J. Bonino, T. J. B. Collins, R. S. Craxton, J. A. Delettrez, D. H. Edgell, R. Epstein, C. J. Forrest, V. Yu. Glebov, D. R. Harding, S. X. Hu, I. V. Igumenshchev, R. Janezic, J.H. Kelly, T. J. Kessler, T. Z. Kosc, S. J. Loucks, J. A. Marozas, F. J. Marshall, A. V. Maximov, P. W. McKenty, D. T. Michel, J. F. Myatt, P. B. Radha, S. P. Regan, W. Seka, W. T. Shmayda, R.W. Short, A. Shvydky, S. Skupsky, C. Stoeckl, and B. Yaakobi (LLE); R. Betti, R. L. McCrory, and D. D. Meyerhofer (LLE and Departments of Mechanical Engineering and Physics and Astronomy, University of Rochester); R. K. Follett, D. H. Froula, R. J. Henchen, and R. Nora (LLE and Department of Physics and Astronomy, University of Rochester); J. A. Frenje, M. Gatu Johnson, and R. D. Petrasso (MIT); and D. T. Casey (LLNL) use the OMEGA Laser System to study the physics of implosions that are hydrodynamically equivalent to the ignition designs on the NIF (p. 18). It is shown that the highest hot-spot pressures (up to 40 Gbar) are achieved in moderate-fuel adiabat ($\alpha \simeq 4$) target designs, which are well understood using 2-D hydrocode simulations. The performance of lower-adiabat implosions is significantly degraded relative to the code predictions, a common feature between direct-drive implosions on OMEGA and indirect-drive cryogenic implosions on the NIF. Simplified theoretical models are developed to gain a physical understanding of the implosion dynamics that dictate the target performance. Such models indicate that degradations in the shell density and integrity (caused

by hydrodynamic instabilities during the target acceleration) coupled with hydrodynamics at stagnation are the main failure mechanisms in low-adiabat designs. To demonstrate ignition hydrodynamic equivalence in cryogenic implosions on OMEGA, the shell stability and laser coupling to the target must be improved.

- D. Haberberger, S. Ivancic, S. X. Hu, R. Boni, M. Barczys, R. S. Craxton, and D. H. Froula describe angular filter refractometry (AFR)—a novel diagnostic technique that has been developed to characterize high-density, long-scale-length plasmas relevant to high-energy-density-physics experiments (p. 50). AFR measures plasma densities up to 10^{21} cm^{-3} with a 263-nm probe laser. AFR is used to study the plasma expansion from CH foil and spherical targets that are irradiated with $\sim 9 \text{ kJ}$ of ultraviolet (351-nm) laser energy. The data elucidate the temporal evolution of the plasma profile for the CH planar targets and the dependence of the plasma profile on target radius for CH spheres.
- J. F. Myatt, R. W. Short, A. V. Maximov, W. Seka, D. H. Froula, D. H. Edgell, D. T. Michel, and I. V. Igumenshchev (LLE); J. Zhang (LLE and Department of Mechanical Engineering, University of Rochester); and D. E. Hinkel and P. Michel (LLNL) review the experimental evidence for multibeam laser–plasma instabilities of relevance to laser-driven inertial confinement fusion at the ignition scale, in both the indirect- and direct-drive approaches (p. 58). The instabilities described are cross-beam energy transfer (in both direct-drive targets and indirectly driven targets on the NIF), multibeam stimulated Raman scattering (in the context of indirect drive), and multibeam two-plasmon–decay instability (in direct drive). Advances in theoretical understanding and numerical modeling of these multibeam instabilities are reviewed.
- S. X. Hu, T. R. Boehly, V. N. Goncharov, and S. Skupsky (LLE); and L. A. Collins (LANL) present new quantum molecular dynamics (QMD) calculations of the thermal conductivity (κ) of deuterium, which plays an important role in understanding and designing inertial confinement fusion (ICF) implosions (p. 81). In particular, the QMD calculations cover the broad density ($\rho = 1.0$ to $\sim 700 \text{ g/cm}^3$) and temperature ($T = 5 \times 10^3 \text{ K}$ to $T = 8 \times 10^6 \text{ K}$) conditions undergone by ICF imploding fuel shells. Over these wide ranges of conditions in such coupled and degenerate plasmas, the extensively used Spitzer model and a variety of other thermal conductivity models break down. Compared with the “hybrid” Spitzer–Lee–More model currently adopted in the hydrocode *LILAC*, hydrodynamic simulations using the calculated κ_{QMD} have shown up to $\sim 20\%$ variations in predicting target performance for different ICF implosions on OMEGA and direct-drive–ignition designs for the NIF. The differences resulting from the use of κ_{QMD} are shown to be particularly relevant for lower-adiabat implosions and shell conditions during the early stages of an implosion.
- C. Dorrer, R. G. Roides, J. Bromage, and J. D. Zuegel demonstrate the use of cascaded nonlinearities in a regenerative laser amplifier to compensate for intracavity self-phase modulation (p. 97). Without compensation, self-phase modulation limits the generation of high-quality short optical pulses because of spatial self-focusing and spectral broadening. Simulations were performed to show that an intracavity negative nonlinearity can compensate for the positive nonlinearity from components at other locations in the cavity of a Nd:YLF regenerative amplifier. Experimental results obtained on two Nd:YLF regenerative amplifiers are in good agreement with predictions. Spectral broadening is significantly reduced, allowing for efficient amplification in a Nd:YLF power amplifier.

Matthew Barczys
Editor

Theory of Hydro-Equivalent Ignition for Inertial Fusion and Its Applications to OMEGA and the National Ignition Facility

Introduction

In inertial confinement fusion (ICF),¹ a spherical capsule is illuminated either directly with laser light² or indirectly within x rays generated by laser irradiation of the walls of a container (hohlraum) enclosing the capsule.³ The capsule consists of a cryogenic layer of deuterium and tritium (DT) frozen onto the inner surface of a spherical shell of ablator material. Photons are absorbed in the coronal plasma surrounding the shell via inverse bremsstrahlung, and the energy is thermally conducted to the surface of the shell, causing it to ablate. The ablating mass creates an equal and opposite force that causes the remaining shell material to implode. This mechanism is typically known as the “rocket effect.” The imploding shell attains a peak implosion velocity before converting a fraction of its kinetic energy into internal energy upon stagnation. The compressed core of an ICF capsule consists of a low-density (tens of g/cm³) and high-temperature (several keV’s) DT plasma (the hot spot) surrounded by a dense (hundreds of g/cm³) and cold (hundreds of eV’s) DT shell. If the thermal energy and areal density of the hot spot are large enough, the alpha particles generated from fusion reactions deposit their energy within the hot spot, triggering a thermal runaway process called “thermonuclear ignition.” A robust ignition would launch an alpha-driven burn wave in the surrounding dense fuel, leading to a significant fusion-energy output. The resulting energy gain (target gain = fusion energy/laser energy on target) depends on the shell’s areal density (ρR), which determines the fraction of fuel burned (Φ) according to the expression $\Phi = \rho R_{\text{g/cm}^2} / (7 + \rho R_{\text{g/cm}^2})$ (Ref. 4). The shell’s areal density is a critical parameter for the onset of ignition since it provides the inertial confinement for the hot-spot pressure.

To date, no significant fusion gain has been achieved in a laboratory setting, although experiments at the National Ignition Facility (NIF) have achieved core conditions, where the fusion energy released exceeds the energy in the fuel and the alpha-particle heating approximately doubles the number of fusion reactions.⁵ The Lawson criterion is the metric used to determine how close these implosions are to ignition.⁶ This criterion is obtained by balancing the energy lost from the

plasma to the total energy gained via fusion reactions, thereby determining the minimum values of performance metrics required to sustain a burning plasma. The Lawson criterion has long been used in magnetic confinement⁷ and only more recently has it been applied to ICF implosions in a useful form that depends on experimentally measured quantities.^{8–10} The criterion can be expressed through an overall ignition parameter $\chi \equiv P\tau/P\tau_{\text{ig}}$, where P is the hot-spot pressure, τ is the hot-spot energy’s confinement time, $P\tau_{\text{ig}} = 24 \epsilon_{\alpha} T^2 / \langle \sigma v \rangle$ is a function of ion temperature only with $\langle \sigma v \rangle$ representing the fusion reactivity $[\langle \sigma v \rangle(T)]$, and $\epsilon_{\alpha} = 3.5$ MeV is the alpha-particle birth energy. The ignition condition is defined such that when $\chi = 1$, the target gain = 1. Other performance metrics such as the ignition threshold factor (ITF and ITFx)¹¹ or the minimum energy required for ignition^{12,13} can be easily related to the Lawson criterion.¹⁰ The generalized Lawson criterion for ICF was first derived in one dimension by Zhou and Betti¹⁰ and later generalized to three dimensions by Chang *et al.*⁹ and Betti *et al.*⁸ Throughout the remainder of this article, we will consider only the generalized Lawson criterion.

The 1.8-MJ NIF Laser System is unique in its ability to field ignition-scale indirect- and direct-drive implosions. Because of high costs and low shot-repetition rates, most of the fundamental physics must be investigated at smaller-scale laser facilities such as the Omega Laser Facility.¹⁴ Experiments on the 30-kJ OMEGA laser are not expected to achieve ignition since the amount of laser energy that couples to the target is not enough to achieve the performance metrics required by the Lawson criterion. This gap in laser energy can be bridged using the theory of hydrodynamic equivalence. Hydro-equivalent implosions share a set of performance metrics that enable one to compare two implosions scaled in laser energy. Because the performance metrics scale hydro-equivalently, the Lawson criterion can be scaled up in energy from OMEGA to the NIF. The core idea of this work is to determine the performance required on an OMEGA-scale implosion to predict the achievement of ignition on a hydro-equivalently scaled NIF-sized target. The extrapolation on which this work is based is from the OMEGA Laser

System to a symmetric direct-drive NIF Laser System with two-dimensional (2-D) smoothing by spectral dispersion (SSD).¹⁵ It is important to emphasize that the NIF is currently not configured for symmetric illumination but could be with significant resource investment. This extrapolation will provide both guidance and a goal for OMEGA-scale cryogenic experiments.

The remaining four sections of this article (1) develop the theory of hydrodynamic equivalence in both one and three dimensions, establish design criteria for hydro-equivalent targets, and discuss the limitations of the theory; (2) present hydro-equivalent designs for the NIF and OMEGA laser-energy scales and confirm the theory developed in the previous section; (3) discuss the Lawson criterion parameter and its hydro-equivalent scaling, develop an analytical derivation of the scaling between hydro-equivalent implosions, present 2-D computational simulations supporting this simple model, and draw conclusions from the results; and (4) summarize the implications of this article.

Theory of Hydrodynamic Equivalence

In this section the theory of hydrodynamic equivalence is developed, showing how it connects to existing scaling relations and describing some of its limitations. As previously stated, hydrodynamic equivalence provides a tool for comparing the performance of implosions driven with different energies. The subsections (1) define hydro-equivalency in one dimension; (2) show that one-dimensional (1-D) hydro-equivalent implosions conserve their equivalency in three dimensions; (3) establish design criteria for hydro-equivalent targets; and (4) discuss the limitations of the theory.

1. One-Dimensional Hydrodynamic Equivalence

The simplest model for a 1-D implosion of a thin shell ($\Delta \ll R$) driven by an applied pressure P_{abl} includes the evolution equation for the shell radius R and the shell thickness Δ :

$$M_{sh}\ddot{R} = -4\pi P_{abl}R^2, \quad (1)$$

$$\Delta = \frac{5M_{sh}}{8\pi\rho_{abl}R^2}, \quad (2)$$

where ρ_{abl} is the density at the ablation surface. This simple model neglects the fraction of ablated mass and assumes that the shell mass is constant. Equation (1) is Newton's law applied to a thin shell driven by a constant pressure P_{abl} ; Eq. (2) shows that the shell expands like $1/R^2$ to conserve mass since the applied pressure maintains a fixed density profile given by $dP/dr = -\rho\dot{R}$ and $P \sim \rho^{5/3}$ for an isentropic implosion. The

resulting density profile is $\rho = \rho_{abl}(1-x/\Delta)^{3/2}$, where Δ is given by Eq. (2) and $x \equiv R_{abl} - r$ with R_{abl} being the radial location of the shell's outer surface. Equations (1) and (2) can be solved using the initial conditions for R and Δ . We define the initial time of the acceleration phase ($t = 0$) as the time soon after the main shock breaks out of the inner shell surface after the shell is set in motion by the initial shock (or shocks merging near the inner shell surface). For a strong shock, the post-shock velocity of the shell is approximately $V_{ps} \approx \xi_0 C_s(0)$, where $C_s(0)$ is the shell's sound speed after the shocks have passed through the shell. The factor $\xi_0 \equiv (3/\sqrt{5})(P_{sh}/P_{abl})^{1/5}$ is of the order of unity and depends on the ratio of the pressure used to drive the initial shock P_{sh} and the peak ablation pressure P_{abl} used to implode the target. The initial conditions for Eqs. (1) and (2) are

$$R(0) = R_0, \quad (3)$$

$$\dot{R}(0) = -\xi_0 C_s(0). \quad (4)$$

By multiplying Eq. (1) by \dot{R} and integrating between $t = 0$ and the end of the acceleration phase when the velocity has reached its maximum value V_{imp} and the radius has shrunk by the convergence ratio $CR_a \equiv R(0)/R_a$, where R_a is the radius at the end of the acceleration phase (note CR_a is the convergence ratio at the end of the acceleration phase and not the total convergence ratio at stagnation), the following energy relation is obtained:

$$\frac{1}{2}M_{sh}V_{imp}^2 \left(1 - \frac{\xi_0^2}{M_*^2}\right) = \frac{4\pi}{3}P_{abl}R_0^3 \left(1 - \frac{1}{CR_a^3}\right), \quad (5)$$

where $M_* = V_{imp}/C_s(0)$ is the implosion Mach number. Substituting the mass of a thin shell $M_{sh} = 4\pi\langle\rho\rangle\Delta R^2$ (with $\langle\rho\rangle = 2\rho_{abl}/5$) into Eq. (5) yields the relation between the in-flight aspect ratio (IFAR) and the Mach number M :

$$IFAR \equiv \frac{R(0)}{\Delta(0)} = M_*^2 \frac{1 - \xi_0^2/M_*^2}{1 - 1/CR_a^3}. \quad (6)$$

In the limit of large Mach numbers and large values of CR_a^3 , Eq. (6) reduces to the well-known scaling relation $IFAR \approx M_*^2$ (Ref. 16). The implosion model in Eqs. (1) and (2) and their initial conditions can be rewritten using the dimensionless variables $\hat{R} = R/R(0)$, $\hat{t} = tV_{imp}/R(0)$, and $\hat{\Delta} = \Delta/\Delta(0)$:

$$\ddot{\hat{R}} \approx -\frac{3}{2} \frac{1 - \xi_0^2/M_*^2}{1 - 1/CR_a^3} \hat{R}^2, \quad (7)$$

$$\hat{\Delta} = \frac{1}{\hat{R}^2}, \quad (8)$$

$$\hat{R}(0) = 1, \quad \dot{\hat{R}}(0) = -\frac{\xi_0}{M_*}, \quad \hat{\Delta}(0) = 1. \quad (9)$$

Equations (3)–(6) show that implosions with the same M_* , ξ_0 , and CR_a exhibit the same dimensionless trajectories and the same IFAR; therefore, this family of implosions is labeled “hydrodynamically equivalent.” By neglecting the term $1/\text{CR}_a^3$ in Eqs. (7)–(9), the dimensionless trajectory of a thin shell is uniquely determined by the Mach number M_* . Interestingly, in the limit of large Mach numbers and large convergence ratios, the dimensionless trajectories of both the radius and thickness approach a universal curve. Note that the thin-shell Eqs. (7)–(9) are valid only for large values of M_* and IFAR and as long as the shell’s time-dependent aspect ratio R/Δ is of the order of M_*^2 . Since R/Δ decreases like R^3 , it will eventually become smaller and of the order of M_* (instead of M_*^2). At this point, Eqs. (7)–(9) are no longer valid and the shell thickness will stop increasing; the shell density will start increasing, while the shell pressure will exceed the applied pressure. This limit is considered by Basko:¹⁷ the resulting final pressure at stagnation is proportional to the applied pressure amplified by a power law of the Mach number. According to Basko, that power law is $P_{\text{stag}} = P_{\text{abl}}M_*^4$, but according to the self-similar solution of Kemp *et al.*,¹³ $P_{\text{stag}} = P_{\text{abl}}M_*^3$. The important point is that by fixing the Mach number M_* and the applied pressure P_{abl} , all hydro-equivalent thin-shell implosions lead to the same final stagnation pressure.

In laser-driven implosions, a significant portion of the shell mass is ablated by the laser. The model [Eqs. (1) and (2)] of laser-driven implosions must be modified to include the effect of mass ablation. In the presence of mass ablation, the equations of motion are well described by the rocket model:¹⁸

$$M_{\text{sh}}\ddot{R} = V_{\text{ex}}\dot{M}_{\text{sh}}, \quad (10)$$

$$\dot{M}_{\text{sh}} = -4\pi\dot{m}_{\text{abl}}R^2, \quad (11)$$

where \dot{m}_{abl} is the mass ablation rate and V_{ex} is the exhaust velocity. Since the exhaust velocity is approximately the sound speed at the critical surface and proportional to a power of the laser intensity or radiation temperature, for a fixed laser intensity, Eq. (10) leads to the well-known rocket equation for the shell velocity,

$$\dot{R} = -\xi_0 C_s(0) - V_{\text{ex}} \ln \frac{M_{\text{sh}}(0)}{M_{\text{sh}}}. \quad (12)$$

Equations (11) and (12) can be rewritten in dimensionless form using the same variables used in Eqs. (7)–(9), leading to

$$\dot{\hat{R}} = -\frac{\xi_0}{M_*} - \frac{V_{\text{ex}}}{V_{\text{imp}}} \ln \frac{1}{\hat{M}_{\text{sh}}}, \quad (13)$$

$$\dot{\hat{M}}_{\text{sh}} = -\Psi \hat{R}^2, \quad (14)$$

where $\hat{M}_{\text{sh}} = M_{\text{sh}}/M_{\text{sh}}(0)$ is the dimensionless shell mass and

$$\Psi = \frac{4\pi\dot{m}_{\text{abl}}R(0)^3}{M_{\text{sh}}(0)V_{\text{imp}}}. \quad (15)$$

Since $\dot{m}_{\text{abl}}V_{\text{ex}}$ is the ablation pressure, the dimensionless parameter Ψ can be rewritten as

$$\Psi = \frac{3}{2} \frac{\text{IFAR}}{M_*^2} \frac{V_{\text{imp}}}{V_{\text{ex}}}. \quad (16)$$

If we consider a family of implosions with the same final fraction of unablated mass (same \hat{M}_{sh}^f), the final implosion velocity is given by Eq. (12):

$$V_{\text{imp}} = \xi_0 C_s(0) + V_{\text{ex}} \ln \left(\frac{1}{\hat{M}_{\text{sh}}^f} \right). \quad (17)$$

Notice that for this family of implosions,

$$\frac{V_{\text{ex}}}{V_{\text{imp}}} = \left(1 - \frac{\xi_0}{M_*} \right) / \ln \frac{1}{\hat{M}_{\text{sh}}^f} \quad (18)$$

and the remaining mass fraction \hat{M}_{sh}^f depends on the Mach number M_* , the parameter ξ_0 , and the ratio $V_{\text{ex}}/V_{\text{imp}}$. In the limit of large Mach numbers, the remaining mass fraction depends only on $V_{\text{ex}}/V_{\text{imp}}$. After substituting Eq. (18) into Eq. (16),

$$\Psi = \frac{3}{2} \frac{\text{IFAR}}{M_*^2} \ln \left(\frac{1}{\hat{M}_{\text{sh}}^f} \right) / \left(1 - \frac{\xi_0}{M_*} \right). \quad (19)$$

To achieve the same dimensionless trajectory and the same unablated mass fraction, Eqs. (13) and (14) require the same values of M_* , ξ_0 , and Ψ . An explicit relation between \hat{M}_{sh} and \hat{R} can be derived by integrating Eq. (13) after multiplying by Eq. (14):

$$\frac{\Psi}{3}(\hat{R}^3 - 1) = \frac{\xi_0}{M_*}(\hat{M}_{\text{sh}} - 1) - \left(1 - \frac{\xi_0}{M_*}\right) \frac{\hat{M}_{\text{sh}} - 1 - \hat{M}_{\text{sh}} \ln \hat{M}_{\text{sh}}}{\ln \hat{M}_{\text{sh}}^f}. \quad (20)$$

Rewriting Eq. (20) at the end of the acceleration phase yields a simple relation for the parameter Ψ :

$$\Psi = \left[\frac{1 - \hat{M}_{\text{sh}}^f}{\ln(1/\hat{M}_{\text{sh}}^f)} - \hat{M}_{\text{sh}}^f + \frac{\xi_0}{M_*} \left[1 - \frac{1 - \hat{M}_{\text{sh}}^f}{\ln(1/\hat{M}_{\text{sh}}^f)} \right] \right] \times \frac{3}{1 - \text{CR}_a^{-3}}, \quad (21)$$

indicating that for large Mach numbers and convergence ratios, the parameter Ψ depends only on the final fraction of unablated mass. Substituting Eq. (20) for Ψ leads to a relation between the IFAR and the Mach number,

$$\text{IFAR} = M_*^2 \frac{1 - \xi_0/M_*}{1 - 1/\text{CR}_a^3} \Theta, \quad (22)$$

$$\Theta = \frac{2}{\ln \hat{M}_{\text{sh}}^f} \left[\frac{1 - \hat{M}_{\text{sh}}^f}{\ln \hat{M}_{\text{sh}}^f} + \hat{M}_{\text{sh}}^f - \frac{\xi_0}{M_*} \left(1 + \frac{1 - \hat{M}_{\text{sh}}^f}{\ln \hat{M}_{\text{sh}}^f} \right) \right]. \quad (23)$$

In the limit of large M_* , the factor Θ depends only on the remaining mass fraction. In the limit of $1 - \hat{M}_{\text{sh}}^f \ll 1$, $\Theta \rightarrow (1 + \xi_0/M_*)$ and Eq. (21) reproduces Eq. (6) for the “no-ablation” case. For arbitrary $\hat{M}_{\text{sh}}^f < 1$, the rocket model maintains the $\text{IFAR} \sim M_*^2$ scaling of the no-ablation case, but the proportionality factor depends mostly on the unablated mass fraction. To preserve hydro-equivalence in the presence of ablation, one must preserve the value of \hat{M}_{sh}^f , thereby requiring that $V_{\text{ex}}/V_{\text{imp}}$ be constant. Within the framework of the rocket model, hydro-equivalence requires constant values for M_* , $V_{\text{ex}}/V_{\text{imp}}$, ξ_0 , and CR_a . Targets with these same dimensionless parameters exhibit the same dimensionless trajectory, IFAR, and unablated mass fraction.

It is useful to consider the ablation velocity V_{abl} , defined as the penetration velocity of the ablation front into the imploding shell. The ablation velocity is given by the ratio

$$V_{\text{abl}} = \frac{\dot{m}_{\text{abl}}}{\rho_{\text{abl}}}. \quad (24)$$

Equation (24) can be normalized to the implosion velocity and rewritten as

$$\frac{V_{\text{abl}}}{V_{\text{imp}}} = \frac{3}{5} \frac{1}{M_*^2} \frac{V_{\text{imp}}}{V_{\text{ex}}}, \quad (25)$$

where the relation $P_{\text{abl}} \approx \dot{m}_{\text{abl}} V_{\text{ex}}$ has been used. This shows that the ratio $V_{\text{abl}}/V_{\text{imp}}$ depends on the Mach number and the ratio $V_{\text{abl}}/V_{\text{imp}}$. Therefore, the requirements for 1-D hydro-equivalence can also be satisfied by fixing the values of M_* , $V_{\text{abl}}/V_{\text{imp}}$, ξ_0 , and CR_a .

For optimized implosions, the value of the convergence ratio at the end of the acceleration phase is not an arbitrary quantity. Typically the shell is driven inward until the remaining implosion time is of the same order of the sound speed’s traveling time through the shell:

$$\frac{R_a}{V_{\text{imp}}} \sim \frac{\Delta_a}{C_{\text{sa}}}, \quad (26)$$

where the subscript “a” indicates the end of the acceleration phase. This condition implies that for $R < R_a$, the shell density and pressure increase, with the latter exceeding the applied pressure. Therefore, even if the laser is still on for $R < R_a$, the effects on the implosion dynamics are negligible since the shell pressure exceeds the applied pressure. For a constant ablation pressure $C_{\text{sa}} = C_{\text{s}}(0)$, Eq. (26) requires that the IFAR at the end of the acceleration phase scales as the Mach number (rather than M_*^2): $\text{IFAR}_a = \nu M_*$, where ν is a constant of proportionality. Since the unablated mass fraction can be written as $\hat{M}_{\text{sh}}^f = \hat{\Delta}_a / \text{CR}_a^2$, $\text{IFAR}_a = \text{IFAR} / (\text{CR}_a^3 \hat{M}_{\text{sh}}^f)$, leading to an end-of-acceleration convergence ratio

$$\text{CR}_a = \left(\frac{M_*}{\nu} \frac{1 - \xi_0/M_*}{1 - 1/\text{CR}_a^3} \frac{\Theta}{M_{\text{sh}}^f} \right)^{1/3} \approx \left(\frac{M_*}{\nu} \frac{\Theta}{M_{\text{sh}}^f} \right)^{1/3}, \quad (27)$$

where the last term on the right-hand side is obtained in the large M_* limit.

In summary, 1-D hydro-equivalence is obtained for fixed values of M_* , V_a/V_{imp} , and ξ_0 . Implosions with equal values of these three dimensionless parameters exhibit the same unablated mass fraction, the same IFAR (both initial IFAR and

at the end of the acceleration phase), the same dimensionless trajectory, and the same dimensionless thickness. Given the importance of the stagnation pressure to the ignition conditions, we consider hydro-equivalent implosions driven by the same ablation pressures P_{abl} , achieving the same final stagnation pressure $P_{\text{stag}} \sim P_{\text{abl}} M_*^3$.

The last step is to translate the hydro-equivalence requirements into constraints on the physical parameters. Using the isentropic relation $P \sim \alpha \rho^{5/3}$ (where α is the adiabat), the Mach number and the ratio $V_{\text{abl}}/V_{\text{imp}}$ can be rewritten as

$$M_*^2 \sim \frac{V_{\text{imp}}^2}{\alpha^{3/5} P_{\text{abl}}^{2/5}}, \quad \frac{V_{\text{abl}}}{V_{\text{imp}}} \sim \frac{\dot{m}_{\text{abl}} \alpha^{3/5}}{P_{\text{abl}}^{3/5} V_{\text{imp}}}. \quad (28)$$

Since both the ablation pressure and ablation rate depend on the laser intensity I_L (for direct drive) or radiation temperature T_{rad} (for indirect drive), Eq. (28) shows that fixing P_{abl} (and \dot{m}_a), M_* , and $V_{\text{abl}}/V_{\text{imp}}$ requires setting the values of implosion velocity V_{imp} , adiabat α , and laser intensity I_L (or radiation temperature T_{rad}). Once the ablation pressure and shell adiabat are set, the parameter ξ_0 is not an independent parameter since the shock pressure P_{sh} is directly proportional to the adiabat $P_{\text{sh}} \sim \alpha \rho_{\text{ps}}^{5/3}$, where the post-shock density ρ_{ps} is roughly $4\times$ the initial density for a strong shock. It follows that all hydro-equivalent implosions designed to achieve the same stagnation pressure in one dimension require equal values of the implosion velocity, shell adiabat, and laser intensity (for direct drive) or radiation temperature (for indirect drive).

2. Three-Dimensional Hydrodynamic Equivalence

In this subsection, we show that the requirements for 1-D hydro-equivalence guarantee equivalence in three dimensions provided that the initial seeds for the hydrodynamic instabilities scale proportionally to the size of the target radius R . The departure from spherical symmetry is caused primarily by the Richtmyer–Meshkov^{19,20} (RM) and Rayleigh–Taylor^{21,22} (RT) instabilities. Below, we will apply the hydro-equivalence concepts to only the RT instability since the RM instability follows similar arguments.

In ICF implosions, the RT instability develops on the ablation front during the acceleration phase and at the inner shell surface during the deceleration phase. We first consider the acceleration phase. Depending on the initial level of nonuniformities and the unstable spectrum, the RT instability can either be contained within the linear regime or develop a fully nonlinear bubble front. We will consider these two cases separately.

In the linear regime, the RT growth rates approximately follow Takabe's formula.^{23,24} The number of e foldings of growth is the integral of the growth rates over the duration of the acceleration phase (t_0), leading to

$$N_e^{\text{RT}} = \int_0^{t_0} \gamma_{\text{RT}} dt = \int_0^{t_0} (\sqrt{k g} - 3k V_{\text{abl}}) dt, \quad (29)$$

where k is the wave number $k \equiv \ell/R$, ℓ is the mode number, R is the time-dependent shell radius, $g = -\ddot{R}$ is the shell acceleration, and V_{abl} is the ablation velocity. Given that all hydro-equivalent targets have the same dimensionless radius \hat{R} and are driven up to the same convergence ratio CR_a , taking the dimensions out of the expression on the right-hand side of Eq. (29) yields

$$N_e^{\text{RT}} = \int_{\text{CR}_a^{-1}}^1 \left(\sqrt{\ell \frac{\ddot{\hat{R}}}{\hat{R}}} - 3 \frac{\ell}{\hat{R}} \frac{V_{\text{abl}}}{V_{\text{imp}}} \right) \frac{d\hat{R}}{\hat{R}}, \quad (30)$$

where $\hat{R} = R/R_0$. As discussed in the previous subsection, 1-D hydro-equivalence requires equal values of $V_{\text{abl}}/V_{\text{imp}}$; therefore Eq. (30) shows that hydro-equivalent implosions exhibit the same RT growth factors for all mode numbers. The effects of the RT instability on target performance can be assessed by comparing the mode amplitude η_ℓ^a with the target thickness Δ_a at the end of the acceleration phase for each mode. Using the results of the rocket model for the target thickness ($\Delta_a = \Delta_0 \text{CR}_a^2 \hat{M}_{\text{sh}}^f$), the ratio η_ℓ^a/Δ_a can be written as

$$\frac{\eta_\ell^a}{\Delta_a} = \frac{\eta_\ell(0) e^{N_e^{\text{RT}}}}{\Delta_0 \text{CR}_a^2 \hat{M}_{\text{sh}}^f}. \quad (31)$$

Since CR_a and \hat{M}_{sh}^f are the same for hydro-equivalent implosions, Eq. (31) shows that three-dimensional (3-D) hydro-equivalence for the linear RT instability is attained when the initial seeds $\eta_\ell(0)$ are proportional to the initial target thickness.

While Eqs. (30) and (31) prove 3-D equivalence in the linear phase of the RT instability, the most important effects of the RT instability occur when the RT bubble front becomes nonlinear and penetrates deeply into the target. It is well known that a fully developed RT bubble front grows proportionally to the distance traveled by the shell during the acceleration phase. By defining the bubble front's penetration distance h_b , the well-known scaling relation $h_b = \beta g t^2$ applies for a fully developed, fully nonlinear multimode bubble front with the coefficient $\beta \approx 0.05$ to 0.07 (Refs. 25–28). For a time-dependent acceleration, the dimensionally correct bubble-front penetration would be $h_b = 2\beta \int_0^t dt' \int_0^{t'} dt'' g(t'')$. At the end of the accel-

eration phase, the parameter h_b can be written in terms of the distance traveled by the shell during the acceleration phase:

$$h_b^a = 2\beta(R_0 - R_a) = 2\beta R_0(1 - CR_a^{-1}). \quad (32)$$

The figure of merit that measures the effects of the RT instability on the target performance is the ratio between the bubble-penetration distance and the shell thickness at the end of the acceleration. Using the results of the rocket model that ratio is

$$\frac{h_b^a}{\Delta_a} = \frac{2\beta}{\hat{M}_{sh}^f} \text{IFAR} \frac{(1 - CR_a^{-1})}{CR_a^2}. \quad (33)$$

Since all 1-D hydro-equivalent implosions exhibit equal values of \hat{M}_{sh}^f , IFAR, and CR_a , the nonlinear RT figure of merit h_b^a/Δ_a will be the same for hydro-equivalent implosions. It follows that the effects of the acceleration-phase RT instability on target performance are the same for hydro-equivalent implosions regardless of whether the RT perturbation growth remains within the linear phase or grows into the fully developed nonlinear regime provided that the initial RT seeds scale with the target thickness.

While the acceleration-phase RT instability is fully hydro-equivalent, the deceleration-phase RT instability is not. The growth rate of the deceleration-phase RT has a similar form to Eq. (30) with the exception that the coefficient of the ablative stabilization is 1.4 instead of 3 (Ref. 29) and that mass ablation is driven by the heat leaving the hot spot rather than the heat flux coming from the laser (or x rays). The RT growth rate in the constant deceleration phase on the inside of the shell was fit to the following equation:

$$\gamma_{RT} = 0.9 \sqrt{\frac{k\langle g \rangle}{1 + k\langle L_m \rangle}} - 1.4k\langle \bar{v}_{abl} \rangle, \quad (34)$$

where k is the wave number, $\langle g \rangle$ is the average acceleration, $\langle L_m \rangle$ is the density scale length, and $\langle \bar{v}_{abl} \rangle$ is the deceleration-phase ablation velocity. In this case the deceleration-phase ablation velocity depends on the Spitzer conductivity³⁰ of the hot spot: $\langle \bar{v}_{abl} \rangle \sim T_0^{5/2}/R_{hs}\rho_{sh}$, where T_0 is the central hot-spot temperature, R_{hs} is the hot-spot radius, and ρ_{sh} is the shell density. It is possible to show that the ablative stabilization term for the deceleration phase is not hydro-equivalent but instead depends on the target size like $\langle \bar{v}_{abl} \rangle \sim R^{-0.5}$. The ablative stabilization of the deceleration-phase RT is important only for

implosion velocities exceeding 400 km/s or when the alpha-particle heating is significantly close to ignition conditions, leading to large ablation velocities. Since alpha-particle heating is clearly not hydro-equivalent, as long as hydro-equivalent targets without alpha-particle energy deposition are compared, the effects of the ablative stabilization on the deceleration-phase RT growth can be neglected for $V_{imp} < 400$ km/s and the conditions for hydro-equivalency of the RT instability are retained as well for the deceleration phase. A more-detailed analysis of hydro-equivalency of the deceleration phase is the subject of a forthcoming publication.

In summary, the conditions of 1-D hydro-equivalency (see **One-Dimensional Hydrodynamic Equivalence**, p. 2) requiring equal values of implosion velocity V_{imp} , shell adiabat α , and laser intensity I_L (for direct drive) or radiation temperature T_{rad} (for indirect drive) guarantee 3-D hydrodynamic equivalence provided that the initial level of surface roughness scales proportionally to the target size. If the main source of nonuniformities is laser imprinting (as in the case of direct drive), 3-D hydro-equivalence requires that the relative size of the laser-intensity variations ($\delta I/I$) be the same among hydro-equivalent targets.

3. Design Criteria for Hydro-Equivalent Targets

This section highlights the design criteria for direct-drive hydro-equivalent implosions. To design a family of implosions with the same V_{imp} , α , and I_L , one must specify the target radius and thickness, as well as the laser pulse shape. The latter consists of an initial low-intensity pulse (also called the “foot”) that sets the adiabat of the shell through one or more shocks and a main drive that accelerates the shell to the final implosion velocity. While there are different ways of designing the foot of the pulse, the main drive is defined by the total energy E_L , the peak power P_L , and the main pulse length t_L . Most of the pulse energy is contained within the main pulse. The energy, power, and length of the main pulse are related through $E_L \approx P_L t_L$. Since the laser power is $P_L \approx 4\pi R_0^2 I_L$, keeping the same intensity on target requires scaling the laser power, with the target surface $P_L \sim R_0^2$. To drive the capsule to the same final implosion velocity, the pulse length must be proportional to the implosion time $t_L \sim R_0/V_{imp}$ and, therefore, the laser energy must scale as $E_L \sim 4\pi R_0^3 I_L/V_{imp}$. It follows that for hydro-equivalent implosions, the laser energy must scale as the target volume $E_L \sim R_0^3$. For hydro-equivalent targets, the final shell kinetic energy scaling is proportional to the laser energy in the main drive, leading to $(1/2)M_{sh}V_{imp}^2 \sim E_L$. To achieve the same implosion velocity, the target mass must, therefore,

scale with the laser energy $M_{\text{sh}} \sim E_L \sim R_0^3$. Since the target mass is proportional to the shell volume $M_{\text{sh}} \sim 4\pi R_0^2 \Delta_0 \rho_0$, for the same initial density, the shell thickness must scale with the target radius $\Delta_0 \propto R_0$.

The basic design criteria for hydro-equivalent implosions consist of specifying the foot of the laser pulse to launch shocks of the same strength to set the shell on the same adiabat α , using a total laser energy proportional to the target volume, $E_L \sim R_0^3$; a peak laser power proportional to the target surface, $P_L \sim R_0^2$;

a pulse length proportional to the target radius, $t_L \sim R_0$; and a shell thickness proportional to the shell radius, $\Delta_0 \propto R_0$. One can express these criteria in terms of laser energy rather than target radius, leading to $R_0 \sim E_L^{1/3}$, $\Delta_0 \sim E_L^{1/3}$, $P_L \sim E_L^{2/3}$, and $t_L \sim E_L^{1/3}$. This scaling can be applied to various performance metrics that have been analytically derived and fit to power laws from simulation databases previously developed.^{8,31} Table 137.I reviews most of the important ICF performance metrics and their hydro-equivalent scaling with laser energy.

Table 137.I: Hydrodynamic scaling relations for ICF implosions and their hydro-equivalent scaling relations for 350-nm light. ($I_{15} = I_L / 10^{15}$; T_n is the neutron-averaged ion temperature.)

Performance Metric	Scaling Relation	Hydro-Equivalent Scaling
Hydrodynamic efficiency	$\eta \approx \frac{0.051}{I_{15}^{0.25}} \left[\frac{V_{\text{imp}}(\text{cm/s})}{3 \times 10^7} \right]^{0.75}$	Constant
Neutron yield ($\times 10^{16}$)	$Y_{1-D} \approx \left(\frac{T_n}{4.7} \right)^{4.72} [\rho R_{\text{tot}(n)}]^{0.56} \left(\frac{m_{\text{sh}}^{\text{stag}}}{0.12} \right)$	$Y_{1-D}^{\text{no } \alpha} \sim E_L^{3/2}$
Shell areal density (g/cm ²)	$(\rho R)_{\text{max}} \approx \frac{1.2}{\alpha_{\text{inn}}^{0.54}} \left[\frac{E_L(\text{kJ})}{100} \right]^{0.33} \left[\frac{V_{\text{imp}}(\text{cm/s})}{3 \times 10^7} \right]^{0.06}$	$(\rho R)_{\text{max}} \sim E_L^{3/2}$
Shell density (g/cm ²)	$\langle \rho \rangle_{\rho R} \approx \frac{425}{\alpha_{\text{inn}}^{1.12}} I_{15}^{0.13} \left[\frac{V_{\text{imp}}(\text{cm/s})}{3 \times 10^7} \right]$	Constant
Shell IFAR	$\text{IFAR} \approx \frac{40}{\langle \alpha_{\text{if}} \rangle^{0.72}} I_{15}^{-0.27} \left[\frac{V_{\text{imp}}(\text{cm/s})}{3 \times 10^7} \right]^{2.12}$	Constant
Hot-spot areal density (g/cm ²)	$\rho R_{\text{hs}} \approx \frac{0.31}{\alpha_{\text{inn}}^{0.55}} \left[\frac{E_L(\text{kJ})}{100} \right]^{0.27} \left[\frac{V_{\text{imp}}(\text{cm/s})}{3 \times 10^7} \right]^{0.62}$	$\rho R_{\text{hs}} \sim E_L^{0.27}$
Hot-spot temperature (keV)	$\langle T_{\text{hs}} \rangle \approx \frac{2.96}{\alpha_{\text{inn}}^{0.15}} \left[\frac{E_L(\text{kJ})}{100} \right]^{0.07} \left[\frac{V_{\text{imp}}(\text{cm/s})}{3 \times 10^7} \right]^{1.25}$	$\langle T_{\text{hs}} \rangle \sim E_L^{0.07}$
Hot-spot pressure (Gbar)	$\langle P_{\text{hs}} \rangle \approx \frac{345}{\alpha_{\text{inn}}^{0.90}} \left[\frac{V_{\text{imp}}(\text{cm/s})}{3 \times 10^7} \right]^{1.85}$	Constant
Stagnation aspect ratio	$A_{\text{stag}} \approx \frac{1.48}{\alpha_{\text{inn}}^{0.19}} \left[\frac{V_{\text{imp}}(\text{cm/s})}{3 \times 10^7} \right]^{0.96}$	Constant

4. Non-Hydro-Equivalent Physics

Although the hydro-equivalent scaling relations hold well over nearly two orders of magnitude in laser energy (see the next section below), not all of the physical processes that occur in ICF implosions scale hydrodynamically. Hydrodynamic equivalence breaks down when non-scalable physics significantly impact target performance. A nonexhaustive list of non-scalable physics includes radiation transport, thermal conduction, fusion reactions, and laser–plasma interactions (LPI’s). Radiation transport can significantly impact radiation and shell-ablation physics in both the acceleration and deceleration phases. If the mean free path of photons is larger than the stopping power of the ablator of an implosion capsule, these photons will penetrate into the DT fuel and deposit their energy, thereby raising the adiabat. This occurs on smaller-scale targets, such as those on OMEGA.

Thermal transport in the hot spot is not hydro-equivalent. As shown by Zhou and Betti,³¹ the hot-spot temperature scales weakly with laser energy (or target size): $T_{\text{hs}} \sim E_L^{0.07} \sim R^{0.21}$. Since the fusion yield is a strong function of temperature, this weak dependence becomes important when scaling ICF implosions from OMEGA to the NIF. Another non-hydro-equivalent effect is the ablative stabilization of the deceleration-phase RT instability as discussed in the next section.

Fusion-energy deposition and laser scattering caused by LPI’s are inherently non-scalable hydrodynamically since alpha-particle energy deposition depends on the shell’s areal density relative to a fixed mean-free path as well as on the proximity to the ignition conditions, and the LPI’s are threshold-dependent instabilities. This means that all hydrodynamic quantities (except the gain) must be calculated without alpha-particle deposition (no-alpha quantities). Therefore, when scaling up in size and energy to assess the target performance with respect to the ignition conditions, one must use an ignition criterion given in terms of no-alpha quantities.^{8,9} LPI’s will not be considered in this work. Although a significant amount of work has been invested in understanding LPI effects on direct-drive target performance^{32–36} and two-plasmon–decay thresholds,^{37–41} this work will assume that if any threshold is exceeded on some energy scale versus another, a mitigation strategy will be employed to address it.

Hydro-Equivalent Implosion Design

In this section we will cover the design and performance of the two hydro-equivalent implosion designs that will be used for the remainder of this article. The latter half of this section will compare the designs to the hydro-equivalent scaling predictions outlined in **Theory of Hydrodynamic Equivalence** (p. 2).

The OMEGA-scale target is based on current cryogenic targets that are routinely imploded on OMEGA.⁴² The OMEGA-scale target [shown in Fig. 137.1(a)] has $\sim 10 \mu\text{m}$ of plastic ablator, $41 \mu\text{m}$ of DT ice, and an outer radius of $430 \mu\text{m}$. This design is imploded with 27 kJ of laser energy, and when simulated with the multidimensional hydrocode *DRACO*,⁴³ it achieves an implosion velocity of $\sim 350 \text{ km/s}$, has an average in-flight adiabat of 3, and an $\text{IFAR}_{R=2/3R_0}$ of 26. The IFAR is calculated when the shell radius is approximately $2/3$ of its initial inner radius. It achieves a neutron-averaged areal density of 300 mg/cm^2 and a neutron yield of 1.6×10^{14} in 1-D simulations. The NIF-scale target [shown in Fig. 137.1(b)] is geometrically scaled from the OMEGA-scale target using the hydro-equivalent scaling relations developed on p. 2. This results in a factor-of-4 increase in the target radius when scaling the laser energy up to 1.84 MJ. Because of differences in radiation transport at these two laser-energy scales, a small change in the target design is required to compensate for deviations from hydro-equivalence. The OMEGA-scale target has insufficient preheat shielding in the CH ablator, which results in an increase in the fuel adiabat when the ablator prematurely ablates. Some of the plastic ablator in the NIF-scale design is mass-equivalently exchanged for DT ice. This leads to lower preheat shielding, resulting in the adiabat remaining the same for the two implosions. The NIF-scale target has the same implosion velocity, adiabat, and IFAR but is predicted to achieve a neutron-averaged areal density of 1.2 g/cm^2 and a 1-D yield of 8.6×10^{16} without alpha-particle deposition. When alpha-particle deposition is turned on, the implosion achieves a neutron yield of 3.3×10^{19} , resulting in a gain of 49.

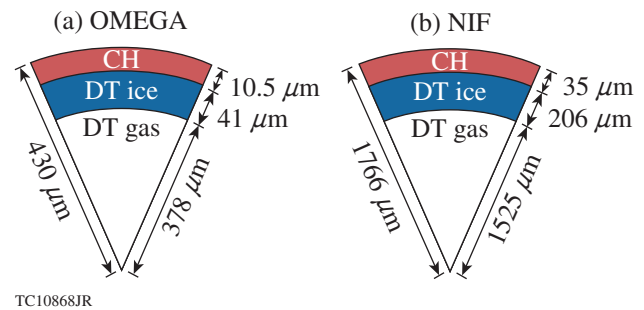
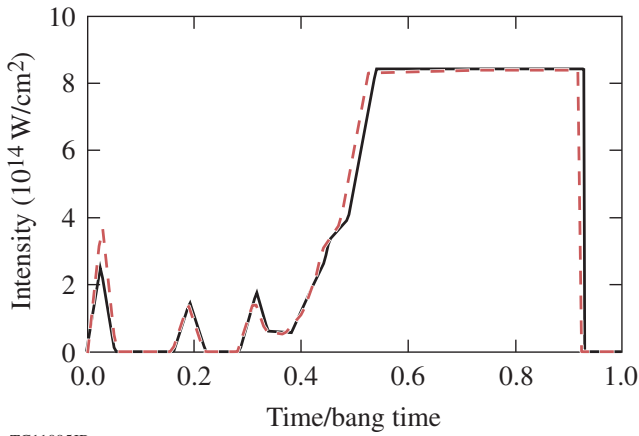


Figure 137.1

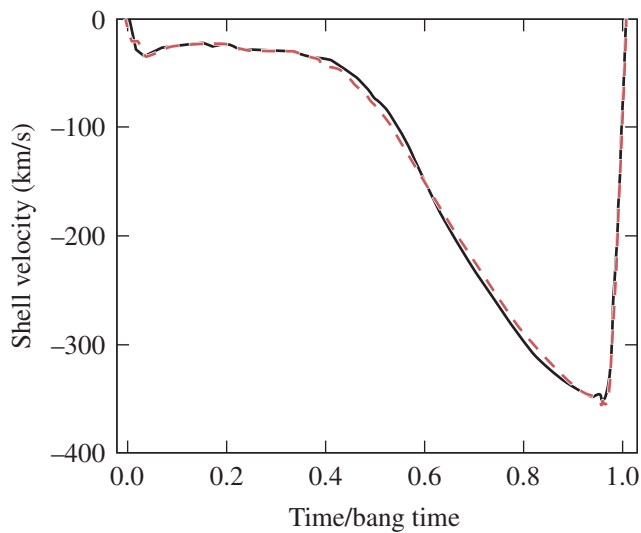
Cryogenic target geometry and composition for (a) OMEGA-scale and (b) NIF-scale targets.

When plotted in terms of laser intensity and dimensionless time t/t_{bang} , the laser pulses for the NIF and OMEGA are virtually identical as shown in Fig. 137.2. Here, t_{bang} is the so-called “bang time,” defined as the time of peak neutron rate. The time evolution of the implosion velocity and IFAR are the same for NIF-scale and OMEGA-scale targets. Figure 137.3 shows the



TC11095JR

Figure 137.2 Triple-picket laser-intensity pulses versus normalized time (t/t_{bang}) for the NIF-scale (solid black line) and OMEGA-scale (dashed red line) targets.

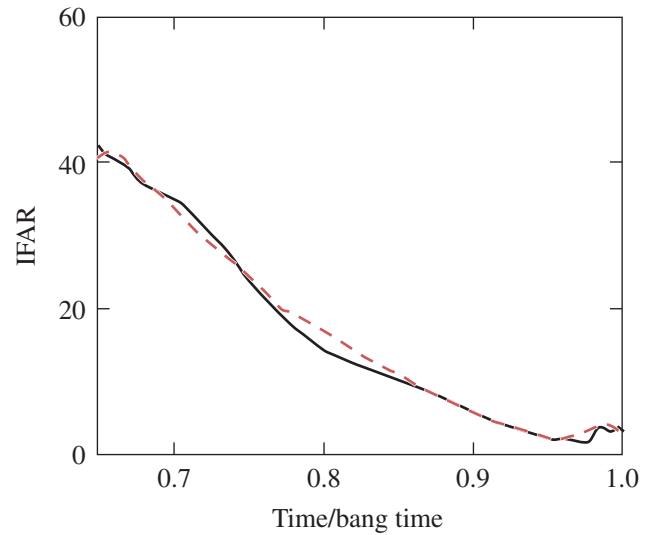


TC10869JR

Figure 137.3 Shell velocity versus normalized time for the NIF-scale (solid black line) and OMEGA-scale (dashed red line) targets.

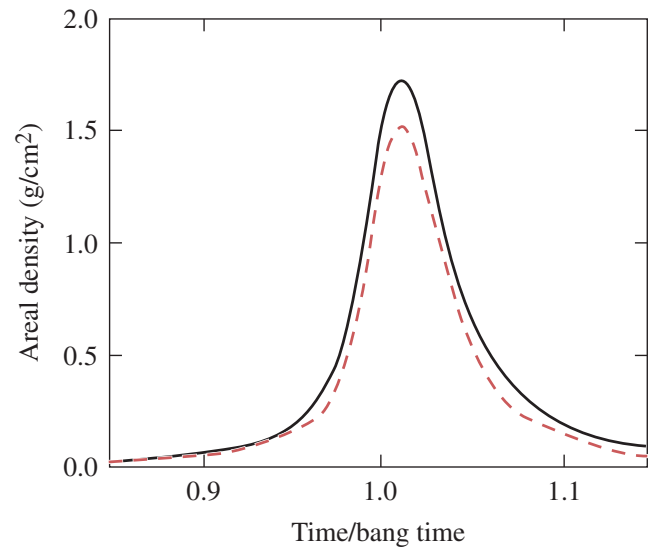
shell velocity versus normalized time for the NIF-scale and OMEGA-scale designs in solid black and dashed red lines, respectively. The two curves are nearly identical, illustrating that they have the same 1-D hydrodynamics. Figure 137.4 plots the IFAR against normalized time and it too shows hydro-equivalent behavior, illustrating that they have the same acceleration-phase RT growth in three dimensions since the adiabats and implosion velocities are the same. Figure 137.5 shows the areal

density versus normalized time for the NIF-scale target (solid black) and the OMEGA-scale target (dashed red) scaled by the energy ratio of the two designs, $\epsilon \equiv E_L^{\text{NIF}} / E_L^{\Omega}$, to the one-third power. This scaling comes from the laws described in **Theory of Hydrodynamic Equivalence** (p. 2) and shows the 1-D



TC10869JR

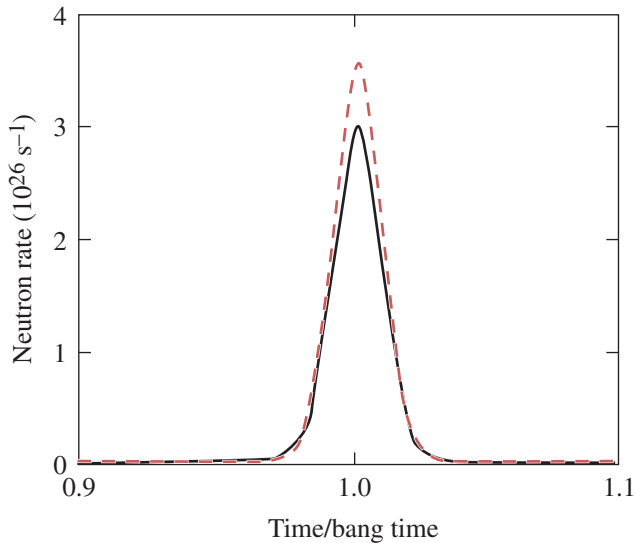
Figure 137.4 In-flight aspect ratio (IFAR) versus normalized time for the NIF-scale (solid black line) and OMEGA-scale (dashed red line) targets.



TC10870JR

Figure 137.5 Scaled total areal density versus normalized time for the NIF-scale (solid black line) and OMEGA-scale (dashed red line) targets multiplied by $\epsilon^{1/3}$.

areal density and neutron rate scale as predicted. Figure 137.6 compares the neutron rate versus normalized time, where the NIF neutron rate is shown as a solid black line and the scaled OMEGA neutron rate as a dashed red line, which scales as $\epsilon^{7/6}$. The neutron rate scales with $E_L^{3/2}$ and time scales as $E_L^{1/3}$. This shows good agreement between the theory and simulations.



TC10870JR2

Figure 137.6

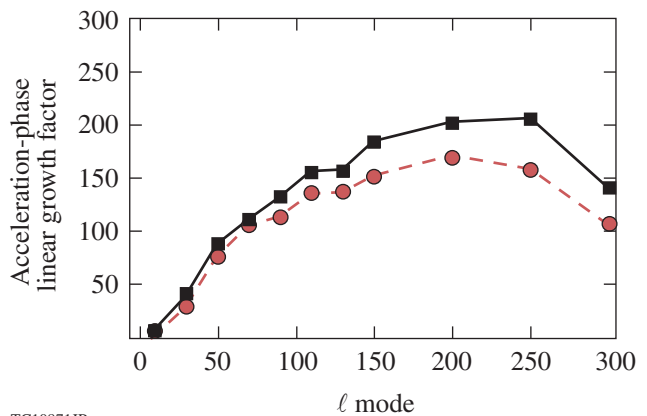
Scaled total neutron rate versus normalized time for the NIF-scale (solid black line) and OMEGA-scale (dashed red line) targets multiplied by $\epsilon^{7/6}$.

In terms of multidimensional performance, the two designs are very nearly hydro-equivalent. Two-dimensional *DRACO* simulations were run to assess the performance of the implosions and compare it with the hydro-equivalent scaling theory. All simulations used the *SESAME*^{44,45} equation of state for the plastic ablator and *FPEOS*⁴⁶ for the DT fuel. Single-mode simulations were performed in half-wavelength wedges with a minimum of 20 azimuthal cells and sufficient radial zoning to ensure a minimum of six points in the $1/k$ distance away from the ablation surface. The radial zoning was increased with ℓ -mode number to keep the same spatial aspect ratio in the Lagrangian mesh throughout the entire set. This ensured that the amplitudes of the higher harmonics were typically smaller than one tenth of the fundamental-mode amplitude. It is important to note that the seed amplitude between the two designs was kept hydro-equivalent by a factor of $\epsilon^{1/3}$ in accordance with the change in target size. It should also be mentioned that all of the simulations containing an inner-surface ice roughness had a power spectrum whose amplitude scaled as ℓ^{-2} , where ℓ spanned every even

mode from 2 to 50, unless otherwise specified. These simulations were performed in 90° wedges, and the minimum number of azimuthal cells required to adequately resolve the physical impact of these perturbations was ten per half-wavelength at mode 50.

In the acceleration-phase RT growth, the seed amplitude was set by a single cosine surface perturbation on the outside of the shell such that the growth of the mode was always in the linear stage. Simulations of the single-mode linear growth factor confirm that the acceleration-phase RT growth factors scale approximately hydro-equivalently. Figure 137.7 shows the acceleration-phase linear growth factor versus the ℓ mode for the NIF-scale (solid black line) and OMEGA-scale (dashed red line) designs. The two curves are close together for ℓ modes ranging from 10 to 300. The small difference between the two curves is attributed to the non-hydro-equivalent radiation transport that increases the scaled density gradient scale length on the OMEGA-scale target with respect to the NIF-scale target. The initial amplitude of the mode is chosen just after the beginning of the acceleration phase, where the effect of any phase inversions resulting from shock breakout have already taken place. Despite these differences, the acceleration-phase growth factors of the two designs are within 20% of each other, justifying the statement of their hydro-equivalence.

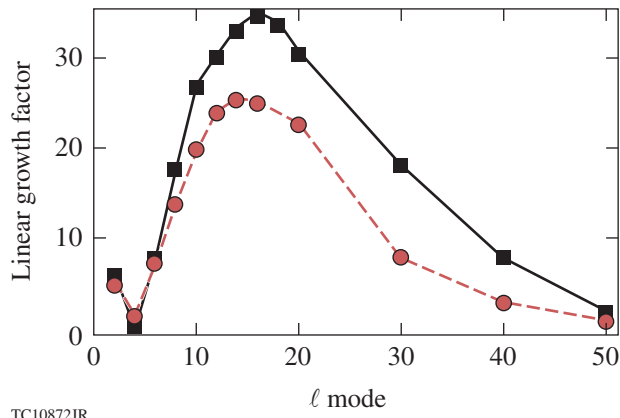
A series of single-mode growth factor simulations in the deceleration phase were performed and verified that the deceleration phase is not exactly hydro-equivalent as expected (see **Non-Hydro-Equivalent Physics**, p. 8). In this case the seed perturbation was set as a single cosine-mode density perturbation



TC10871JR

Figure 137.7

Single-mode linear growth factors versus ℓ mode for acceleration-phase RT growth for the NIF-scale (solid black line) and OMEGA-scale (dashed red line) targets.



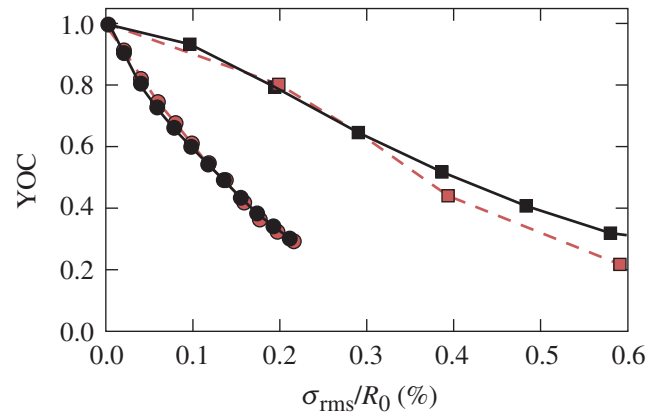
TC10872JR

Figure 137.8
Single-mode linear growth factors versus ℓ mode for deceleration-phase RT growth for the NIF-scale (solid black line) and OMEGA-scale (dashed red line) targets.

on the inside of the target at the DT gas/ice interface. Figure 137.8 shows the total linear growth factor versus ℓ mode for the two designs. It shows that the linear growth factors are comparable for low- ℓ modes but diverge for $\ell > 10$. A phase inversion first occurs at mode $\ell = 4$ (and for every mode greater than 4), giving the illusion that the mode does not grow. The difference between the growth factors of the two designs can be explained by applying the theory developed in Ref. 29, as outlined in **Theory of Hydrodynamic Equivalence** (p. 2). The difference in the linear RT growth factors has little impact on the yield-over-clean (YOC) when performing more-representative simulations, where we define the YOC as the multidimensional yield divided by the 1-D yield. A series of multimode ice spectrum simulations were performed to study their effect on the YOC, where the amplitudes of the modes were not constrained to be within the linear regime. As shown in Fig. 137.9, the YOC decreases at the same rate for both the NIF-scale (solid black line) and OMEGA-scale (dashed red line) targets as a function of the normalized ice roughness. This is the case for both spectrums where the ℓ mode ranged from 2 to 36 (squares) and 10 to 36 (circles). Altering the starting mode in the spectrum made it possible for a different ℓ mode to dominate the hot-spot dynamics to ensure the YOC was the same for any implosion. Choosing an end mode of 36 in this case instead of 50 had no significant effect in the simulations other than decreasing the required computation time.

To summarize, hydro-equivalent designs were presented and tested against the hydro-equivalent theory to ensure hydro-equivalence. In terms of 1-D hydro-equivalence, the designs had identical implosion velocities, laser intensities, adiabats,

and IFAR's. The target geometry scaled with the laser energy, and when applied to the scaling laws shown in Table 137.I, the simulated performance metrics were in good agreement with theory (Figs. 137.3 and 137.4). In terms of multidimensional hydro-equivalence, similar RT growth in the acceleration phase (Fig. 137.7) was predicted by theory and corroborated by simulations. Slight differences in the deceleration phase were predicted by linear theory and seen in simulations (Fig. 137.8); however, this effect is negligible in terms of performance for these two designs (as shown in Fig. 137.9). The OMEGA-scale and NIF-scale designs presented are approximately hydro-equivalent.



TC11081JR

Figure 137.9
Results from two-dimensional *DRACO* simulations plotting yield-over-clean (YOC) versus normalized ice roughness for NIF-scale (solid black lines) and OMEGA-scale (dashed red lines) targets for an ice spectrum with ℓ modes from 2 to 36 (squares) and 10 to 36 (circles).

Hydro-Equivalent Ignition Scaling of ICF Implosions

In this section, the hydrodynamic equivalence theory developed on p. 2 is applied to the Lawson criterion to create hydro-equivalent ignition-scaling relations for ICF implosions. A simple clean-volume analysis will be derived to estimate the scaling. Numerical simulations at the NIF and OMEGA scales are shown to support this result. Finally, ignition threshold performance metrics for hydro-equivalent ignition on OMEGA will be presented and discussed.

The Lawson criterion parameter defines the performance threshold required for an igniting plasma. It is defined as $\chi \equiv P\tau/P\tau_{ig}$, where P is the plasma pressure, τ is the confinement time, and $P\tau_{ig}$ is the product of the two required for ignition. The Lawson parameter can be expressed in terms of measurable parameters for ICF:^{8,9}

$$\chi \equiv (\rho R_{\text{g/cm}^2})^{0.61} \left(\frac{0.24 Y_{16}}{m_{\text{mg}}^{\text{DT}}} \right)^{0.34} \text{YOC}^{0.06}, \quad (35)$$

where $\rho R_{\text{g/cm}^2}$ is the 3-D neutron-averaged areal density in units of g/cm^2 , Y_{16} is the 3-D neutron yield in units of 10^{16} , $m_{\text{mg}}^{\text{DT}}$ is the mass of the DT fuel in milligrams, and YOC is the yield-over-clean defined as the measured yield over the simulated 1-D yield. All hydrodynamic quantities are calculated without alpha-particle deposition. The YOC is used as a measure of the impact of the 3-D nonuniformities such that $Y_{3\text{-D}} = Y_{1\text{-D}} \times \text{YOC}$. The YOC is also used to account for 3-D degradation of the areal density, where

$$\rho R_{3\text{-D}} \sim \rho R_{1\text{-D}} \times \text{YOC}^{0.17}. \quad (36)$$

The power index of 0.17 is derived by fitting the areal-density degradation from several 2-D simulations as shown in Fig. 137.10. This stipulates the Lawson parameter to scale as $\text{YOC}^{0.5}$:

$$\chi = (\rho R_{\text{g/cm}^2}^{1\text{-D}})^{0.61} \left(\frac{0.24 Y_{16}^{1\text{-D}}}{m_{\text{mg}}^{\text{DT}}} \right)^{0.34} \text{YOC}^{0.5}. \quad (37)$$

The Lawson parameter can be scaled from OMEGA to the NIF using the hydro-equivalence scaling laws derived in **Theory of Hydrodynamic Equivalence** (p. 2), where $\rho R_{1\text{-D}} \sim E^{1/3}$, $Y_{1\text{-D}} \sim E^{3/2}$, and $m \sim E$, to find

$$\chi \sim E^{0.37} \text{YOC}^{0.5}. \quad (38)$$

Taking the ratio of Eq. (38) from two different implosions, we can compare one hydro-equivalent implosion to another in terms of the Lawson parameter. In this way it is possible to determine how close non-igniting implosions would be to achieving ignition if the laser energy and target geometry were hydro-equivalently scaled to an implosion that could ignite. Taking the definition of ignition to be when the implosion achieves marginal gain ($\chi = 1$), and assuming that ignition will occur at NIF's laser energy, the Lawson parameter for an OMEGA-scale implosion considered to be hydro-equivalently igniting would be

$$\chi_{\Omega\text{-eq ig}} = 0.21 \left(\frac{\text{YOC}_{\text{NIF}}}{\text{YOC}_{\Omega}} \right)^{-0.5}. \quad (39)$$

The YOC ratio in Eq. (39) is inferred using both an analytical clean volume analysis and 2-D hydrodynamic simulations.

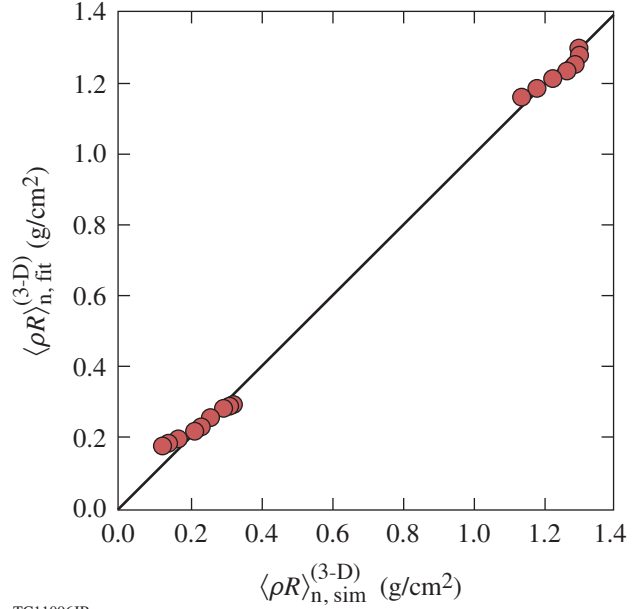


Figure 137.10

Neutron-averaged 3-D areal density from simulations (red circles) compared to its numerical fit of Eq. (37) (solid black line).

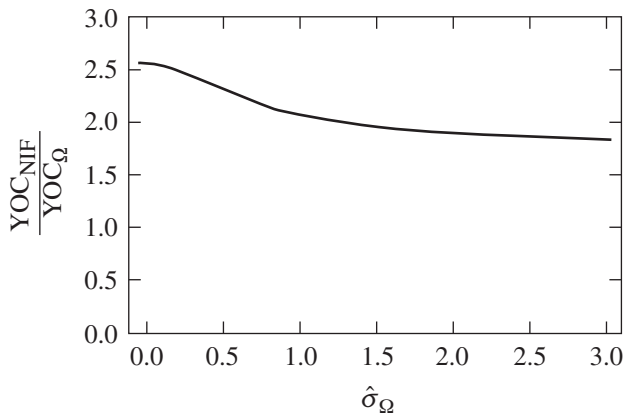
A rough estimate of the YOC can be obtained by assuming that the YOC is proportional to the ratio of the clean volume to the 1-D volume: $\text{YOC} \approx R_{3\text{-D}}^3 / R_{1\text{-D}}^3$ (Ref. 47). Using this approximation, it is possible to estimate the YOC ratio resulting from the RT growth in the deceleration phase. If we assume that the clean radius will decrease with the amplitude of the largest RT spike $R_{3\text{-D}} = R_{1\text{-D}} - \sigma_0 G_{\text{RT}}$, where σ_0 is the initial nonuniformity amplitude for the deceleration-phase RT and G_{RT} is the growth factor for RT modes, then a simple set of algebraic steps can relate the YOC's for the two hydro-equivalent implosions:

$$\text{YOC}_{\text{NIF}} = \left[1 - \frac{\sigma_0^{\text{NIF}}}{\sigma_0^{\Omega}} \left(\frac{E_L^{\Omega}}{E_L^{\text{NIF}}} \right)^{1/3} (1 - \text{YOC}_{\Omega}^{1/3}) \right]^3, \quad (40)$$

where the growth factors are identical for the two hydro-equivalent implosions. Equation (40) recovers the results from the simulations shown in Fig. 137.9, where equal YOC's are obtained when using the same normalized σ_0 . In most ICF implosions, however, laser-imprinting feedthrough will dominate the RT growth in the deceleration phase. It is possible to take this into account by setting $\sigma_0 \equiv \sqrt{\sigma_{\text{ice}}^2 + \sigma_{\text{laser}}^2}$, where σ_{laser} is the deceleration-phase nonuniformity seed amplitude resulting from laser imprinting. If the RT amplitude resulting from laser imprinting scales with the target size and the number of overlapping beams (N_b) such that $\sigma_{\text{laser}} \sim E^{1/3} N_b^{-1/2}$, then

$$\frac{\sigma_0^{\text{NIF}}}{\sigma_0^{\Omega}} = \sqrt{\frac{1 + (E_L^{\text{NIF}}/E_L^{\Omega})^{2/3} (N_b^{\Omega}/N_b^{\text{NIF}}) \hat{\sigma}_{\Omega}^2}{1 + \hat{\sigma}_{\Omega}^2}}, \quad (41)$$

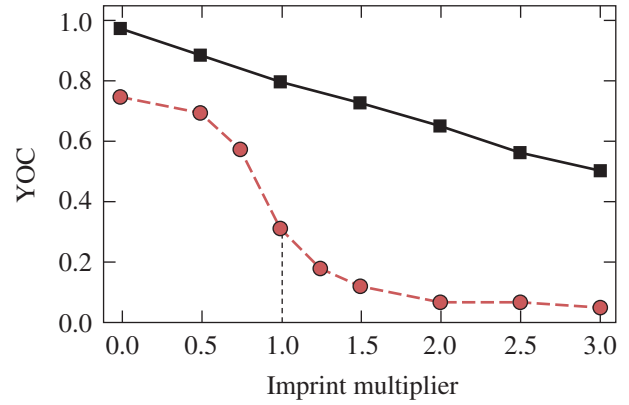
where $\hat{\sigma}_{\Omega} \equiv \sigma_{\text{laser}}/\sigma_{\text{ice}}$. Large values of $\hat{\sigma}_{\Omega}$ indicate that laser imprinting dominates the deceleration-phase nonuniformity seeds over the inner-ice-surface roughness. Inserting Eq. (41) into Eq. (40) and dividing by YOC_{Ω} gives an analytic expression for the YOC ratio and is shown in Fig. 137.11 for $N_b^{\text{NIF}} = 192$, $N_b^{\Omega} = 60$, and $\text{YOC}_{\Omega} = 0.3$. YOC_{Ω} is set to a value of 0.3 because this is a typical YOC experimentally inferred from the current best-performing cryogenic implosions on OMEGA.⁴² This function asymptotes to a YOC ratio of 1.8 for large values of $\hat{\sigma}_{\Omega}$, representing the realistic regime where laser imprinting dominates over ice roughness. The YOC improvement of 1.8 \times is a result of the lower imprinting level in a NIF symmetric illumination configuration caused by the larger number of overlapping beams. Inserting this YOC ratio into Eq. (39) indicates that hydro-equivalent ignition would occur on an OMEGA-scale target obtaining $\chi_{\Omega\text{-eq ig}} = 0.15$. It is important to emphasize that this conclusion is valid only within the simple YOC model shown above and assumes that the NIF imprinting level is lower than on OMEGA by a factor of $\sqrt{60/192}$.



TC11082JR

Figure 137.11
Analytic calculation of the YOC ratio versus perturbation parameter $\hat{\sigma}_{\Omega}$ using a simple clean volume analysis. Large values of $\hat{\sigma}_{\Omega}$ are expected in experiments.

Two-dimensional multimode ice and imprinting simulations can be used to determine the YOC scaling ratio. These simulations have an imprint spectrum for a range of even ℓ modes from 2 to 100, a 1- μm root-mean-square ice roughness spectrum, and 2-D SSD laser-beam smoothing. Figure 137.12 plots the YOC of several simulations with varying degrees of laser



TC10877JR

Figure 137.12
Results from two-dimensional *DRACO* simulations plotting YOC versus an imprint multiplier for NIF-scale (solid black line) and OMEGA-scale (dashed red line) targets with expected inner-ice-surface roughness and variable laser imprinting. The vertical dashed line indicates a YOC_{Ω} of 0.30.

imprinting for both the NIF-scale and OMEGA-scale designs. The x axis is an amplitude multiplier on the imprint spectrum, where an imprint multiplier of zero indicates the simulation has perfectly smooth beams and an imprint multiplier of 1 indicates the expected level of imprint modulations being applied to the target for the 60-beam OMEGA or 192-beam symmetric NIF Laser Systems. The NIF-scale target with an imprint multiplier of zero has a YOC of 0.98, as a result of the relatively small effect of ice roughness, and decreases with increasing imprint multiplier. At an imprint multiplier of 2.67, the NIF-scale target achieves marginal ignition (gain = 1) when alpha-particle deposition is turned on. On the OMEGA-scale target, the reduction in YOC related to ice roughness only ($\sim 75\%$) is significantly larger than on the NIF-scale target. This is because the relative size of the ice roughness is larger by a factor of $\epsilon^{1/3}$ on OMEGA with respect to the NIF, while the absolute magnitude of the ice roughness remains the same. The YOC of the OMEGA-scale target decreases as the imprint multiplier increases, albeit at a faster rate because the imprint spectrum is smoothed by a smaller number of beams. Above an imprint multiplier of 1, the OMEGA-scale target can be considered to be broken up. The OMEGA-scale line in Fig. 137.12 is an average of two sets of simulations where the phases of the ice roughness are reversed. Phase coupling's impact on target performance between the ice-roughness spectrum and the RT modes driven by laser imprinting can be significant and may lead to misinterpretation of the set of simulation results. For example, if the phases of the ice spectrum and laser imprinting destructively interfere, increasing the amount of laser imprinting can appear to have a positive effect on the YOC. Similarly, if the modes constructively interfere, the YOC reduction could

be grossly exaggerated. Averaging the YOC's from these two ice spectrums generalizes the impact of phase coupling and allows one to compare targets where phase coupling does not have a significant impact on target performance (such as the NIF-scale target).

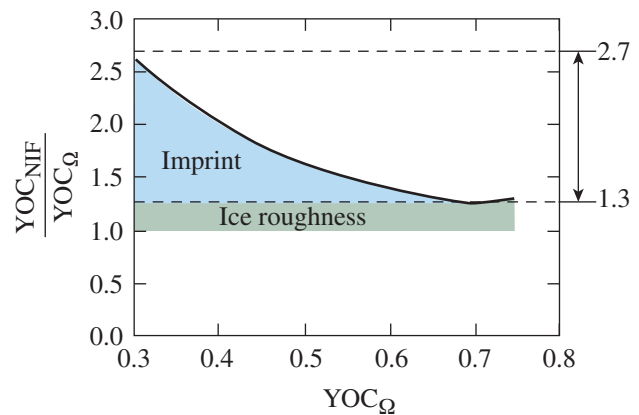
The two curves in Fig. 137.12 contain all of the information necessary to infer the YOC ratio numerically. It is important to notice that the OMEGA-scale target exhibits a cliff in YOC when the imprint multiplier is above ~ 0.6 . This occurs because the OMEGA-scale target begins to break up for such levels of nonuniformities, while the corresponding NIF target maintains its macroscopic integrity. Although the growth of hydrodynamic instabilities is essentially identical (i.e., hydro-equivalent) between the OMEGA-scale and NIF-scale targets, the seeds are not, resulting in very different behavior of the YOC as shown in Fig. 137.12. The difference in the relative level of nonuniformities between OMEGA-scale and NIF-scale targets breaks the hydro-equivalency. Even in the absence of laser imprinting, the relative size of the ice roughness is $4\times$ larger on OMEGA than on the NIF. Therefore, both seeds of the RT instability (ice roughness and imprinting) are not hydro-equivalent. To achieve a final assessment of the performance requirements on OMEGA, we identify three possible extrapolations from OMEGA to the NIF:

1. A quasi-hydro-equivalent extrapolation corresponding to values of the YOC for OMEGA above 0.6 in Fig. 137.12. As shown in Fig. 137.12, in the range of $YOC = 0.6$ to 1.0, both the OMEGA and NIF targets remain integral during the implosion and are both above the shell's breakup "cliff." Full hydro-equivalency is not achieved because of the difference in relative ice roughness. The behavior of the YOC versus imprint multiplier is similar, however, even though the two curves are shifted and maintain an approximately constant ratio of 1.3. In this regime, extrapolations from OMEGA scales to NIF scales are likely to be quite reliable since the departure from hydro-equivalency is rather small (a factor of $1.3\times$ in YOC and $1.05\times$ in areal density).
2. A semi-hydro-equivalent extrapolation corresponding to values of the YOC for OMEGA between 0.3 and 0.6 in Fig. 137.12. The OMEGA shell is highly distorted and within the cliff in YOC. The OMEGA YOC is still reasonably high, however, and the clean hot-spot radius is larger than about 60% to 70% of its 1-D value. In this case, extrapolating from OMEGA scales to NIF scales requires a reliance on the hydrocode. This is not an

optimal or robust extrapolation since it relies on a large difference in calculated YOC's when extrapolating from OMEGA to the NIF.

3. A non-hydro-equivalent extrapolation corresponds to values of the YOC for OMEGA below 0.3 in Fig 137.12. The OMEGA shell is broken in flight and its performance is at the bottom of the YOC cliff, while the NIF target is still integral. The departure from hydro-equivalency is so great that it would be unreasonable to attempt an extrapolation from OMEGA experimental results to the NIF scale. We do not consider this regime viable for performance extrapolation.

We restrict our analysis to quasi- and semi-hydro-equivalent implosions [(1) and (2)] and limit the OMEGA-scale target YOC to values ≥ 0.3 . Note that YOC's of 30% to 40% are the typical YOC's inferred from current high-performance implosions on OMEGA.⁴² Figure 137.13 plots the YOC ratio versus YOC_{Ω} . It is observed that the YOC ratio varies from 1.3 to 2.7, depending on the level of laser imprinting. For smooth beams leading to a $YOC_{\Omega} \geq 0.6$ (quasi-hydro-equivalent regime), the YOC ratio is approximately 1.3—the predicted value given by the analytic scaling from Eq. (40) (for a YOC_{Ω} of 0.7). Larger imprinting levels increase the YOC ratio up to a factor of 2.7 at a YOC_{Ω} of 0.3 (semi-hydro-equivalent regime). It is important to note that the YOC ratio is not necessarily 2.7 but can range from 1.3 to 2.7, depending on the beam uniformity that is present on the NIF scale.

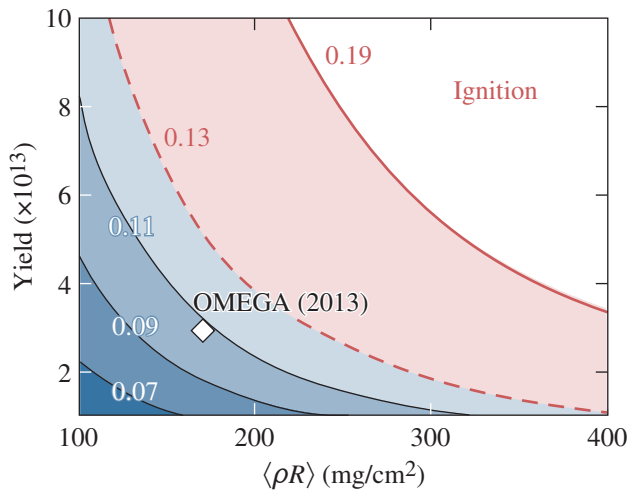


TC10878JR

Figure 137.13

YOC ratio determined from 2-D DRACO simulations as a function of YOC_{Ω} . A YOC ratio of 1.3 results from the impact of equal ice-roughness amplitudes, while a YOC ratio up to 2.7 resulting from laser imprinting is observed at YOC_{Ω} of 0.30.

The areal densities and neutron yields required for quasi- and semi-hydro-equivalent ignition on OMEGA follow from the 3-D Lawson criterion. Given the bounding values for the YOC ratio, $\chi_{\Omega\text{-eq ig}}$ can be calculated to be ~ 0.19 for quasi-hydro-equivalent ignition (YOC ratio of 1.3) and between 0.13 and 0.19 for semi-hydro-equivalent ignition (YOC ratio between 1.3 and 2.7). This indicates that any implosion occurring on OMEGA that obtains $\chi \geq \chi_{\Omega\text{-eq ig}}$ would equate to either quasi- or semi-hydro-equivalent ignition. Figure 137.14 is a contour plot of the 3-D Lawson criterion plotted against its two dependent variables—the 3-D neutron yield and the neutron-averaged areal density; the $\text{YOC}^{0.06}$ dependence is small enough to be ignored within a 10% error. For comparison, the white diamond indicates OMEGA’s current best-performing shot in terms of the Lawson criterion ($\chi = 0.10$) (Ref. 42).



TC10879JR

Figure 137.14
Contour plot of the Lawson criterion parameter indicating the hydro-equivalent ignition threshold for OMEGA-scale targets (for YOC = 1). An OMEGA implosion lying within the white region indicates ignition would occur on a hydro-equivalent NIF-scale target. An implosion lying within the red region indicates potential hydro-equivalent ignition depending on the level of laser imprinting. An implosion lying within the blue region indicates ignition would not occur. The white diamond is the current best-performing implosion on OMEGA in terms of χ [note $\chi_{\Omega} = 0.10$ when taking into account the YOC term in Eq. (35)].

In summary, to claim quasi-hydro-equivalent ignition in a NIF symmetric illumination configuration, OMEGA’s performance must increase from at least $\chi = 0.10$ to a minimum value of $\chi = 0.19$. To claim semi-hydro-equivalent ignition in a symmetric NIF illumination configuration, OMEGA’s performance must increase from at least $\chi = 0.10$ to a minimum value of $\chi = 0.13$. It is important to emphasize that semi-hydro-

equivalent ignition for $\chi_{\Omega\text{-eq ig}} = 0.13$ uses a large enhancement (2.7 \times) in calculated yields from OMEGA to the NIF, thereby decreasing the reliability of such a conclusion. Table 137.II provides reasonable sample values required to demonstrate ignition on a quasi- and semi-hydro-equivalent symmetric NIF-scale target at the OMEGA scale in terms of neutron-averaged areal density and total neutron yield.

Table 137.II: Current OMEGA record performance metrics for experimentally measured neutron yields and neutron-averaged areal densities along with its calculated Lawson parameter χ . Sample values required to demonstrate hydro-equivalent ignition on OMEGA-scale cryogenic implosions are also provided.

	Neutron Yield ($\times 10^{13}$)	Areal Density (mg/cm ²)	$\chi_{\Omega\text{-eq ig}}$
OMEGA’s current record (shot 69514)	3.0	173	0.10
Hydro-equivalent ignition (2.7 \times YOC improvement)	3.0	240	0.13
Hydro-equivalent ignition (1.3 \times YOC improvement)	6.0	300	0.19

Conclusions

Hydro-equivalence combined with ignition theory allows one to compare OMEGA-scale implosions to ignition-scale targets on a symmetric NIF illumination configuration with the same 2-D SSD smoothing as OMEGA. Hydro-equivalent implosions are energetically scalable and have identical implosion velocities, laser intensities, and adiabats. Hydro-equivalent implosions exhibit the same 1-D dynamics and the same hydrodynamic instability growth. The measurable Lawson criterion was used to assess the performance of an implosion using experimental observables and can also be used in conjunction with hydro-equivalent scaling relations. Analytical derivations were developed and numerical simulations were performed to predict the hydro-equivalent ignition threshold on OMEGA-scale targets and are in good agreement with one another.

While OMEGA and NIF targets can be designed to be approximately hydro-equivalent, the difference in the initial level of nonuniformities prevents an exactly hydro-equivalent extrapolation. Ice roughness is inherently non-hydro-equivalent since the ice σ_{rms} is the same for OMEGA and the NIF while the OMEGA-scale’s target size is roughly 4 \times smaller. Laser

imprinting is also non-hydro-equivalent because of the different number of beams between OMEGA and the NIF. In the absence of perfect hydro-equivalency, two OMEGA-to-NIF extrapolations have been identified: (a) a quasi-hydro-equivalent extrapolation including realistic ice roughness and relatively low levels of laser imprinting; (b) a semi-hydro-equivalent extrapolation applicable for a larger level of laser imprinting. A quasi-hydro-equivalent extrapolation requires OMEGA target performance characterized by $YOC \geq 0.6$. The performance of such targets can be reliably extrapolated from OMEGA scale to the NIF scale since it requires a relatively small improvement in YOC of only 30%. A semi-hydro-equivalent extrapolation requires an OMEGA YOC of 0.3 to 0.6. The extrapolation to NIF scales from OMEGA-scale semi-hydro-equivalent implosions is less reliable since it requires a large calculated YOC improvement for ignition at NIF scales (up to $2.7\times$ for an OMEGA YOC of 0.3).

In summary, the theory of hydro-equivalency and 2-D simulations of hydro-equivalent implosions indicates that a reliable extrapolation to ignition (quasi-hydro-equivalent ignition) on a symmetrically illuminating NIF configuration requires OMEGA target performance with an areal density of about 0.3 g/cm^2 and a neutron yield of about 6×10^{13} . As a short-term goal, semi-hydro-equivalent ignition on OMEGA requires less-demanding implosions that achieve areal densities and neutron yields as low as 0.24 g/cm^2 and 3×10^{13} , respectively.

ACKNOWLEDGMENT

This material is based upon work supported by the Department of Energy National Nuclear Security Administration under Award Number DE-NA0001944, the University of Rochester, and the New York State Energy Research and Development Authority. The support of DOE does not constitute an endorsement by DOE of the views expressed in this article.

REFERENCES

1. J. Nuckolls *et al.*, *Nature* **239**, 139 (1972).
2. S. E. Bodner, D. G. Colombant, J. H. Gardner, R. H. Lehberg, S. P. Obenschain, L. Phillips, A. J. Schmitt, J. D. Sethian, R. L. McCrory, W. Seka, C. P. Verdon, J. P. Knauer, B. B. Afeyan, and H. T. Powell, *Phys. Plasmas* **5**, 1901 (1998).
3. J. D. Lindl, *Inertial Confinement Fusion: The Quest for Ignition and Energy Gain Using Indirect Drive* (Springer-Verlag, New York, 1998).
4. S. Atzeni and J. Meyer-ter-Vehn, *The Physics of Inertial Fusion: Beam Plasma Interaction, Hydrodynamics, Hot Dense Matter*, International Series of Monographs on Physics (Clarendon Press, Oxford, 2004).
5. O. A. Hurricane *et al.*, *Nature* **506**, 343 (2014).
6. J. D. Lawson, *Proc. Phys. Soc. Lond. B* **70**, 6 (1957).
7. J. P. Freidberg, *Plasma Physics and Fusion Energy* (Cambridge University Press, Cambridge, England, 2007).
8. R. Betti, P. Y. Chang, B. K. Spears, K. S. Anderson, J. Edwards, M. Fatenejad, J. D. Lindl, R. L. McCrory, R. Nora, and D. Shvarts, *Phys. Plasmas* **17**, 058102 (2010).
9. P. Y. Chang, R. Betti, B. K. Spears, K. S. Anderson, J. Edwards, M. Fatenejad, J. D. Lindl, R. L. McCrory, R. Nora, and D. Shvarts, *Phys. Rev. Lett.* **104**, 135002 (2010).
10. C. D. Zhou and R. Betti, *Phys. Plasmas* **15**, 102707 (2008).
11. B. K. Spears *et al.*, *Phys. Plasmas* **19**, 056316 (2012).
12. M. C. Herrmann, M. Tabak, and J. D. Lindl, *Nucl. Fusion* **41**, 99 (2001).
13. A. Kemp, J. Meyer-ter-Vehn, and S. Atzeni, *Phys. Rev. Lett.* **86**, 3336 (2001).
14. T. R. Boehly, D. L. Brown, R. S. Craxton, R. L. Keck, J. P. Knauer, J. H. Kelly, T. J. Kessler, S. A. Kumpan, S. J. Loucks, S. A. Letzring, F. J. Marshall, R. L. McCrory, S. F. B. Morse, W. Seka, J. M. Soures, and C. P. Verdon, *Opt. Commun.* **133**, 495 (1997).
15. S. Skupsky, R. W. Short, T. Kessler, R. S. Craxton, S. Letzring, and J. M. Soures, *J. Appl. Phys.* **66**, 3456 (1989).
16. J. D. Lindl, *Phys. Plasmas* **2**, 3933 (1995).
17. M. M. Basko, *Nucl. Fusion* **35**, 87 (1995).
18. W. M. Manheimer, D. G. Colombant, and J. H. Gardner, *Phys. Fluids* **25**, 1644 (1982).
19. R. D. Richtmyer, *Commun. Pure. Appl. Math.* **XIII**, 297 (1960).
20. E. E. Meshkov, *Fluid Dyn.* **4**, 101 (1969).
21. Lord Rayleigh, *Proc. London Math Soc.* **XIV**, 170 (1883).
22. G. Taylor, *Proc. R. Soc. London Ser. A* **201**, 192 (1950).
23. H. Takabe *et al.*, *Phys. Fluids* **28**, 3676 (1985).
24. R. Betti, V. N. Goncharov, R. L. McCrory, P. Sorotokin, and C. P. Verdon, *Phys. Plasmas* **3**, 2122 (1996).
25. D. L. Youngs, *Physica* **12D**, 32 (1984).
26. D. Oron, U. Alon, and D. Shvarts, *Phys. Plasmas* **5**, 1467 (1998).
27. S. W. Haan, *Phys. Fluids B* **3**, 2349 (1991).
28. S. W. Haan, *Phys. Rev. A* **39**, 5812 (1989).
29. V. Lobatchev and R. Betti, *Phys. Rev. Lett.* **85**, 4522 (2000).
30. L. Spitzer, *Physics of Fully Ionized Gases* (Interscience Publishers, New York, 1956).
31. C. D. Zhou and R. Betti, *Phys. Plasmas* **14**, 072703 (2007).

32. J. F. Myatt, J. Zhang, R. W. Short, A. V. Maximov, W. Seka, D. H. Froula, D. H. Edgell, D. Michel, I. V. Igumenshchev, D. E. Hinkel, and P. Michel, "Multibeam Laser-Plasma Interactions in Inertial Confinement Fusion," to be published in *Physics of Plasmas*.
33. I. V. Igumenshchev, D. H. Edgell, V. N. Goncharov, J. A. Delettrez, A. V. Maximov, J. F. Myatt, W. Seka, A. Shvydky, S. Skupsky, and C. Stoeckl, *Phys. Plasmas* **17**, 122708 (2010).
34. I. V. Igumenshchev, W. Seka, D. H. Edgell, D. T. Michel, D. H. Froula, V. N. Goncharov, R. S. Craxton, L. Divol, R. Epstein, R. Follett, J. H. Kelly, T. Z. Kosc, A. V. Maximov, R. L. McCrory, D. D. Meyerhofer, P. Michel, J. F. Myatt, T. C. Sangster, A. Shvydky, S. Skupsky, and C. Stoeckl, *Phys. Plasmas* **19**, 056314 (2012).
35. D. H. Froula, I. V. Igumenshchev, D. T. Michel, D. H. Edgell, R. Follett, V. Yu. Glebov, V. N. Goncharov, J. Kwiatkowski, F. J. Marshall, P. B. Radha, W. Seka, C. Sorce, S. Stagnitto, C. Stoeckl, and T. C. Sangster, *Phys. Rev. Lett.* **108**, 125003 (2012).
36. D. H. Edgell, W. Seka, J. A. Delettrez, R. S. Craxton, V. N. Goncharov, I. V. Igumenshchev, J. F. Myatt, A. V. Maximov, R. W. Short, T. C. Sangster, and R. E. Bahr, *Bull. Am. Phys. Soc.* **54**, 145 (2009).
37. W. Seka, D. H. Edgell, J. F. Myatt, A. V. Maximov, R. W. Short, V. N. Goncharov, and H. A. Baldis, *Phys. Plasmas* **16**, 052701 (2009).
38. R. W. Short, *Bull. Am. Phys. Soc.* **53**, 245 (2008).
39. D. T. Michel, A. V. Maximov, R. W. Short, S. X. Hu, J. F. Myatt, W. Seka, A. A. Solodov, B. Yaakobi, and D. H. Froula, *Phys. Rev. Lett.* **109**, 155007 (2012).
40. J. F. Myatt, J. Zhang, J. A. Delettrez, A. V. Maximov, R. W. Short, W. Seka, D. H. Edgell, D. F. DuBois, D. A. Russell, and H. X. Vu, *Phys. Plasmas* **19**, 022707 (2012).
41. D. T. Michel, A. V. Maximov, R. W. Short, J. A. Delettrez, D. Edgell, S. X. Hu, I. V. Igumenshchev, J. F. Myatt, A. A. Solodov, C. Stoeckl, B. Yaakobi, and D. H. Froula, *Phys. Plasmas* **20**, 055703 (2013).
42. T. C. Sangster, V. N. Goncharov, R. Betti, P. B. Radha, T. R. Boehly, D. T. Casey, T. J. B. Collins, R. S. Craxton, J. A. Delettrez, D. H. Edgell, R. Epstein, C. J. Forrest, J. A. Frenje, D. H. Froula, M. Gatu-Johnson, V. Yu. Glebov, D. R. Harding, M. Hohenberger, S. X. Hu, I. V. Igumenshchev, R. Janezic, J. H. Kelly, T. J. Kessler, C. Kingsley, T. Z. Kosc, J. P. Knauer, S. J. Loucks, J. A. Marozas, F. J. Marshall, A. V. Maximov, R. L. McCrory, P. W. McKenty, D. D. Meyerhofer, D. T. Michel, J. F. Myatt, R. D. Petrasso, S. P. Regan, W. Seka, W. T. Shmayda, R. W. Short, A. Shvydky, S. Skupsky, J. M. Soures, C. Stoeckl, W. Theobald, V. Versteeg, B. Yaakobi, and J. D. Zuegel, *Phys. Plasmas* **20**, 056317 (2013).
43. P. B. Radha, V. N. Goncharov, T. J. B. Collins, J. A. Delettrez, Y. Elbaz, V. Yu. Glebov, R. L. Keck, D. E. Keller, J. P. Knauer, J. A. Marozas, F. J. Marshall, P. W. McKenty, D. D. Meyerhofer, S. P. Regan, T. C. Sangster, D. Shvarts, S. Skupsky, Y. Srebro, R. P. J. Town, and C. Stoeckl, *Phys. Plasmas* **12**, 032702 (2005).
44. G. I. Kerley, *Phys. Earth Planet. Inter.* **6**, 78 (1972).
45. G. I. Kerley, Sandia National Laboratory, Albuquerque, NM, Report SAND2003-3613 (2003).
46. S. X. Hu, B. Militzer, V. N. Goncharov, and S. Skupsky, *Phys. Rev. B* **84**, 224109 (2011).
47. R. Kishony and D. Shvarts, *Phys. Plasmas* **8**, 4925 (2001).

Improving Hot-Spot Pressure and Demonstrating Ignition Hydrodynamic Equivalence in Cryogenic Deuterium–Tritium Implosions on OMEGA

Introduction

To ignite the deuterium–tritium (DT) fuel in an inertial confinement fusion^{1,2} (ICF) implosion, the ion temperature and areal density of the central, lower-density region (hot spot) of the compressed DT fuel assembly must be sufficient to create self-heating by alpha particles produced as a result of fusing D and T. A typical ICF target consists of a higher-density shell filled with a lower-density fuel vapor. The shell has outer layers of ablator materials and an inner layer of frozen DT fuel. To compress the main fuel and initiate burn, the shell is accelerated inward by a temporally shaped pressure drive created by laser energy that is delivered either directly to the target (direct drive) or indirectly by converting its energy to x rays inside a hohlraum (indirect drive).^{1,2}

The peak hot-spot pressure is a critical parameter in ICF implosions. It determines the minimum shell kinetic energy required to create an igniting hot spot. This follows from a simple argument² that if the shell's kinetic energy is converted into the internal energy of the hot spot at stagnation, $E_k \rightarrow p_{\max} R_{\text{hs}}^3$, then $E_k \sim (\rho R_{\text{hs}})^3 T^3 / p_{\max}^2$, where R_{hs} , $p_{\max} \sim \rho T / m_i$, ρ , and T are the hot-spot radius, maximum pressure, mass density, and temperature, respectively, and m_i is the average ion mass. Since the hot spot must satisfy^{1–3}

$$(\rho R_{\text{hs}}) \times T > 0.3 \text{ g/cm}^2 \times 5 \text{ keV} \quad (1)$$

to ignite, the fuel's kinetic energy must exceed a threshold value $E_k > E_{k,\min}$, which depends on the peak pressure

$$E_{k,\min} \sim p_{\max}^{-2}. \quad (2)$$

Equation (2) shows that achieving higher pressures in the hot spot relaxes the requirement for the shell's kinetic energy and the laser drive energy. Equation (1) sets the requirement for the hot-spot pressure in an igniting target. Since $p = (1 + Z)\rho T / m_i$ (for DT fuel, $Z = 1$ is the ion charge, $m_i \simeq 2.5 m_p$ is the average ion mass, and m_p is the proton mass), Eq. (1) gives

$$p_{\text{hs}} > 200 \text{ Gbar} \left(\frac{50 \mu\text{m}}{R_{\text{hs}}} \right). \quad (3)$$

The peak pressure also determines the neutron yield for subigniting ICF implosions. Indeed, the DT fusion reaction rate is $dn_i/dt \sim V_{\text{hs}} \times n_i^2 \times \langle \sigma v \rangle$ and the reaction cross section is $\langle \sigma v \rangle \sim T^{4.5}$ (at temperatures $T \sim 2$ to 4 keV, which are typical for sub-ignition ICF implosions). This leads to a total neutron yield of

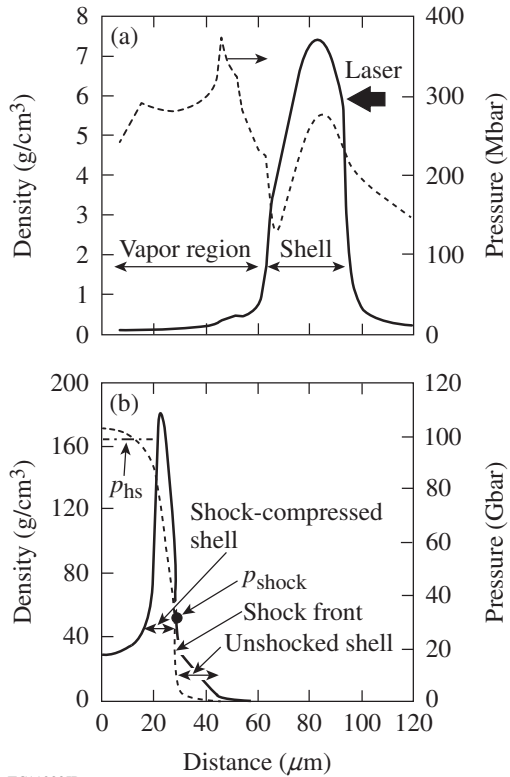
$$Y \sim V_{\text{hs}} \times p_{\max}^2 \times T^{2.5} \times \Delta t_{\text{burn}}, \quad (4)$$

where n_i is the ion density, V_{hs} is the hot-spot volume, and Δt_{burn} is the burn duration. Using the adiabatic condition for the hot spot^{3,4} $p \sim V_{\text{hs}}^{-5/3}$ (see also the discussion later in the text), Eq. (4) becomes

$$Y \sim p_{\max}^{7/5} \times T^{2.5} \times \Delta t_{\text{burn}}. \quad (5)$$

Equation (5) shows that higher hot-spot pressures lead to higher target yields.

The maximum pressure depends mainly on the following two effects: first, the conversion efficiency of the shell's kinetic energy into the hot-spot internal energy at shell stagnation; second, the hot-spot size since larger hot-spot volumes lead to smaller peak pressures for a given hot-spot internal energy E_{int} , $p_{\max} \sim E_{\text{int}} / V_{\text{hs}}$. The first effect depends on the fraction of shell mass that stagnates at peak compression. At the beginning of shell deceleration [see Fig. 137.15(a)], the pressure of the central vapor region of an imploding target (which, together with the material ablated from the inside of the shell during acceleration, forms a hot spot at the peak compression) exceeds the shell pressure and an outgoing shock wave is formed at the inner edge of the shell. The vapor (hot-spot) pressure increases while the inner part of the shell converges, performing the $p dV$ work on the vapor region. The inward shell motion is limited



TC11083JR

Figure 137.15

The mass-density (solid lines, left axes) and pressure (dashed lines, right axes) profiles at (a) the beginning of shell deceleration and (b) the maximum hot-spot compression for OMEGA cryogenic targets.

by the deceleration force caused by the pressure gradient in the shock-compressed region [see Fig. 137.15(b)]. This pressure gradient is determined first by the pressure behind the shock front (which depends on density ρ and velocity v of the incoming shell ahead of the shock, $p_{\text{shock}} \sim \rho v^2$) and second, by the hot-spot pressure, which depends on the hot-spot convergence ratio $p_{\text{hs}} \sim V_{\text{hs}}^{-5/3}$. If two implosions are considered where the shells have different ρv^2 , the pressure behind the shock is lower and the pressure gradient (for a given hot-spot volume) is higher in the shell with a smaller ρv^2 . This shell, therefore, experiences a stronger deceleration force, leading to a larger hot-spot volume at stagnation. The amount of shell material overtaken by the outgoing shock is smaller in this case, resulting in a reduced fraction of the shell's kinetic energy being converted into hot-spot internal energy. Since the shell's deceleration depends on the density of the incoming shell, the excessive decompression of the shell by either the Rayleigh–Taylor (RT) instability growth^{5,6} or preheat caused by radiation and suprathreshold electrons must be prevented.

Predicting the evolution of the hot-spot pressure using hydrodynamic code simulations requires accurate modeling of many physical processes that take place during the target implosion. It is essential, therefore, to validate code predictions of key target-performance characteristics at each stage of the implosion against the experimental data. In addition, experiments can help to identify new physical phenomena (not included in the code simulations) that limit target performance. For such purposes, cryogenic DT capsules are being imploded on the OMEGA Laser System⁷ using direct-drive laser illumination. The targets are 7.3- to 12- μm -thick deuterated plastic (CD) shells with outer diameters of 860 μm and 40- to 65- μm -thick cryogenic DT layers. These targets are driven using single and multiple-picket pulses⁸ with laser energies of 23 to 27 kJ_{UV} at a peak intensity of 0.4 to 1×10^{15} W/cm², reaching implosion velocities (defined as the peak mass-averaged shell velocity) of 2.2 to 4×10^7 cm/s.

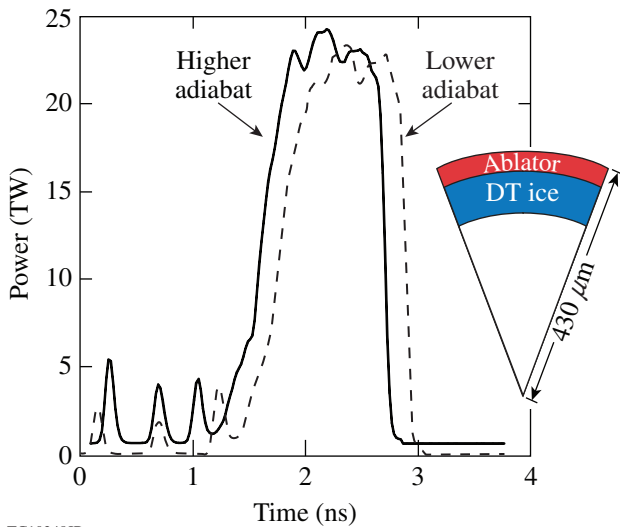
This article describes recent progress in understanding cryogenic implosion performance on OMEGA. The following sections (1) describe the cryogenic target designs and the experiments carried out to validate one-dimensional (1-D) implosion parameters; (2) discuss target performance; (3) present hydrodynamic modeling results; and (4) discuss the performance degradation mechanisms, where we also present the strategies for demonstrating the ignition hydrodynamic equivalence on OMEGA, followed by the conclusions.

Target Designs and Validation of 1-D Implosion Parameters

This section describes the cryogenic target designs and discusses the experimental campaigns carried out on OMEGA to validate the key predicted implosion parameters. The simulation results discussed here are obtained using the 1-D hydrocode *LILAC*.⁹ These simulations include nonlocal electron thermal transport¹⁰ and the cross-beam energy transfer model.^{11–13}

The compression of cryogenic DT fuel is studied for a range of shell adiabat values of $1.5 < \alpha < 6$ [adiabat α is defined as a ratio of the shell pressure to Fermi-degenerate pressure at shell density (see **Target Performance**, p. 23, for more details)], implosion velocities, and the peak laser intensities. Implosion velocity is controlled by varying the CD thickness in a range from 7.2 to 12 μm and an ice thickness from 40 to 65 μm .

Two OMEGA cryogenic target designs are shown in Fig. 137.16. The shell adiabat and the in-flight aspect ratio (IFAR) in implosions are controlled by changing the energies



TC10248JR

Figure 137.16

Lower- (dashed line) and higher- (solid line) adiabat OMEGA cryogenic designs. Fuel adiabat and in-flight aspect ratio (IFAR) are controlled by changing the energies and separating the lower-intensity pickets. The inset shows target dimensions.

and separating of intensity pickets ahead of the main drive pulse. The lower-adiabat design, shown as a dashed line in Fig. 137.16, has lower-intensity pickets and larger picket-to-picket and picket-to-main-pulse separations.

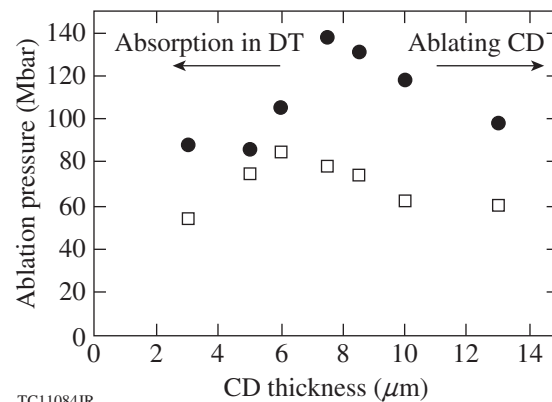
The plastic overcoat is ablated during the main drive pulse either fully or partially, depending on its thickness. For a given laser energy, there is an optimum CD layer thickness that maximizes the drive (ablation) pressure. This is determined by the interplay of the laser absorption efficiency, radiation losses, electron thermal conduction from the laser-absorption region to the ablation front, and ablation efficiency.

Inverse bremsstrahlung *absorption*² is proportional to the average square of the ion charge $\langle Z^2 \rangle$. Consequently, having CD plasma in the laser-deposition region is beneficial for the overall laser absorption because $\langle Z^2 \rangle_{\text{CD}} / \langle Z^2 \rangle_{\text{DT}} \approx 18.5$. The higher absorption also leads to a larger coronal temperature and an increased threshold for the two-plasmon-decay (TPD) instability.^{14,15} Furthermore, the higher average ion charge $\langle Z \rangle$ and the low fraction of hydrogen atoms in the plasma corona give an additional reduction in TPD growth because of the lower damping rates of ion-acoustic waves.¹⁶ A thicker CD layer also shields the main fuel against radiation preheat from the plasma corona (despite the small opacity of DT, calculations indicate that the amount of radiation from the plasma corona absorbed in the main fuel is sufficient to raise the fuel adiabat by 30% to 50% during target acceleration).

Using ablator materials with higher $\langle Z^2 \rangle$, on the other hand, leads to larger *radiation losses*. Higher- Z materials also reduce the *heat conduction* from the plasma region, where laser energy is absorbed to the ablation front since the thermal conductivity is proportional to $\langle Z \rangle / \langle Z^2 \rangle$. This reduces the mass ablation rate and the ablation pressure.

The *ablation efficiency*, which depends on the ratio of atomic weight A and the averaged ion charge $\langle Z \rangle$, is higher in DT. This dependence follows from the steady-state ablation model,¹⁷ where the incoming absorbed laser power flux (laser intensity) I is balanced by the outgoing energy flux of expanding plasma flow, ρv^3 . Here, ρ is the plasma mass density and v is the expansion velocity. Such a model predicts the ablation-pressure and the mass-ablation-rate scalings to be $p_a \sim I^{2/3} (A/Z)^{1/3}$ and $\dot{m} \sim I^{1/3} (A/Z)^{2/3}$, respectively. Since $(A/Z)_{\text{DT}} / (A/Z)_{\text{CH}} \approx 1.25$, the ablation pressure and mass ablation rate, as a fraction of absorbed laser energy, are higher in DT by 8% and 16%, respectively.

Considering these competing effects leads to the conclusion that absorbing the laser energy in CD and ablating DT result in a higher ablation pressure. Since the ablation and absorption regions are spatially separated, an optimum CD thickness for which the ablation pressure is maximized requires the ablation front to propagate in DT while the ablated CD plasma is still present in the laser-deposition region. For an OMEGA-scale laser system, the optimum CD thickness is ~ 7.5 to $8 \mu\text{m}$. This is shown in Fig. 137.17, where the ablation pressure is plotted as a function of the CD thickness for targets with a fixed shell mass and a different ratio of CD to DT layer thicknesses. The squares in the figure represent the ablation pressure calculated



TC11084JR

Figure 137.17

Simulated ablation pressure versus the initial CD thickness plotted at the beginning of the shell acceleration (squares) and when the shells have converged by a factor of 2.5 (circles).

at the beginning of the shell acceleration and the circles represent pressures when the shell has converged by a factor of 2.5. The CD thickness that maximizes the ablation pressure changes from $\sim 6 \mu\text{m}$ earlier in the pulse to $7.5 \mu\text{m}$ at later times. This change occurs because a CD layer thicker than $6.5 \mu\text{m}$ is still being ablated at earlier times, resulting in a lower rocket efficiency. By the time the shell has converged by a factor of 2.5, a CD layer thinner than $\sim 10 \mu\text{m}$ is completely ablated, resulting in an increased rocket efficiency. If the initial CD thickness is less than $7 \mu\text{m}$, however, the ablated DT plasma expands into the laser-absorption region, significantly reducing the absorption fraction (as a result of a reduced $\langle Z^2 \rangle$).

Since the physics of the ablatively driven implosions is complex, it is important to verify that the key implosion parameters are modeled correctly. The predicted ablation pressure and the mass ablation rate are validated by comparing the simulated shell trajectory, the power and spectrum of the scattered laser light, and timing of the neutron-production history (bang time) with the data. The shell trajectory is verified by comparing the measured spatial profile of the x-ray emission from plasma corona¹⁸ with the predictions. Figure 137.18(a) shows a schematic of the x-ray emission map together with a lineout of the self-emission image

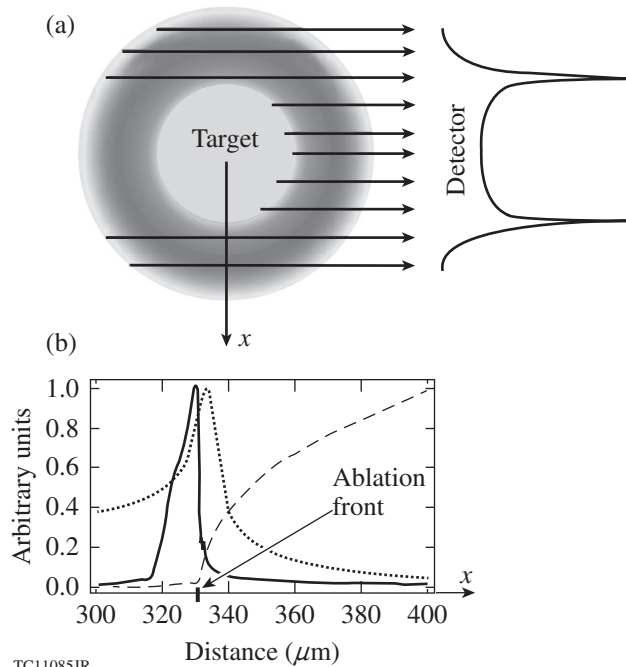


Figure 137.18
 (a) Schematic of the coronal x-ray emission and a lineout of the self-emission image as measured by an x-ray framing camera. (b) Simulated electron density (solid line), electron temperature (dashed line), and the path-integrated plasma self-emission (dotted line) projected on the detector plane.

as measured by an x-ray framing camera. Figure 137.18(b) plots the simulated electron density (solid line), electron temperature (dashed line), and the line-integrated self-emission projected on the detector plane (dotted line) for a typical cryogenic implosion on OMEGA. This figure shows that the ablation front is in very close proximity to the peak in the x-ray emission. Therefore, comparing the measured and simulated positions of the peak or the inner edge of the emission profile provides a good measure of the accuracy in predicting the ablation-front trajectory. Taking the time derivative of the ablation-front trajectory gives the ablation-front velocity.¹⁹ It peaks at a value smaller than the implosion velocity v_{imp} since the convergence effects move the location of the peak pressure from the ablation front to the inner part of the shell, creating a force that decelerates only the ablation-front region while the average shell velocity continues to increase (see **Implosion Modeling**, p. 27, for more details). Figure 137.19 shows, as an example, (a) one of the 16 gated self-emission images taken during a cryogenic implosion, together with (b) inferred ablation-front trajectory, and (c) its velocity. There is excellent agreement between the simulation results and the measurements.

Laser absorption and the ablated plasma evolutions are inferred by measuring the power and spectrum of the scattered

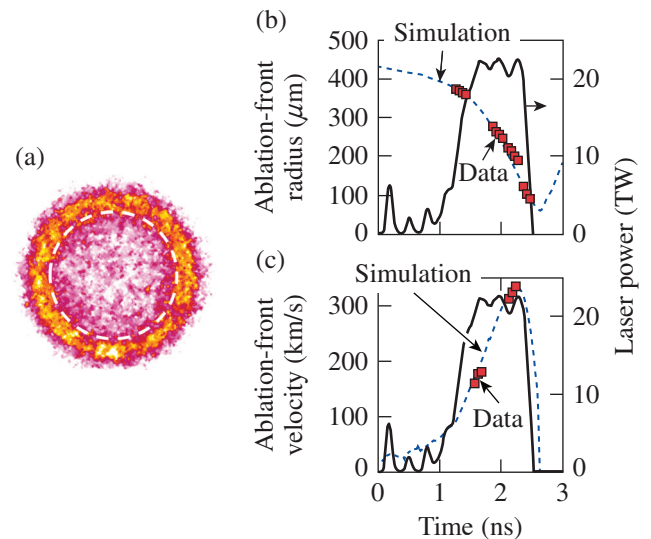
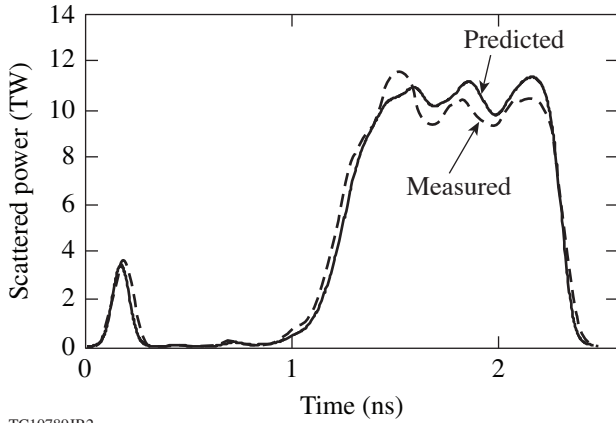


Figure 137.19
 (a) Self-emission image as measured by the x-ray framing camera. The white dashed circle marks the position of the inner edge in the emission profile. (b) The predicted ablation-front position (dashed line) and the measured location of the inner edge of self-emission (red squares) for the OMEGA cryogenic implosion (shot 70030). (c) The predicted ablation-front velocity (dashed line) and the velocity of the measured inner edge of self-emission profile (red squares). The laser pulse is shown as a solid line.

light.²⁰ Figure 137.20 shows the measured scattered power (dashed line), which agrees very well with predictions (solid line). The measured and predicted laser-absorption fractions are $55 \pm 4\%$ and 55%, respectively.

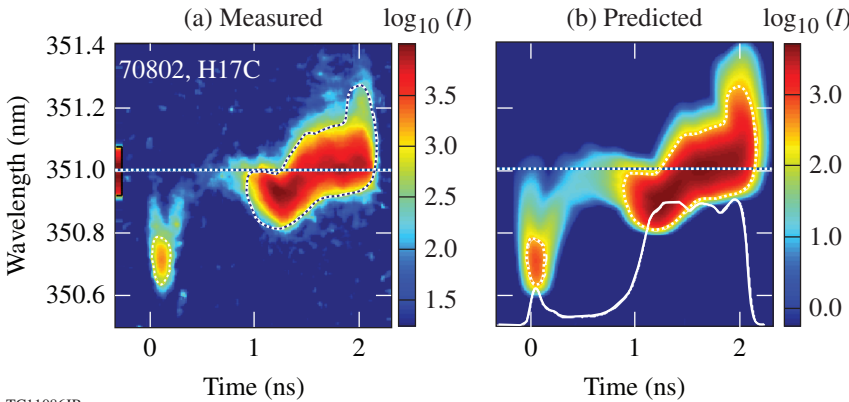


TC10789JR2

Figure 137.20
The measured (dashed line) and predicted (solid line) scattered-light power for the OMEGA cryogenic implosion (shot 69514).

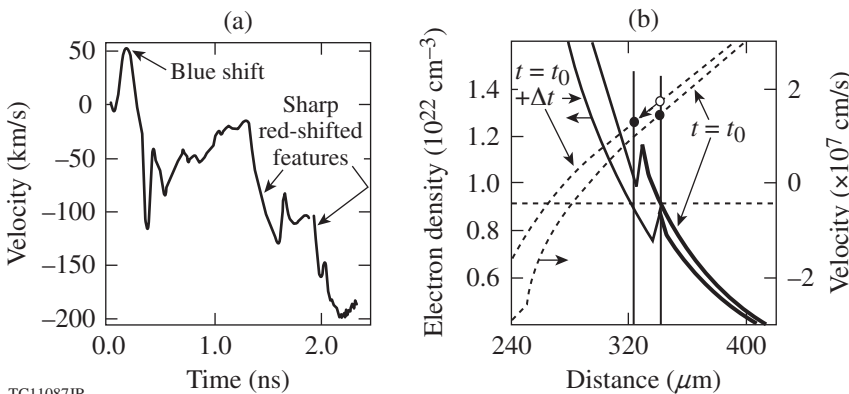
The measured time-resolved scattered-light spectrum is compared with the simulations in Fig. 137.21. The temporal shifts in the scattered laser light are caused by changing the optical path length in the plasma traversed by the laser rays. *LILAC* modeling of the scattered-light spectrum includes calculating frequency shifts²¹ and convolving the results with the incident laser spectrum resulting from smoothing by spectral dispersion (SSD).²² Except for a discrepancy at the beginning of the main drive, both spectra agree very well.

The temporal behavior of the spectrum can be understood by using a simplified description based on a frequency shift of the light reflected from a moving surface (which corresponds to the critical surface where the electron density is equal to $n_{cr} \approx 9 \times 10^{21} \text{ cm}^{-3}$). The velocity of the critical surface is plotted in Fig. 137.22(a). At the early times, $t < 0.3 \text{ ns}$, this velocity is positive, making the reflecting surface move toward the observer and causing a blue shift in the spectrum. Later, as the laser intensity begins to rise during the main pulse, the velocity rapidly changes to a negative value, causing a red shift in the spectrum at $t \approx 1.3 \text{ ns}$. An additional sharp velocity shift occurs at $t \approx 1.9 \text{ ns}$. This is caused by the onset of the laser



TC11086JR

Figure 137.21
The (a) measured and (b) predicted scattered-light spectra for a OMEGA cryogenic implosion (shot 70802). The white dashed lines mark the 50% simulated intensity contour. They are also shown on the measured spectrum to help compare with the data. The pulse shape is shown with the solid white line on the simulated image.



TC11087JR

Figure 137.22
(a) Simulated velocity of the critical surface. The positive velocity early in the pulse ($t \approx 0.1$ to 0.3 ns) results in a blue-shifted part of the scattered-light spectrum (see Fig. 137.21). The sharp velocity variations at $t \approx 1.3$ and $t \approx 1.9 \text{ ns}$ lead to the sharp red-shifted features in the spectrum. The pulse shape is shown in Fig. 137.21(b) with the white line. (b) The electron density (solid lines) and flow velocity (dashed lines) in a cryogenic implosion as predicted by *LILAC*. The two vertical lines indicate the positions of the critical electron density at two different times during the implosion.

deposition in the ablated DT plasma and a mismatch in the electron density across the CD/DT interface, which is a consequence of the continuity in pressure (resulting from momentum conservation) and the electron and ion temperatures (because of thermal conduction):

$$n_{e,DT} = n_{e,CD} \frac{1 + T_i / (Z_{CD} T_e)}{1 + T_i / (Z_{DT} T_e)} < n_{e,CD}, \quad (6)$$

where $n_{e,CD(DT)}$ and $Z_{CD(DT)}$ are the electron density and the ion charge of the plasma on the CD(DT) side of the CD–DT interface, and T_i and T_e are the ion and electron temperatures, respectively. This is illustrated in Fig. 137.22(b), where the electron density profiles (solid lines) predicted by *LILAC* are plotted at two different times for a typical cryogenic implosion. After the electron density in the expanding CD plasma drops below the critical density at the CD/DT interface, the critical surface position jumps farther inward. This is shown in Fig. 137.22(b) as the critical density (dotted horizontal line) at $t = t_0$ is inside the CD plasma at $R \simeq 340 \mu\text{m}$. At $t = t_0 + \Delta t$, the critical density moves into DT at $R \simeq 324 \mu\text{m}$. The separation between the two density profiles in the CD region is only $\sim 5 \mu\text{m}$. Therefore, an additional $\sim 10\text{-}\mu\text{m}$ shift in the critical-surface position is caused by a transition from the CD to DT plasma. As the CD/DT interface travels through the plasma corona region toward the lower electron densities (because of the ablated-plasma expansion), T_i becomes much smaller than T_e (the electron–ion energy exchange rate is reduced at lower plasma densities), leading to continuity in the electron density. When the interface is at the critical density, however, $T_i \simeq T_e/2$ and $n_{e,DT} < n_{e,CD}$.

The jump in the position of n_{cr} leads to a reduction in the expansion flow velocity [shown with the dashed lines in Fig. 137.22(b)] at the critical density. Such a reduction is caused by the continuity in the mass flux, ρv (where $\rho = Am_p n_e / Z$, A is atomic mass, and m_p is proton mass). Without the material change, the velocity at the critical density would change from a value marked by the solid circle at $t = t_0$ to the open circle at $t = t_0 + \Delta t$. With the transition from CD to DT, the flow velocity is reduced to a value marked by the solid circle at $R = 324 \mu\text{m}$:

$$v_{DT}(n_e) = v_{CD}(n_e) \frac{(A/Z)_{CH}}{(A/Z)_{DT}} \simeq 0.8 v_{CD}(n_e). \quad (7)$$

The reduction in the expansion velocity at the critical surface causes the critical surface to move inward faster, lead-

ing to a sharp variation in the critical-surface velocity [see Fig. 137.22(a)] and the red-shifted feature in the scattered-light spectrum at $t \simeq 1.9 \text{ ns}$. Figure 137.21 shows that the observed red-shifted part in the spectrum at the end of the pulse is delayed and has a somewhat slower rise than that predicted by *LILAC*. This suggests a more-gradual transition from CD to DT at the interface, likely a result of mixing of CD and DT in the expanding plasma corona.

In summary, the 1-D dynamics of cryogenic imploding shells is modeled correctly using *LILAC*. This is achieved by including the nonlocal electron thermal transport¹⁰ and the cross-beam energy transfer¹² models. This result is very important since the measured performance degradation relative to the 1-D predictions can be attributed to the multidimensional effects, mainly the growth of hydrodynamic instabilities.

Target Performance

Target performance is quantified by several key observables, including the neutron-averaged areal density, neutron yield, neutron-production history, neutron-average ion temperature, and hot-spot pressure.

1. Neutron Yield and Ion Temperature

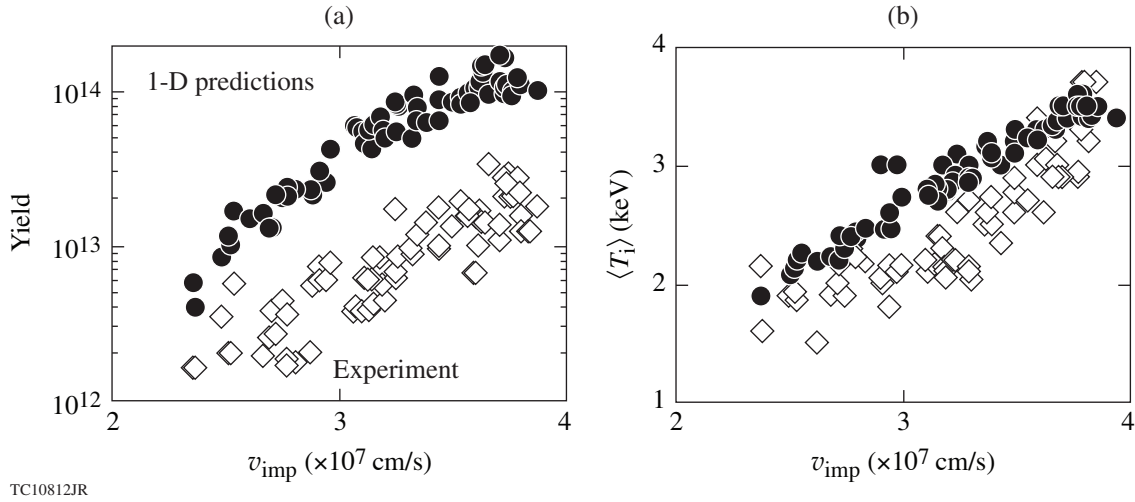
Figure 137.23 shows the calculated and measured neutron yields and the neutron-averaged ion temperatures as functions of the calculated implosion velocity. The implosion velocity in the simulations is defined as the peak in mass-averaged shell velocity:

$$v_{\text{imp}} = \max_{\text{time}} \left(\left| v_{\text{shell}} \right| \right), \quad v_{\text{shell}} = \frac{\int_{r_1}^{r_2} \rho(r,t) v(r,t) r^2 dr}{\int_{r_1}^{r_2} \rho(r,t) r^2 dr}, \quad (8)$$

where r_1 and r_2 are the positions where the shell density equals ρ_{max}/e at the inner and outer sides from shell peak density, and ρ and v are mass density and flow velocity, respectively.

The neutron-averaged ion temperature is calculated using the width of the neutron spectrum f_n , which includes both the thermal and bulk velocity broadenings:^{23–25}

$$\langle f_n(E) \rangle_V = \frac{\int dV n_1 n_2 \langle \sigma v \rangle_{12} e^{-[\alpha(E) - M_a \cos \theta]^2}}{\int dV n_1 n_2 \langle \sigma v \rangle_{12}}, \quad (9)$$



TC10812JR

Figure 137.23

(a) The measured (diamonds) and 1-D predicted (circles) neutron yields; (b) the neutron-averaged ion temperatures for OMEGA cryogenic implosions. The typical error bar for the measured ion temperature is $\pm 4\%$.

where θ is the angle between flow velocity and the neutron detector, $\langle \sigma v \rangle_{12}$ is the reaction cross section between species 1 and 2, n_1 and n_2 are the ion densities of species 1 and 2, respectively, $\alpha(E) = (E - E_0)/\Delta E$, $M_a = v/c_s$ is the flow Mach number, v is the flow velocity, $c_s = \sqrt{T_i/m_i}$ is the ion sound speed, $m_i = (m_n + m_\alpha)/2$ is the average ion mass of reaction products, $E_0 = m_\alpha/(m_n + m_\alpha)Q$, Q is the nuclear energy released in a fusion reaction ($Q = 17.6$ MeV for D + T reaction), m_n and m_α are the masses of the reaction products (neutron and alpha particle for DT), and

$$\Delta E = 2\sqrt{\frac{m_n T_i E_0}{m_n + m_\alpha}}.$$

Taking the integral over the angles [assuming the spherical symmetry in Eq. (9)] yields

$$\langle f_n(E) \rangle_V = \sqrt{\pi} \quad (10)$$

$$\times \frac{\int_0^R dr r^2 n_1 n_2 \langle \sigma v \rangle_{12} \{ \text{erf} [\alpha(E) + M_a] - \text{erf} [\alpha(E) - M_a] \}}{4M_a \int_0^R dr r^2 n_1 n_2 \langle \sigma v \rangle_{12}},$$

where $\text{erf}(x)$ is the error function and R is the size of the neutron-production region. Integrating Eq. (10) over the neutron-production time and fitting the result with a Gaussian with a full width at half maximum (FWHM) = ΔE_{fit} ,

$$\int dt \langle f_n(E) \rangle_V \xrightarrow{\text{fit}} \exp \left[-4 \ln 2 \left(\frac{E - E_0}{\Delta E_{\text{fit}}} \right)^2 \right],$$

defines an effective temperature

$$\langle T_i \rangle_{n,\text{fit}} = \frac{\Delta E_{\text{fit}}^2}{E_0} \frac{1 + m_\alpha/m_n}{16 \ln 2}, \quad (11)$$

which for DT reactions leads to²⁵ $\langle T_i \rangle_{n,\text{fit}} = (\Delta E_{\text{fit}}/177)^2$. Both ΔE and T_i in the latter equation are in keV. The ion temperature is inferred in an experiment by measuring the temporal width of the neutron time of flight, Δ_{TOF} . Using the relation between the neutron energy spread ΔE and Δ_{TOF} ,

$$\frac{\Delta E}{E_0} = 2 \frac{\Delta_{\text{TOF}}}{\text{TOF}} \quad \left(\text{where } \text{TOF} = \sqrt{\frac{m_n}{2E_0}} L \right) \quad (12)$$

in Eq. (11) gives

$$\langle T_i \rangle_{n,\text{exp}} = E_0^2 \frac{1 + m_\alpha/m_n}{m_n 2 \ln 2} \left(\frac{\Delta_{\text{TOF}}}{L} \right)^2. \quad (13)$$

For DT, Eq. (13) reduces to

$$\langle T_i \rangle_{n,\text{exp}} = 68 \frac{\Delta_{\text{TOF}}^2}{L^2}, \quad (14)$$

where L is the distance from detector to target in meters and Δ_{TOF} is in nanoseconds.²⁵

The predicted neutron yield in Fig. 137.23(a) scales as

$$Y_{1\text{-D}} \sim v_{\text{imp}}^6 \alpha^{-0.8}, \quad (15)$$

while the best fit to the experimental yield gives

$$Y_{\text{exp}} \sim v_{\text{imp}}^5 \alpha, \quad (16)$$

where α is defined as the mass-averaged adiabat

$$\alpha = \frac{1}{m_{\text{shk}} - m_{\text{b}}} \int_{m_{\text{b}}}^{m_{\text{shk}}} \frac{p(m)}{\mu \rho(m)^{5/3}} dm, \quad (17)$$

calculated using *LILAC*, $dm = 4\pi\rho r^2 dr$ is a differential of the mass coordinate, m_{b} is the position in the mass coordinate where $\rho(m_{\text{b}}) = \rho_{\text{max}}/e$ at the inner shell surface, ρ_{max} is the peak density, m_{shk} is the shell mass (shocked mass) overtaken by the return shock at the time of the peak neutron production (bang time),

$$\mu = \frac{(3\pi^2)^{2/3}}{5} \frac{\hbar^2 Z^{5/3}}{m_e m_i^{5/3}}, \quad (18)$$

m_i and m_e are the average ion and electron masses, respectively, Z is the average ion charge, and \hbar is the Planck constant. In general, α increases with time during the shell acceleration, mainly because of radiation heating from the plasma corona. In this article, adiabat α is calculated near the beginning of shell acceleration, when $R_a = 2/3 R_{\text{vapor}}$, where R_a is the ablation-front radius and R_{vapor} is the radius (initial radius) of the vapor region of an undriven shell.

The lower-adiabat implosions are predicted to result in higher fuel compression and higher ion temperatures. This leads to higher yields if the multidimensional effects are not taken into account. The target performance in an experiment is strongly degraded, however, as the adiabat is reduced²⁶ (because of a weaker ablative stabilization and, consequently, the larger growth of the RT instability), leading to a linear dependence of the measured yields on α . Figure 137.24 plots the neutron yields normalized to *LILAC* predictions. As the fuel adiabat gets smaller, the yields drop with respect to the 1-D predictions. This indicates that the shell stability plays a crucial role in determining target performance.

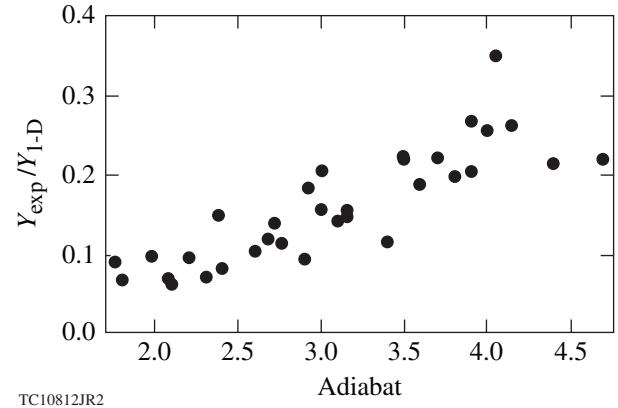


Figure 137.24

Experimental yields normalized to *LILAC* predictions. Only data for shells with CD thicknesses of 7.5 to 8.3 μm are shown.

2. Areal Density

In addition to the target yields, the performance degradation is quantified by plotting the neutron-averaged areal-density reductions (with respect to the 1-D predictions) as a function of adiabat and the target IFAR. Here,

$$\text{IFAR} = \frac{R_{a,2/3}}{\Delta_{2/3}} \quad (19)$$

is defined near the beginning of shell acceleration, when the ablation front is at $R_{a,2/3} = 2/3 R_{\text{vapor}}$. The shell thickness Δ is defined as the distance between the inner and outer positions where the shell density equals the initial density of the ablator ($\rho = 1.08 \text{ g/cm}^2$ for CD). Figure 137.25(a) shows the map of the absolute values of the areal density averaged over two independent measurements using the magnetic recoil spectrometer (MRS)²⁷ and a highly collimated neutron time-of-flight (nTOF) detector.²⁸ The black points represent the individual OMEGA shots. The map was created by interpolating the ρR values between the experimental points.

As the fuel adiabat gets smaller and the shell IFAR larger, the measured ρR drops with respect to the 1-D predictions. Figure 137.25(b) shows that a stability boundary, defined by

$$\text{IFAR}_{\text{boundary}} \simeq 20(\alpha/3)^{1.1}, \quad (20)$$

separates the region where more than 85% of the 1-D-predicted areal density is observed (on the right side from the boundary) and the region where shell compressibility is compromised by the nonuniformity growth and the measured areal density is reduced.

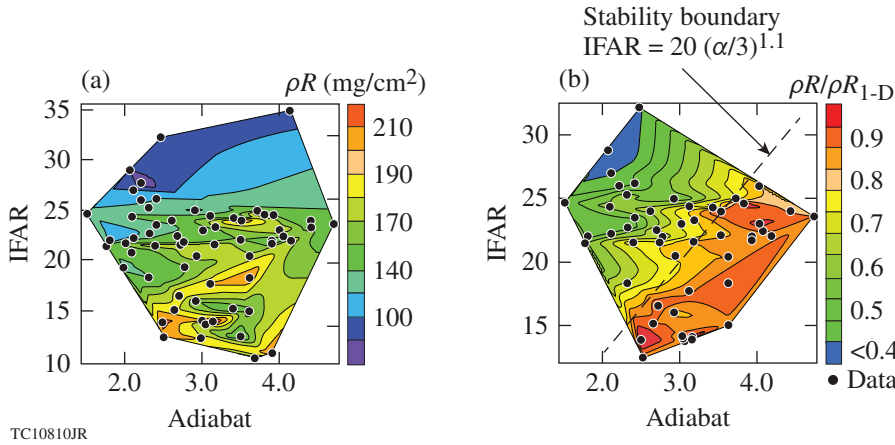


Figure 137.25

(a) Contour map of the measured areal density as a function of calculated adiabat and IFAR. The contours represent a linear fit to the experimental data (black points). (b) Contour map of the measured areal density normalized to *LILAC* predictions. The dashed line (a stability boundary) separates the region where more than 85% of the 1-D-predicted areal density is observed and the region where the shell areal density is significantly reduced because of the hydrodynamic instability growth.

3. Hot-Spot Pressure

The hot-spot pressure evolution in the experiments is estimated using the ratio of the predicted and measured neutron-production histories. With the help of Eq. (5), the neutron-production rate can be written as

$$\dot{N} = \frac{dN}{dt} \sim p_{\text{hs}}^{7/5} T_i^{2.5}. \quad (21)$$

Then, taking the ratio of the experimental and predicted \dot{N} and using the result to obtain the hot-spot pressure inferred in the experiment $p_{\text{hs}}^{\text{exp}}$ gives

$$p_{\text{hs}}^{\text{exp}} \simeq p_{\text{hs}}^{\text{theory}} \left(\frac{T_{\text{exp}}}{T_{\text{theory}}} \right)^{-1.8} \left(\frac{\dot{N}_{\text{exp}}}{\dot{N}_{\text{theory}}} \right)^{-0.7}. \quad (22)$$

The neutron-production measurement is time resolved,²⁹ while the neutron-averaged ion temperature is a time-integrated quantity. In evaluating Eq. (22), therefore, the time-integrated neutron-averaged temperatures are used in both the measured T_{exp} and predicted T_{theory} ion temperatures. Figure 137.26 shows the temporal evolutions of the measured and 1-D-predicted neutron-production rates; the predictions include the instrumental as well as the thermal and bulk-velocity broadening, as shown in Eq. (10). The calculated and inferred hot-spot pressures are plotted in Fig. 137.27 for two OMEGA shots with similar 1-D implosion parameters ($\alpha \sim 4$). The figure indicates that 35% to 40% of the hot-spot pressures predicted by *LILAC* is achieved in OMEGA cryogenic implosions at these moderate adiabat values. These pressure values are consistent with the results of the hot-spot model described in Ref. 30.

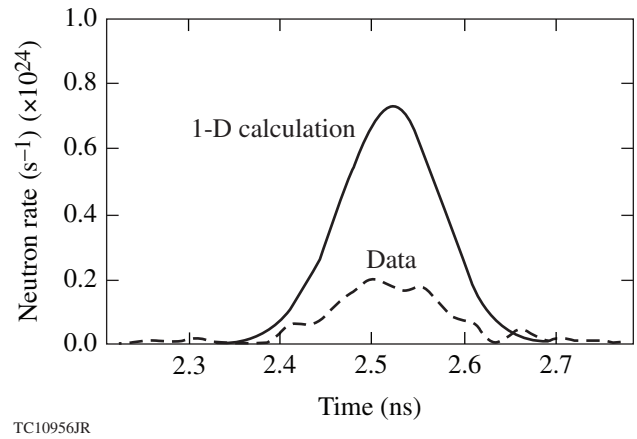


Figure 137.26

The measured (dashed line) and predicted (solid line) neutron-production histories for an $\alpha = 4$ cryogenic implosion (shot 69514).

The hot-spot pressure evolution for a lower-adiabat implosion ($\alpha \sim 2$) is shown in Fig. 137.28. Although the predicted peak pressure increases to 150 Gbar, the pressure inferred in the experiment is reduced compared to that in the inferred higher-adiabat implosions.

A two-dimensional (2-D) map of the neutron-averaged hot-spot pressures and the ratios of the inferred and predicted pressures is shown in Fig. 137.29. The hot-spot pressure peaks at $\alpha \sim 4$ and an IFAR ~ 22 . The pressure is lower in implosions with a smaller IFAR because of the reduced predicted values [lower implosion velocities or higher adiabats lead to lower hot-spot pressures (see **Discussion**, p. 35)]. A reduced pressure for the higher-IFAR implosions is due to a loss in the target stability. This will be discussed in more detail in the next section.

Implosion Modeling

This section describes the analysis of the cryogenic target performance based on 2-D simulations in the next subsection and using simplified analytic models, see p. 28).

1. Integrated Two-Dimensional Simulations

To improve the target performance and demonstrate the ignition hydrodynamic equivalence of cryogenic implosions on OMEGA, it is important to understand the trends in the experi-

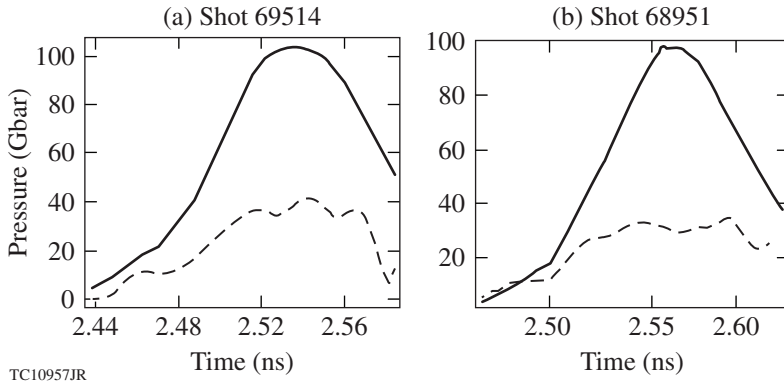


Figure 137.27
The calculated (solid lines) hot-spot pressure and the pressure inferred (dashed lines) using the measured neutron-production history and ion temperature for two $\alpha \simeq 4$ implosions. The predicted and inferred peaks in the central pressure p_{\max} are 100 Gbar and 41 Gbar (shot 69514) and 100 Gbar and 33 Gbar (shot 68951), respectively. The predicted and inferred neutron-averaged hot-spot pressures $\langle p \rangle_n$ are 72 Gbar and 29 Gbar (shot 69514) and 66 Gbar and 24 Gbar (shot 68951), respectively.

TC10957JR

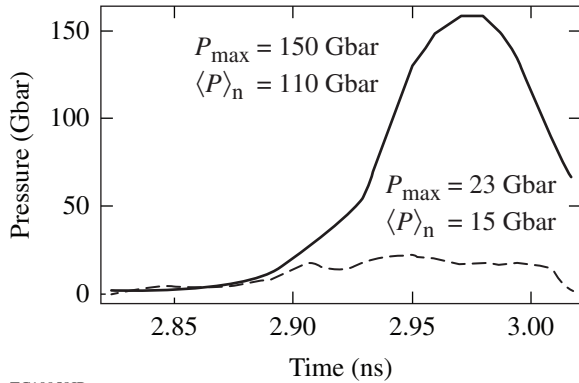


Figure 137.28
The predicted (solid line) and inferred (dashed line) hot-spot pressure for an $\alpha \simeq 2.1$ implosion (shot 69236).

TC10958JR

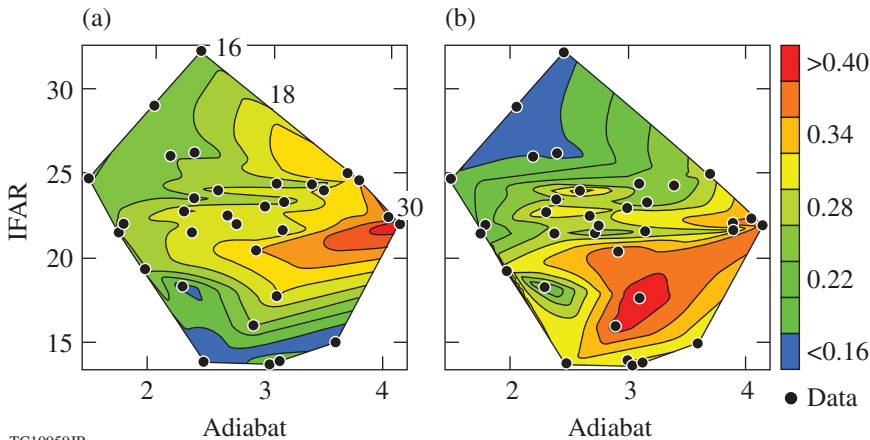


Figure 137.29
(a) Contour map of the inferred neutron-averaged hot-spot pressure. The constant-pressure contours with $\langle p \rangle_n = 16, 18, \text{ and } 30$ Gbar are labeled on the map. (b) Contour map of the inferred pressure normalized to LILAC predictions.

TC10959JR

mental data shown in Figs. 137.24 and 137.29. As a first step, the 2-D hydrocode *DRACO*³¹ was used to calculate the effects of the target-surface roughness, the short-wavelength, single-beam nonuniformity (laser imprint), and the long-wavelength illumination nonuniformities caused by the beam power imbalance, the beam-overlap pattern, the beam mistiming, and target offset. Figure 137.30 shows the simulation results³² of the mid-adiabat ($\alpha \sim 4$) implosion (OMEGA shot 69514). Table 137.III summarizes the predicted and measured performance parameters. Table 137.III and Fig. 137.30 indicate that the neutron yield, areal density, and burnwidth are in very good agreement with the observables. The size of the x-ray image calculated using the *DRACO* simulation post-processed with the radiative transfer code *Spect3D*³³ is also in good agreement with measurements made using the gated x-ray imager (GMXI).³⁴

Simulations of lower-adiabat ($\alpha \sim 2$) implosions, however, fail to reproduce the experimental data. The measured areal densities are significantly lower than the simulated values (by

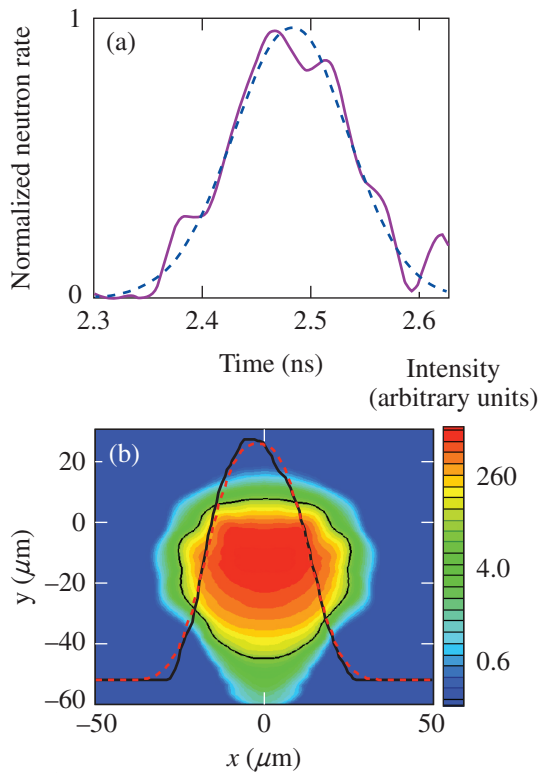


Figure 137.30
(a) Measured (solid line) and simulated using the 2-D hydrocode *DRACO* (dashed line) neutron-production history for a mid-adiabat ($\alpha \sim 4$ shot 69514) implosion. (b) A lineout of the measured time-integrated x-ray emission (red dashed line) and the results of a *DRACO* simulation post-processed using *Spect3D* [shown as a contour map of intensity and a lineout of this map (black line)].

a factor of 1.5 to 2), the experimental burn width is larger by almost a factor of 2, and the size of the x-ray emission region is significantly larger as well. The results of simulations are compared with the data in Table 137.IV.

Table 137.III: Summary of the measured and *DRACO*-calculated target performance parameters for an $\alpha = 4$ cryogenic implosion (shot 69514).

Observables	Simulation	Experiment
Yield ($\times 10^{13}$)	3.9	3.0 ± 0.1
T_i (keV)	3.7	3.6 ± 0.3
ρR (mg/cm ²)	180	175 ± 15
p_{hs} (Gbar)	32	30 ± 5

Table 137.IV: Summary of the measured and *DRACO*-calculated target performance parameters for an $\alpha = 2$ cryogenic implosion (shot 69236).

Observables	Simulation	Experiment
Yield ($\times 10^{13}$)	1.7	1.1 ± 0.1
T_i (keV)	2.9	3.0 ± 0.2
ρR (mg/cm ²)	190	110 ± 13
Burnwidth (ps)	80	115 ± 10
p_{hs} (Gbar)	41	18 ± 5

This limited ability of the hydrodynamic simulations to explain the observables in the low-adiabat implosions on OMEGA is common to that in indirect-drive cryogenic implosions³⁵ at the National Ignition Facility (NIF).³⁶ To understand the factors limiting the target performance, it is not sufficient to rely solely on the simulations because of uncertainties in the physical models used in these codes. In addition, not all the sources of the target and illumination nonuniformities can be identified and characterized with the precision required to resolve the performance-relevant spatial scales. Simplified theoretical models can help in developing a physical understanding of the implosion dynamics and failure mechanisms. Such models will be described in the next section.

2. Simplified Models of the Implosion Dynamics

The peak hot-spot pressure can be estimated using the argument that stopping the incoming shell with density ρ_{shell} and velocity v_{imp} by a strong shock requires a shock pressure of

$$p_{max} \simeq 4/3 \rho_{shell} v_{imp}^2. \quad (23)$$

Using the in-flight shell quantities (an ablation pressure of 100 Mbar, fuel adiabat $\alpha \sim 1$, and shell velocity $v_{\text{imp}} = 4 \times 10^7$ cm/s), Eq. (23) gives only

$$\begin{aligned} p_{\text{max}} &\simeq 4/3(p_a/2.2\alpha)^{3/5} v_{\text{imp}}^2 \\ &= 4/3(100 \text{ Mbar}/2.2)^{3/5} (4 \times 10^7)^2 = 21 \text{ Gbar}, \end{aligned}$$

an order of magnitude lower than the peak pressure predicted in a hydrodynamic code simulation at these conditions. The source of the pressure deficiency in using this simple argument is the spherical convergence effects that are important during the final stages of the hot-spot formation ($\rho_{\text{shell}} \gg \rho_{\text{in flight}}$). The shell convergence increases the density of the incoming shell during the deceleration. Because peak stagnation pressures exceeding 100 Gbar are required in an igniting hot spot, it is crucial to understand the dynamics of shell deceleration and the hot-spot pressure amplification near stagnation.

The hot-spot pressure's dependence on the shell convergence provides a starting point in describing the deceleration dynamics. Since the thermal conduction losses from the hotter central region to the colder shell material are balanced by the internal energy flux of the ablated material back into the hot spot, pressure inside the hot spot is not affected by the ablation and can be calculated using the adiabatic approximation³ $p_{\text{hs}} \sim V_{\text{hs}}^{-5/3}$, where V_{hs} is the hot-spot volume. If $V_{\text{hs},0}$ and $p_{\text{hs},0}$ are the volume and pressure of the vapor region at the beginning of shell deceleration, the time evolution of the hot-spot pressure can be described by

$$p_{\text{hs}} = p_{\text{hs},0} \left(\frac{V_{\text{hs},0}}{V_{\text{hs}}} \right)^{5/3}. \quad (24)$$

As the hot spot approaches stagnation and the electron temperature starts to rise (the electron-ion energy exchange rate increases with the hot-spot density), the hot-spot mass increases because of the mass ablation from the inner part of the shell. Consequently, the temporal behavior of the ventral pressure cannot be described by the central density alone, $p_{\text{hs}} \approx \rho_{\text{hs}}^{5/3}$, even though Eq. (24) is satisfied. The central pressure peaks as the hot-spot volume reaches its minimum value V_{min} ,

$$p_{\text{max}} = p_{\text{hs},0} \left(\frac{V_{\text{hs},0}}{V_{\text{min}}} \right)^{5/3}. \quad (25)$$

Calculating the peak central pressure, therefore, reduces to determining the vapor pressure $p_{\text{hs},0}$ at the beginning of the shell's deceleration and the hot-spot volume reduction fraction during deceleration $V_{\text{hs},0}/V_{\text{min}}$ [this is related to the hot-spot convergence ratio (CR), $p_{\text{max}} \sim \text{CR}^5$, in a 1-D implosion].

The shell position and the vapor volume $V_{\text{hs},0}$ at the start of deceleration are the key parameters since the farther the shell moves inward before it begins to decelerate, the higher the shell density ρ_{shell} (because of the convergence effects) and, according to Eq. (23), the higher the maximum pressure ($\rho_{\text{shell}} v_{\text{imp}}^2$ is larger because of the higher ρ_{shell}). The shell deceleration begins when the vapor pressure, amplified by the shell convergence, exceeds the shell pressure (which is higher for the higher ablation pressures). Therefore, the onset of shell deceleration depends on the vapor and shell pressure evolutions during the shell acceleration. The vapor pressure history will be discussed first.

a. Vapor-pressure evolution. Three main effects contribute to the increase in vapor pressure during the implosion: (1) the compression of the initial vapor mass introduced into the central part of the target during the cryogenic-layer formation; (2) the density rarefaction (material release) at the inner part of the shell during the acceleration; and (3) the excessive nonuniformity growth that leads to the shell breakup, injecting the cold shell and plasma-corona materials into the vapor region. The first contribution can be calculated using the pressure-density relation

$$p_{v,1} = \mu \alpha_v \rho_v^{5/3}, \quad (26)$$

where α_v is the adiabat of the vapor region, $p_{v,1}$ and ρ_v are the vapor pressure and density, respectively, and μ is defined in Eq. (18). The vapor volume V_v gets smaller during the shell's convergence, so the average vapor density increases as

$$p_v = \rho_{v,0} V_{v,0} / V_v, \quad (27)$$

where $\rho_{v,0}$ and $V_{v,0}$ are the density and volume of the vapor region in an undriven target. Neglecting the kinetic effects of ions, the vapor adiabat is determined mainly by shock heating:

$$\alpha_v = \frac{P_{v,\text{shk}}}{\mu \rho_{v,\text{shk}}^{5/3}}, \quad (28)$$

where $p_{v,\text{shk}}$ and $\rho_{v,\text{shk}}$ are the pressure and density behind the leading shock that travels in the vapor and μ is defined in Eq. (18). Since the leading shock is strong, $\rho_{v,\text{shk}} \simeq 4\rho_{v,0}$;

it can be shown that the relation between the ablation and shock pressures takes the form

$$p_{v,shk} \simeq p_{a,0} \frac{\rho_{v,0}}{\rho_0} \left\{ 1 + 2\sqrt{5} \left[1 - \left(\frac{\rho_{v,0}}{\rho_0} \right)^{1/5} \right] \right\}, \quad (29)$$

where $p_{a,0}$ is the ablation pressure at the beginning of shell acceleration and ρ_0 is the initial (undriven) main fuel density ($\rho_0 \simeq 0.25 \text{ g/cm}^3$ for DT ice). Using Eqs. (26)–(29) gives the vapor adiabat

$$\alpha_v = \frac{p_{a,0}}{4^{5/3} \mu \rho_{v,0}^{2/3} \rho_0} \left\{ 1 + 2\sqrt{5} \left[1 - \left(\frac{\rho_{v,0}}{\rho_0} \right)^{1/5} \right] \right\}, \quad (30)$$

and the contribution to the vapor pressure related to the convergence of the initial vapor mass becomes

$$p_{v,1} \simeq \frac{p_{a,0}}{4^{5/3}} \frac{\rho_{v,0}}{\rho_0} \left\{ 1 + 2\sqrt{5} \left[1 - \left(\frac{\rho_{v,0}}{\rho_0} \right)^{1/5} \right] \right\} \left(\frac{V_{v,0}}{V_v} \right)^{5/3}. \quad (31)$$

The convergence effects of the leading shock wave break the validity of Eq. (29) near the target center, so Guderley's solution³⁷ must be used. The volume of the vapor region where this occurs, however, is small compared to the total vapor volume. A correction to the vapor pressure caused by an increase in the shock strength near the origin, therefore, is small.

Strictly speaking, the shock convergence effects near the target center cannot be described using Guderley's solution either because of ion heating that becomes strong enough to raise the ion temperatures to a few keV at the shock front. The ions in the high-energy tail of the distribution function travel ahead of the shock in this case,³⁸ preheating the vapor region and raising its adiabat. The higher adiabat leads to an increase in the vapor pressure (for a given vapor mass), causing shell deceleration to start sooner.

Equation (31) shows that the vapor pressure decreases when the initial vapor mass and density are reduced. Therefore, minimizing the initial vapor mass improves the areal densities at peak compression by increasing the shell convergence prior to the onset of the deceleration. The lower limit of the vapor pressure (when

the initial vapor mass is very small) is determined by the density rarefaction formed at the inner part of the shell during the implosion. A low-density tail of the released material travels ahead of the higher-density part of the shell, contributing to the vapor mass. A simplified scaling for the vapor mass with the implosion parameters can be obtained by assuming that a strong shock with a pressure p_a breaks out of a material with the post-shock sound speed c_{sa} and density ρ_a into the material with density $\rho_{v,0}$. The released material moves inward with the velocity³⁹

$$v_{\text{tail}} = v_{\text{shell}} + 3c_{sa} \left[1 - \left(\frac{p_{v,shk}}{p_a} \right)^{1/5} \right], \quad (32)$$

where $p_{v,shk}$ is calculated using Eq. (29). The accumulated mass in the rarefaction tail calculated from the lowest-density point up to the density ρ is

$$m_{\text{rf}}(\rho) \simeq 4\pi R^2 c_{sa} \rho_a t \left[\left(\frac{\rho}{\rho_a} \right)^{4/3} - \left(\frac{p_{v,shk}}{p_a} \right)^{4/5} \right], \quad (33)$$

where R is shell position and t is time. Since the tail expands with a velocity greater than the shell's velocity [see Eq. (32)], the accumulated mass in the rarefaction increases with time, as shown in Eq. (33). Using the total shell acceleration time $t = t_{\text{imp}} \sim E_L / (4\pi R^2 I)$ (where E_L is the laser energy and I is the laser intensity) in Eq. (33) and writing the mass density as $\rho_a \sim (p_a / \alpha_{\text{inner}})^{3/5}$ gives the scaling for the mass in the rarefaction tail at the end of the shell acceleration:

$$m_{\text{rf}} \sim \left(\frac{E_L}{I} \right) \alpha_{\text{inner}}^{-3/10} p_a^{4/5} C_\rho, \quad (34)$$

$$C_\rho = \left(\frac{\rho}{\rho_a} \right)^{4/3} - \left(\frac{p_{v,shk}}{p_a} \right)^{4/5},$$

where α_{inner} is the adiabat of the inner part of the shell. Then, the contribution to the vapor pressure caused by the mass buildup from the rarefaction tail (the second contribution to the vapor pressure in our notation)

$$p_{v,2} = \mu \alpha_{\text{inner}} \left(\frac{m_{\text{rf}}}{V_v} \right)^{5/3} \quad (35)$$

with the help of Eq. (34) and the scaling for the initial vapor size [see Eq. (71) later in the text] becomes

$$p_{v,2} \sim C_{\rho}^{5/3} \sqrt{\alpha_{\text{inner}}} \frac{P_a^{4/3}}{v_{\text{imp}}^{5/3}} \left(\frac{V_{v,0}}{V_v} \right)^{5/3}. \quad (36)$$

Matching Eq. (36) with the simulation results leads to using $\rho/\rho_a \sim 0.1$ in the coefficient C_{ρ} . As the fill pressure (vapor density) increases, $p_{v,\text{shk}}/p_a$ increases as well and the contribution to the hot-spot pressure from the material release into the target center becomes small. Equation (36) tends to overestimate the pressure because Eqs. (32) and (33) are written in the shell's frame of reference, assuming that v_{shell} is a constant in time. The shell velocity in ICF implosions, however, increases with time, reducing the velocity difference between the shell and the trailing edge of the rarefaction wave. This makes the mass in the rarefaction tail smaller than predicted by Eq. (34).

Since the rarefaction's contribution to the vapor pressure depends on the adiabat α_{inner} , material heating at the inner part of the shell caused by the shock mistiming, radiation, or suprathermal-electron preheat can result in a greater material expansion. In addition, significant reduction in the hot-spot pressure can occur compared to the case when such heating is not taken into account. In an optimized design, the gain in mass of the vapor region from the release is minimized by accurately timing shocks emerging from the cold fuel shell.

The third contribution to the pressure and the mass enhancement in the vapor region is due to multidimensional effects. These include jets of material created by local shell nonuniformities as well as fluxes of the ablated plasma through the holes in the shell that result from the excessive RT growth at the ablation front. These effects lead to an injection of the material with relatively high adiabat $\alpha_{\text{mix}} \gg \alpha_{\text{shell}}$ (Ref. 40). The vapor pressure contribution caused by the mix is

$$p_{v,3} = \mu \alpha_{\text{mix}} \left(\frac{m_{\text{mix}}}{V_v} \right)^{5/3}, \quad (37)$$

where m_{mix} is the injected mix mass.

The effect of shell breakup and the ablator mass injection into the vapor region was studied in Ref. 40, where a series of 2-D *DRACO* simulations were performed assuming localized mass perturbations of 5 to 30 μm in diameter and 0.5 to 1 μm in height as an initial nonuniformity source on the outside of the target. The simulations show that these features significantly distort the first shocks launched by the intensity pickets early in the laser pulse, introducing significant modulations in

the lateral mass flow and creating low-density bubbles inside the ablator and the main fuel layer at the beginning of shell acceleration. Since the ablation stabilization is not efficient inside the cold bubbles,⁴¹ the bubble growth is significantly enhanced as the shell starts to accelerate. The bubble velocity⁴² $v_{\text{bubble}} \sim \sqrt{d_{\text{bubble}} g}$ (where d_{bubble} is the bubble diameter and g is the shell acceleration) competes with the material release rate at the inner surface of the shell [see Eq. (34)] and shell thickening resulting from convergence. When the bubble amplitude exceeds the in-flight shell thickness, the bubble "bursts" into the vapor region, injecting the ablator and the cold fuel mass into the central part of the target. In addition, the pressure difference between the ablation front and the vapor region creates a flow of ablated material from the plasma corona into the vapor region. Since the material releases more slowly in lower-adiabat shells and the main shell is thinner, the shells in such implosions are more likely to break up because of the bubble growth.

The simulation results, summarized in Fig. 9 of Ref. 40, indicate that to reduce the peak areal density by a factor of 2, the ablator and cold fuel material must be injected with a mass that is $\sim 15\times$ larger than the initial vapor mass. For the DT vapor at the triple point, the initial mass density is $\sim 0.6 \text{ mg/cm}^3$, which corresponds to the initial vapor mass of 0.12 μg for OMEGA cryogenic targets.

Next, the inferred hot-spot pressure and the measured neutron-production rate in an $\alpha \sim 2$ cryogenic implosion are compared with the results of *DRACO* simulations. The level of the pre-imposed local defects in such simulations was varied to match the observed areal density and neutron yield. This leads to 2 μg of ablator and main fuel material being injected into the vapor region because of hydrodynamic instability growth during acceleration. The simulation results and the data are compared in Fig. 137.31. Observe the excellent agreement between simulation results and the data. This suggests that, indeed, the degradation in the performance of the low-adiabat implosions results from a significant mixing of the ablator material into the vapor region. The main source of the localized nonuniformities in OMEGA cryogenic targets, however, remains unknown. Significant shock distortions can be caused by either surface features or ice defects localized at the CD/DT interface created, for example, as a result of the early-time laser shinethrough.⁴³

In summary, the pressure buildup inside the converging target is caused by compression of the original vapor mass, the material release from the inner part of the shell during accelera-

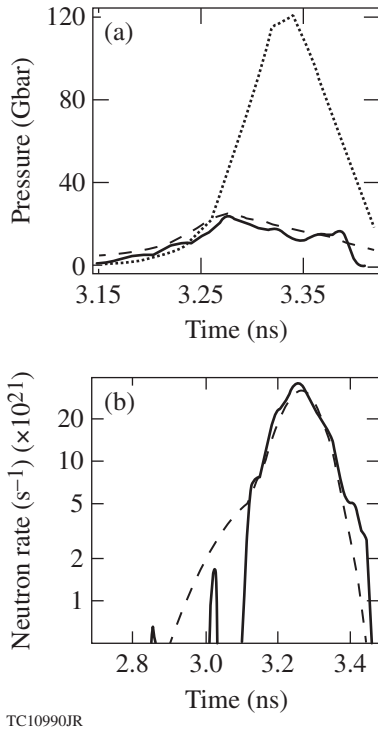


Figure 137.31

(a) The hot-spot pressure evolution inferred from the measurements (shot 66613, $\alpha = 2$) using Eq. (22) (solid line) and predicted using *LILAC* (dotted line) and *DRACO* (dashed line). (b) The neutron-production history measured (solid line) and predicted (dashed line) using *DRACO* simulations with the pre-imposed local defects on the outer surface of the target.

tion, and mixing of the ablator and cold fuel inside the target's vapor region because of the RT growth at the ablation front. The central pressure increase causes the early shell deceleration and stagnation, resulting in lower final fuel compression.

b. Shell acceleration and shell-pressure evolution. The onset of the shell deceleration depends not only on the vapor but also on the shell pressures because the shell begins to slow down when the radial pressure gradient pointing toward the target center is formed. During the early stages of an implosion, when the convergence effects are not important, the maximum shell pressure is equal to the ablation pressure and the pressure peak is localized near the ablation front. When convergence becomes important, the pressure maximum exceeds the ablation pressure and the pressure peak moves inside the shell. The basic features of the shell dynamics in convergent geometry can be studied using a model based on an approximate solution of the momentum-conservation equation. This model is described in **Appendix A**, p. 43, where the shell pressure is written as a second-order polynomial in the mass coordinate:

$$p(m, t) = p_a \left[1 + \hat{p}_1(t) \left(1 - \frac{m}{M} \right) + \hat{p}_2(t) \left(1 - \frac{m}{M} \right)^2 \right], \quad (38)$$

where m is the mass coordinate defined by a differential equation $dm/dr = 4\pi\rho r^2$ and M is the shell mass. The maximum shell pressure p_{shell} equals the ablation pressure p_a when $\hat{p}_1 < 0$; p_{shell} exceeds p_a when \hat{p}_1 becomes positive because of convergence effects [see Eq. (A2) for the dependence of \hat{p}_1 on the implosion parameters]. In the latter case, the peak pressure moves inside the shell and, consequently, the ablation front stops accelerating [see Eq. (A9)]. The time at which the pressure gradient at the ablation front changes from a positive to a negative value plays an important role in designing a target because this is when the absorbed laser energy no longer contributes to the shell's acceleration. Therefore, in an optimized implosion, the end of the laser drive must occur when $\hat{p}_1 \simeq 0$.

The ablation-front position at this time can be calculated with the help of Eq. (A13):

$$R_a \simeq R_0 \left[\frac{\epsilon}{3} \frac{M \dot{R}_a^2 / 2}{4\pi R_0^3 p_{a,0}} (2 - 3/5\beta)(1 - \beta/5) \right]^{1/(6 - 8/5\beta)}, \quad (39)$$

where R_a is the ablation-front radius and $p_{a,0}$ is the ablation pressure at the beginning of the shell's acceleration. The power index of the ablation-pressure evolution β and parameter ϵ are defined in Eqs. (A5) and (A7), respectively. Equation (39) can be rewritten as

$$\frac{M}{\rho_a V_a} \times \frac{M \dot{R}_a^2 / 2}{(3/2)p_a V_a} = \frac{1}{(1 - 3\beta/10)(1 - \beta/5)} \sim 1, \quad (40)$$

where $V_a = (4\pi/3)R_a^3$ is the target volume and ρ_a is the shell density at the ablation front (peak shell density). The first term in the left-hand side of Eq. (40) is proportional to the ratio of the shell's thickness to the ablation-front radius (this ratio is inversely proportional to the IFAR). The second term is the ratio of the shell's kinetic energy E_k and the internal energy $E_{\text{in},a} = (3/2)p_a V_a$. The IFAR decays and the ratio of energies increases as the shell converges and accelerates. Therefore, the ablation front stops being accelerated when

$$\text{IFAR} \sim \frac{E_k}{E_{\text{in},a}}. \quad (41)$$

The shell's kinetic energy and the ablation pressure do not depend on the shell adiabat, and, for a given shell radius, the IFAR is larger when the shell adiabat is lower. According to Eq. (41), compared to the higher adiabat, the lower-adiabat shells accelerate for longer distances.

Equation (40) can also be written in terms of the ablation-front Mach number $|\dot{R}_a|/c_s$:

$$\rho_a V_a = M \frac{|\dot{R}_a|}{c_s} \sqrt{\left(\frac{1}{3} - \frac{\beta}{10}\right) \left(\frac{5}{3} - \frac{\beta}{3}\right)}, \quad (42)$$

where $c_s = \sqrt{(5/3)(p_a/\rho_a)}$ is the shell's sound speed. The numerical factor in Eq. (42) varies from 0.45 to 0.65 for values of β relevant to the ICF implosions. During the implosion, the shell's density times the target volume $\rho_a V_a$ decreases (mainly because of a reduction in volume) and the shell's Mach number increases (because of an increase in $|\dot{R}_a|$). The ablation pressure stops accelerating the ablation front when these two terms are equal: $\rho_a V_a \sim M |\dot{R}_a|/c_s$. Even though the ablation-front velocity does not increase after that time, the parts of the shell where the pressure gradient is positive are still being accelerated. The total shell kinetic energy, therefore, keeps increasing until the vapor pressure exceeds the shell's pressure and a return shock is launched into the incoming shell. The longer the time delay between the end of the ablation-front acceleration and the return shock formation, the larger the velocity gradient in the shell and the lower the shell density, which results in lower stagnation pressures (for more details, see the discussion in **Shell Deceleration** below). Furthermore, the longer acceleration distances in the lower-adiabat implosions lead to enhanced RT growth factors at the ablation front. Note that the onset of ablation-front deceleration can be measured experimentally by imaging the x-ray emission from the plasma corona, as discussed in **Target Designs and Validation of 1-D Implosion Parameters**, p. 19.

After the location of the peak pressure moves from the ablation front inside the shell (because of the convergence effects), the shell mass coordinate of this location and the value of the peak pressure become

$$m_p = M \left(1 - \frac{1 + \hat{p}_2}{2\hat{p}_2}\right), \quad (43)$$

$$p_{\text{shell}} = -p_a \frac{(1 - \hat{p}_2)^2}{4\hat{p}_2}, \quad (44)$$

respectively. Note that p_{shell} is positive because \hat{p}_2 is negative. At this stage in the implosion, \hat{p}_2 can be simplified to

$$\hat{p}_2 \simeq -\frac{M\dot{R}_a^2/2}{3/2\rho_a V_a} \frac{C_\beta}{1 + 6/(4 - 3/5\beta)\rho_a V_a/M}, \quad (45)$$

where the coefficient $C_\beta = (2 - 3/5\beta)(3 - 3/5\beta)/(4 - 3/5\beta) \simeq 1$ changes from 0.8 to 1.2 for the values of β relevant to the direct-drive implosions.

In summary, the start of shell deceleration is determined by the relative evolutions of the vapor [Eqs. (31), (36), and (37)] and the shell [Eq. (44)] pressures. The target performance increases when the onset of deceleration is delayed. This is achieved by maximizing the shell and ablation pressures and minimizing the vapor pressure. The ablation front stops accelerating when $\rho_a V_a/M \sim |\dot{R}_a|/c_s$. The early ablation-front deceleration in the shells with higher adiabats, larger masses, and lower ablation-front densities leads to larger shell-velocity gradients and lower shell densities during the shell deceleration, resulting in lower stagnation pressures.

c. Shell deceleration. Soon after the vapor pressure exceeds the shell pressure [see Fig. 137.15(a)], a shock is formed at the inner surface of the shell, as illustrated in Fig. 137.32. The shock travels from the vapor region toward the ablation front. The inner part of the shell overtaken by the return shock (the shocked shell) is being decelerated by a force that is a

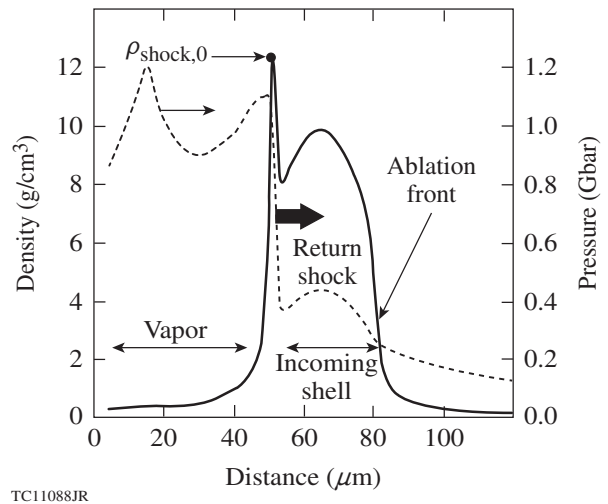


Figure 137.32

The density (solid line, left axis) and pressure (dashed line, right axis) profiles at the time when the return shock is launched into the incoming shell.

consequence of the higher pressure at the hot spot p_{hs} and the lower pressure at the shock front p_{shock} (see Fig. 137.33). The hot-spot pressure continues to increase while the shocked shell converges inward, reducing the hot-spot volume (if the multi-dimensional effects are taken into account, the volume history depends also on the hot-spot distortion growth).

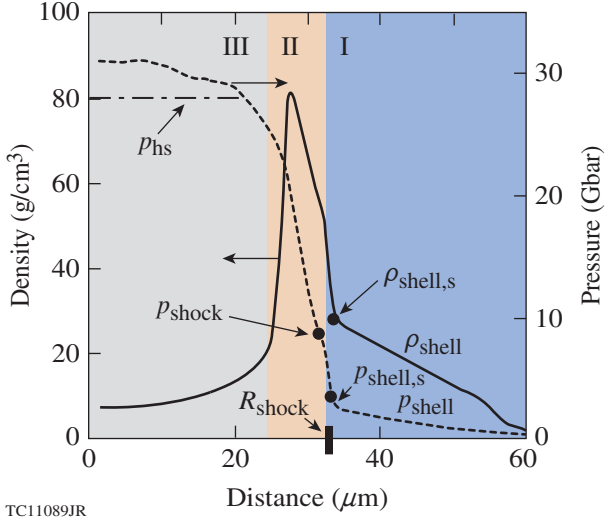


Figure 137.33
Snapshots of the density (solid line, left axis) and pressure (dashed line, right axis) profiles during shell deceleration. The following three regions can be identified at this time: (I) the unshocked shell, (II) the shocked shell, and (III) the vapor region (hot spot).

The model describing the shell and hot-spot evolutions during the shell deceleration is presented in **Appendix B** (p. 45). Here, the main results are summarized.

The hot-spot radius R_{hs} is determined by the momentum–conservation equation (Newton’s law)

$$\ddot{R}_{hs} = S_{hs} \frac{p_{hs} - p_{shock}}{M_s} \left(1 - \frac{M_s}{6\rho_{shock,0} V_{hs,0}} \right)^{-1}, \quad (46)$$

where S_{hs} is the surface area of the hot spot, $\rho_{shock,0}$ and $V_{hs,0}$ are the shell’s density at the inner edge of the shell and hot-spot volume at the beginning of shell deceleration, respectively (see Fig. 137.32), and M_s is the mass of the shocked shell (shocked mass). The factor inside the brackets in Eq. (46) is due to the nonlinear variation of the shell’s pressure with the mass coordinate. The shocked mass, shock pressure, and shock position are determined by Hugoniot conditions:³⁹

$$\frac{dM_s}{dt} = \sqrt{\frac{\rho_{shell,s}}{3}} \sqrt{4p_{shock} + p_{shell,s}} S_{shock}, \quad (47)$$

$$p_{shock} = p_{shell,s} - \sqrt{\frac{\rho_{shell,s}}{3} (4p_{shock,s} + p_{shell,s})} \times (v_{shell,s} - v_{shock}), \quad (48)$$

and

$$\frac{dR_{shock}}{dt} = \sqrt{\frac{4p_{shock} + p_{shell,s}}{3\rho_{shell,s}}} + v_{shell,s}, \quad (49)$$

where S_{shock} is the shock-front area. Refer to Fig. 137.33 for definitions of $\rho_{shell,s}$, $v_{shell,s}$, and v_{shock} . In the strong-shock approximation, these relations are reduced to the expressions shown in Eq. (B9).

The shock pressure p_{shock} increases during the deceleration because of an increase in ρ_{shell} (resulting from the shell convergence) and the deceleration of the shocked shell (which leads to a reduction in $|v_{shock}|$). The rate of increase in p_{shock} is reduced by the deceleration of the unshocked shell (which leads to a reduction in $|v_{shock}|$).

Because of convergence, the density of the unshocked shell increases as

$$\rho(m,t) \simeq \rho_0(m) \left[\frac{r_0(m)}{r(m,t)} \right]^2 \times \left[1 + 4\pi C_d \frac{c_{s,0}}{M} (t - t_d) \rho_0(m) r_0(m)^2 \right]^{-1}, \quad (50)$$

where the numerical coefficient $C_d = \sqrt{2(2 - 3/5\beta)/5 - \beta}$ ranges from 0.8 to 0.9 for the values of β relevant to the direct-drive implosions, $c_{s,0}$ is the shell’s sound speed at the beginning of deceleration, $\rho_0(m)$ and $r_0(m)$ are the shell density and position as functions of mass coordinate at the beginning of shell deceleration, and t_d is the starting time of the shell deceleration. The deviation from a $1/r^2$ dependence in the density evolution is due to the velocity gradient inside the unshocked shell.

The reduction in the shocked shell velocity v_{shock} is calculated by relating it to the convergence rate of the hot spot,

$$v_{\text{shock}} = \dot{R}_{\text{hs}} \left(1 + \frac{M_s}{3\rho_{\text{shock},0} V_{\text{hs},0}} \right). \quad (51)$$

The velocity slowdown in the unshocked region is calculated using the momentum conservation $dv_{\text{shell}}/dt \sim -S_{\text{shock}} \partial p / \partial m$, where the pressure gradient is

$$\begin{aligned} \frac{\partial p}{\partial m} \simeq & \left(\frac{r_0}{r} \right)^{10/3} \Sigma^{-8/3} \left[\frac{\partial p_0}{\partial m} + \frac{5p_0}{6\pi\rho_0 r_0^3} \right] \\ & - \left(\frac{r_0}{r} \right)^{13/3} \Sigma^{-2/3} \frac{5p_0}{6\pi\rho_0 r_0^3}, \end{aligned} \quad (52)$$

and

$$\Sigma = 1 + 4\pi C_d \frac{c_{s,0}}{M} (t - t_d) \rho_0(m) r_0(m)^2.$$

The second term in Eq. (52) grows faster than the first term. This leads to a negative pressure gradient and deceleration of the unshocked shell.

Equations (46)–(51), together with the hot-spot pressure's dependence on shell convergence [see Eq. (24)], define the deceleration model. It can be used to study the effects of different implosion parameters on the peak hot-spot pressure. Using these equations, simplified scalings for the hot-spot pressure and shocked mass are derived in **Implosion Scaling Laws** (below) to guide a physical understanding of deceleration dynamics.

In summary, the maximum hot-spot pressure depends on the convergence ratio of the shocked shell, which, in turn, depends on the shell's deceleration rate. The larger the pressure gradient inside the shocked shell (larger difference between p_{hs} and p_{shock}) and the smaller the rate of increase in the shocked mass (dM_s/dt), the larger the shell deceleration rate and the smaller the final convergence ratio of the shell. The pressure gradient increases and the rate of the shocked mass growth is reduced if the density and velocity of the incoming shell are reduced. The pressure gradient is also increased in implosions with a larger vapor mass and pressure at the onset of shell deceleration.

Discussion

This section derives the simplified scaling laws for the hot-spot pressure and the shocked mass at stagnation. Then, to quantify the effects of the ablation-front mix and the ablator-

to-vapor mix on target performance, the measured areal density is shown as a function of the predicted unshocked-shell mass.

1. Implosion Scaling Laws

The model described in the previous section suggests the following simplified description of shell deceleration and hot-spot formation: The hot-spot pressure continues to increase until the shell's material overtaken by the return shock stagnates. If the duration of shell deceleration is Δt_{dec} , Eq. (46) gives

$$\frac{v_{\text{imp}}}{\Delta t_{\text{dec}}} \sim S_{\text{hs}} (p_{\text{hs}} - p_{\text{shock}}) / M_s. \quad (53)$$

The shell mass overtaken by the shock (the shocked mass), according to Eq. (B9), is

$$\frac{M_s}{\Delta t_{\text{dec}}} \sim \frac{p_{\text{shock}}}{v_{\text{imp}}} S_{\text{shock}}. \quad (54)$$

Eliminating the mass M_s and the time Δt_{dec} from Eqs. (53) and (54) yields a relation between the hot-spot and shock pressures:

$$p_{\text{hs}} \sim p_{\text{shock}} \left(1 + S_{\text{shock}} / S_{\text{hs}} \right) \simeq 2p_{\text{shock}} \sim \rho_{\text{shell}} v_{\text{imp}}^2. \quad (55)$$

Neglecting the velocity gradient inside the unshocked shell, the density increase caused by the shell's convergence becomes [see Eq. (50)]

$$\rho_{\text{shell}} \sim \rho_{\text{shell},0} \left(\frac{R_{\text{hs},0}}{R_{\text{hs}}} \right)^2, \quad (56)$$

and the hot-spot pressure scales with the convergence ratio as [see Eq. (25)]

$$p_{\text{hs}} = p_{\text{hs},0} \left(\frac{R_{\text{hs},0}}{R_{\text{hs}}} \right)^5. \quad (57)$$

Eliminating p_{hs} from Eqs. (55) and (57) gives the hot-spot convergence ratio

$$\frac{R_{\text{hs},0}}{R_{\text{hs}}} \sim \left(\frac{\rho_{\text{shell},0} v_{\text{imp}}^2}{p_{\text{hs},0}} \right)^{1/3}. \quad (58)$$

Equation (58) shows that having a larger vapor pressure (because of a larger initial vapor mass, higher shell adiabat, or ablator-to-vapor mix) at the start of shell deceleration leads to a lower hot-spot convergence ratio and a smaller peak pressure.

Combining Eq. (58) with Eq. (25) gives a scaling for the hot-spot pressure:

$$p_{\text{hs}} \sim p_{\text{hs},0} \left(\frac{\rho_{\text{shell},0} v_{\text{imp}}^2}{p_{\text{hs},0}} \right)^{5/3} = \left(\rho_{\text{shell},0} v_{\text{imp}}^2 \right)^{5/3} p_{\text{hs},0}^{-2/3}. \quad (59)$$

Similar to Eq. (58), Eq. (59) also demonstrates the benefit of reducing the vapor pressure $p_{\text{hs},0}$ at the start of shell deceleration. Since the vapor pressure at that time equals the shell's pressure (which scales as the ablation pressure p_a), $p_{\text{hs},0} = p_{\text{shell},0} \sim p_a$, $\rho_{\text{shell},0} \sim \alpha_{\text{shell}} \rho_{\text{shell},0}^{5/3}$, and the scaling for the maximum pressure reduces to

$$p_{\text{hs}} \sim \frac{p_a^{1/3} v_{\text{imp}}^{10/3}}{\alpha_{\text{shell}}}. \quad (60)$$

Using Eq. (60) in Eq. (2) leads to a scaling for the minimum shell kinetic energy required for ignition,

$$E_{\text{k,min}} \sim v_{\text{imp}}^{-20/3} p_a^{-2/3} \alpha_{\text{shell}}^2. \quad (61)$$

This scaling is similar to that obtained using simulation results.⁴⁴

Because of its limited region of validity, the scaling law given in Eq. (60) should be used mainly as a guiding tool in understanding the effects of different implosion parameters on the shell's properties at peak compression. The limitations in applicability of Eq. (60) include the following: According to Eq. (50), the shell density's dependence on the convergence ratio is somewhat weaker than that shown in Eq. (56). This leads to a smaller power index in the velocity dependence than shown in Eq. (60).

Second, as the implosion velocity increases or the shell adiabat decreases, Eq. (60) becomes invalid since the shocked mass predicted by Eq. (54) exceeds the total shell mass. To clarify the latter statement, the shocked mass is estimated by using the energy-conservation equation. The kinetic energy of the shocked shell $M_s v_{\text{imp}}^2 / 2$ is converted into the internal energy of the hot spot $3/2 p_{\text{hs}} V_{\text{hs}}$ and the shocked shell $E_{\text{shell}} = 3/2 \int p dV$. The latter term is estimated by using the expression for the pressure profile as shown in Eq. (B1):

$$E_{\text{shell}} = 3/2 M \int_0^{M_s/M} \frac{p(m')}{\rho(m')} dm', \quad (62)$$

where $m' = m/M$ is the normalized mass coordinate, $\rho = (p/\mu \alpha_{\text{shock}})^{3/5}$, and α_{shock} is the adiabat of the shocked shell. It can be shown that the integral in Eq. (62) scales as $E_{\text{shell}} \sim M_s v_{\text{imp}}^2$. As a result, energy conservation leads to

$$M_s v_{\text{imp}}^2 \sim p_{\text{hs}} V_{\text{hs}}, \quad (63)$$

which, in combination with Eq. (55), gives

$$M_s \sim \rho_{\text{shell}} V_{\text{hs}}. \quad (64)$$

Substituting the scalings for the shell's density and the hot-spot volume from Eqs. (56) and (58) gives

$$M_s \sim \frac{p_a^{11/15} R_{\text{hs},0}^3}{\alpha^{2/5} v_{\text{imp}}^{2/3}}. \quad (65)$$

The scaling for the shocked mass must be compared with the scaling for the total shell mass. The latter is derived by combining the relations between the initial shell radius and the implosion velocity, $R \sim v_{\text{imp}} t_{\text{imp}}$, and the shell mass and the ablation pressure (Newton's law), $M v_{\text{imp}} / t_{\text{imp}} \sim R^2 p_a$. The implosion time can be written as the ratio of the laser energy and laser power, $t_{\text{imp}} \sim E_{\text{laser}} / R^2 I$, where I is the laser intensity. This gives

$$M \sim \frac{p_a E_{\text{laser}}}{v_{\text{imp}} I}, \quad R \sim \left(\frac{E_{\text{laser}} v_{\text{imp}}}{I} \right)^{1/3}. \quad (66)$$

Substituting Eq. (66) into Eq. (65) and assuming that the scalings of $R_{\text{hs},0}$ and the initial shell radius R are the same yield,

$$\frac{M_s}{M} \sim \frac{v_{\text{imp}}^{4/3}}{\alpha^{2/5} p_a^{4/15}}, \quad M_s \sim \frac{p_a^{11/15} v_{\text{imp}}^{1/3} E_{\text{laser}}}{\alpha^{2/5} I}. \quad (67)$$

To increase v_{imp} for a given laser energy and intensity, the shell mass, according to Eq. (66), must be reduced. The shocked mass, however, increases with v_{imp} [see Eq. (67)]. Consequently, as v_{imp} keeps increasing, Eq. (67) becomes invalid at some point when M_s exceeds M . This defines the validity region for the scaling laws shown in Eqs. (67) and (60).

2. Relating Target Performance to the Unshocked Mass

In optimizing the target performance, there is a trade-off between maximizing 1-D performance and controlling the hydrodynamic instabilities. Indeed, the larger the fraction of the shell overtaken by the return shock at the hot-spot stagnation, the larger the fraction of the shell’s kinetic energy being converted into the hot-spot internal energy. Equation (67) shows that increasing the implosion velocity and reducing the shell’s adiabat results in a larger shocked mass and, according to Eq. (60), a higher hot-spot pressure.

The lower-adiabat shells, however, are more susceptible to the RT growth during the acceleration because of reduced ablative stabilization. The larger instability growth leads to a larger region of relaxed density at the outer part of the shell. As the outgoing shock travels through such a lower-density mix region during shell deceleration, the shock pressure $p_{shock} \sim \rho_{shell} v_{imp}^2$ is reduced and the shell’s deceleration rate increases [see Eq. (53)]. The stronger deceleration force stops the shell while the hot spot is at a larger radius, leading to a reduction in the hot-spot pressure. This also follows from Eq. (59), which shows that $p_{hs} \sim \rho_{shell}^{5/3}$.

Degradation of the target performance depends on the mass (or size) of the mix region that contributes to the shocked mass at stagnation. If the hot spot stagnates before the return shock reaches the mix zone, the effect of the RT growth is small, as illustrated in Fig. 137.34. Vice versa, if the shocked mass at stagnation includes a significant fraction of the mixed mass, the hot-spot convergence and peak pressure are reduced. This

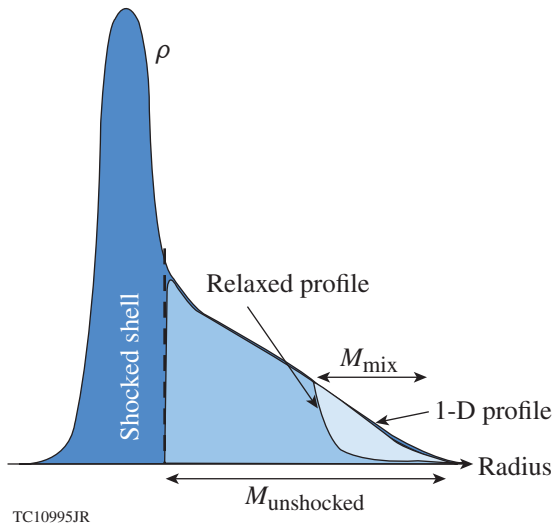


Figure 137.34 An illustration of the shell density at peak compression.

is illustrated in Fig. 137.35, which plots the results of a series of LILAC simulations of cryogenic implosions where the shell’s density was artificially relaxed (without changing the shell velocity or mass) at the beginning of shell deceleration. A reduction in the hot-spot pressure in these simulations depends on the fraction of relaxed material in the shocked mass at peak compression. In the case where the mix region extends to include 60% of the shocked mass (as calculated in the no-mix run), the peak areal density is reduced by 50% and the peak pressure by 60% compared to the results of the no-mix simulation.

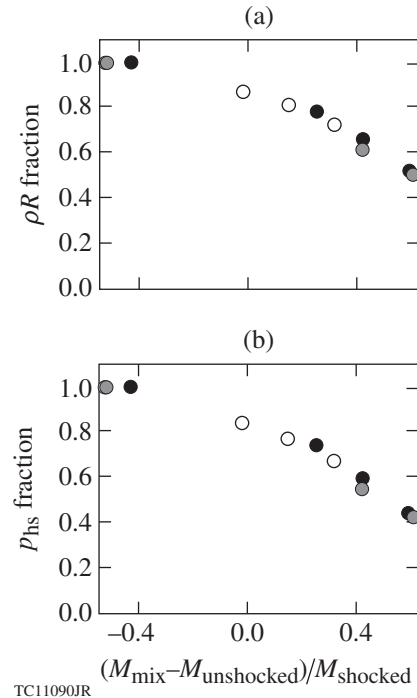
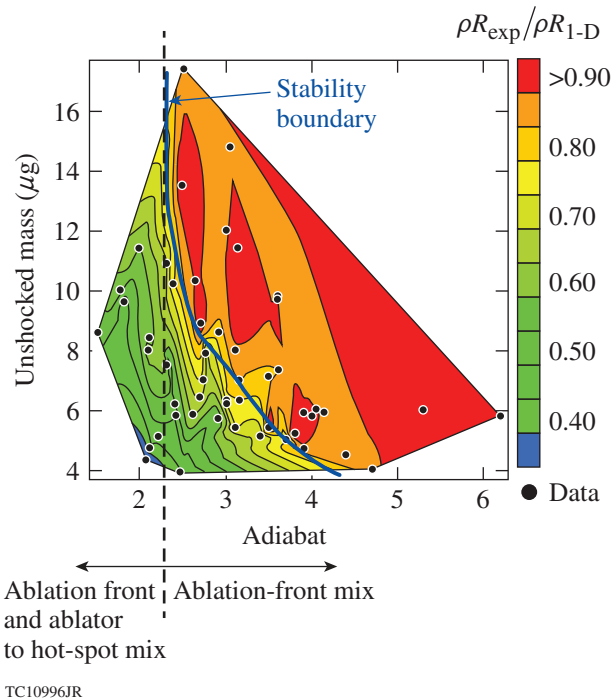


Figure 137.35 LILAC predictions of (a) the areal density and (b) the peak hot-spot pressure fractions as functions of the relaxed shell fraction in the shocked mass at peak compression. Different symbols indicate different target designs.

To quantify the effects of hydrodynamic instability growth on target performance, the measured areal-density reduction relative to 1-D predictions is plotted as a function of the calculated unshocked mass at bang time. Figure 137.36 shows the experimental areal-density (normalized to LILAC predictions) contours in the shell adiabat/unshocked mass parameter space. A stability boundary can be identified (plotted with a thick solid line) that separates the region where more than 85% of the predicted areal density is measured and the region of reduced areal densities, where the effect of the instability growth is significant.



TC10996JR

Figure 137.36

Contour map of the measured areal-density reduction relative to 1-D predictions. The unshocked mass is calculated at bang time using *LILAC*. The vertical dashed line separates the parameter space into a region (on the right from the line) where a line representing implosions with a fixed adiabat intersects with the stability boundary (thick solid line) and a region (on the left from the dashed line) where the measured areal densities are below 70% of 1-D predictions for all values of the unshocked mass.

According to Fig. 137.36, the measured areal-density fraction, for a given shell adiabat, increases with the unshocked mass. The 1-D–predicted values are achieved, however, only if $\alpha > 2.3$. For these implosions, a vertical line representing a fixed adiabat always intersects with the stability boundary. The mass given by a point of intersection of the vertical line with the stability boundary represents the mass $M_{\text{mix}}\alpha$ of the mix region at the ablation front. A line with $\alpha = 3$, for example, intersects the stability boundary at $M_{\text{mix}}(3) = 8 \mu\text{g}$, indicating that the shell compression is not degraded if the unshocked mass is larger than M_{mix} . Then, according to Fig. 137.35, M_{mix} is equal to the mass of relaxed density at the ablation front (mix mass), and the stability boundary represents the points where the mix mass is equal to the shocked mass. The dependence of the mix mass on shell adiabat (the position of the stability boundary) is shown in Fig. 137.37.

For implosions with $\alpha < 2.3$ (the region to the left of the dashed vertical line in Fig. 137.36), a line of constant adiabat never intersects the stability boundary. This indicates that, in addition to the density relaxation at the ablation front, a

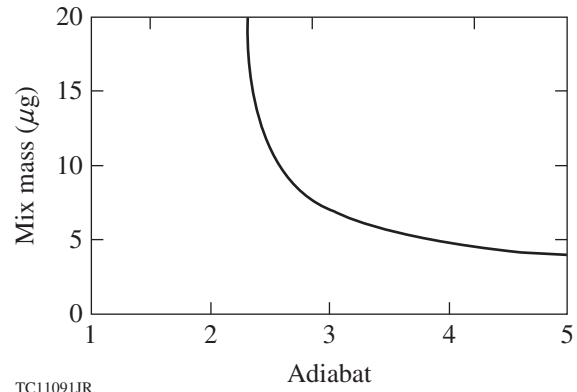


Figure 137.37

Mix mass M_{mix} as a function of shell adiabat. The mix mass equals the total shell mass for $\alpha < 2.3$ since these shells are broken during acceleration.

different performance degradation mechanism limits the target compression. A possible mechanism is suggested by the observed correlation between the measured x-ray emission and the shell adiabat. This is shown in Fig. 8 of Ref. 23, where the calculated and measured core x-ray emission in the sensitivity range of the gated x-ray imager (4 to 7 keV) and normalized to neutron yield to the power of 0.57 is plotted for different values of the shell adiabat. The enhanced x-ray emission from the target core is observed in the low-adiabat implosions with $\alpha < 2.3$ and can be explained by the presence of carbon in the hot spot at the peak of x-ray production. This is due to shell breakup and the CD ablator penetrating into the vapor region during the shell's acceleration. Breakup of the shell increases the vapor mass and reduces the shell's density. Both effects lead to an early shell deceleration and a significant reduction in the peak areal densities and hot-spot pressures. Because the CD layer in these implosions is totally ablated by the end of the drive pulse, the only mechanism that is capable of mixing the CD ablator into the vapor region is the nonlinear evolution of the localized surface defects (or ice features) at the early stages of the implosion.⁴⁰ The bubbles of the lower-density material break shell integrity at the beginning of the shell's acceleration, bringing the cold fuel, the ablator material, and the ablated plasma into the vapor region and compromising target performance. This result suggests that the bubble velocity $v_{\text{bubble}} \sim \sqrt{d_{\text{bubble}}g}$ (where g is the shell acceleration and d_{bubble} is the bubble diameter) in the implosions with $\alpha < 2.3$ exceeds the rate of increase in the in-flight shell thickness.

3. Toward Demonstration of the Ignition Hydrodynamic Equivalence in Cryogenic Implosions on OMEGA
 - a. The hot-spot pressure requirement for an igniting target. As shown in **Target Performance** (p. 23), cryogenic implosions

on OMEGA have reached maximum hot-spot pressures of up to ~ 40 Gbar. The pressure requirement for ignition demonstration on the NIF can be derived using Eq. (3), which, with the help of Eq. (24), reduces to

$$\left(\frac{p_{\text{hs}}}{100 \text{ Gbar}}\right)^{4/5} \left(\frac{p_{\text{hs},0}}{100 \text{ Gbar}}\right)^{1/5} > \frac{100 \mu\text{m}}{R_{\text{hs},0}}. \quad (68)$$

The size of the vapor region at the beginning of shell deceleration $R_{\text{hs},0}$ is determined by equating the vapor and shell pressures. Assuming that the convergence of the original vapor mass has the largest contribution to $p_{\text{hs},0}$ (see **Vapor Pressure Evolution**, p. 29), Eq. (31) is used to obtain

$$p_{\text{hs},0} = p_{\text{a},0} F \left(\frac{\rho_{\text{v},0}}{\rho_{\text{ice},0}} \right) \left(\frac{R_{\text{v},0}}{R_{\text{hs},0}} \right)^5, \quad (69)$$

where $R_{\text{v},0}$ is the initial (undriven) size of the vapor region, $\rho_{\text{v},0}$ and $\rho_{\text{ice},0}$ are the initial densities of the vapor and the main fuel, respectively, and the function $F(x)$ is defined as

$$F(x) = \frac{x}{4^{5/3}} \left[1 + 2\sqrt{5} (1 - x^{1/5}) \right]. \quad (70)$$

At the DT triple point, $\rho_{\text{v},0} \simeq 0.6 \text{ mg/cm}^3$ and $\rho_{\text{ice},0} \simeq 0.25 \text{ g/cm}^3$, so $F \simeq 10^{-3}$. The initial vapor radius scales with the target radius. The latter is given in Eq. (65), which, including the numerical coefficients, takes the form

$$R_{\text{v},0} \simeq 0.85 \left(\frac{E_{\text{laser}} v_{\text{imp}}}{4\pi I} \right)^{1/3}. \quad (71)$$

Combining Eqs. (68)–(71) leads to the following requirement for the minimum hot-spot pressure in an igniting target:

$$p_{\text{hs}} > 120 \text{ Gbar} \left(\frac{100 \text{ Mbar}}{p_{\text{a},0}} \right)^{1/4} I_{15}^{5/12} \left(\frac{E_{\text{laser}}}{1.5 \text{ J}} \right)^{-5/12} \times \left(\frac{v_{\text{imp}}}{3.7 \times 10^7 \text{ cm/s}} \right)^{-5/12}, \quad (72)$$

where I_{15} is the incident laser intensity in 10^{15} W/cm^2 . Equation (72) shows that the cryogenic implosions, hydrodynamically

equivalent to an igniting target on the NIF, must achieve central pressures in excess of ~ 100 Gbar. Therefore, the maximum hot-spot pressures inferred in the cryogenic implosions on OMEGA are lower by a factor of 2 to 3 than what is required for ignition demonstration on the NIF.

According to Figs. 137.25 and 137.29, the reduction in the central pressure is larger than the reduction in areal density. More than 85% of the 1-D–predicted ρR values are observed in the implosions without significant ablator mixing into the vapor region or density relaxation at the ablation front. In contrast, the inferred central pressures in such implosions are reduced by more than 60%. This is a result of the hot-spot distortion growth during the shell’s deceleration. When integrity of the in-flight shell is not compromised by the RT growth, a large fraction of predicted areal density is observed if the mix mass at the ablation front does not exceed the unshocked mass at bang time (see Fig. 137.36). Perturbations at the inner edge of the shell (seeded because of the feedthrough from the ablation front) grow during the deceleration as a result of the RT instability since the pressure and density gradients have opposite signs at the inner surface of the shell. Such a growth leads to an increase in the hot-spot volume and the surface area. The larger surface area of the colder shell leads to enhanced thermal-conduction losses from the hotter central region and larger mass ablation from the shell into the hot spot. This reduces the hot-spot temperature and truncates the neutron production before the hot spot reaches its minimum volume. Since the hot-spot pressure is inferred from the nuclear-reaction products, the early burn truncation prevents sampling the pressures at higher hot-spot convergence ratios, thereby reducing the inferred pressure values.

The second multidimensional effect that leads to a reduction in the hot-spot pressure is the growth of the nonradial flow caused by the shell’s distortion growth. This reduces the fraction of the shell’s kinetic energy that is converted into hot-spot internal energy. In a spherically symmetric implosion, the full kinetic energy of the shocked shell, $1/2 M_{\text{s}} v_{\text{shell}}^2$, is converted into the internal energy of the hot spot and shocked shell:

$$\frac{1}{2} M_{\text{s}} v_{\text{shell}}^2 \rightarrow \frac{3}{2} p_{\text{hs}} V_{\text{hs}} \quad (73)$$

(spherically symmetric implosion). In the presence of asymmetries, there is a residual fluid motion in the shocked region because of the RT growth. This leads to

$$\frac{1}{2} M_{\text{s}} v_{\text{shell}}^2 \rightarrow \frac{3}{2} p_{\text{hs}} V_{\text{hs}} + \frac{1}{2} M_{\text{s}} v_{\text{RT}}^2 \quad (74)$$

(asymmetric implosion) and a reduction in $p_{\text{hs}}V_{\text{hs}}$ compared to the symmetric implosion. In addition, only the velocity component normal to the shock front $v_{\text{shell},\perp}$ contributes to the shock pressure shown in Eqs. (B7) and (55), so only a fraction of the incoming shell dynamic pressure is converted into shock pressure p_{shock} :

$$\frac{4}{3}\rho_{\text{shell}}v_{\text{shell},\perp}^2 \rightarrow p_{\text{shock}} \quad (75)$$

(asymmetric implosion). This reduces the shock pressure and increases the pressure gradient inside the shocked shell, leading to a larger deceleration force, larger hot-spot volume, and smaller hot-spot pressure at peak compression.

b. Direct-drive target designs with improved shell stability.

Since the numerical simulations and the experimental data suggest that only $\sim 40\%$ of the 1-D-predicted peak pressures are observed in the presence of the perturbation growth, demonstrating the ignition hydrodynamic scaling on OMEGA with peak pressures of ~ 100 Gbar requires a 1-D design that reaches $p_{\text{hs}} \sim 200$ Gbar at stagnation. Such a design is shown in Fig. 137.38 (the pulse shape is plotted in red and the target is labeled “nominal CBET”). This design is driven at a peak laser intensity of 9.5×10^{14} W/cm² and reaches an implosion velocity

of 3.7×10^7 cm/s. The calculated unshocked mass, fuel adiabat, and in-flight aspect ratio are $m_{\text{unshocked}} = 6 \mu\text{g}$, $\alpha = 1.65$, and IFAR = 30, respectively. Figures 137.25(b) and 137.36 both show, however, that such a design is unstable, assuming the nonuniformity seeds currently present in OMEGA cryogenic implosions. Therefore, the shell’s stability must be improved to demonstrate the hydrodynamic equivalence. This can be achieved by reducing the level of the nonuniformity seeds [which will move the stability boundary shown in Figs. 137.25(b) and 137.36 to a region with lower adiabat values, unshocked shell masses, and higher IFAR’s] and by increasing the hydrodynamic efficiency of the imploding target. At higher hydrodynamic efficiency of the laser drive, the required peak hot-spot pressure can be reached in the implosions with the higher-adiabat values, unshocked masses, and lower IFAR’s, moving the hydro-equivalent design into the stable region in the adiabat/IFAR and adiabat/unshocked mass parameter spaces.

Identifying the dominant nonuniformity seed is currently underway at LLE. The possible sources include the target defects introduced during the fill, cooling, and layer formation, as well as the early laser shintthrough, and the first shock interaction with modulations in the solid-state properties of the ablator.

Improving the shell’s stability by raising its adiabat and IFAR (keeping the hot-spot pressure fixed) can be achieved [according to the scaling shown in Eq. (60)] by increasing the ablation pressure p_a . The main factor limiting the laser absorption and ablation pressure in direct-drive implosions is cross-beam energy transfer (CBET).¹² Therefore, the most-efficient mechanism in raising p_a is to mitigate the CBET. LLE is currently pursuing several mitigation approaches,^{12,45} including reducing the laser-beam size relative to the target size, increasing the laser bandwidth, and introducing layers of mid-Z (Si, for example) materials inside the ablator. The benefit of CBET mitigation on target characteristics is illustrated in Fig. 137.38, where the designs with various fractions of laser-deposition reduction caused by CBET are shown. The maximum hot-spot pressure, shell velocity, and peak areal density in these designs are kept constant. The effect of CBET in simulations is varied by introducing a multiplication factor in front of the growth rate for the stimulated Brillouin scattering (SBS)¹⁴ (the design labeled “1/2 CBET” is simulated using a factor of 1/2 in front of the SBS growth rate, and the simulation of the “no CBET” design shows no effect from CBET). Reducing CBET increases the ablation pressure, leading to a hydro-equivalent design with an increased fuel adiabat. The shell parameters for these designs are summarized in Table 137.V. The shell IFAR, fuel adiabat, and unshocked mass for the three designs are indicated in Fig. 137.39 by the solid circles. Also shown are the

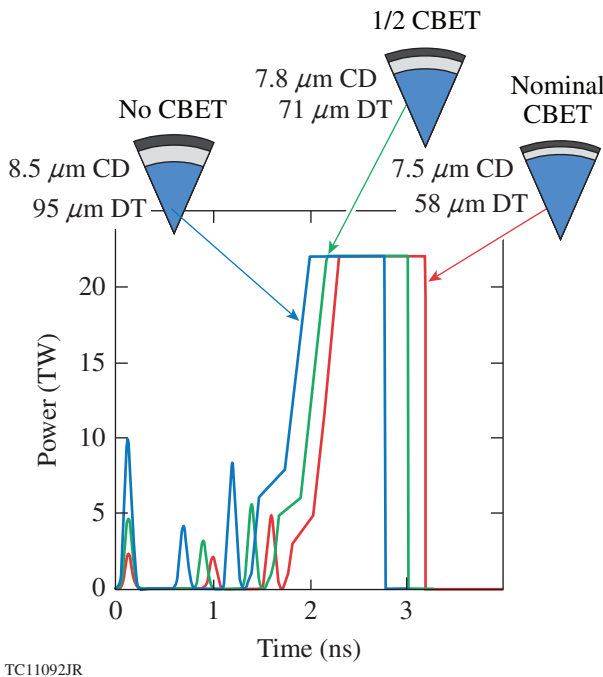


Figure 137.38
OMEGA cryogenic target designs with 1-D central pressures of 180 Gbar at stagnation, the implosion velocity of 3×10^7 cm/s, and neutron-averaged areal density of 300 mg/cm^2 .

Table 137.V: Summary of the shell parameters for the designs shown in Fig. 137.38. All designs have a peak hot-spot pressure of 180 Gbar, a neutron-averaged areal density of 300 mg/cm², and an implosion velocity of 3.7×10^7 cm/s.

Parameters	Nominal CBET	1/2 CBET	No CBET
Ablation pressure (Mbar)	138	162	213
IFAR	30	23	17
In-flight adiabat	1.6	2.2	3.2
Unshocked mass (μg)	6.0	7.5	11.3
Total unablated shell mass (μg)	17.4	19.4	23.7
Initial shell mass (ablator and DT) (μg)	47.1	53.1	63.4

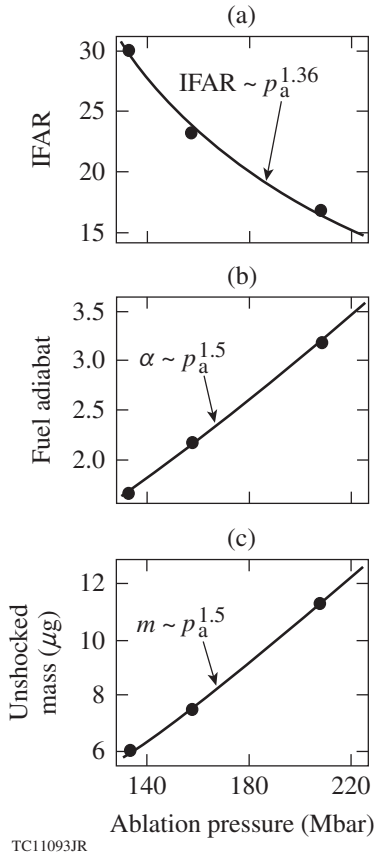


Figure 137.39 (a) Shell IFAR, (b) fuel adiabat, and (c) the unshocked mass at peak neutron production as functions of ablation pressure for the designs shown in Fig. 137.38. Solid lines represent the best fit to the simulation results. Solid circles show the simulation results.

best fits to the simulation data. The IFAR scales with the ablation pressure as $IFAR \sim p_a^{1.36}$, while the fuel adiabat and the unshocked mass scale as $p_a^{1.5}$.

c. CBET mitigation strategies. Different CBET mitigation strategies are compared by calculating the ablation pressure using the CBET model in *LILAC*.¹² As discussed in Refs. 12 and 45, reducing the beam size relative to the target size mitigates the effect of CBET. Figure 137.40 shows the predicted ablation pressure in OMEGA cryogenic implosions as a function of the ratio of the beam to the target radii. $R_{\text{beam}}/R_{\text{target}} \sim 0.8$ is equivalent to the 1/2 CBET design; reducing the beam radius to $R_{\text{beam}} \sim 0.6 R_{\text{target}}$ leads to an ablation pressure similar to that of the no CBET design shown in Fig. 137.38. This does not mean, however, that CBET is completely suppressed at such a beam radius. Two effects cause an increase in the ablation pressure with a reduction in the beam size.¹² The first is a reduction in CBET; the second is a decrease in the average angle of incidence in the laser illumination. The beam rays, which have a smaller incident angle to the target surface, propagate farther toward the higher electron densities,¹⁴ depositing their energy more efficiently. Consequently, a combination of CBET reduction and a decrease in the average angle of incidence in the illumination leads to matching the ablation pressure in the $R_{\text{beam}}/R_{\text{target}} \simeq 0.6$ design with a pressure when the CBET is fully mitigated at $R_{\text{beam}}/R_{\text{target}} \simeq 1$.

The smaller beams produce, however, an increased illumination asymmetry. Using the smaller beams at the beginning of the laser drive increases nonuniformity caused by the limited beam overlap. The reduced beam overlap also increases the sensitivity

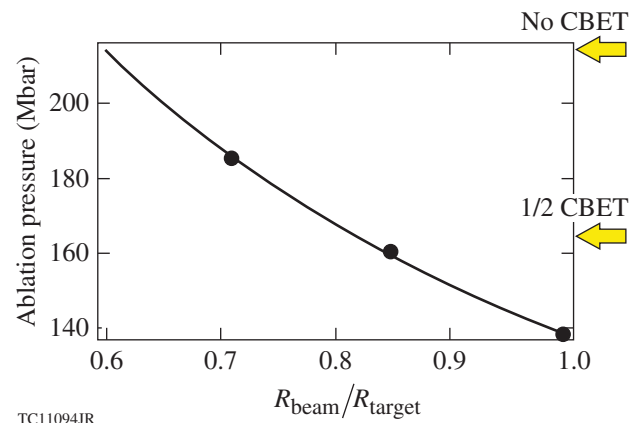


Figure 137.40 The ablation pressure as predicted by *LILAC* (including the CBET effect) versus the ratio of the beam to the target radii. Data points show the simulation results; the solid line is the best fit to the simulations.

of the target design to the power imbalance and beam mistiming. To mitigate the increased early-time overlap nonuniformity, a two-stage zooming scheme has been proposed,⁴⁵ where $R_{\text{beam}}/R_{\text{target}} \simeq 1$ is used until the onset of the main drive and $R_{\text{beam}}/R_{\text{target}} < 0.7$ is used thereafter. Controlling the single-beam uniformity for modes $20 < \ell < 100$ is the main challenge for this mitigation scheme. To optimize the target design, one must find a compromise between improving the target stability properties (reduced IFAR but increased adiabat and unshocked mass) and increasing illumination nonuniformity seeds (but keeping them at a tolerable level). Several zooming implementation options are currently being pursued on OMEGA.

Mitigating CBET by increasing the laser bandwidth¹² requires wavelength separation in excess of 5 \AA at a laser wavelength of $\lambda = 351 \text{ nm}$. The CBET model implemented in *LILAC* suggests¹² that this effectively reduces the SBS gain by a factor of 2, leading to the 1/2 CBET target design shown in Fig. 137.38. Currently, this is considered to be the best option in mitigating CBET in the polar-drive implosions on the NIF.

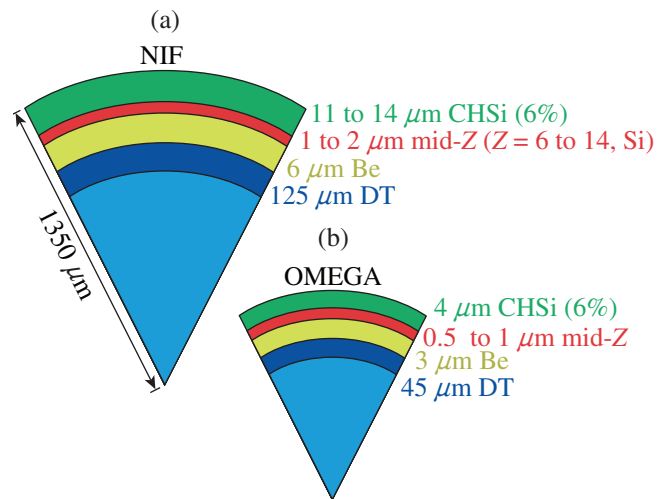
There are several beneficial effects from introducing a mid-Z layer inside the ablator: First, having a higher-Z material inside the laser-absorption region leads to increased inverse bremsstrahlung absorption, as discussed in **Target Designs and Validation of 1-D Implosion Parameters**, p. 19. Consequently, even if the laser-deposition reduction caused by CBET is held constant, the higher-Z ablators lead to higher absorption. This also increases the coronal temperature, which, in turn, reduces the SBS gain that governs the CBET.

An additional benefit in using a mid-Z layer is the mitigation of TPD instability. Again, as mentioned on p. 19 and discussed in detail in Ref. 16, the higher-Z plasma at quarter-critical surface reduces the ion-wave damping rate, leading to a reduction in TPD growth. An increase in the coronal temperature caused by the higher laser absorption is also beneficial for the mitigation of TPD instability.

The higher-Z materials have several disadvantages [such as low hydroefficiency, radiation losses, radiation preheat, etc. (see discussion on p. 19)] that diminish the benefits of the CBET reduction. To overcome these shortcomings, a relatively thin layer of a mid-Z material (such as Si) is introduced inside the lower-Z materials to combine the higher laser absorption with the larger ablation efficiency of the innermost layer in the ablator. DT has the highest ablation efficiency (because of the large ratio of atomic mass to the ion charge) but the lowest ion charge and, therefore, the smallest inverse bremsstrahlung

absorption. Having the mid-Z layer extended all the way to the DT layer causes either significant radiation preheat of the main fuel because of radiation from the plasma corona (if the layer is thick) or a significant loss in the laser absorption by depositing laser energy in the DT during the main pulse (if the layer is thin). Both reduce the benefits of having a higher ion charge in the plasma corona.

The best design option is to introduce an intermediate layer between the mid-Z layer and the DT ice. The material in this layer must have high ablation efficiency, while the ion charge must be larger than 1 to avoid significant losses in laser absorption. From a target-manufacturing point of view, beryllium is the best choice for such a purpose.¹⁹ The hydro-equivalent “multilayer” design for OMEGA and the ignition design for the NIF are shown in Fig. 137.41. The OMEGA multilayer cryogenic design is predicted to absorb 60% of the incident laser energy. This is compared with the 54% absorption achieved in the plastic-ablator designs. The higher absorption fraction results in an increase in the ablation pressure to 147 Mbar, fuel adiabat to $\alpha \simeq 2$, and the unshocked mass to $7 \mu\text{g}$. These indicate a moderate improvement in the design parameters compared to the “nominal CBET” design shown in Table 137.V. The NIF multilayer design, shown in Fig. 137.41, is predicted to ignite in 1-D and produce a gain of 5 if no additional CBET mitigation strategies are used. Employing a laser wavelength separation of 5 \AA in the UV further reduces CBET and increases the gain to 20. Additional strategies that will increase the shell’s convergence and target gain are currently being considered at LLE.



TC10544JR

Figure 137.41

(a) Multilayer ignition design for the NIF and (b) hydro-equivalent design for OMEGA. The outer plastic layer is doped with Si to reduce laser imprint.⁴⁶

Although much more work is required to validate the predicted benefits and access the stability properties of the multilayer design, the first experiments performed on OMEGA using the multilayer warm targets, where a cryogenic layer is replaced by an extra layer of Be, have confirmed an increased coronal temperature compared to that in implosions using the pure plastic shells.⁴⁷ The generation of suprathermal electrons caused by TPD instability is also observed to be reduced in the multilayer design.

Conclusions

The target performance of cryogenic implosions on OMEGA has been discussed. The implosion velocity was varied from 2.2 to 3.8×10^7 cm/s and the shell adiabat from 1.5 to 5. Based on the results of these experiments, the stability boundaries in the IFAR adiabat and unshocked mass-adiabat parameter spaces were identified. These show that the target designs operating above the boundary achieve more than 85% of the 1-D-predicted areal densities. The hot-spot pressures and yields are up to 35% and 40% of the predictions, respectively. The target performance of the implosions in this stability regime is well understood using *DRACO* simulations.

A measure of the effect that ablative RT growth has on target performance is the fraction of the mix-region mass in the shocked mass. If the return shock has not reached the mixed region at peak neutron production and the mix mass is smaller than the unshocked mass, the effect of the ablative RT mix on the target performance is small. Despite this, the target yield and peak pressure are reduced in such implosions to ~30% to 40% of the 1-D-predicted values because of the growth non-uniformities during the shell's deceleration.

To demonstrate the ignition hydrodynamic equivalence, OMEGA implosions must reach central pressures in excess of 100 Gbar. With the current laser-absorption limitations caused by CBET, the fuel adiabat in the hydro-equivalent designs must be at $\alpha < 2$ and the shell IFAR ~ 30 , both of which are currently outside the shell's stability region. The target performance of such designs is significantly degraded with respect to 1-D predictions. Two-dimensional simulations using the known sources of target and illumination nonuniformities also fail to reproduce the experimental data. This limited ability of the hydrodynamic simulations to explain the observables in the low-adiabat implosions on OMEGA is also common in indirect-drive cryogenic implosions on the NIF.

To understand the factors limiting the target performance, simplified models describing implosion dynamics have been

developed. Such models revealed that the vapor pressure evolution during shell acceleration and shell density relaxation caused by hydrodynamic instability growth and preheat are the main factors controlling the target performance. It was shown that 2-D *DRACO* simulations that use the localized features on the target surface as the nonuniformity seed reproduce the observables for $\alpha \simeq 2$ implosions. The shells in these simulations are totally broken, and the cold shell material, ablator, and blowoff plasma are injected into the target center, significantly reducing the final shell convergence and hot-spot pressure.

Based on the analysis using the simplified models and the simulations with the localized defects, it was concluded that ignition hydrodynamic equivalence can be achieved on OMEGA by making the cryogenic designs more robust against the hydrodynamics instabilities. This requires a reduction in nonuniformity sources and an increase in hydroefficiency by mitigating the CBET. LLE is currently pursuing several CBET-mitigation strategies, including a reduced beam size relative to the target size, an enhanced laser bandwidth, and multilayer ablaters.

ACKNOWLEDGMENT

This material is based upon work supported by the Department of Energy National Nuclear Security Administration under Award Number DE-NA0001944, the University of Rochester, and the New York State Energy Research and Development Authority. The support of DOE does not constitute an endorsement by DOE of the views expressed in this article.

Appendix A: Shell Acceleration Model

The momentum-conservation equation in the mass-time coordinate system has the form

$$\frac{\partial^2 r(m,t)}{\partial t^2} = -4\pi r(m,t)^2 \frac{\partial p(m,t)}{\partial m}, \quad (\text{A1})$$

where p is shell pressure, r is position, m is the mass coordinate defined as $dm = 4\pi\rho r^2 dr$, and ρ is mass density. A rigorous approach for finding $r(m,t)$ requires solving a nonlinear partial differential equation by substituting $p(m,t) = \mu\alpha(m,t) / [4\pi r(\partial r / \partial m)^2]^{5/3}$ into Eq. (A1). Here, the shell's adiabat $\alpha(m,t)$ is a function of time during shell acceleration because of secondary shocks, radiation, or suprathermal electron preheat, and μ is defined in Eq. (18). Instead, an approximate solution of Eq. (A1) is obtained by using the following simplifications: First, the pressure profile inside the shell is written as a second-order polynomial in the mass coordinate,

$$p(m,t) \simeq p_a(t) \left[1 + \hat{p}_1(t)\eta + \hat{p}_2(t)\eta^2 \right], \quad (\text{A2})$$

where $\eta = (1-m/M)$ is the normalized mass with zero value at the ablation front, p_a is the ablation pressure, and M is the total shell mass. Second, a solution of Eq. (A1) is obtained near the ablation region as an expansion in η , assuming $\eta \ll 1$. Finally, the adiabat is assumed to be determined by the early shock propagation through the shell and does not change significantly during the shell's acceleration. The relation between the position and mass is determined by substituting

$$p(m, t) = \mu \alpha \rho^{5/3} \quad (\text{A3})$$

into the mass-conservation equation [here, μ is defined in Eq. (18)]. The result is

$$\frac{\partial r^3}{\partial m} = \frac{3\mu^{3/5}}{4\pi} \left(\frac{\alpha}{p} \right)^{3/5}. \quad (\text{A4})$$

Next, the ablation pressure is written as a function of the ablation-front position R_a . Since the critical surface and the laser-deposition region move inward during the shell's implosion, the ablation pressure (or drive pressure) increases with the shell convergence. Assuming that the ablation pressure scales with the laser intensity as $p_a \sim I^{\beta_a}$, the pressure change with the ablation-front radius R_a becomes $p_a \sim (P_{\text{laser}}/R_a^2)^{\beta_a} = P_{\text{laser}}^{\beta_a} R_a^{-2\beta_a}$, where P_{laser} is the laser power. The power index β_a depends on the details of the laser-absorption mechanism and thermal conduction (see, for example, Ref. 48). To generalize, we write the drive pressure as $p_a \sim R_a^{-\beta}$, where the values of power index β typically range from 0.5 to 1.5 for various laser-deposition and thermal-conduction models and ablator materials. Introducing the normalized position $\xi(\eta, t) = r(\eta, t)/R_0$, where R_0 is the ablation-front position at the beginning of the shell's acceleration, the ablation pressure can be written as

$$p_a = p_{a,0} \xi_a^{-\beta} \quad (\text{A5})$$

and Eq. (A4) takes the form

$$\frac{\partial \xi^3}{\partial \eta} = -\epsilon \xi_a^{3\beta/5} \left(\frac{\alpha/\alpha_a}{1 + \hat{p}_1 \eta + \hat{p}_2 \eta^2} \right)^{3/5}, \quad (\text{A6})$$

where α_a is the shell's adiabat in the ablation-front region and $\xi_a = R_a/R_0$. The small parameter ϵ is defined as

$$\epsilon = \frac{3\mu^{3/5}}{4\pi} \left(\frac{\alpha_a}{p_{a,0}} \right)^{3/5} \frac{M_{\text{shell}}}{R_0^3} = \frac{M_{\text{shell}}}{4\pi \rho_{a,0} R_0^3 / 3} \ll 1, \quad (\text{A7})$$

where $p_{a,0}$ and $\rho_{a,0}$ are the ablation pressure and the peak shell density at the beginning of shell acceleration, respectively. Keeping only the terms up to the order of η , the solution of Eq. (A6) becomes

$$\xi(\eta, t) = \xi_a(t) \left[1 - \frac{\epsilon}{3} \xi_a(t)^{3\beta/5-3} \eta \right]. \quad (\text{A8})$$

Substituting Eq. (A8) back into Eq. (A1) determines the temporal evolution of the normalized ablation-front radius ξ_a and shell pressure p :

$$\xi_a'' = \frac{4\pi R_0}{M} p_{a,0} \xi_a^{2-\beta} \hat{p}_1, \quad (\text{A9})$$

$$\begin{aligned} \hat{p}_2 = & \frac{\epsilon}{6} \xi_a^{3/5\beta-3} \left[\hat{p}_1 \left(4 - \frac{3}{5}\beta \right) - \frac{M}{4\pi R_0 p_{a,0}} \right. \\ & \left. \times \left(2 - \frac{3}{5}\beta \right) \left(3 - \frac{3}{5}\beta \right) \frac{\xi_a'^2}{\xi_a^{3-\beta}} \right]. \end{aligned} \quad (\text{A10})$$

Assuming that the pressure at the inner shell boundary ($\eta = 1$) is $p(\eta = 1) = p_{\text{bk}}(t)$ ($p_{\text{bk}} \ll p_a$ during the shell acceleration) relates \hat{p}_2 with \hat{p}_1 :

$$\hat{p}_1 = -1 + p_{\text{bk}}/p_a - \hat{p}_2. \quad (\text{A11})$$

The shell pressure at the inner surface p_{bk} is determined from Eq. (29):

$$p_{\text{bk}} \simeq p_{a,0} \frac{\rho_{v,0}}{\rho_0} \left\{ 1 + 2\sqrt{5} \left[1 - \left(\frac{\rho_{v,0}}{\rho_0} \right)^{1/5} \right] \right\} \left(\frac{V_{\text{bk},0}}{V_{\text{bk}}} \right), \quad (\text{A12})$$

where V_{bk} and $V_{\text{bk},0}$ are the volume surrounded by the inner surface of the shell and its value at the beginning of the shell's acceleration, respectively. The volume ratio in Eq. (A12) is due to the convergence effects. Then, Eq. (A10) gives

$$\begin{aligned} \hat{p}_2 = & -\frac{\epsilon}{6} (4 - 3/5\beta) \xi_a^{3/5\beta-3} \\ & \times \frac{\xi_a'^2 / \xi_a^{3-\beta} C_\beta (M/4\pi R_0 p_{a,0}) + 1 - p_{\text{bk}}/p_a}{1 + \epsilon (4 - 3/5\beta) \xi_a^{3/5\beta-3} / 6}, \end{aligned} \quad (\text{A13})$$

where

$$C_\beta = \frac{(2 - 3/5\beta)(3 - 3/5\beta)}{4 - 3/5\beta}.$$

When the shell convergence is not significant ($R_a \sim R_0$, $\xi_a \sim 1$), $\hat{p}_1 \simeq -1$ and the ablation-front velocity, obtained by integrating Eq. (A9), reduces to

$$\xi_a'^2 = \frac{8\pi R_0 p_{a,0}}{M} \frac{1 - \xi_a^{3-\beta}}{3 - \beta}. \quad (\text{A14})$$

Since the velocity gradient inside the shell is small at this stage in the implosion, the mass-averaged shell velocity v_{shell} can be approximated by the ablation-front velocity $v_{\text{shell}} \simeq \dot{R}_a = R_0 \xi_a'$. This gives the shell's kinetic energy as a function of the ablation-front radius:

$$\begin{aligned} \frac{M v_{\text{shell}}^2}{2} &= \frac{4\pi}{3 - \beta} \left[p_{a,0} R_0^3 - p_a(t) R_a^3 \right] \\ &= \frac{4\pi}{3 - \beta} p_{a,0} R_0^3 \left[1 - \left(\frac{R_a}{R_0} \right)^{3-\beta} \right]. \end{aligned} \quad (\text{A15})$$

Equation (A15) shows, as expected, that as the shell converges and R_a gets smaller, the shell's kinetic energy increases and the larger values of β [which correspond to a faster rise in the ablation pressure during the shell convergence; see Eq. (A5)] lead to increased kinetic energy. Note that Eq. (A15) is not valid for $\beta = 3$. Integrating Eq. (A9) in this case leads to

$$\frac{M v_{\text{shell}}^2}{2} = 4\pi p_{a,0} R_0^3 \ln \frac{R_0}{R_a}, \quad \beta = 3. \quad (\text{A16})$$

Appendix B: Model of Shell Deceleration

1. Equation for the Hot-Spot Radius

Following the analysis used in modeling the shell's acceleration [see Eqs. (A2)–(A10)], pressure of the shocked shell is written as

$$p = p_{\text{hs}}(t) \left[1 + \hat{p}_1^{\text{hs}} \frac{m}{M} + \hat{p}_2^{\text{hs}} \left(\frac{m}{M} \right)^2 \right], \quad (\text{B1})$$

and the solution of Eq. (A1) is found near the inner surface of the shell as a series expansion in $m/M \ll 1$. If M_s is the mass of the

shocked shell and the pressure at the shock front is $p(M_s) = p_{\text{shock}}$, substituting $p_{\text{hs}}(t)$ from Eq. (24) into Eq. (B1) gives

$$\hat{p}_2^{\text{hs}} = -\frac{M}{6\rho_{\text{shock},0} V_{\text{hs},0}} \hat{p}_1^{\text{hs}}, \quad (\text{B2})$$

$$\hat{p}_1^{\text{hs}} = -(p_{\text{hs}} - p_{\text{shock}}) \frac{M}{M_s p_{\text{hs}}} \left(1 - \frac{M_s}{6\rho_{\text{shock},0} V_{\text{hs},0}} \right)^{-1}, \quad (\text{B3})$$

and the hot-spot radius is determined by

$$\ddot{R}_{\text{hs}} = S_{\text{hs}} \frac{p_{\text{hs}} - p_{\text{shock}}}{M_s} \left(1 - \frac{M_s}{6\rho_{\text{shock},0} V_{\text{hs},0}} \right)^{-1}, \quad (\text{B4})$$

where S_{hs} is the surface area of the hot spot and $\rho_{\text{shock},0}$ and $V_{\text{hs},0}$ are the shell density at the inner edge of the shell and hot-spot volume at the beginning of the shell's deceleration, respectively (see Fig. 137.32). As described earlier [see Eq. (25)], the maximum hot-spot pressure depends on the hot-spot convergence ratio during deceleration. Equation (B4) shows that the hot-spot convergence is determined by the pressure difference between the hot spot and the shock fronts, $p_{\text{hs}} - p_{\text{shock}}$, and the shocked-shell mass (the shocked mass M_s). If the vapor pressure for a given hot-spot radius is increased in an experiment compared to the code predictions (as a result of the larger vapor mass, for example), the shell's deceleration is stronger and the shocked mass is smaller. This results in a smaller fraction of the shell's kinetic energy being converted into the internal energy of the hot spot, leading to reduced hot-spot pressures.

2. Equations for the Shocked Mass and Shock Pressure

The conservation laws at the shock front are used to determine M_s and p_{shock} . The change in momentum of the shell's material as it passes through the shock surface, $-dM_s/dt(v_{\text{shell},s} - v_{\text{shock}})$, is balanced by the pressure force, $-(p_{\text{shell},s} - p_{\text{shock}})S_{\text{shock}}$, yielding

$$\frac{dM_s}{dt}(v_{\text{shell},s} - v_{\text{shock}}) = (p_{\text{shell},s} - p_{\text{shock}})S_{\text{shock}}, \quad (\text{B5})$$

where v_{shock} , p_{shock} , and $v_{\text{shell},s} < 0$, $p_{\text{shell},s}$ are the velocity and pressure at the shock front in the shock-compressed (region II in Fig. 137.33) and unshocked (region I in Fig. 137.33) regions, respectively, and S_{shock} is the surface area of the outgoing shock wave. The mass flux across the shock is determined from the Hugoniot conditions,³⁹

$$\frac{dM_s}{dt} = \sqrt{\frac{\rho_{\text{shell},s}}{3}} \sqrt{4p_{\text{shock}} + p_{\text{shell},s}} S_{\text{shock}}. \quad (\text{B6})$$

Eliminating dM_s/dt from Eqs. (B5) and (B6) gives

$$p_{\text{shock}} = p_{\text{shell},s} - \sqrt{\frac{\rho_{\text{shell},s}}{3}} (4p_{\text{shock}} + p_{\text{shell},s}) \times (v_{\text{shell},s} - v_{\text{shock}}). \quad (\text{B7})$$

The position of the outgoing shock wave R_{shock} is determined by

$$\frac{dR_{\text{shock}}}{dt} = \sqrt{\frac{4p_{\text{shock}} + p_{\text{shell},s}}{3\rho_{\text{shell},s}}} + v_{\text{shell},s}. \quad (\text{B8})$$

In the strong-shock approximation $p_{\text{shock}} \gg p_{\text{shell}}$, these equations reduce to

$$\begin{aligned} \frac{dM_s}{dt} &\simeq \frac{4}{3} \rho_{\text{shell},s} (v_{\text{shock}} - v_{\text{shell},s}) S_{\text{shock}}, \\ p_{\text{shock}} &\simeq \frac{4}{3} \rho_{\text{shell},s} (v_{\text{shock}} - v_{\text{shell},s})^2, \\ \frac{dR_{\text{shock}}}{dt} &= \frac{4}{3} v_{\text{shock}} - \frac{1}{3} v_{\text{shell},s}. \end{aligned} \quad (\text{B9})$$

The shock pressure p_{shock} continues to increase while the shell converges inward. This is a result of two effects: first, an increase in shell density ahead of the shock ρ_{shell} (because of the shell's convergence); second, a decrease in the absolute value of the post-shock velocity v_{shock} caused by the shell's deceleration. The rate of increase in p_{shock} is limited, however, by the deceleration of the unshocked shell and a reduction in $|v_{\text{shell}}|$. The shell density and pressure evolutions will be discussed next.

3. Equation for the Unshocked Shell Density

The velocity gradient across the shell is calculated by taking the time derivative of Eq. (A4):

$$\frac{1}{v} \frac{\partial v}{\partial m} = -\frac{2}{3\rho(m)V(m)} \left(1 + \frac{3}{10} \frac{\partial p}{\partial t} \frac{r}{p v} \right). \quad (\text{B10})$$

Assuming that the velocity gradient is uniform across the shell, Eq. (B10) is evaluated at the ablation front. This gives an estimate of the velocity difference Δv across the shell:

$$\frac{\Delta v}{vM} \simeq -\frac{2}{3\rho_a V_a} \left(1 + \frac{3}{10} \frac{dp_a}{dR_a} \frac{R_a}{p_a} \right). \quad (\text{B11})$$

Equation (B11) shows that the velocity difference between the outer and inner parts of the shell is amplified during the implosion because of convergence ($\rho_a V_a$ decreases). This effect is absent, for example, in planar geometry where the shell's velocity profile is nearly flat. The ablation pressure scales with the ablation radius as $p_a \sim R_a^{-\beta}$ [see Eq. (A5)], leading to $dp_a/dR_a (R_a/p_a) = -\beta$. Then, Eq. (42) is used to evaluate Eq. (B11) at the end of the ablation-front acceleration, giving

$$\Delta v \simeq \sqrt{\frac{2(2-3/5\beta)}{(5-\beta)}} c_s. \quad (\text{B12})$$

For the values of β relevant to the ICF implosions, $\Delta v \simeq 0.8 c_s - 0.9 c_s$. Equation (B12) shows that at the end of the ablation-front acceleration, the velocity variation across the shell is proportional to the shell's sound speed. Therefore, as the return shock starts propagating through the shell at the beginning of the shell's deceleration, it first interacts with the shell's inner part, which moves inward with the larger velocity. Then, as the shock travels through the shell, the incoming shell velocity at the shock front decreases with time because of the velocity gradient shown in Eq. (B12). An additional decrease in the incoming shell velocity is caused by the pressure gradient that creates a force decelerating the unshocked shell.

To calculate the pressure gradient and the density evolution in the unshocked shell, the mass-conservation equation is used:

$$\frac{\partial}{\partial t} \left(\frac{1}{\rho r^2} \right) = 4\pi \frac{\partial v}{\partial m}. \quad (\text{B13})$$

Then, substituting $\partial v/\partial m \simeq \Delta v/M$ and using Eq. (B12) gives

$$\begin{aligned} \rho(m,t) &\simeq \rho_0(m) \left[\frac{r_0(m)}{r(m,t)} \right]^2 \\ &\times \left[1 + 4\pi C_d \frac{c_{s,0}}{M} (t - t_d) \rho_0(m) r_0(m)^2 \right]^{-1}, \end{aligned} \quad (\text{B14})$$

where the coefficient $C_d = \sqrt{2(2-3/5\beta)/(5-\beta)}$ ranges from 0.8 to 0.9 for the values of β relevant to the direct-drive implo-

sions, $c_{s,0}$ is the shell's sound speed at the beginning of deceleration, $\rho_0(m)$ and $r_0(m)$ are the shell's density and position, respectively, as functions of mass coordinate at the beginning of shell deceleration, and t_d is the starting time of shell deceleration. Strictly speaking, the velocity gradient $\Delta v/M$ is not a constant. It increases during shell deceleration because of the pressure gradient along the radial direction. This pressure gradient decelerates the ablation-front region, increasing Δv . Consequently, Eq. (B14) overestimates the density increase. Results of the hydrodynamic simulations indicate, however, that Eq. (B14) is accurate within a few-percent error.

4. Equations for the Unshocked Shell Velocity and Pressure

The velocity slowdown ahead of the outgoing shock wave is calculated using $d v_{\text{shell}}/dt \sim -S_{\text{shock}} \partial p/\partial m$. Assuming that the shell adiabat does not change significantly inside the unshocked shell, the shell pressure is calculated by substituting Eq. (B14) into $p \sim \rho^{5/3}$, giving

$$p_{\text{shell}} \simeq p_0(m) \left[\frac{r_0(m)}{r(m,t)} \right]^{10/3} \Sigma^{-5/3}, \quad (\text{B15})$$

$$\Sigma = 1 + 4\pi C_d \frac{c_{s,0}}{M} (t - t_d) \rho_0(m) r_0(m)^2,$$

and the pressure gradient becomes

$$\begin{aligned} \frac{\partial p}{\partial m} \simeq & \left(\frac{r_0}{r} \right)^{10/3} \Sigma^{-8/3} \left(\frac{\partial p_0}{\partial m} + \frac{5p_0}{6\pi\rho_0 r_0^3} \right) \\ & - \left(\frac{r_0}{r} \right)^{13/3} \Sigma^{-2/3} \frac{5p_0}{6\pi\rho_0 r_0^3}. \end{aligned} \quad (\text{B16})$$

5. Relation Between the Post-Shock Velocity and the Hot-Spot Convergence Rate

To complete defining the model for the shell's deceleration and the hot-spot formation, the hot-spot convergence rate \dot{R}_{hs} must be related to the post-shock velocity v_{shock} . This is accomplished using the mass-conservation equation in the form shown in Eq. (B13). The shell's density at the inner edge of the shell satisfies $\rho_{\text{shell}} V_{\text{hs}} = \text{const}$. Therefore,

$$\frac{\dot{R}_{\text{hs}}}{3\rho_{\text{shock},0} V_{\text{hs},0}} \simeq \frac{v_{\text{shock}} - \dot{R}_{\text{hs}}}{M_s} \quad (\text{B17})$$

and the shocked-shell velocity at the shock front becomes

$$v_{\text{shock}} = \dot{R}_{\text{hs}} \left(1 + \frac{M_s}{3\rho_{\text{shock},0} V_{\text{hs},0}} \right). \quad (\text{B18})$$

Since $\dot{R}_{\text{hs}} < 0$ prior to shell stagnation, the velocity gradient is negative inside the shock-compressed region.

REFERENCES

1. J. D. Lindl, *Inertial Confinement Fusion: The Quest for Ignition and Energy Gain Using Indirect Drive* (Springer-Verlag, New York, 1998).
2. S. Atzeni and J. Meyer-ter-Vehn, *The Physics of Inertial Fusion: Beam Plasma Interaction, Hydrodynamics, Hot Dense Matter*, International Series of Monographs on Physics (Clarendon Press, Oxford, 2004).
3. R. Betti, K. Anderson, V. N. Goncharov, R. L. McCrory, D. D. Meyerhofer, S. Skupsky, and R. P. J. Town, *Phys. Plasmas* **9**, 2277 (2002).
4. V. N. Goncharov, in *Laser-Plasma Interactions*, edited by D. A. Jaroszynski, R. Bingham, and R. A. Cairns, Scottish Graduate Series (CRC Press, Boca Raton, FL, 2009), pp. 409–418.
5. S. Chandrasekhar, *Hydrodynamic and Hydromagnetic Stability*, International Series of Monographs on Physics (Dover Publications, New York, 1981), Chap. X, pp. 428–480.
6. J. Sanz, *Phys. Rev. Lett.* **73**, 2700 (1994); V. N. Goncharov, R. Betti, R. L. McCrory, P. Sorotokin, and C. P. Verdon, *Phys. Plasmas* **3**, 1402 (1996).
7. T. R. Boehly, D. L. Brown, R. S. Craxton, R. L. Keck, J. P. Knauer, J. H. Kelly, T. J. Kessler, S. A. Kumpan, S. J. Loucks, S. A. Letzring, F. J. Marshall, R. L. McCrory, S. F. B. Morse, W. Seka, J. M. Soures, and C. P. Verdon, *Opt. Commun.* **133**, 495 (1997).
8. V. N. Goncharov, T. C. Sangster, T. R. Boehly, S. X. Hu, I. V. Igumenshchev, F. J. Marshall, R. L. McCrory, D. D. Meyerhofer, P. B. Radha, W. Seka, S. Skupsky, C. Stoeckl, D. T. Casey, J. A. Frenje, and R. D. Petrasso, *Phys. Rev. Lett.* **104**, 165001 (2010).
9. J. Delettrez, R. Epstein, M. C. Richardson, P. A. Jaanimagi, and B. L. Henke, *Phys. Rev. A* **36**, 3926 (1987).
10. V. N. Goncharov, T. C. Sangster, P. B. Radha, R. Betti, T. R. Boehly, T. J. B. Collins, R. S. Craxton, J. A. Delettrez, R. Epstein, V. Yu. Glebov, S. X. Hu, I. V. Igumenshchev, J. P. Knauer, S. J. Loucks, J. A. Marozas, F. J. Marshall, R. L. McCrory, P. W. McKenty, D. D. Meyerhofer, S. P. Regan, W. Seka, S. Skupsky, V. A. Smalyuk, J. M. Soures, C. Stoeckl, D. Shvarts, J. A. Frenje, R. D. Petrasso, C. K. Li, F. Séguin, W. Manheimer, and D. G. Colombant, *Phys. Plasmas* **15**, 056310 (2008).
11. I. V. Igumenshchev, D. H. Edgell, V. N. Goncharov, J. A. Delettrez, A. V. Maximov, J. F. Myatt, W. Seka, A. Shvydky, S. Skupsky, and C. Stoeckl, *Phys. Plasmas* **17**, 122708 (2010).
12. I. V. Igumenshchev, W. Seka, D. H. Edgell, D. T. Michel, D. H. Froula, V. N. Goncharov, R. S. Craxton, L. Divol, R. Epstein, R. Follett, J. H.

- Kelly, T. Z. Kosc, A. V. Maximov, R. L. McCrory, D. D. Meyerhofer, P. Michel, J. F. Myatt, T. C. Sangster, A. Shvydky, S. Skupsky, and C. Stoeckl, *Phys. Plasmas* **19**, 056314 (2012).
13. C. J. Randall, J. R. Albritton, and J. J. Thomson, *Phys. Fluids* **24**, 1474 (1981).
 14. W. L. Kruer, in *The Physics of Laser Plasma Interactions, Frontiers in Physics*, Vol. 73, edited by D. Pines (Addison-Wesley, Redwood City, CA, 1988).
 15. A. Simon, R. W. Short, E. A. Williams, and T. Dewandre, *Phys. Fluids* **26**, 3107 (1983).
 16. J. F. Myatt, H. X. Vu, D. F. DuBois, D. A. Russell, J. Zhang, R. W. Short, and A. V. Maximov, *Phys. Plasmas* **20**, 052705 (2013).
 17. W. M. Manheimer, D. G. Colombant, and J. H. Gardner, *Phys. Fluids* **25**, 1644 (1982).
 18. D. T. Michel, C. Sorce, R. Epstein, N. Whiting, I. V. Igumenshchev, R. Jungquist, and D. H. Froula, *Rev. Sci. Instrum.* **83**, 10E530 (2012).
 19. D. T. Michel, V. N. Goncharov, I. V. Igumenshchev, R. Epstein, and D. H. Froula, *Phys. Rev. Lett.* **111**, 245005 (2013).
 20. W. Seka, D. H. Edgell, J. P. Knauer, J. F. Myatt, A. V. Maximov, R. W. Short, T. C. Sangster, C. Stoeckl, R. E. Bahr, R. S. Craxton, J. A. Delettrez, V. N. Goncharov, I. V. Igumenshchev, and D. Shvarts, *Phys. Plasmas* **15**, 056312 (2008).
 21. T. Dewandre, J. R. Albritton, and E. A. Williams, *Phys. Fluids* **24**, 528 (1981).
 22. S. Skupsky, R. W. Short, T. Kessler, R. S. Craxton, S. Letzring, and J. M. Soures, *J. Appl. Phys.* **66**, 3456 (1989).
 23. *LLE Review Quarterly Report* **130**, 72, Laboratory for Laser Energetics, University of Rochester, Rochester, NY, LLE Document No. DOE/NA/28302-1058 (2012).
 24. V. N. Goncharov, in *Laser-Plasma Interactions and Applications*, edited by P. McKenna, D. Neely, R. Bingham, and D. A. Jaroszynski, Scottish Graduate Series (Springer, Switzerland, 2013), Chap. 7, pp. 135–183.
 25. H. Brysk, *Plasma Phys.* **15**, 611 (1973).
 26. T. C. Sangster, V. N. Goncharov, R. Betti, P. B. Radha, T. R. Boehly, D. T. Casey, T. J. B. Collins, R. S. Craxton, J. A. Delettrez, D. H. Edgell, R. Epstein, C. J. Forrest, J. A. Frenje, D. H. Froula, M. Gatu-Johnson, V. Yu. Glebov, D. R. Harding, M. Hohenberger, S. X. Hu, I. V. Igumenshchev, R. Janezic, J. H. Kelly, T. J. Kessler, C. Kingsley, T. Z. Kosc, J. P. Knauer, S. J. Loucks, J. A. Marozas, F. J. Marshall, A. V. Maximov, R. L. McCrory, P. W. McKenty, D. D. Meyerhofer, D. T. Michel, J. F. Myatt, R. D. Petrasso, S. P. Regan, W. Seka, W. T. Shmayda, R. W. Short, A. Shvydky, S. Skupsky, J. M. Soures, C. Stoeckl, W. Theobald, V. Versteeg, B. Yaakobi, and J. D. Zuegel, *Phys. Plasmas* **20**, 056317 (2013).
 27. J. A. Frenje, C. K. Li, F. H. Séguin, D. T. Casey, R. D. Petrasso, T. C. Sangster, R. Betti, V. Yu. Glebov, and D. D. Meyerhofer, *Phys. Plasmas* **16**, 042704 (2009); J. A. Frenje, D. T. Casey, C. K. Li, F. H. Séguin, R. D. Petrasso, V. Yu. Glebov, P. B. Radha, T. C. Sangster, D. D. Meyerhofer, S. P. Hatchett, S. W. Haan, C. J. Cerjan, O. L. Landen, K. A. Fletcher, and R. J. Leeper, *Phys. Plasmas* **17**, 056311 (2010).
 28. C. J. Forrest, P. B. Radha, V. Yu. Glebov, V. N. Goncharov, J. P. Knauer, A. Pruyne, M. Romanofsky, T. C. Sangster, M. J. Shoup III, C. Stoeckl, D. T. Casey, M. Gatu-Johnson, and S. Gardner, *Rev. Sci. Instrum.* **83**, 10D919 (2012).
 29. C. Stoeckl, V. Yu. Glebov, S. Roberts, T. C. Sangster, R. A. Lerche, R. L. Griffith, and C. Sorce, *Rev. Sci. Instrum.* **74**, 1713 (2003).
 30. C. Cerjan, P. T. Springer, and S. M. Sepke, *Phys. Plasmas* **20**, 056319 (2013).
 31. P. B. Radha, V. N. Goncharov, T. J. B. Collins, J. A. Delettrez, Y. Elbaz, V. Yu. Glebov, R. L. Keck, D. E. Keller, J. P. Knauer, J. A. Marozas, F. J. Marshall, P. W. McKenty, D. D. Meyerhofer, S. P. Regan, T. C. Sangster, D. Shvarts, S. Skupsky, Y. Srebro, R. P. J. Town, and C. Stoeckl, *Phys. Plasmas* **12**, 032702 (2005).
 32. S. X. Hu, P. B. Radha, V. N. Goncharov, R. Betti, R. Epstein, F. J. Marshall, R. L. McCrory, D. D. Meyerhofer, T. C. Sangster, and S. Skupsky, *Bull. Am. Phys. Soc.* **58**, 324 (2013).
 33. Prism Computational Sciences, Inc., Madison, WI 53711; J. J. MacFarlane *et al.*, *High Energy Density Phys.* **3**, 181 (2007).
 34. F. J. Marshall and J. A. Oertel, *Rev. Sci. Instrum.* **68**, 735 (1997).
 35. M. J. Edwards, P. K. Patel, J. D. Lindl, L. J. Atherton, S. H. Glenzer, S. W. Haan, J. D. Kilkenny, O. L. Landen, E. I. Moses, A. Nikroo, R. Petrasso, T. C. Sangster, P. T. Springer, S. Batha, R. Benedetti, L. Bernstein, R. Betti, D. L. Bleuel, T. R. Boehly, D. K. Bradley, J. A. Caggiano, D. A. Callahan, P. M. Celliers, C. J. Cerjan, K. C. Chen, D. S. Clark, G. W. Collins, E. L. Dewald, L. Divol, S. Dixit, T. Doeppner, D. H. Edgell, J. E. Fair, M. Farrell, R. J. Fortner, J. Frenje, M. G. Gatu Johnson, E. Giraldez, V. Yu. Glebov, G. Grim, B. A. Hammel, A. V. Hamza, D. R. Harding, S. P. Hatchett, N. Hein, H. W. Herrmann, D. Hicks, D. E. Hinkel, M. Hoppe, W. W. Hsing, N. Izumi, B. Jacoby, O. S. Jones, D. Kalantar, R. Kauffman, J. L. Kline, J. P. Knauer, J. A. Koch, B. J. Kozioziemski, G. Kyrala, K. N. LaFortune, S. Le Pape, R. J. Leeper, R. Lerche, T. Ma, B. J. MacGowan, A. J. MacKinnon, A. Macphee, E. R. Mapoles, M. M. Marinak, M. Mauldin, P. W. McKenty, M. Meezan, P. A. Michel, J. Milovich, J. D. Moody, M. Moran, D. H. Munro, C. L. Olson, K. Opachich, A. E. Pak, T. Parham, H.-S. Park, J. E. Ralph, S. P. Regan, B. Remington, H. Rinderknecht, H. F. Robey, M. Rosen, S. Ross, J. D. Salmonson, J. Sater, D. H. Schneider, F. H. Séguin, S. M. Sepke, D. A. Shaughnessy, V. A. Smalyuk, B. K. Spears, C. Stoeckl, W. Stoeffl, L. Suter, C. A. Thomas, R. Tommasini, R. P. Town, S. V. Weber, P. J. Wegner, K. Widman, M. Wilke, D. C. Wilson, C. B. Yeamans, and A. Zylstra, *Phys. Plasmas* **20**, 070501 (2013).
 36. J. Paisner *et al.*, *Laser Focus World* **30**, 75 (1994).
 37. Von G. Guderley, *Luftfahrtforschung* **19**, 302 (1942).
 38. C. Bellei *et al.*, *Phys. Plasmas* **20**, 012701 (2013); C. Bellei *et al.*, *Phys. Plasmas* **20**, 044702 (2013).
 39. L. D. Landau and E. M. Lifshits, *Fluid Mechanics* (Pergamon, Oxford, 1982).

40. I. V. Igumenshchev, V. N. Goncharov, W. T. Shmayda, D. R. Harding, T. C. Sangster, and D. D. Meyerhofer, *Phys. Plasmas* **20**, 082703 (2013).
41. R. Betti and J. Sanz, *Phys. Rev. Lett.* **97**, 205002 (2006).
42. D. Layzer, *Astrophys. J.* **122**, 1 (1955); D. Oron *et al.*, *Phys. Plasmas* **8**, 2883 (2001); V. N. Goncharov, *Phys. Rev. Lett.* **88**, 134502 (2002).
43. D. H. Edgell, W. Seka, R. E. Bahr, T. R. Boehly, and M. J. Bonino, *Phys. Plasmas* **15**, 092704 (2008).
44. M. C. Herrmann, M. Tabak, and J. D. Lindl, *Phys. Plasmas* **8**, 2296 (2001).
45. I. V. Igumenshchev, D. H. Froula, D. H. Edgell, V. N. Goncharov, T. J. Kessler, F. J. Marshall, R. L. McCrory, P. W. McKenty, D. D. Meyerhofer, D. T. Michel, T. C. Sangster, W. Seka, and S. Skupsky, *Phys. Rev. Lett.* **110**, 145001 (2013); D. H. Froula, T. J. Kessler, I. V. Igumenshchev, R. Betti, V. N. Goncharov, H. Huang, S. X. Hu, E. Hill, J. H. Kelly, D. D. Meyerhofer, A. Shvydky, and J. D. Zuegel, *Phys. Plasmas* **20**, 082704 (2013).
46. S. X. Hu, G. Fiksel, V. N. Goncharov, S. Skupsky, D. D. Meyerhofer, and V. A. Smalyuk, *Phys. Rev. Lett.* **108**, 195003 (2012); G. Fiksel, S. X. Hu, V. N. Goncharov, D. D. Meyerhofer, T. C. Sangster, V. A. Smalyuk, B. Yaakobi, M. J. Bonino, and R. Jungquist, *Phys. Plasmas* **19**, 062704 (2012).
47. R. J. Henchen, V. N. Goncharov, D. T. Michel, R. K. Follett, J. Katz, and D. H. Froula, *Bull. Am. Phys. Soc.* **58**, 151 (2013).
48. C. E. Max, C. F. McKee, and W. C. Mead, *Phys. Fluids* **23**, 1620 (1980).

Measurements of Electron Density Profiles Using an Angular Filter Refractometer

Introduction

An understanding of the underdense plasma conditions in laser–plasma experiments at large laser facilities is important for many high-energy-density (HED) physics studies.¹ The growth of laser–plasma instabilities depends on the coronal plasma density profile, flow, and temperature. When they are above threshold, they can feed back onto the hydrodynamics often requiring *ad hoc* modeling of the laser absorption or heat transport.² In high-temperature plasmas, the primary instabilities of interest are stimulated Brillouin scattering,³ stimulated Raman scattering,³ and two-plasmon decay.⁴

Quantitative characterization of HED plasma density profiles in the corona where the laser–plasma interactions are most active is challenging. Incoherent x-ray sources are useful for diagnosing cold ($T_e \leq 10$ eV) and dense ($n_e \approx 10^{23}$ cm⁻³) plasmas, where absorption and scattering techniques such as radiography/penumbral imaging⁵ and x-ray Thomson scattering⁶ are employed. Optical wavelengths are typically employed to probe lower-density ranges where the plasma density is inferred from the phase change of the probe beam. These diagnostics are designed to access the plasma density by measuring the probe beam's phase (interferometry⁷), refraction angle (schlieren imaging,⁸ grid image refractometry,⁹ and Moire deflectometry¹⁰), or displacement (shadowgraphy⁸). In the range of densities above 10²⁰ cm⁻³, typical HED plasmas present large integrated optical phases that make it difficult to quantitatively measure the density profile. Soft x-ray lasers present an alternative to access these density ranges,¹¹ but are a complex radiation source and often not practical for application to large-scale diagnostic systems.

A qualitative picture of the underdense plasma gradients can be made using shadowgraph and schlieren imaging, although these techniques are not precise enough to extract the plasma density profile.⁸ In shadowgraphy, the displacement of probe rays is mapped by imaging a plane behind the object in question. An image is recorded not of the object, but of its shadow, which does not have a 1:1 spatial correspondence with the object. Extracting the plasma density would involve deconvolving the spatial correspondence, calculating the absorption

profile of the probe beam, and a double integration to achieve the probe's phase. This typically introduces an unacceptable amount of error into the density measurement. Schlieren techniques map the refraction of the probe beam by blocking all or part of the unrefracted probe beam with a knife edge or a circular stop. In the case of using a coherent probe pulse produced by a laser, only a single refraction angle is measured, lending this technique to be used for the observation of sharp density gradients such as in the presence of a shock,¹² where the binary response of the diagnostic is useful. Extracting quantitative information from the density gradients with a significant dynamic range involves the use of an incoherent probe pulse such as a light-emitting diode with an extended source size.¹³

Interferometry is the most-common technique used for measuring plasma density profiles in underdense plasmas. As the probe passes through higher-density regions of the plasma, the interferometric fringes become closer and are eventually unresolvable. It is difficult to quantify this limitation in resolution, but for a particular profile, synthetic interferograms can be generated to study the peak plasma density that can be resolved using interferometry. Taking a typical HED laser–plasma plume from a planar target modeled as $n_e = n_0 \exp[-(x^2 + y^2)/L_g^2] \exp(-z/L_n)$ with $L_g = 400$ μm and $L_n = 300$ μm , the maximum peak density resolvable with a 263-nm probe on a standard detector is $\sim 10^{20}$ cm⁻³, which is consistent with the peak densities measured by D. Ress *et al.*¹⁴ for a comparable-sized plasma.

Angular filter refractometry (AFR),^{15,16}—a novel diagnostic—has been developed to characterize the plasma density profile up to densities of 10²¹ cm⁻³ by producing a contour map of refraction angles. This is accomplished by using angular filters that block certain bands of refraction angles, casting shadows in the image plane. The plasma density is calculated from the measured refraction angles of a probe beam after passing through the plasma. The maximum measured density is limited by the *f* number of the optical collection system, the length of plasma in the direction of the probe, and the magnitude of the transverse gradients. AFR provides an accurate

diagnosis of the underdense plasma profiles in experiments relevant to laser–plasma instabilities.

The following sections (1) describe the operation of the AFR diagnostic and how the experimental images can be analyzed to produce two-dimensional (2-D) plasma density profiles; (2) review experiments in which the diagnostic was used to characterize the plasma expansion from ultraviolet irradiated CH planar and spherical targets; and (3) present the conclusions. The error analysis of the AFR diagnostic is presented in the Appendix.

Angular Filter Refractometry

The AFR diagnostic is a part of the fourth-harmonic probe system¹⁷ on OMEGA EP.¹⁸ A simplified optical schematic of the system is shown in Fig. 137.42. The red lines represent the incoming ray path of the probe beam. It originates from the conversion of a Nd:glass laser pulse to its fourth harmonic (probe wavelength $\lambda_p = 263$ nm) and has a pulse width of 10 ps with 10 mJ of energy. The beam passes through the target chamber center (TCC) slightly diverging at $f/25$ with a beam diameter of ~ 3.5 mm. After passing through the TCC, the probe is collected at $f/4$ and collimated for transport over >4 m to the diagnostic table, where the plasma plane is relay imaged to a charge-coupled–device (CCD) camera with a resolution of ~ 5 μm over a 5-mm field of view.¹⁵

1. Diagnostic Setup and Calibration

The AFR diagnostic uses an angular filter [Fig. 137.43(a)] placed at the focus of the unrefracted probe beam (Fourier plane¹⁹). The opaque regions of the angular filter block bands of refraction angles, resulting in shadows in the image plane. The diagnostic relies on the direct proportionality between the angle of refraction of a probe ray at the object plane and its radial location in the Fourier plane. This relation correlates the shadows produced by the angular filter to contours of the constant refraction angle. For a single-lens imaging system and a collimated probe beam, it can be shown that a ray refracted at the object plane passes through the Fourier plane at a distance from the optical axis r , which is equal to the focal length of the collection lens f , times the refraction angle θ , regardless of its spatial origin in the object plane [assuming paraxial propagation $\cos(\theta) \approx 1$] (Ref. 20). For the case of a diverging probe beam (used in the AFR diagnostic), a more-general relation is determined using geometric optics where r is equal to a constant times the refraction angle θ_{ref} , according to

$$r = \theta_{\text{ref}} \times \left(\frac{d_s f}{d_1 + d_s - f} \right), \quad (1)$$

where $\theta_{\text{ref}} = \theta_{\text{tot}} - \theta_0$, θ_{tot} is the ray angle with respect to the optical axis, θ_0 is the initial unrefracted angle, d_1 is the dis-

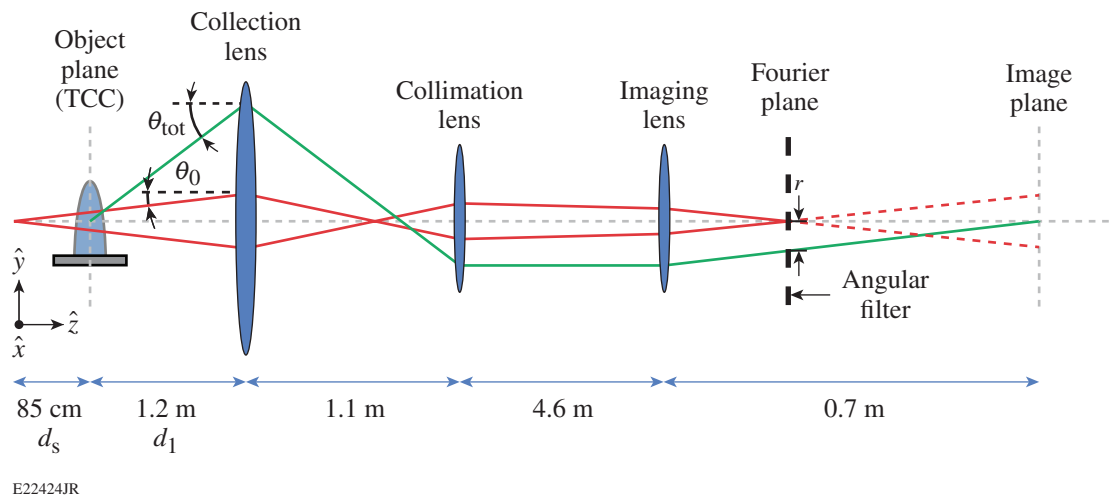
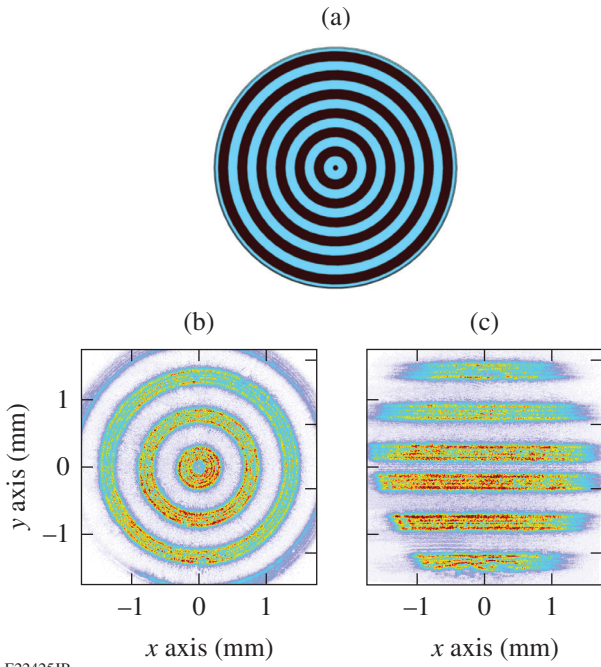


Figure 137.42

A schematic representation of angular filter refractometry using the fourth-harmonic probe on OMEGA EP (distances not to scale). The unrefracted probe (red) focuses at the Fourier plane, where distinct refraction angles are filtered out by an angular filter. Shadows from the opaque regions of the angular filter form contours of constant refraction angle in the image plane. TCC: target chamber center.



E22425JR

Figure 137.43

(a) An angular filter consisting of a central opaque dot of 500- μm diameter surrounded by 2-mm-wide concentric rings alternating between transparent and opaque. (b) An image formed when a negative-focal-length ($f = -20$ mm) spherical lens placed at target chamber center (TCC) is used to deterministically refract the probe beam to calibrate the system. The light rings correspond to specific bands in the angular filter, and their spatial locations correspond to specific refraction angles on the surface of the lens. (c) A similar image is formed as in (b) but with a cylindrical lens of negative focal length ($f = -20$ mm). The refraction takes place in one direction, producing the lines in the image plane.

tance from the object plane to the collection lens, and d_s is the distance from the point source to the object plane ($d_s = \infty$ for the collimated beam). The direct proportionality of the spatial location of a ray to the amount of refraction allows for filtration of specific refraction angles in a deterministic manner.

To accurately determine the constant of proportionality in Eq. (1) (bracketed term), the diagnostic is calibrated by placing a planoconcave lens with a focal length of -20 mm at TCC that imparts a known amount of refraction as a function of space transverse to the propagation direction (x, y). Probe rays that exit the lens with a refraction angle of $\theta_{\text{ref}} = 0.09^\circ$ graze the edge of the central dot at $r = 250 \mu\text{m}$ and return to their location (x', y') in the magnified image plane, where they form the edge of the central blue circle seen in Fig. 137.43(b). Higher refraction angles are either blocked by the opaque rings or transmitted between them, forming the other light and dark bands in the image. By measuring the radial distance of each band, the posi-

tions of the rays at the calibration lens are determined, allowing one to calculate the refraction angles. The resultant calibration for the image shown relates the angle of refraction to the radial position on the angular filter, $\theta_{\text{ref}} = [0.368 \pm 0.0029] \times r$.

Figure 137.43(c) shows an image created by using a cylindrical calibration lens where the probe light is refracted only in the vertical direction. At the Fourier plane, the beam has a vertical line focus. Upon returning to the image plane, the filtered regions form bands in the horizontal direction showing the contours of constant refraction of a cylindrical lens.

2. Analysis

The angle of refraction of a probe ray exiting a plasma is related to the transverse gradient of phase accrued by that ray according to⁷

$$\theta_\alpha = \frac{\lambda_p}{2\pi} \frac{\partial \phi}{\partial \alpha}, \quad (2)$$

where α ($= x$ or y) represents the spatial component of the measured refraction in the x - y plane (see Fig. 137.42), λ_p is the probe laser wavelength, $\phi = \int k_p dz$ is the total accumulated phase of a probe ray passing through the plasma, k_p is the probe wave number, and z is the propagation direction of the probe. The phase of the probe is related to the plasma density since the refractive index is given by $(1 - n_e/n_{\text{cr}})^{1/2}$, giving

$$\phi(x, y) = \frac{\pi}{\lambda_p n_{\text{cr}}} \int_{-\infty}^{\infty} n_e(x, y, z) dz, \quad (3)$$

where $n_e(x, y, z)$ is the plasma density and

$$n_{\text{cr}} = 1.1 \times 10^{21} / \lambda_p^2 (\mu\text{m}) \text{ cm}^{-3} = 1.6 \times 10^{22} \text{ cm}^{-3}$$

is the critical plasma density for a probe wavelength of $\lambda_p = 263$ nm. It is assumed that $n_e \ll n_{\text{cr}}$. In Eq. (3), changes in x and y along the ray path are ignored. Assuming the plasma density profile is axisymmetric around the y axis, this equation can be Abel inverted for a fixed y coordinate to solve for the density as a function of the probe phase:

$$n_e(R = \sqrt{x^2 + z^2}) = -\frac{\lambda_p n_{\text{cr}}}{\pi^2} \int_0^{-\infty} \frac{\partial \phi}{\partial x} \frac{ds}{\sqrt{s^2 + R^2}}. \quad (4)$$

To arrive at Eq. (4) from the standard Abel integral, the substitution $s = \sqrt{x^2 - R^2}$ was made to eliminate the singularity at $x = R$.

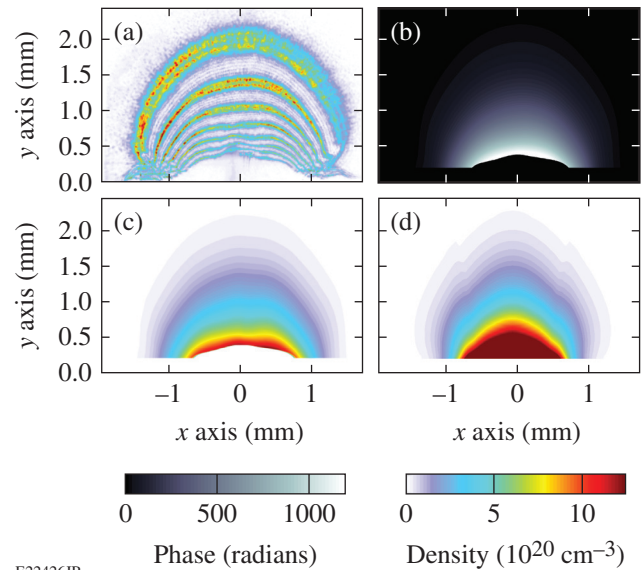
For the circular angular filter shown in Fig. 137.43(a), the total refraction angle is measured, $\theta_{\text{tot}} = \sqrt{\theta_x^2 + \theta_y^2}$. Owing to the shape of the plasmas expanding from the flat and spherical targets studied here, the direction of the refraction is assumed to be radial; therefore, Eq. (2) is integrated in the radial direction about the assumed center of the plasma to solve for the phase of the probe beam exiting the plasma. The gradient of the phase in the x direction (perpendicular to the axis of symmetry) is used to solve for the plasma density using Eq. (4). An error analysis of the data reduction and calibration is presented in **Appendix A** (p. 56).

To reduce the numerical error introduced by calculating the gradient in phase, an angular filter with straight lines parallel to the y axis can be used to directly determine the component of the refraction in the x direction ($\partial\phi/\partial x$). In this case the measured refraction angle (θ_x) can be directly inserted into Eq. (4) so that both the integration in Eq. (2) and the derivative in Eq. (4) are skipped.

Experimental Results

The plasma density profiles for flat and spherical plastic CH targets driven by four ultraviolet laser beams ($\lambda_0 = 351$ nm) incident at an angle of 23° with respect to the target normal were measured. Each beam had ~ 2 kJ of energy in a 2-ns square temporal pulse shape. Distributed phase plates²¹ were used to produce a 9.5-order super-Gaussian spot with 430- μm ($1/e$) width on the target surface, resulting in a total peak overlapped intensity of 8×10^{14} W/cm². The fourth-harmonic probe pulse passed transverse to the target normal. The short probe pulse's duration of 10 ps ensures that there is minimal hydrodynamic movement of the plasma over the course of the measurement. The timing of the probe is defined from the 2% intensity of the ultraviolet drive beams to the peak intensity of the probe.

Figure 137.44 illustrates the AFR technique. Figure 137.44(a) shows the AFR image obtained from probing an irradiated flat CH target (3 mm \times 3 mm \times 0.125 mm) at 1.5 ns. The contour lines of the total refraction angle show the general shape of the plasma plume expanding from the surface of the target located at $y = 0$. The diffraction pattern seen in the image is a result of the sharp edges of the angular filter aperturing the beam in between image planes. This effect can corrupt the spatial location of the edges of the refractive bands; therefore, the analysis was based on the central location of the refractive band, which is unaffected by diffraction. The spatial registration of the image to the target surface is described in **Appendix A**. Images similar to Fig. 137.44(a) but with only one angular band were reported from a schlieren setup in Ref. 22. These images did not contain



E22426JR

Figure 137.44

(a) An angular filter refractometry (AFR) image obtained by probing a CH target irradiated with ~ 9 kJ of 351-nm light at 1.5 ns into the drive. (b) Two-dimensional phase map calculated from the refraction angles in (a) using Eq. (2). (c) Abel-inverted 2-D plasma density profile calculated from (b) using Eq. (4). (d) The 2-D density profile produced by a *DRACO* hydrodynamic simulation using the laser and target parameters from (a). In all frames the original target surface was located at $y = 0$.

enough information to allow for reconstruction of the plasma density but they compared well with hydrodynamic simulations.

The phase map was calculated by radially integrating the refractive contours using Eq. (2) and applying a 2-D interpolation to obtain a phase value on each pixel [Fig. 137.44(b)]. It is instructive to note that absolute phases of greater than 1000 rad are observable by this diagnostic before the $f/4$ cutoff of the collection lens is reached. This is equivalent to over 150 fringe shifts across ~ 1 mm of plasma, illustrating the challenges of using interferometry with these types of plasmas. Figure 137.44(c) shows the calculated plasma density profile that reaches densities up to 10^{21} cm⁻³. This may be compared with the density profile in Fig. 137.44(d) from a 2-D *DRACO*^{23,24} hydrodynamic simulation. The *DRACO* simulations reported here use a flux-limited heat transport model that limits the Spitzer–Harm flux to a fraction (0.06) of the free-streaming value.²⁵

1. Flat CH Foil Experiments

Figure 137.45 shows the temporal evolution of the plasma expansion from flat CH targets irradiated under nominally identical conditions and probed at different times. The expansion of the plasma is illustrated by the movement of the contours

in the radial direction away from the target surface ($y = 0$). Figure 137.45(d) is from the same shot as Fig. 137.44(a). An estimate of the plasma expansion is obtained by assuming a 2-D Gaussian-shaped plasma in the target plane direction and an exponential profile in the target normal direction of the form $n_e(y) = n_0 \exp(-y/L_n)$, where L_n is the plasma scale length. Taking two points in the center of the profile at $x = 0$, Eqs. (2) and (3) can be used to show $L_n = (y_1 - y_2) / \ln(\theta_2 / \theta_1)$. Fol-

lowing two points of constant refraction yields the proportionality $L_n \propto y_1 - y_2$. As time increases, the widening and separating of the refractive bands signify a proportionate increase in the plasma scale length as the plasma expands away from the target.

Figure 137.46 shows 1-D density profiles along the y axis obtained from the experimental images shown in Fig. 137.45. Density data are extracted over almost two orders of mag-

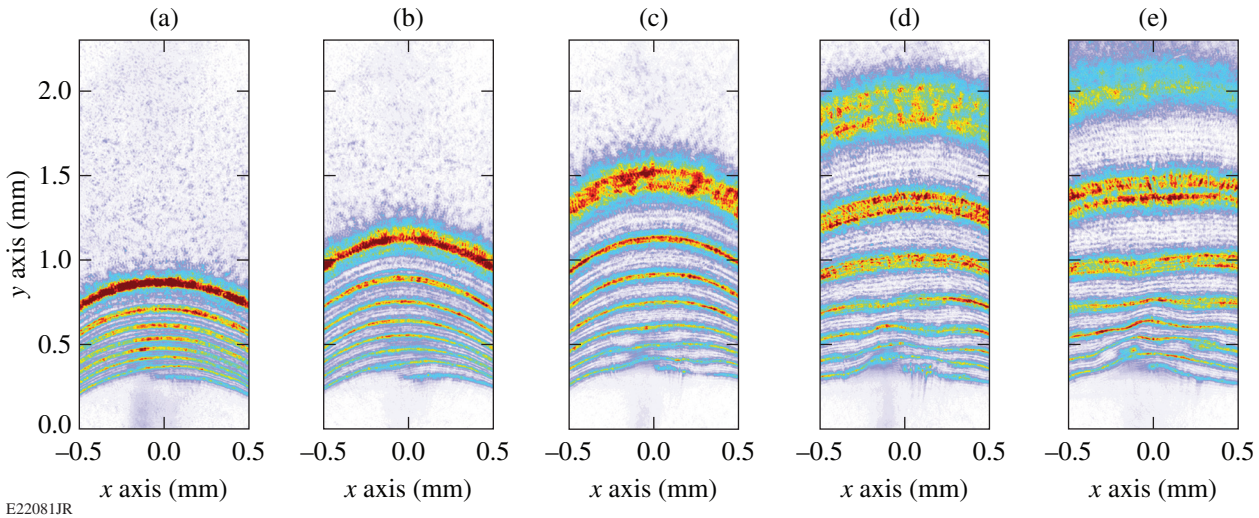


Figure 137.45
Central portions of AFR images illustrating plasma expansion from flat CH targets irradiated with ~ 9 kJ of ultraviolet (351-nm) light in a 1-mm spot. The images were obtained at probe timings of (a) 0.56 ns, (b) 0.84 ns, (c) 1.1 ns, (d) 1.5 ns, and (e) 2.0 ns.

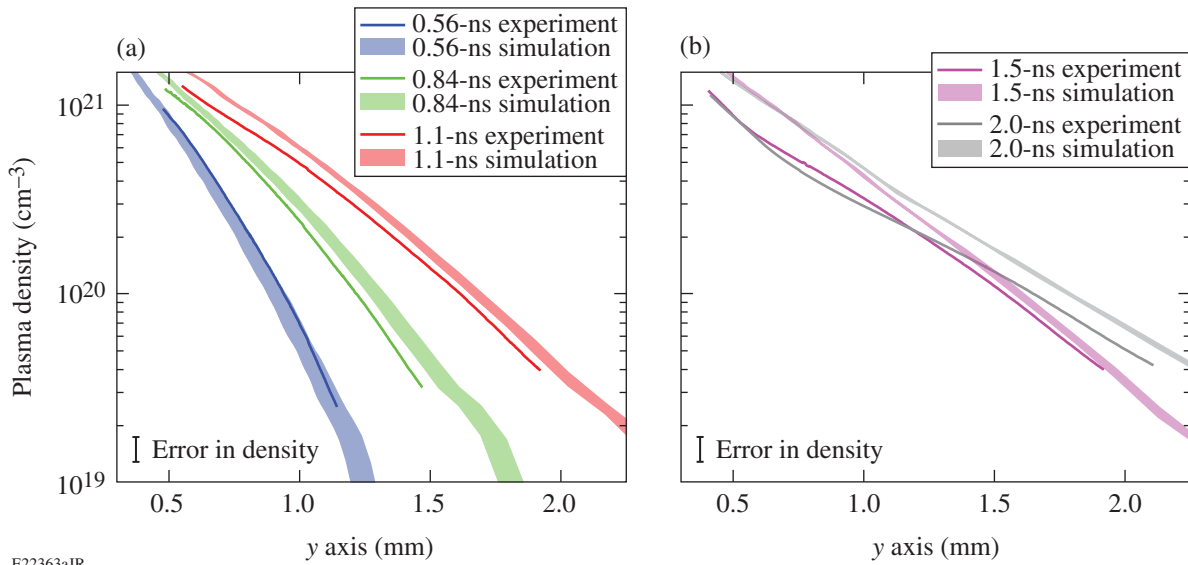


Figure 137.46
Plasma density profiles along the target normal at the center of the plasma profile ($x = 0$) obtained from the AFR images of Fig. 137.45 (solid lines). The shaded regions represent DRACO simulations covering a time span of 40 ps, corresponding to the \pm error in measuring the probe-pulse timing with respect to the ultraviolet drive pulses. The original target position is located at $y = 0$. The error bars on the experimental data represent $\pm 15\%$ as derived in **Appendix A** (p. 56).

nitude ranging from $\sim 3 \times 10^{19}$ to 10^{21} cm^{-3} . The upper end is limited by refraction of the probe beam outside of the $f/4$ collection optics, and the lower end is limited by the smallest measurable refraction angle by this angular filter (0.21°). The profiles are approximately exponential,²⁶ and for the early times (≤ 1.1 ns) shown in Fig. 137.46(a), the plasma expands away from the surface driven by the ablation. This is evident in the increase in the position for a given value of density as time increases. The expansion ceases at later times (≥ 1.5 ns) shown in Fig. 137.46(b) except at the low-density region of the profile. The shaded regions in Fig. 137.46 represent lineouts from the *DRACO*-simulated plasma profiles, where the width of the shaded region accounts for the ± 20 -ps timing error in the probe pulse. The experimental data agree very well with the simulations for early times (< 1 ns). For times ≥ 1.1 ns, the simulations predict higher plasma densities than are experimentally measured. This can also be seen from a comparison between Figs. 137.44(c) and 137.44(d).

2. CH Spherical Experiments

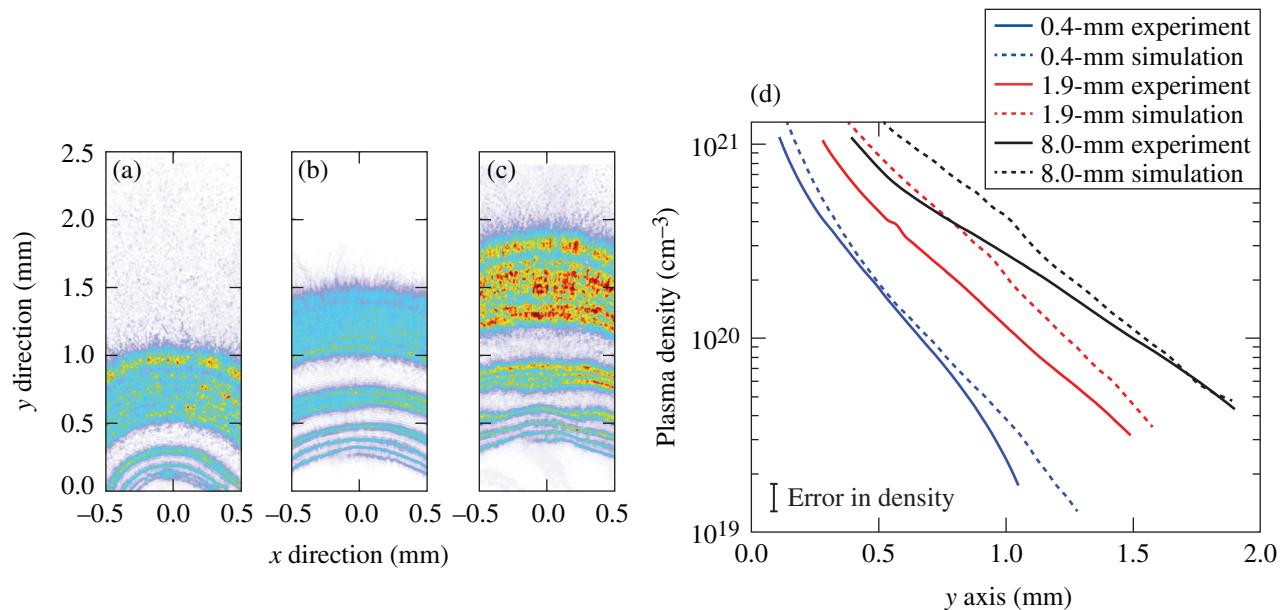
Experiments designed to change the density profiles while maintaining a constant drive intensity varied the radius of curvature of the targets using spheres of different diameters. As the radius of curvature is decreased, the plasma flow becomes more

three dimensional, reducing the density scale length along the target symmetry axis. Figure 137.47 compares the plasmas from irradiated CH spheres with diameters varying from 0.4 mm to 8 mm. In the three AFR images of Figs. 137.47(a)–137.47(c), the contour spacing and thickness increase with the diameter of the spheres, indicating that the plasma scale length is increasing. This is a result of the plasma expansion becoming more divergent with decreasing radius.

Figure 137.47(b) compares the measured density profiles with profiles calculated with *DRACO*. At the smallest diameter of 0.4 mm, the calculated profile agrees well with the measured profile. For the larger diameters of 1.9 mm and 8 mm, there are clear discrepancies between the profiles. This observation is consistent with the discrepancy seen at 1.5 ns for the flat CH target [Fig. 137.46(b), purple line]. The profiles for a diameter of 8 mm are very close to the corresponding profiles in Fig. 137.46(b).

Conclusion

A characterization of the density profiles in HED-relevant long-scale-length plasmas was presented. Angular filter refractometry—a novel diagnostic—was used to map the refraction angle of a 263-nm probe after it passed through a plasma, enabling one to measure densities of 10^{21} cm^{-3} in millimeter-



E22427JR

Figure 137.47

AFR images obtained at a probe timing of 1.5 ns for ultraviolet-irradiated CH spheres with radii equal to (a) $400 \mu\text{m}$, (b) 1.9 mm, and (c) 8 mm. The number of bands in these images is less than in those of Fig. 137.45 because a different angular filter with fewer opaque rings was used. (d) Corresponding plasma density profiles along the target normal at the center of the plasma profile ($x = 0$). The solid lines represent the experimental data and dashed lines the *DRACO* simulations. The original target surface is located at $y = 0$.

scale plasmas. The plasma expansion from kilojoule-level, ultraviolet-irradiated CH targets was studied as a function of time for planar targets and radius for spherical targets. These results were compared with 2-D *DRACO* hydrodynamic simulations showing good agreement for the planar targets at early times and for the spherical targets at small radii. The hydrodynamic simulations predict higher densities for the planar targets at late times and for the spherical targets with larger radii. The difference between the experimental and simulation data is under active investigation and focused on correlations to laser-plasma instabilities that could possibly modify the plasma profile at large scale lengths.

ACKNOWLEDGMENT

This material is based upon work supported by the Department of Energy National Nuclear Security Administration under Award Number DE-NA0001944, the University of Rochester, and the New York State Energy Research and Development Authority. The support of DOE does not constitute an endorsement by DOE of the views expressed in this article.

Appendix A: Error Analysis

The calibration of refraction angles and the post-analysis process are the two significant sources of error in the calculation of plasma density from the AFR images. To estimate the error in the calibration process, the system was calibrated four times over a two-month period to take into account the reproducibility of the lens placement at TCC and the accuracy of marking the edges of the refractive bands. For each calibration, a constant of proportionality relating the refraction angle θ_{ref} to the radial location on the angular filter r was calculated. The standard deviation in that constant was found to be $\sigma = 0.0029\%$ /mm. This error was propagated through the analysis process and yielded a corresponding standard deviation error in the plasma density of 2%.

The reduction of an experimental AFR image to a plasma density profile includes many steps: locating the refraction bands, radially integrating the refraction angle to produce a phase, and Abel inverting the phase to produce plasma density. There is an error in the optical imaging system caused by the continuous refraction by an extended plasma around the object plane. It is difficult to estimate the contribution of each of these effects to the error. The error was therefore extracted by analyzing a synthetic AFR image created by an optical model. The optical ray-trace code *FRED*²⁷ was used to assess the performance of the optical probe system and data-reduction method. *FRED* is a nonsequential ray-trace package that provides synthetic probe images for an assumed plasma density

profile. The full diagnostic system was simulated in *FRED*. An analytic plasma density profile was used in the optical model to create a synthetic AFR image. This image was post-processed and the resulting plasma density profile was compared to the original to extract the error. The standard deviation of the error in a pixel-by-pixel comparison of the two profiles was 12.2%. Adding this to the error in calibration gives a total error in the plasma density calculation of $\pm 14.2\%$.

It is important to register the AFR images with respect to the original position of the target surface, especially for comparing to hydrodynamic simulations. For this purpose a background shot (without the drive beams) is taken to produce a shadow of the target onto the CCD by removing the angular filter. The front surface of the target is determined by measuring the position of an alignment fiber (80- μm diameter) that is attached to the middle of the flat target on the rear surface. In this manner, any difficulty in clearly observing the front surface, which extends about a millimeter beyond the object plane, is mitigated. The fiber tip resides at TCC and is imaged sharply. With prior knowledge of the separation between the fiber tip and the front surface of the target, the position of the original surface is accurately determined within $\pm 10\ \mu\text{m}$, near the resolution limit of the diagnostic. For spherical targets, the surface is sharply imaged and therefore directly observed without a fiducial.

The timing of the optical probe is measured with respect to the ultraviolet drive laser beams by comparison to a timing fiducial used to synchronize all laser beams on OMEGA EP. A small portion of each beam is picked off upstream of TCC and measured on a UV streak camera to compare to the fiducial on shot. The absolute calibration of the distance between these timing diagnostic signals and TCC is measured periodically with a time-resolved x-ray target diagnostic, also referenced to the facility timing fiducial. Multiple calibrations measured over several months have shown a scattering of ± 20 ps. This error is taken into account when comparing to *DRACO* simulations by using two time steps and shading the area between $t_0 - 20$ ps and $t_0 + 20$ ps, where t_0 is the measured experimental timing of the optical probe.

REFERENCES

1. National Research Council (U.S.) Committee on High Energy Density Plasma Physics, *Frontiers in High Energy Density Physics: The X-Games of Contemporary Science* (The National Academies Press, Washington, DC, 2003).
2. P. Michel *et al.*, *Phys. Plasmas* **20**, 056308 (2013).

3. W. L. Kruer, in *The Physics of Laser Plasma Interactions*, Frontiers in Physics, Vol. 73, edited by D. Pines (Westview Press, Boulder, CO, 2003).
4. M. V. Goldman, *Ann. Phys.* **38**, 117 (1966).
5. S. Fujioka *et al.*, *Rev. Sci. Instrum.* **73**, 2588 (2002).
6. S. H. Glenzer, G. Gregori, F. J. Rogers, D. H. Froula, S. W. Pollaine, R. S. Wallace, and O. L. Landen, *Phys. Plasmas* **10**, 2433 (2003).
7. I. H. Hutchinson, *Principles of Plasma Diagnostics*, 2nd ed. (Cambridge University Press, Cambridge, England, 2002).
8. G. S. Settles, *Schlieren and Shadowgraph Techniques: Visualizing Phenomena in Transparent Media* (Springer, Berlin, 2001).
9. R. S. Craxton, F. S. Turner, R. Hoefen, C. Darrow, E. F. Gabl, and Gar. E. Busch, *Phys. Fluids B* **5**, 4419 (1993).
10. J. Ruiz-Camacho, F. N. Beg, and P. Lee, *J. Phys. D: Appl. Phys.* **40**, 2026 (2007).
11. D. Ress *et al.*, *Science* **265**, 514 (1994).
12. M. T. Carnell and D. C. Emmony, *Opt. Laser Technol.* **26**, 385 (1994).
13. D. Estruch *et al.*, *Rev. Sci. Instrum.* **79**, 126108 (2008).
14. D. Ress *et al.*, *Phys. Fluids B* **2**, 2448 (1990).
15. D. Haberberger, S. Ivancic, M. Barczys, R. Boni, and D. H. Froula, in *CLEO: Applications and Technology*, CLEO 2013: Technical Digest (Optical Society of America, Washington, DC, 2013), Paper ATu3M.3.
16. U. Kogelschatz and W. R. Schneider, *Appl. Opt.* **11**, 1822 (1972).
17. D. H. Froula, R. Boni, M. Bedzyk, R. S. Craxton, F. Ehrne, S. Ivancic, R. Jungquist, M. J. Shoup, W. Theobald, D. Weiner, N. L. Kugland, and M. C. Rushford, *Rev. Sci. Instrum.* **83**, 10E523 (2012).
18. J. H. Kelly, L. J. Waxer, V. Bagnoud, I. A. Begishev, J. Bromage, B. E. Kruschwitz, T. J. Kessler, S. J. Loucks, D. N. Maywar, R. L. McCrory, D. D. Meyerhofer, S. F. B. Morse, J. B. Oliver, A. L. Rigatti, A. W. Schmid, C. Stoeckl, S. Dalton, L. Folsbee, M. J. Guardalben, R. Jungquist, J. Puth, M. J. Shoup III, D. Weiner, and J. D. Zuegel, *J. Phys. IV France* **133**, 75 (2006).
19. J. W. Goodman, *Introduction to Fourier Optics*, 3rd ed. (Roberts and Company Publishers, Englewood, CO, 2005).
20. J. T. Verdeyen, *Laser Electronics*, 3rd ed. (Prentice-Hall, Englewood Cliffs, NJ, 1995).
21. T. J. Kessler, Y. Lin, J. J. Armstrong, and B. Velazquez, in *Laser Coherence Control: Technology and Applications*, edited by H. T. Powell and T. J. Kessler (SPIE, Bellingham, WA, 1993), Vol. 1870, pp. 95–104.
22. W. Seka, R. S. Craxton, R. E. Bahr, D. L. Brown, D. K. Bradley, P. A. Jaanimagi, B. Yaakobi, and R. Epstein, *Phys. Fluids B* **4**, 432 (1992).
23. D. Keller, T. J. B. Collins, J. A. Delettrez, P. W. McKenty, P. B. Radha, B. Whitney, and G. A. Moses, *Bull. Am. Phys. Soc.* **44**, 37 (1999).
24. P. B. Radha, T. J. B. Collins, J. A. Delettrez, Y. Elbaz, R. Epstein, V. Yu. Glebov, V. N. Goncharov, R. L. Keck, J. P. Knauer, J. A. Marozas, F. J. Marshall, R. L. McCrory, P. W. McKenty, D. D. Meyerhofer, S. P. Regan, T. C. Sangster, W. Seka, D. Shvarts, S. Skupsky, Y. Srebro, and C. Stoeckl, *Phys. Plasmas* **12**, 056307 (2005).
25. R. C. Malone, R. L. McCrory, and R. L. Morse, *Phys. Rev. Lett.* **34**, 721 (1975).
26. S. Atzeni and J. Meyer-ter-Vehn, *The Physics of Inertial Fusion: Beam Plasma Interaction, Hydrodynamics, Hot Dense Matter*, International Series of Monographs on Physics (Clarendon Press, Oxford, 2004).
27. Photon Engineering, LLC, Tucson, AZ 85711.

Multibeam Laser–Plasma Interactions in Inertial Confinement Fusion

Introduction

Of the many challenges facing laser-driven inertial confinement fusion (ICF),^{1,2} controlling the impact of laser–plasma interactions (LPI’s) is one of the most difficult and uncertain.³ The importance of LPI’s in indirect-drive–ignition experiments at the National Ignition Facility (NIF) is now widely appreciated because of the dramatic impact of instabilities on the capsule implosion symmetry.^{4,5} Perhaps less well known are the effects in the alternative direct-drive approach.⁶ This article highlights some of the discoveries and recent advances in understanding these instabilities—the most important of which is the realization that the collective interaction of multiple beams is ubiquitous throughout laser fusion.

It is important to understand the instabilities resulting from intense LPI’s in ICF because they place bounds on the available ignition regimes/design space. For example, higher radiation temperatures in indirect drive or higher ablation pressures in direct drive, minimize hydrodynamic instabilities and improve target performance, but they require higher laser intensities, which are more vulnerable to instability.⁷ Instabilities involving the cooperation between multiple laser beams are particularly dangerous because their onset can occur at intensities significantly below that of non-cooperative, i.e., single-beam, interactions. The mitigation of multibeam instabilities is therefore of great importance to the success of ICF.

Laser–plasma instabilities are fundamentally difficult to understand and predict because they involve a severe coupling of spatial and temporal scales. Large-scale plasma hydrodynamics are evolved with radiation–hydrodynamics codes (e.g., *LASNEX*⁸ or *DRACO*⁹) over spatial regions that are millimeters in extent and over times that span tens of nanoseconds. On the other hand, LPI’s involve the coherent interaction between waves that have high characteristic frequencies ($\sim 10^{15}$ s⁻¹) and short wavelengths (~ 0.1 μ m). The plasma conditions and laser irradiation determine the conditions under which LPI’s can grow,¹⁰ but the instabilities, in turn, modify the hydrodynamics by redirecting the laser light,¹¹ modifying absorption, or producing hot electrons. The only practical approach to

addressing these problems is by developing simplified models that can be run self-consistently in the hydrodynamics codes (for examples of such “in-line” models, see **SBS-Mediated CBET in ICF Experiments**, p. 63).

The difficulties of multiple scales exist even in numerical models of LPI’s that do not attempt to describe large-scale hydrodynamic evolution. Explicit particle-in-cell (PIC) codes,^{12,13} such as *OSIRIS*¹⁴ and *VPIC*,¹⁵ are highly detailed plasma-kinetic models that make few simplifying assumptions regarding the plasma response; however, they are too expensive to run in three dimensions for scale lengths and times of relevance for ignition conditions (the advent of petascale computing may change this in the future). These problems have been partially addressed by the development of reduced models that exploit temporal and/or spatial enveloping (multiple scales)¹⁶ and either ignore the particle kinetics (i.e., plasma-fluid codes) or treat the kinetics in a simplified way (e.g., the codes *pF3D*,¹⁷ *Harmony*,¹⁸ and *ZAK3D*.^{19,20} Several examples of the application of these models will be described in this article.

The above comments apply to single-beam interactions as well as to situations involving the cooperative interaction between multiple laser beams. The importance of multibeam interactions places a much-greater emphasis on the three-dimensional (3-D) geometry than before and requires numerical simulations to be more “realistic.” This article will review recent advances in this regard.

The following sections (1) introduce LPI’s in laser fusion, describing the two major approaches and discussing the similarities and differences with respect to LPI conditions; (2) describe three-wave parametric instabilities, focusing on the interaction of instabilities occurring in different beams; (3) introduce cross-beam energy transfer (CBET), describing the effect and reviewing the experimental impact in both direct- and indirect-drive experiments; (4) describe multibeam stimulated Raman scattering and two-plasmon decay; (5) describe strategies that have been designed to mitigate multibeam instabilities; and, finally, (6) present our summary and conclusions.

Two Approaches to Laser Fusion at the National Ignition Facility

There are two primary approaches to laser-driven ICF: indirect drive, where the laser energy is first converted to x rays in a hohlraum (Fig. 137.48) that subsequently drives the target,²¹ and direct drive, where the laser light deposits its energy directly onto the capsule (Fig. 137.49).

A major effort^{22,23} is underway to demonstrate indirect-drive ignition on the NIF.²⁴ Since the NIF beamlines are not configured for spherically symmetric direct drive, LLE has developed the polar-drive (PD) concept.²⁵ This concept makes it possible to explore direct-drive ignition on the NIF while the beamlines are in the indirect-drive configuration.

LLE's Omega Laser Facility^{26–28} performs direct-drive ICF research in both the favored spherically symmetric and polar-drive configurations at relatively modest driver energies with the goal of validating designs that, when scaled to the NIF, would show ignition and gain (i.e., hydro-equivalent designs).²⁹ Recent progress has led to a series of PD designs that are predicted to marginally ignite on the NIF,³⁰ provided LPI's at the NIF scale do not present new challenges.

1. Indirect Drive

The NIF is currently configured for the polar illumination that is required for indirect-drive experiments. The individual 192 beams are clustered into groups of four (called quadruplets, or “quads”) that share a common entrance port on the target chamber. At each pole of the target chamber the quads are grouped into two cones. There are eight quads in each inner cone and 16 in the outer cones. With this arrangement one-third of the laser energy is in the inner cones that preferentially drive the waist (or equator) of the capsule, while the remaining two-thirds of the energy preferentially drives the polar regions of the indirect-drive target/capsule. Figure 137.48 shows this arrangement, together with the specific beam angles.

The cylindrical NIF hohlraum (Fig. 137.48) is ~10 mm long and slightly more than 5 mm in diameter. The laser beams enter through two laser entrance holes (LEH's), one at each end, propagate through the gas-filled interior, and deposit their energy at the high-Z hohlraum walls, generating soft x-ray radiation. These x rays drive the implosion of the capsule that is suspended in the hohlraum. By design, the beam pointing and dynamically varying relative power between the two cones of beams are chosen so that the x-ray drive, as seen by the cap-

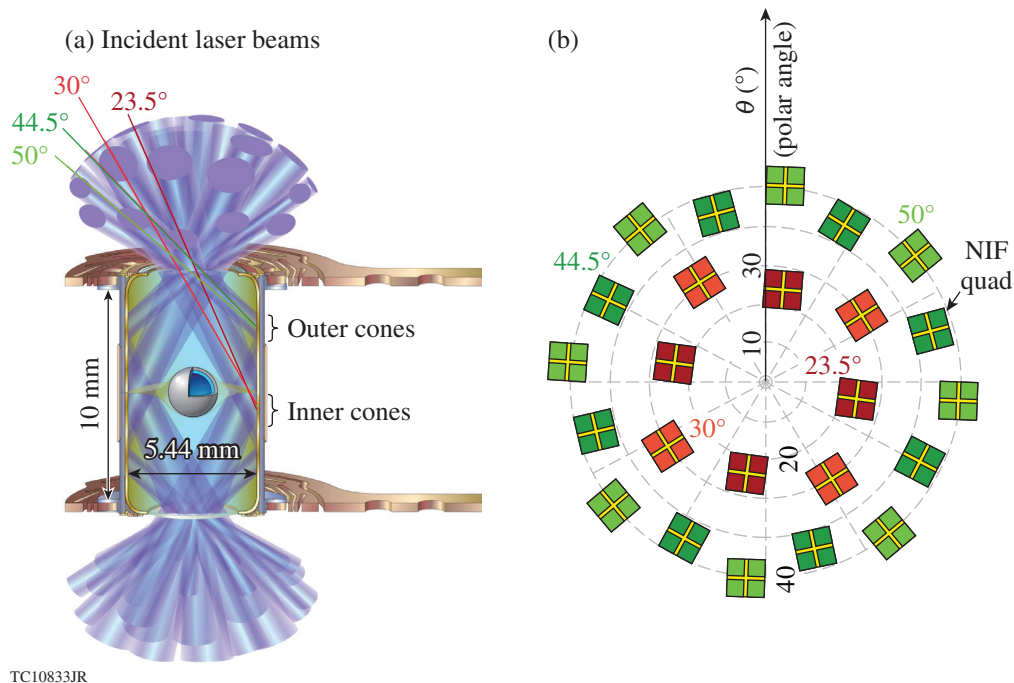


Figure 137.48

(a) A schematic of a NIF ignition hohlraum with the approximate dimensions, showing the inner and outer beam cones entering the hohlraum through the two laser entrance holes. (b) The specific angles of the NIF beam quads, which are color coded: inner quads orange ($\theta = 30^\circ$) and red ($\theta = 23.5^\circ$), and outer quads light ($\theta = 50^\circ$) and dark green ($\theta = 44.5^\circ$), where θ is the polar angle.

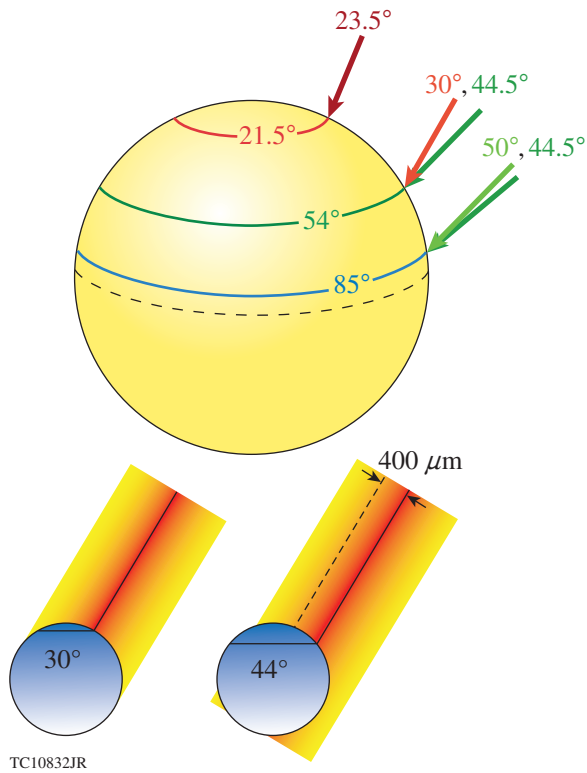


Figure 137.49
 Polar drive on the NIF is achieved by repointing the NIF beams to compensate for the lack of beams at the equator (Fig. 137.48). The repointing is greatest for beams in the outer cone (having angles of 44.5° and 50°) to provide sufficient drive on the equator of the target (dashed line).

sule, is uniform (to within 1% time averaged).³¹ The cryogenic ignition hohlraum is filled with a low-density helium gas fill that is quickly ionized and becomes a high-temperature, low-density plasma. Its purpose is to retard the inward expansion of the gold hohlraum walls as they are heated.

As will be described in **Cross-Beam Energy Transfer** (p. 63), the frequencies (or, equivalently, the wavelengths) of the NIF quads may be shifted with respect to one another. The two-color separation on the NIF consists of shifting the wavelength of the outer cone of beams with respect to that of the inner cones by $\sim \Delta\lambda = 0$ to 8 \AA (at $1\omega_0$). A three-color option also exists, where there are two tunable wavelength separations: (1) the separation between the frequency of the outer cones and the inner 30° quads; and (2) the separation between the inner 30° quad and the inner 23.5° quad.^{11,32}

2. Polar Drive

The NIF was designed so that an option remains for imploding spherically symmetric direct-drive-ignition targets.³¹ In direct drive, the laser beams illuminate and implode the

target directly without the intermediate step of converting to x rays. As a result, direct drive is predicted to couple $7\times$ to $9\times$ more energy to the compressed capsule than indirect drive.³³ Because reconfiguration of the NIF beam architecture is very invasive, the PD scheme was conceived so that directly driven experiments can be performed while the NIF remains in the indirect-drive configuration.²⁵

Polar-drive-ignition designs rely on repointing the NIF beams (Fig. 137.48) toward the equator of the target (Fig. 137.49) by using different pulse shapes for different rings of the NIF configuration and using specialized phase plates to achieve sufficient implosion symmetry in the absence of equatorial beams. Accurate modeling of oblique-beam energy deposition, the effect of beam obliquity on LPI's in the underdense corona, and heat transport to the ablation surface are critical to achieving sufficient symmetry, implosion velocity, and shell adiabat.^{6,30}

3. Comparison of LPI Between Indirect-Drive and Polar-Drive Schemes

Figure 137.50(a) shows a contour plot of the coronal electron plasma density (normalized to the critical density) for an ignition-scale direct-drive target, with the approximate dimensions indicated. Sample ray trajectories, approximately corresponding to three cones of beams, are overlaid. For comparison, a NIF-scale indirect-drive hohlraum is shown in Fig. 137.50(b). Again, the electron plasma density is shown with the laser-beam trajectories overlaid. The two figures are not shown on the same scale.

The plasma conditions differ quite significantly between the two cases. The plasma density scale length for the direct-drive target is $L_n \sim 500$ to $600 \mu\text{m}$ (the density decreasing with radius r), the coronal electron temperature is approximately isothermal with $T_e = 3$ to 4 keV , and the baseline design uses a CH ablator. The plasma-flow velocity is directed radially outward, increasing with radius. The Mach-1 surface is located at a radius where the electron plasma density n_e is approximately one quarter of the critical density $n_e(r) \approx n_c/4$ (the quarter-critical surface), where $n_c = m_e \omega_0^2 / (4\pi e^2)$ is the density at which electromagnetic (EM) waves of frequency ω_0 are reflected (see Fig. 137.50).³ The quantities e and m_e are the electron charge and mass, respectively. This is to be contrasted with the indirect-drive hohlraum. The plasma density inside the hohlraum is more homogeneous ($L_n \sim \text{mm}$'s) and the plasma flow structure is quite complicated, with the Mach-1 surface falling just outside the LEH's. [The LEH has been shown to act like a sonic nozzle (in analogy with gas dynamics) so the flow external to the nozzle is quite insensitive to changes within the

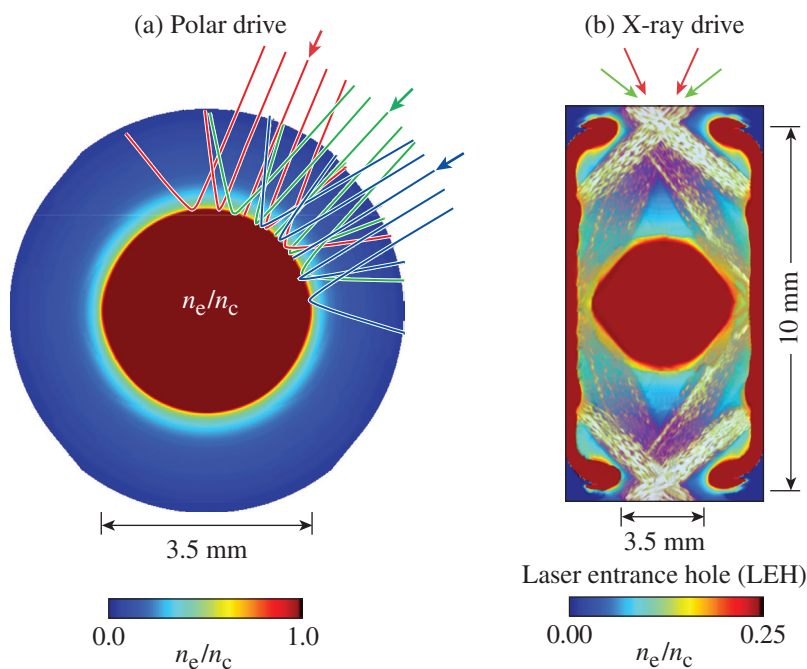


Figure 137.50

(a) In direct-drive targets, multiple laser beams overlap everywhere in the underdense corona over a wide range of angles (rays corresponding to three representative beams are shown). (b) In indirect-drive targets, multiple beams overlap in the neighborhood of the laser entrance holes with a limited number of angles. The color bars indicate the electron plasma density normalized to the critical density (note the different density scales on the left and right).

hohlraum.^{34]} The electron temperature is $T_e = 2$ to 4 keV and is highest in the beam-overlap region near the LEH. The laser light interacts with a mixture of different materials: the He (or He/H) gas that fills the hohlraum, Au plasma ablated from the hohlraum walls, and CH plasma ablated from the target.

The laser-beam intensities are quite different between the two schemes. In indirect drive, the single-beam intensities are nominally 1×10^{15} W/cm² for the outer cone quads and 0.5×10^{15} for the inner cone at the LEH, while in direct drive, the single-beam intensities are lower: $\sim 1 \times 10^{14}$ W/cm². The differences in laser intensity are determined by design considerations. In indirect drive, the LEH's through which the beams propagate must be as small as possible since the area of the LEH is a sink for x rays. This requires small beam spots and high beam intensities. In direct drive, the beam spots should be as large as possible, to maximize beam overlap to ensure drive uniformity, leading to lower single-beam intensities.

The gains for LPI's that are driven by single-beam interaction can be computed by ray-based methods.^{35,36} For indirect drive, the largest single-beam gains correspond to stimulated Raman scattering (SRS) on the inner cone of beams deep inside the hohlraum and to stimulated Brillouin scattering (SBS) from the outer beam cones near the hohlraum wall.³⁷ For direct-drive designs, the single-beam gains/thresholds are not generally exceeded—a result of the lower beam intensities and the shorter plasma scale lengths relative to indirect drive.

In both approaches, there are ample opportunities for multibeam instabilities. In indirect drive, all beams from one side must overlap to get through the LEH, and the two rings of the inner cone overlap well into the hohlraum's interior. In direct drive, beams overlap everywhere in the underdense corona with a wide range of crossing angles. An understanding of the degree to which different beams can become cooperatively unstable with respect to LPI's is now realized to be crucial.

Three-Wave Interactions

Unmagnetized plasmas support EM waves, electron plasma waves (EPW's), and ion-acoustic waves (IAW's).³ The incident laser light is the source of large-amplitude EM waves. The quadratic nonlinearities associated with the plasma response, in the coronal or hohlraum plasma, result in the coupling between a given EM wave and the other linear waves supported by the plasma. As will become evident later, interactions that involve the coupling of three waves are seen as the most important for current ignition experiments.

A parametric instability involving three waves is possible when the frequency- and wave-number-matching conditions are satisfied:

$$\omega_0 = \omega_1 + \omega_2, \quad (1)$$

$$\vec{k}_0 = \vec{k}_1 + \vec{k}_2, \quad (2)$$

where ω_i and \vec{k}_i ($i = 0,1,2$) are the frequencies and wave numbers satisfying the dispersion relation for the i th wave. Typically, wave “0” represents the large-amplitude (pump) wave that drives the instability, while waves “1” and “2” are the decay (or daughter) waves.

The particular form of instability for coherent waves satisfying the matching conditions [Eqs. (1) and (2)] can be determined by solving the canonical coupled-mode equations.^{38,39} Schematically, these are

$$L_0 A_0 = i\gamma_0 A_1 A_2, \quad (3)$$

$$L_1 A_1 = i\gamma_1 A_0 A_2^*, \quad (4)$$

$$L_2 A_2 = i\gamma_2 A_0 A_1^*, \quad (5)$$

where L_i represents the linear propagator for wave i , A_i is the corresponding wave action (related to the wave amplitude), and the γ 's are the coupling constants that depend on the wave type.³⁹ Instability, if present (i.e., wave growth is sufficient to overcome the effective dissipation or damping), can be either absolute or convective. Absolute instability corresponds to unstable eigenmodes that grow temporally, while convective instability is limited to spatial amplification.^{40–42} The effects of plasma inhomogeneity, or deviation from exact resonance, result in the appearance of phase factors on the right-hand side of Eqs. (3)–(5). Plasma inhomogeneity, which is always present experimentally (see Fig. 137.50), introduces a threshold condition on the intensity of the pump wave. Absolutely unstable couplings can become convective in its presence. The expression for Rosenbluth gain⁴³ is the most well-known:

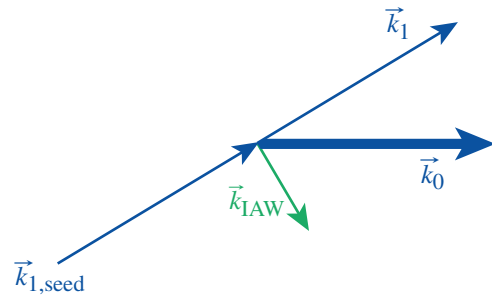
$$A_1 = A_{1,\text{seed}} \exp(G), \text{ where } G = \frac{2\pi\gamma^2}{|\kappa' V_{g,1} V_{g,2}|}, \quad (6)$$

which describes the finite amplification of wave amplitudes arising from wave convection out of the region where the three waves are resonantly matched [i.e., where Eqs. (1) and (2) are satisfied]. The gain exponent G depends on the square of the homogeneous temporal growth rate γ , the spatial derivative of the phase mismatch $\kappa' = \partial/\partial x (\vec{k}_0 - \vec{k}_1 - \vec{k}_2)$, where x is the direction of the inhomogeneity, and the group velocities of the two daughter waves, $V_{g,i}$. If the gain is large enough, the seed large enough, or the instability absolute, it will no longer be possible to neglect nonlinear effects such as particle trapping, nonlinear frequency shifts, harmonic generation, etc., which are not described by Eqs. (4) and (5). In this case, one must

often resort to numerical calculations of the type discussed in **Numerical Investigations of Multibeam TPD** (p. 72).

The following possibilities are specific to the case where the primary wave (0) is a large-amplitude EM wave: SBS results when the decay waves are EM and ion acoustic; SRS when they are EM and electron plasma waves; and two-plasmon decay (TPD) when both decay waves are EPW's. The decay into an EPW and an IAW can occur, but it is not seen to be important, while decay into two EM waves or two IAW's is not possible.

There are several ways in which multiple beams can cooperate to produce instability of the above types. Daughter waves can be shared between decays occurring in different beams⁴⁴ or instability can be seeded (or induced) because one of the daughter waves is present, either in the laser drive or as a result of decays occurring elsewhere in the plasma (see Fig. 137.51).⁴⁵ In this way, rescatter and multibeam amplification of backscatter can occur.⁴⁶ When daughter waves can be shared, the growth rates (or convective gains) can be expected to depend on the combined EM wave intensities.⁴⁴



TC11003JR

Figure 137.51

Wave-vector diagram for cross-beam energy transfer. The decay of the pump electromagnetic (EM) wave (with wave vector \vec{k}_0) into an ion-acoustic wave (\vec{k}_{IAW}) and a scattered-light wave (\vec{k}_1) is induced because the light wave $\vec{k}_{1,\text{seed}}$ is already present at levels greatly exceeding the thermal noise.

Although filamentation has been a concern, particularly for indirect drive, and important work has been done to understand filamentation driven by multiple beams^{47,48} and the related effect of beam bending,^{49,50} which was experimentally confirmed,⁵¹ it will not be described here.

Cross-beam (or multibeam) interactions in plasmas and their potential uses have quite a long history. Examples include the beat-wave generation of EPW's⁵² or IAW's⁵³ by crossing EM beams, or four-wave mixing and phase conjugation.^{53,54} More

recently there has been great interest in the use of cross-beam interactions to achieve laser-pulse compression⁵⁵ or Raman amplification.^{46,56,57} These topics are beyond the scope of this article and will not be discussed nor will many other subscale experiments or theory that were performed under conditions that are not directly relevant to ICF ignition. The recent review articles by Kirkwood^{46,58} address these.

Cross-Beam Energy Transfer

1. Description of the Mechanism

Cross-beam energy transfer (CBET) can be thought of as an induced SBS process,⁴⁵ occurring when multiple EM waves of similar (or equal) frequencies overlap in a plasma. This can be understood most simply for the case of two crossing plane EM waves (“beams”) of frequencies ω_0 , ω_1 and wave vectors \vec{k}_0 , \vec{k}_1 , respectively (Fig. 137.51). Therefore, with reference to Eq. (2), both wave vectors \vec{k}_0 and \vec{k}_1 are EM waves (defined by the illumination geometry), while $\vec{k}_2 \equiv \vec{k}_{IAW}$ is the wave vector of an IAW defined by $\vec{k}_{IAW} = \vec{k}_0 - \vec{k}_1$.

The frequencies (or, equivalently, wavelengths) of the overlapping EM beams (i.e., ω_0 and ω_1) control the proximity of the plasma response at the frequency $\omega_0 - \omega_1$ to the ion-acoustic resonance ω_2 ,

$$\omega_0 - \omega_1 = \omega_2 \equiv \omega_{IAW} = \pm c_s \left| \vec{k}_{IAW} \right| + \vec{v} \cdot \vec{k}_{IAW}. \quad (7)$$

Here c_s is the ion-acoustic speed and \vec{v} is the plasma (hydrodynamic) flow velocity. At (or near) resonance, the system [Eqs. (3)–(5)] becomes parametrically unstable (convectively), and substantial power can be transferred from the higher-frequency EM wave to the lower-frequency wave (where “higher” and “lower” refers to the frequencies determined in the reference frame where the plasma flow velocity vanishes). Energy transfer can occur if both laser beams have the same frequency (wavelength) in the presence of a Mach-1 flow ($|\vec{v}| \sim c_s$) aligned with \vec{k}_{IAW} .

Interest arising from indirect-drive ICF (see the next subsection) stimulated a great deal of both theoretical/numerical^{34,45,59–63} and experimental^{64–72} activity in CBET starting in the mid-90s. Experiments were performed for frequency-mismatched beams^{67,73} and equal-frequency beams.^{65,68,69,72,74,75}

2. SBS-Mediated CBET in ICF Experiments

The potential importance of induced SBS (CBET) was recognized early in both indirect- and direct-drive approaches to ICF. Haan’s paper in 1995 (Ref. 31) cites forward SBS resulting in energy transfer between the NIF beam cones (Fig. 137.48) as a concern for indirect drive. At the time, the baseline pro-

posal for indirect drive on the NIF incorporated a four-color scheme that was proposed as an option for the control of LPI’s occurring in the hohlraum.³¹ Kruer showed theoretically that the intensity and frequency separation of the beams in this baseline proposal were such that ion waves could be driven resonantly, causing a significant energy transfer among the beams.⁴⁵ Kruer’s calculations highlighted the effectiveness of detuning by wavelength shifting the NIF beams and determined that nonlinear effects would not play a strong role in limiting energy transfer for the parameters of interest. The ability to induce a wavelength shift between the two beam cones was implemented on the NIF, specifically to reduce vulnerability of the NIF point design to this energy transfer.^{34,76,77} In practice, the frequency shift was applied to the outer cones, resulting in a “two-color” capability that could be used to prevent unwanted changes to the illumination symmetry caused by CBET. The frequency shifts were chosen to be sufficient to prevent IAW resonances inside the beam-crossing volume (see **Indirect Drive**, p. 59 and Fig. 137.50).

In the context of direct drive, Randall *et al.*⁷⁸ showed that unabsorbed light reflected from the critical surface could act as an EM seed to induce SBS in the corona. The importance of cross-beam interactions in direct-drive implosions on OMEGA was first investigated experimentally by Seka,⁷⁹ and numerical investigations of these experiments were performed in two dimensions using the paraxial *pF3D* code⁸⁰ and a non-paraxial model.⁸¹ It was not possible to make more-general 3-D numerical calculations of the kind made for indirect drive (and described later in **CBET in Indirect Drive on the NIF**, p. 64)^{76,77} because the complex beam geometries precluded the use of the paraxial approximation for the crossing beams.

A detailed spectroscopic analysis of the scattered light in spherical implosion experiments was performed on OMEGA, and the spectral shifts were compared with the expected Dewandre shift,⁸² arising from the time-varying optical path, based on *LILAC*⁸³ predictions for the hydrodynamic profiles assuming collisional absorption³ of the laser light alone.⁸⁴ This provided experimental evidence of the CBET effect in spherical implosion experiments.^{84–87} The spectroscopy helped guide the development of a ray-based model of CBET that generalized Randall’s earlier analysis to the complex illumination geometry present in direct-drive experiments (Fig. 137.50).^{84–87} The model solves the coupled-mode equations [Eqs. (3)–(5)] pairwise along rays, making use of the strong damping approximation for the IAW, which is physically motivated and makes the model practical to implement. Reference 35 gives a detailed description of ray-based calculations in indirect drive.

CBET has turned out to be of major significance in ICF experiments over the past few years, both in direct- and indirect-drive geometries. Because of differences in the drive (**Comparison of LPI Between Indirect-Drive and Polar-Drive Schemes**, p. 60), its behavior is somewhat different in each case and is described separately below.

a. CBET in direct drive. When a detailed ray-based CBET model was self-consistently incorporated into one-dimensional (1-D) radiation-hydrodynamics calculations (*LILAC*⁸³), its impact on target performance for spherically symmetric implosions could be computed and compared with OMEGA experimental data.^{88,89}

It was realized that, in direct drive, CBET preferentially transfers energy from the central portion of each laser beam to the outer portions (or “wings”).^{85,90} Light rays in the wings of each beam, with large impact parameters, are not well absorbed and turn at densities below critical³ (e.g., the purple ray in Fig. 137.52). On their outward trajectory, after turning, these rays cross incoming rays (e.g., the blue ray in Fig. 137.52), where they provide an enhanced EM seed for SBS side- or backscatter (Fig. 137.51). Since the hydrodynamic flow velocity is directed radially outward in the underdense corona, the outgoing rays are red shifted relative to the incoming rays in the frame where the plasma is locally at rest. If all beams have the same frequency in the lab frame, the energy transfer is directed from the incoming rays to the outgoing rays (shown schematically by the green arrow in Fig. 137.52). This represents a loss in laser coupling. The process becomes resonant near the Mach-1 surface, for equal-frequency beams (in the lab frame) [Eq. (7)], although the gains are small because of the strong radial gradients in flow velocity [large κ' in Eq. (6)]. The EM seed provided by the reflected light is very large relative to thermal fluctuation levels, so even small gains can have a significant effect on the absorbed energy.

The best agreement between 1-D *LILAC* calculations and measured absorption and scattered-light spectra was obtained for OMEGA spherical implosions when the CBET model was used in conjunction with nonlocal thermal transport.^{88,89,91} Figure 137.53 compares the (a) measured and the calculated implosion trajectory with (b) the scattered power for a spherical implosion on OMEGA (shot 63912).

The implosion trajectory (defined as the radius of the ablation surface as a function of time), which is a gauge of the hydrodynamic efficiency of the target, is inferred from x-ray self-emission images,⁹² while the time-dependent laser

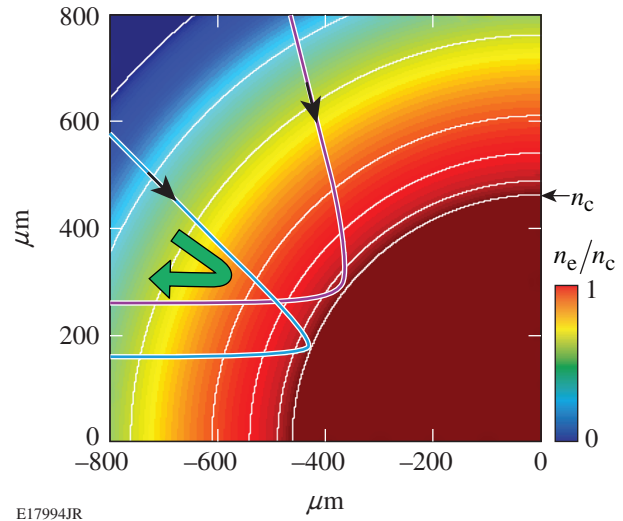


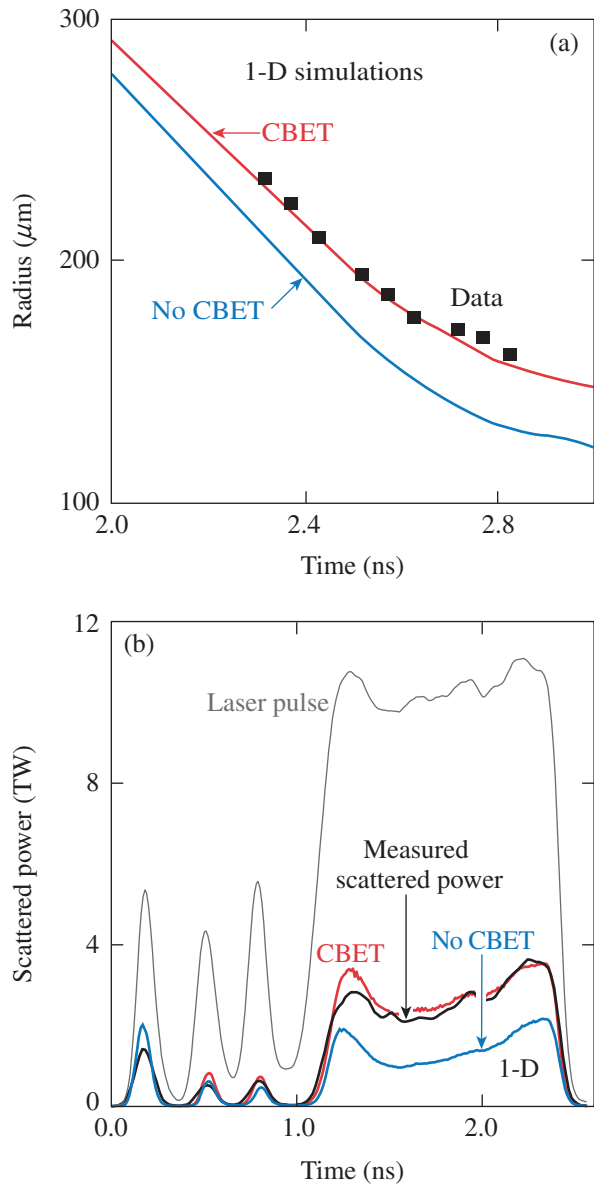
Figure 137.52

The coronal electron density n_e , normalized to the critical density n_c , is plotted in one quadrant of an OMEGA-scale spherically symmetric implosion. Two sample ray trajectories (shown as blue and purple lines) serve to illustrate the transfer of beam energy (see text).

absorption fraction and scattered-frequency spectra (not shown) tightly constrain the laser coupling.⁸⁷ Both of these observables are well matched by the 1-D *LILAC* CBET model, while calculations with collisional absorption alone fail to reproduce the results (Fig. 137.53).

These observations led to the conclusion that between 10% to 20% of the laser drive could be lost relative to expectations based on collisional absorption alone. This motivated further work to test the predictions of these models and to search for mitigation strategies.^{89,93} Experiments were performed on OMEGA that demonstrated the expected enhancement in laser coupling in implosions with narrow-beam illumination relative to the target size.^{89,93} The effect of narrowing the beam is to reduce the EM seed (the purple rays in Fig. 137.52) and mitigate the CBET effect. Mitigation strategies are discussed in more detail in **Mitigation of Multibeam Instabilities** (p. 74).

b. CBET in indirect drive on the NIF. The first comprehensive assessment of CBET in indirect drive was made prior to the NIF ignition campaign using a 3-D steady-state paraxial model for the nonlinear interaction between pairs of NIF quads.^{76,77} The energy transfer between the NIF beam cones was calculated by summing the contribution from nearest-neighbor quads in the forward-scattering geometry (a geometry similar to that shown in Fig. 137.51) (this was predicated on the interquad power transfer being small). The nearest-neighbor interaction was greatly simplified because



E21315JR

Figure 137.53

(a) The implosion trajectory for a spherical implosion on OMEGA (shot 63912). The experimentally determined trajectory (solid squares) is compared against two 1-D *LILAC* calculations: collisional absorption of laser light only (blue curve) and the CBET model (red curve). (b) The scattered power as a function of time. The solid black curve is the measured scattered power and the red (blue) curves are the corresponding *LILAC* predictions. The laser pulse shape is shown for reference.

neighboring quads are close in angle ($<14^\circ$) (Fig. 137.48), which permitted a paraxial treatment of the beam propagation (such an approximation is invalid for the direct-drive geometry). (The induced SBS process is forward scattering for indirect drive, unlike the dominant process in spherically symmetric drive where it is predominantly backscatter.) These calculations took

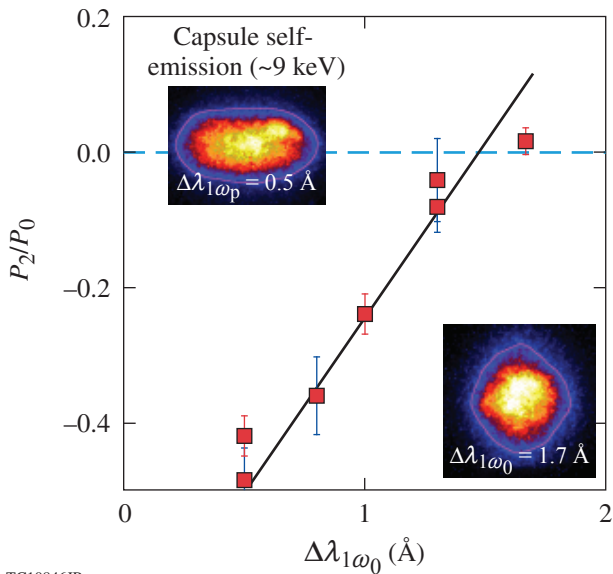
into account the expected hohlraum hydrodynamics conditions (obtained with *LASNEX*⁸) and laser-beam smoothing.^{76,77}

The energy transfer in these calculations reached significant levels ($\geq 15\%$) because of the high laser intensities and the long propagation distances over which the coupling takes place (**Comparison of LPI Between Indirect-Drive and Polar-Drive Schemes**, p. 60), despite the forward SBS coupling being off resonance [Eq. (7) is not satisfied]. (Note: In direct drive, the interaction distance is much shorter but the coupling is resonant.) The ion-wave amplitudes remained small $\delta n/n \approx 10^{-4}$, which justified the neglect of nonlinearity in the IAW response.³⁴

These calculations indicated that the two-color scheme [wavelength shifting of the outer cone relative to the inner cone (**SBS-Mediated Cross-Beam Energy Transfer in ICF Experiments**, p. 63)] could mitigate CBET to a level sufficient to maintain the required implosion symmetry while keeping the coupling in the linear, or small-gain, regime. At the same time, it was foreseen that CBET could be used for symmetry control (by shifting laser power between the beam cones) if the margin for cone balance⁹⁴ on the laser system was limited for some reason.^{76,77}

With the first experiments of the ignition campaign in 2009 (~200-TW “emulator” targets),⁹⁵ it became clear that the NIF cone fraction was unsuitable for creating symmetric implosions. The cone fraction, defined as the ratio of inner-cone energy to the total energy, needed to be 40% to 45% to obtain a round implosion.³² This could not be achieved because the inner beams did not propagate to the hohlraum wall as well as expected,^{4,96} and the cone fractions could not be adjusted to compensate for the loss related to power limitations of the inner cone of beams.

It was experimentally demonstrated that wavelength shifting could be used to compensate for the impaired propagation of the inner beams.⁴ Figure 137.54 shows two snapshots of the capsule x-ray self-emission at the time of peak emission. The pole–equator asymmetry variation is measured by the ratio of the second- to the first-Legendre polynomial coefficients P_2/P_0 in the spherical harmonic expansion of the x-ray flux isocontours from the self-emission images. Note that the hohlraum axis is vertical in these images, as in Fig. 137.48. Figure 137.54 shows that the implosions were oblate ($P_2 < 0$) for small wavelength shifts, P_2/P_0 varied linearly with the wavelength shift, and implosions became round ($P_2 = 0$) at $\Delta\lambda \approx 1.7 \text{ \AA}$ (at $1\omega_0$).



TC10846JR

Figure 137.54

Experimental demonstration of symmetry tuning by cross-beam energy transfer (figure taken from Ref. 4). The second Legendre (P_2) coefficient of the x-ray self-emission contour (purple line on inset figures) increases linearly with wavelength separation between the inner and outer beam cones $\Delta\lambda$, becoming zero (“round”) at $\Delta\lambda = 1.7 \text{ \AA}$ (at $1\omega_0$).

The linear dependence of the P_2/P_0 symmetry with wavelength was predicted by a simpler CBET model that was developed for use in “rapid assessment.”⁹⁶ While this model neglected refraction and the beam speckle structure/smoothing of the earlier paraxial work, the coupling of all quads was calculated simultaneously, i.e., all interquad couplings were computed, including pump depletion. As before, *LASNEX*⁸ (or *HYDRA*⁹⁷) hydrodynamics were used, but the hydrodynamics were not evolved self-consistently (cf., e.g., direct-drive calculations described in **CBET in Direct Drive**, p. 64). These calculations using the linear response of an ion wave to the beat ponderomotive force were in reasonable agreement with the 2009 experiments where NIF was operating at 200 TW of peak laser power with small wavelength shifts ($\Delta\lambda = 1.5$ to 5 \AA at $1\omega_0$), leading to small amounts of transfer. When the NIF reached its design energy (laser powers in the range of 400 to 500 TW), combined with changes to the LEH (CH liners were removed modifying the flow structure), the $\Delta\lambda$ required to achieve good symmetry became very large ($\Delta\lambda = 6$ to 9 \AA at $1\omega_0$) as did the energy transfer.

The successful demonstration of outer- to inner-beam energy transfer for P_2 symmetry control was followed by a demonstration of two successive CBET steps.^{11,32} This involved an additional transfer step between the two rings of quads that

comprise the inner cone (Fig. 137.48), which was accomplished by introducing a second wavelength shift (i.e., three colors).

For the three-color operations on the NIF, the wavelength of the 23.5° quads was placed between that of the outer cone and the 30° inner cone of beams. As before, power was transferred from the outer quads to the inner quads near the LEH (where all quads overlap) to maintain P_2 symmetry. Because of the second frequency shift, the 23.5° quads were higher in frequency compared to the 30° quads and a second transfer (from the 23.5° to the 30.0° quads) occurred deeper in the hohlraum when the outer cones had separated (the separation can be seen in Fig. 137.48).

This redirection of energy toward the 23.5° quad was motivated by experimental evidence that showed a decrease in laser–target coupling as energy was transferred to the inner beams as a result of SRS. This was not unexpected since the inner cones are the most prone to SRS backscatter instabilities (see **Stimulated Raman Scattering in Indirect Drive**, p. 67). However, the loss was specifically identified as resulting from increases in SRS on the 23.5° quads.³² Redirecting energy from the 23.5° quads to the 30° quads (keeping the inner-cone energy constant) before the SRS gain region (p. 67) decreased backscatter and improved the coupling to the target, thereby increasing the radiation drive.^{11,32}

Although the ignition campaign started out in the linear gain regime and the models had a good degree of predictability, it ended with large gains and the linear models were no longer predictive.^{32,98,99} Indeed, the linear calculations fail to reproduce the experimental observables, and usually predict full pump depletion of the outer beams, which has never been observed.^{98,99} To obtain an integrated working model, an *ad hoc* adjustment parameter was applied to the density response: a saturation amplitude of $\delta n/n = 3$ to 4×10^{-4} (Ref. 32). Michel *et al.*^{98,99} have recently shown that stochastic ion heating can occur when multiple laser beams overlap in plasma. The electrostatic field created in response to the ponderomotive force of multiple overlapping beams was shown to transfer energy and momentum to the ions. For typical NIF conditions, it was calculated that such stochastic heating is an important mechanism driving hydrodynamic evolution in the beam-overlap region. The modifications to the ion temperature were predicted to reduce the CBET linear gains by a factor of 4 to 5 over the course of a nanosecond. Such considerations may remove the *ad hoc* density saturation parameter and restore agreement with experimental observations. In this same work, a simplified model of the effect in a form suitable for inline

implementation in hydrocodes was presented (see comments in the **Introduction**, p. 58).

Interactions in Competition with CBET

In laser-driven fusion experiments, CBET occurs before the laser beams have fully deposited their energy in the target (i.e., the walls of the hohlraum in indirect drive or at the critical surface in direct drive).

In indirect drive, CBET occurs in the beam-overlap region near the LEH (as previously described). Gain calculations show that backscattering and filamentation instabilities occur deeper in the hohlraum, outside of the volumes where the beams cross and transfer energy.⁷⁶ SRS in the NIF hohlraum has been identified to occur midway between the LEH and the hohlraum wall along the path of the inner beam cones (Fig. 137.55).³⁷ All potential interactions taking place in the hohlraum's interior are therefore “downstream” of CBET. An understanding of these downstream instabilities should take into account not only the changes in hydrodynamics caused by CBET but also the angular and spatial redistribution of energy within the beams. These problems highlight the complexity of LPI's in general and show how the nonlocal and scale mixing can occur between the macroscopic (hydrodynamic) and microscopic (plasma physics) scales.

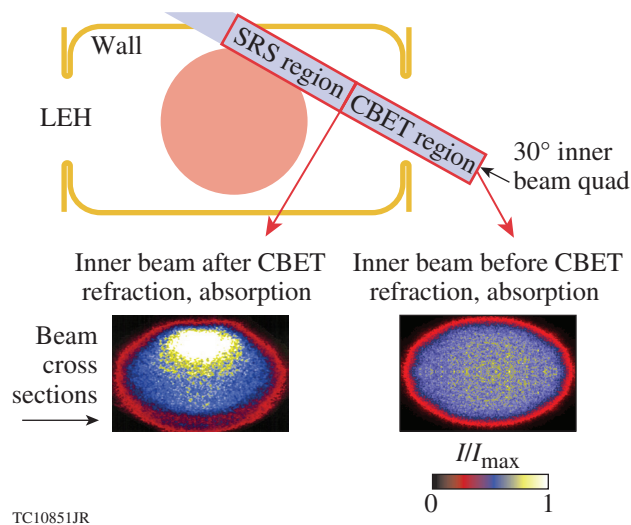


Figure 137.55

A drawing showing the path of a 30° inner-cone quad as it propagates from the LEH to the wall of a NIF hohlraum. The spatial regions where CBET and SRS occur are indicated. The intensity of the quad is shown, in cross section, just before entering the LEH and after propagation through the CBET region. The increase in the quad intensity is not spatially uniform.^{100,101} (Figure taken from Ref. 101.)

Figure 137.55 shows an example of how these problems can be tackled through the sequential combination of multiple numerical models. The intensity of a 30° inner-cone quad is shown, in cross section, both before and after the energy transfer has occurred. CBET distorts the transverse intensity profile of the laser beam and gives rise to an effective shift in pointing.⁷⁷ The propagation from the LEH to the region where SRS occurs, including refraction, absorption, and CBET, has been calculated using a steady-state paraxial model.⁹⁶ When the SRS gain region is reached, the spatially dependent laser intensity is used as input for a second calculation using the code *pF3D*, which is able to compute the SRS coupling (the results of these types of *pF3D* calculation are discussed in the next subsection). Both of these stages assume plasma hydrodynamic profiles calculated using *LASNEX* (or *HYDRA*). The self-consistency between LPI calculations and hydrodynamics calculations was discussed previously in **CBET in Direct Drive** and **CBET in Indirect Drive on the NIF** (p. 64).

Similar arguments are expected to apply in directly driven targets, although the degree of spatial separation between different instability regions is less clear. The correct modeling of CBET is a prerequisite for the understanding of instabilities occurring deeper in the target. The most important of these are considered to be SRS (in indirect drive) and two-plasmon decay (in direct drive).

1. Stimulated Raman Scattering in Indirect Drive

Analyses of SRS prior to the NIF ignition campaign were based mostly on the computation of single-beam gains and beam propagation^{31,35,102} that were tested in subscale OMEGA experiments.^{103,104} The results suggested that tolerable levels of SRS were to be expected. However, SRS from the inner cones of NIF hohlraums was routinely observed during the ignition campaign, with reflectivities of the order of 20% ($E_{\text{SRS}} \geq 100$ kJ) (Ref. 95). As a result, SRS is the primary LPI mechanism responsible for the reduction in energy coupling in the hohlraum.⁹⁵

A spectral analysis of SRS scattered light [diagnosed in a full-aperture backscatter station (FABS) on the 30° inner cone]¹⁰⁵ pointed to lower hohlraum temperatures than predicted, which in part motivated an assessment of the way plasma conditions were calculated. This reassessment led to the implementation of the detailed configuration accounting (DCA)/high-flux (HF) model in hydrodynamic modeling.^{106,107} With the HF model, SRS was predicted to occur halfway between the LEH and the hohlraum wall (Fig. 137.55), where there is still overlap between the inner cones, instead of closer to the wall,

where there is none (as earlier predictions had suggested).¹⁰² This new model removed the gross discrepancies between SRS observations and predictions.³⁷

The modification in plasma conditions, as predicted by the HF model, did not fully explain the SRS spectra from the inner quads. It was noticed that a discrepancy between linear single-beam gains and the observed spectra of SRS light could be improved by combining the intensities of neighboring beams/quads. When the overlap intensity of the 23.5° and 30° quads was included in SRS gain calculations (**Three-Wave Interactions**, p. 61), agreement with the experimental SRS scattered-light spectrum was improved.³⁷ It seems likely that multibeam SRS occurs through the sharing of the EM decay waves where the two inner cones overlap [Fig. 137.56(a)].³⁷

A “proof-of-principle” calculation to test this multibeam effect was performed by simulating the propagation of two³⁷ and three¹⁰¹ overlapping quads using the code *pF3D* (as described above in **Interactions in Competition with CBET**, p. 67). The three overlapped quads used to initialize *pF3D*

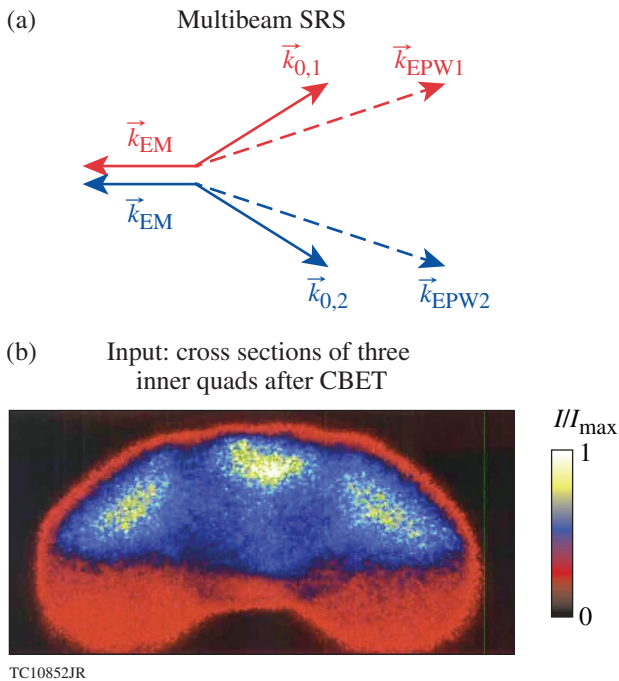


Figure 137.56

(a) A wave-vector decay diagram for SRS occurring in two beams (with wave vectors $\vec{k}_{0,1}$ and $\vec{k}_{0,2}$) that share a common backscattered electromagnetic wave (\vec{k}_{EM}). The two electron plasma waves (\vec{k}_{EPW1} and \vec{k}_{EPW2}) are not shared. (b) Cross sections of the spatial intensity profile of three overlapping NIF inner-cone quads. The sharing of scattered EM waves is possible where there is significant overlap between beams (lower panel was taken from Ref. 101).

calculations of multibeam SRS are shown in Fig. 137.56(b). A 30° quad at the center overlaps with two 23.5° quads (one on either side). The *pF3D* calculations demonstrated that the quads can share a reflected SRS light wave to which they resonantly match through separate electron plasma waves [Fig. 137.56(b)]. Furthermore, multibeam (three-quad) predictions for the SRS reflectivity on the diagnosed 30° quad approached measured values.¹⁰¹

While these results are compelling, *pF3D* is a fluid-based code and it is possible that some discrepancies may be kinetic in origin. It would be interesting to see how multibeam kinetic calculations (e.g., including effects of the type described recently by Chapman *et al.*¹⁰⁸ and Yin *et al.*^{109–111}) affect agreement between multibeam predictions and measurements.

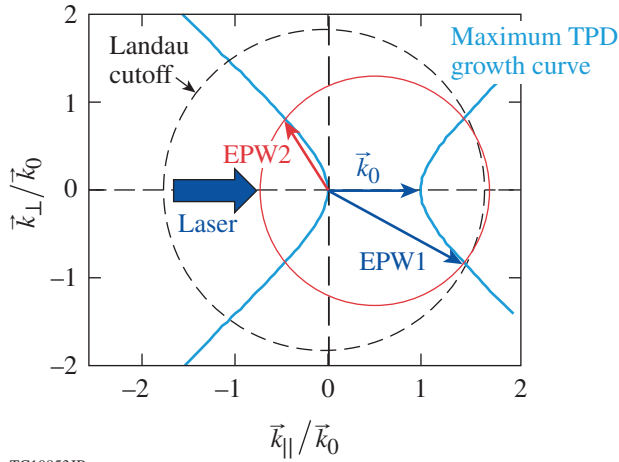
2. Two-Plasmon Decay (TPD) in Directly Driven ICF

TPD has been observed in the blow-down of the LEH windows in indirect drive,¹¹² but it is generally considered to be more important for direct drive,¹¹³ where it is undesirable because of the anomalous absorption of laser light at densities below the critical density and the potential to accelerate electrons to high energies.^{114–118} High-energy electrons can preheat the target and severely degrade performance since efficient implosions require the fuel to remain on a low adiabat.

TPD^{43,119–123} is a three-wave-decay instability in which an EM wave parametrically decays into two longitudinal EPW’s in the neighborhood of the quarter-critical density surface (**Three-Wave Interactions**, p. 61). Its decay diagram is shown schematically in Fig. 137.57 for a single-plane EM wave pump. As described in on p. 61, the three waves satisfy the frequency- and wave-number-matching conditions [Eqs. (1) and (2)]. These conditions, together with the dispersion relations for the EM wave [$\omega_0^2 = \omega_{pe}^2 + c^2 |\vec{k}_0|^2$] and the EPW’s

$$\omega_{EPW1}, \omega_{EPW2} = \pm \omega_{pe}^2 + 3v_{Te}^2 |\vec{k}_{EPW1, EPW2}|^2,$$

where $\omega_{pe} = (4\pi n_e e^2 / m_e)^{1/2}$ is the electron plasma frequency, define the allowable wave vectors for decays at a given density. The decay wave vectors must lie on a sphere centered on $\vec{k}_0/2$, having a radius that is a monotonically decreasing function of the density (shown by the red circle in Fig. 137.57).¹²⁴ This defines the maximum density at which TPD can occur to be slightly below the quarter-critical density. Larger wave-number decays occur at lower densities, but for $|\vec{k}| \lambda_{De} \gtrsim 0.25$, i.e., beyond the Landau cutoff (dashed circle in Fig. 137.57), EPW’s are very heavily Landau damped [$\lambda_{De} \equiv (T_e / 4\pi n_e e^2)^{1/2}$ is the electron Debye length].



TC10853JR

Figure 137.57

A wave-vector decay diagram showing the decay of a single EM plane-wave pump beam of wave vector \vec{k}_0 into two EPW's having wave vectors \vec{k}_{EPW1} and \vec{k}_{EPW2} in the plane of polarization. The maximum growth rate for the instability in homogeneous plasma falls on a hyperbola which is parameterized by the electron plasma density. For a given density, decay wave vectors lie on a circle (red) and the most-unstable modes occur at the intersection of the red circle and the blue hyperbolas. The dashed line is the Landau cutoff $|\vec{k}| = 0.25 k_D$.

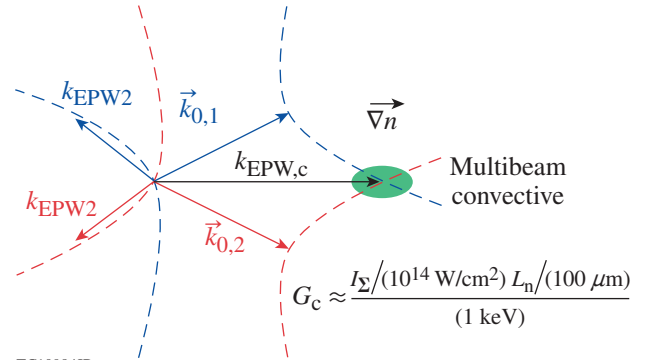
The linear stability of a single-plane EM wave subject to TPD in homogeneous plasma is well known.^{43,119–123,125,126} The temporal growth rate γ_0 for a decay of wave vector \vec{k} (in the absence of EPW damping) is given by

$$\gamma_0 = \frac{\vec{k} \cdot \vec{v}_{\text{osc}}}{4} \frac{[(\vec{k}_0 - \vec{k})^2 - k^2]}{k |\vec{k}_0 - \vec{k}|}, \quad (8)$$

where $\vec{v}_{\text{osc}} = e\vec{E}_0/(\omega_0 m_e)$ is the oscillation velocity of an electron in the electric field of the plane EM wave \vec{E}_0 (Ref. 3). The relation between k_{\parallel} and k_{\perp} (parallel and perpendicular components of \vec{k} with respect to \vec{k}_0) corresponding to maximum growth defines a hyperbola in k space, $k_{\perp}^2 = k_{\parallel}(k_{\parallel} - k_0)$ (shown by the solid blue hyperbolas in Fig. 137.57).

For homogeneous plasma, the square of the multibeam growth rate is the sum of the squares of the single-beam growth rates [Eq. (8)] for all beams (i) that share a common (symmetric) decay EPW ($\gamma^2 = \sum_i \gamma_{0,i}^2$) (Ref. 127). This is a general result for three-wave instabilities.⁴⁴ Figure 137.58 shows how two coherent, equal-frequency beams can share a common daughter EPW. It can be easily seen that the angle between the common wave \vec{k} vector ($\vec{k}_{\text{EPW,c}}$) and the \vec{k} vectors of participating beams ($\vec{k}_{0,1}$ and $\vec{k}_{0,2}$) must be the same. Maximum growth

occurs when the single-beam maximum growth rate curves (the blue and red dashed hyperbolas in Fig. 137.58) intersect. This can occur only at a specific density.¹²⁴



TC10984JR

Figure 137.58

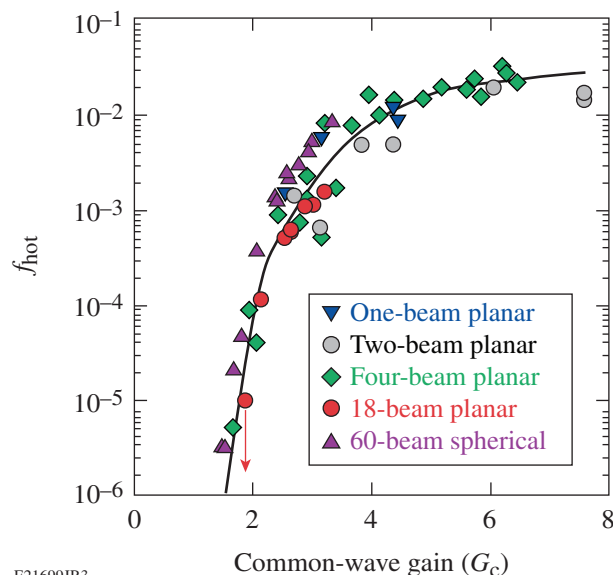
A schematic TPD decay diagram for two overlapping EM waves (having \vec{k} vectors $\vec{k}_{0,1}$ and $\vec{k}_{0,2}$) whose bisector is in the direction of a constant gradient in plasma density $\vec{\nabla}n$. The multibeam homogeneous temporal growth rate is maximized for decays $\vec{k}_{\text{EPW,c}}$ occurring at densities that correspond to the intersection of the individual maximum growth rate curves (red and blue dashed hyperbolas). Since these waves are often associated with large group velocity, a linear analysis predicts convective instability in the presence of the density gradient, and a common-wave gain can be computed.¹²⁷

In plasma with a linear inhomogeneity in the electron plasma density, even the single-beam case is complicated. The linear variation in plasma density can be shown to lead to convective saturation for most decays,¹²⁸ leading to spatial amplification of unstable EPW's by the Rosenbluth gain [i.e., Eq. (6)]. A careful linear stability analysis of small wave-number decays, which are near their turning point (invalidating the Rosenbluth analysis), revealed the presence of absolute instability.^{120,123,125,129} The threshold for the absolute instability was first calculated correctly by Simon *et al.*,¹²³ resulting (for conditions of relevance to direct-drive-ignition experiments) in an absolute threshold below the nominal convective threshold ($G = 2\pi$) (Ref. 128). For a single beam, absolute instability involves small \vec{k} -vector decays and is restricted to a narrow region of densities in the neighborhood of the quarter-critical density. Larger wave-number decays are convectively unstable and occur at lower densities. The very restricted range of purely convective growth means that single-beam TPD is inherently nonlinear.¹³⁰

The linear stability analysis of multibeam TPD in a linearly varying density profile is more complicated, but significant progress has been made recently. The case of convective multibeam decays has been described by computing the expression for the multibeam homogeneous growth rate and applying the

directions, produce the same K_α signal as one beam when the overlapped intensities are equal (similar to 2003). These experiments also demonstrated that four beams produce the same hot electrons as a single beam when the overlapped four-beam intensity is a factor of 2 higher—a result consistent with the expected reduction in growth rate based on common-wave considerations for the polarization of the OMEGA EP beams.¹²⁷ The hot-electron production from a variety of different targets (on both OMEGA and OMEGA EP) with varying scale lengths and temperatures was compared by plotting the inferred hot-electron fraction against the predicted common-wave gain for each configuration. Figure 137.60 shows the results taken from Ref. 131; when plotted against common-wave gain, a universal curve is obtained for the inferred hot-electron fraction.

b. Optical signatures of multibeam TPD. Optical signatures of TPD are important because, unlike scattering instabilities (such as SBS or SRS), the direct products of the decay (two EPW's) do not exit the plasma. Scattered light with frequencies near $3\omega_0/2$ and $\omega_0/2$ has been used to investigate TPD for many years.^{136–144} Three-halves-harmonic emission ($3\omega_0/2$) is generated by Thomson up-scattering of the incident laser light by TPD-produced plasma waves (i.e., self-Thomson scattering), or possibly by higher-order nonlinear processes. Half-harmonic emission ($\omega_0/2$) can be generated in a variety of ways. These



E21699JR3

Figure 137.60
Experimental observation of hot-electron production in both planar and spherical experiments on OMEGA/OMEGA EP (figure taken from Michel *et al.*¹³¹). The hot-electron production is inferred from a combination of hard x-ray bremsstrahlung and/or K_α fluorescence.¹¹⁸ This is plotted against the gain for common TPD EPW's (see Fig. 137.58).

include absolute Raman instability; the high-frequency hybrid instability, where the $\omega_0/2$ light is a primary decay product; inverse resonance absorption; Thomson down-scattering; and inverse parametric decay of TPD plasmons, where the $\omega_0/2$ light is generated as a secondary process.¹¹³

In Seka *et al.*¹¹³ the onset of half-integer harmonic emission in spherical implosion experiments on OMEGA was observed to be consistent with the single-beam threshold of Simon *et al.*,¹²³ provided that the single-beam intensity in the threshold formula was replaced by the total overlapped intensity (i.e., by the incoherent sum of the intensities of all overlapping beams). Further analysis of the $3\omega_0/2$ and $\omega_0/2$ signatures led to the conclusion that the unstable EPW spectrum is much broader than would be expected on the basis of linear theory [see **Numerical Investigations of Multibeam TPD** (p. 72) for comparisons with nonlinear TPD theory]. While the EPW spectrum was determined to be broad, it was shown that the Landau cutoff is respected. Similar broad EPW spectra were inferred by Meyer and Zhu in early single-beam CO₂ laser experiments.¹³⁹

As in earlier work,¹³⁶ the multibeam nature of TPD was not explored beyond the threshold observation. More recently, images of the half-harmonic emission from similar OMEGA experiments have been obtained.¹⁵¹ Since the spatial regions that emit most brightly coincide with locations where multibeam TPD is expected to be driven most strongly, this has been interpreted as evidence of a multibeam effect in spherical implosion experiments.¹⁵¹

The most-direct observation of TPD EPW is obtained by Thomson scattering using a probe beam that is higher in frequency than the TPD interaction beam(s). For single-beam irradiation, the first such observations of TPD EPW's were obtained by Schuss *et al.*¹⁵² and Baldis *et al.*¹⁵³ for CO₂ laser irradiation. The unstable TPD spectrum was determined by Meyer and Zhu using Thomson scattering, again for a single CO₂ interaction beam.¹³⁹ Very recently, Thomson-scattering experiments have been performed in multibeam planar experiments on OMEGA at 0.351 μm using a 4ω (0.263- μm) Thomson-scattering probe beam.¹⁵⁴ Plasma waves were observed and found to be localized near the quarter-critical surface. The intensity of these EPW depended on the overlapped intensity of all the interaction beams.¹⁵⁴ These experiments promise to constrain numerical/theoretical predictions and provide a deeper understanding of multibeam interactions.

c. Angular properties of hot-electron production by multibeam TPD. The angular divergence of hot electrons produced

as a result of TPD instability is an important factor in determining hot-electron preheat in direct-drive experiments. In typical cryogenic direct-drive experiments,¹⁵⁵ the fast-electron energy deposited as preheat can be significantly less than the total energy of fast electrons produced. This is due to the factor-of-2 difference in radii between the cold shell and the quarter-critical surface.¹⁵⁶ It is therefore important to characterize the angular properties of hot electrons produced by multibeam TPD.

The directionality and energy spectrum of hot electrons produced by the TPD instability are difficult to predict because neither the saturated EPW wave-number spectrum nor the electron acceleration processes are well understood (see **Numerical Investigations of Multibeam TPD** below). The angular distribution of hot electrons and its dependence on the plane of polarization of a single-incident CO₂ laser beam were determined in early experiments by Ebrahim *et al.*¹¹⁴ The results were obtained by measuring the spectra of hot electrons escaping the target at various angles. A strong peak in emission was observed at angles of $\pm 45^\circ$ with respect to the wave vector of the incident light in the plane of polarization. This was thought to be consistent with the direction of the most-unstable TPD wave vectors for the parameters of the experiment [large wave-number decays consist of two plasmons propagating at angles of almost 45° and 135° with respect to the pump wave vector \vec{k}_0 (see Fig. 137.57)]. Similar single-beam experiments with a $0.351\text{-}\mu\text{m}$ interaction beam saw much weaker directionality, although emission was again stronger in the plane of polarization.¹¹⁶

Since the largest growth rates for multibeam interactions can involve TPD decay wave vectors that are symmetrically oriented with respect to the propagation direction of the interaction beams,¹²⁷ and experiments support the notion of common waves, a strong asymmetry might be expected in the direction of emission of hot electrons in multibeam experiments. An experimental technique was recently developed to estimate the angular divergence of hot electrons for conditions relevant to directly driven implosions.¹⁵⁷ Molybdenum-coated glass balls of varying diameters were suspended concentrically inside CH shell targets, which were then irradiated on the 60-beam OMEGA laser at intensities $I \sim 1 \times 15 \text{ W/cm}^2$. The hot-electron divergence was inferred from the dependence of the hot-electron-produced Mo K_α signal on the varying diameter of the Mo shell (while maintaining similar interaction conditions in the underdense corona). The relative K_α signal was best fit by a widely divergent hot-electron source, even after considerations of hot-electron recirculation,¹⁵⁶ scattering, and return-current instabilities were taken into account. The results of nonlinear

numerical models of TPD-produced hot electrons (described below) suggest possible reasons for these observations.

4. Numerical Investigations of Multibeam TPD

Although advances have been made in understanding the linearized theory of multibeam TPD instability,^{21,127,128,131–133} which are important for defining thresholds, linear theory alone is not sufficient. The presence of absolute instability guarantees that a nonlinear theory is necessary to describe its evolution beyond the picosecond time scale (i.e., nonlinear saturation) of importance to experiments that are several nanoseconds in duration. A nonlinear theory is required to describe hot-electron production and to interpret broad, odd half-harmonic emission spectra (see **Optical Signatures of Multibeam TPD**, p. 71).

Several numerical methods have been used to investigate the nonlinear evolution of TPD excited by a single EM wave. Since the TPD growth rate vanishes for decay wave vectors \vec{k} that are parallel to the pump wave vector \vec{k}_0 [i.e., $\vec{k}_0 \cdot \vec{v}_{\text{osc}} = 0$ for EM waves in Eq. (8)], the instability must be studied in at least two dimensions. For a single EM wave, the maximum growth rate is obtained for decays in the plane of polarization (i.e., the plane defined by the vectors \vec{k}_0 and \vec{v}_{osc}); consequently, the majority of single-beam calculations performed to date have been two-dimensional (2-D) calculations in the plane of polarization. These include extended Zakharov models,^{130,137,156} Zakharov models with quasilinear evolution of the electron distribution function,¹⁴⁹ explicit particle-in-cell calculations,^{129,158–161} and reduced particle-in-cell (RPIC) techniques employing time enveloping.^{124,162,163} These calculations have demonstrated the importance of ion-turbulence and profile modification in determining the saturated EPW spectrum¹⁵⁸ and hot-electron production.¹⁵⁹ For long-scale-length plasma relevant to ignition, the importance of collisional EPW damping has been noted, in both the linear and nonlinear turbulent states.^{149,159} Although computationally challenging, several 3-D PIC calculations of single-beam TPD have been performed.¹⁶⁴

Comparatively little work has been performed to investigate the nonlinear evolution of TPD excited by multiple beams. In two dimensions, RPIC calculations considered two crossed beams¹²⁴ and subsequent hot-electron production.^{162,163} Calculations were performed with two EM waves arranged symmetrically about the density gradient with angles of $\pm 23^\circ$, both polarized in the simulation plane. These investigations determined the conditions for the existence of shared waves¹²⁴ and emphasized their importance in the nonlinear state. The scaling of hot-electron production with laser intensity was

obtained¹⁶² and described in terms of “cavitating” Langmuir turbulence¹⁶³ (for a review of strong Langmuir turbulence see Robinson¹⁶⁵ or Goldman¹⁶⁶). These RPIC calculations motivated the quasilinear Zakharov model of TPD, where in addition to solving the extended Zakharov equations of TPD, the spatially averaged electron-velocity distribution is evolved in the quasilinear approximation, self-consistently determining the Landau damping of the EPW’s.^{149,167,168}

The extended Zakharov model of TPD is a fluid-based model that describes the nonlinear coupling between EPW’s and IAW’s. Figure 137.61 shows the results of a 2-D extended-Zakharov calculation of TPD driven by two overlapping EM waves, having a total intensity of 1.2×10^{14} W/cm², taken from Zhang *et al.*^{19,169} The density scale length is ignition relevant ($L_n = 660 \mu\text{m}$), the electron temperature $T_e = 2$ keV, and both EM waves are polarized in the plane (similar quasilinear calculations are described in more detail in Myatt *et al.*¹⁴⁹). At early times $t < 6$ ps the EPW spectrum is consistent with linear theory [Fig. 137.61(a)]. Both the convectively saturated common EPW and the absolutely unstable collective modes are observed. The common EPW’s can be seen close to $\vec{k}/k_0 = (1.5, 0)$, where the single-beam growth-rate curves intersect (cf. Fig. 137.58). The amplitude of these EPW’s has convectively saturated and is no longer growing. The bright “doublets” in the figure [$\vec{k}/k_0 \sim (0, 0)$ and $\vec{k}/k_0 \sim (0.9, \pm 0.4)$] correspond to the multi-beam absolute instability (cf. Fig. 137.59). These modes are

temporally growing and saturate only by nonlinear processes. For this particular case, the parameters set the absolute instability to be slightly above multibeam threshold, but the convective common wave is below threshold.

The late-time ($t \geq 50$ ps) EPW spectrum [Fig. 137.61(b)] is much broader than the linearly unstable spectrum. It is dominated by the common plasma waves (which are much greater in amplitude than before), while there are no obvious signatures of the cooperative absolute instability. It appears that a combination of profile modification and IAW turbulence excited by the nonlinear evolution of the absolutely unstable modes is able to restore growth to modes that were previously convectively saturated [Eq. (6)].^{19,169} The turbulent restoration of temporal growth in parametric instabilities has been noted in the past.^{170–173}

The broad EPW spectrum predicted by the extended Zakharov model in the nonlinear saturated state is consistent with experimental observations of half-harmonic optical emission and Thomson-scattering spectra (**Optical Signatures of Multibeam TPD**, p. 71). Similar calculations to those shown in Fig. 137.61, where the electron distribution function is evolved in the quasilinear approximation, also see a broad emission angle for TPD-produced hot electrons.¹⁴⁹ In the quasilinear approximation, electron acceleration is a stochastic process. As described in **Angular Properties of Hot-Electron Production**

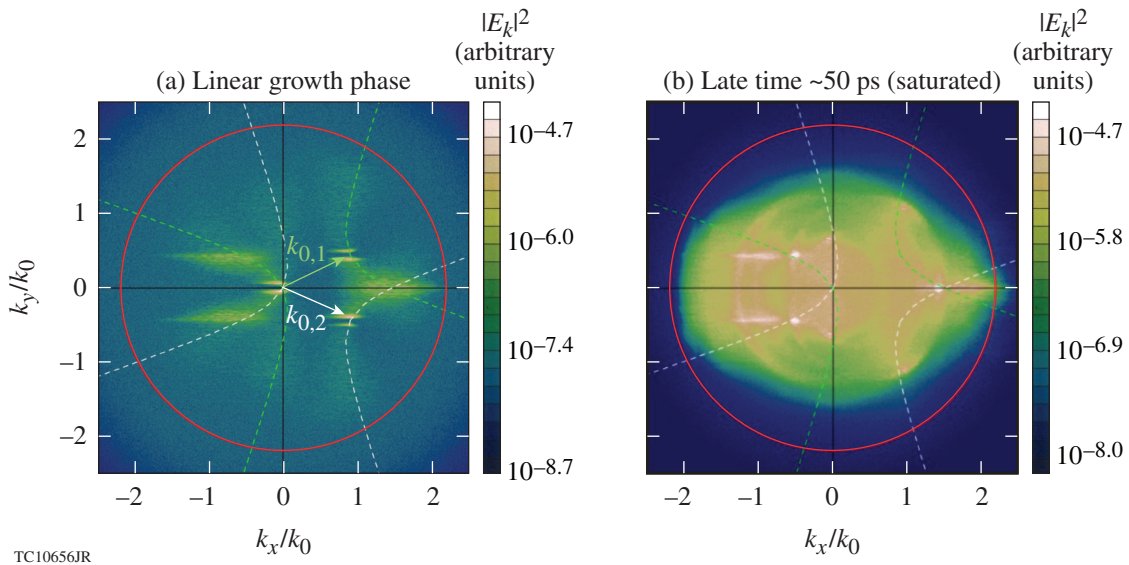


Figure 137.61 EPW spectra obtained from extended Zakharov calculations of TPD initiated by two crossing EM waves with wave vectors $\vec{k}_{0,1}$ and $\vec{k}_{0,2}$ (Refs. 19 and 169). The single-beam maximum growth-rate curves are shown for each (dashed hyperbolas) and the red circle is the Landau cutoff ($|\vec{k}| \lambda_{De} = 0.25$). The spectrum at (a) early times ($t = 6$ ps) and (b) late times ($t \geq 50$ ps) when the instability has nonlinearly saturated (the simulation parameters are given in the text).

by **Multibeam TPD** (p. 71), a broad angular distribution of hot electrons is observed experimentally in multibeam interactions.

The computational efficiency of the quasilinear Zakharov model of TPD is such that 3-D calculations are quite practical to perform.^{132,169} Since it is in only three dimensions that the full effects of multibeam interactions can be investigated, this approach holds much promise.

Mitigation of Multibeam Instabilities

In general, despite the beneficial use of CBET in the indirect-drive-ignition campaign to control symmetry, it is preferable to avoid multibeam interactions wherever possible, i.e., mitigate their effects.

A few general principles apply to the mitigation of multibeam instabilities. If the instabilities are convective, and of the “induced” type (**Three-Wave Interactions**, p. 61), then for a given gain, the effect can be reduced by lowering the amplitude of the seed from which it grows. For CBET in indirect drive, this is not possible since the drive beams are themselves the seed. In direct drive, the seed is provided by unabsorbed light (**CBET in Direct Drive**, p. 64) that can be modified. This observation has led to concepts such as the use of smaller focal spots,⁸⁹ or focal-spot zooming, where the spot sizes are reduced during the main drive.^{174–177}

The gain for convectively unstable multibeam instabilities involving low-frequency daughter waves (IAW’s) (i.e., CBET) may be reduced by modifying the frequencies of the interacting beams on existing laser systems, as demonstrated in indirect drive on the NIF (**CBET in Indirect Drive on the NIF**, p. 64). Direct-drive implosions require a larger $\Delta\lambda$ among the beams to eliminate the resonant couplings relative to indirect drive because of the backscattering (compared with forward-scattering) geometry. Calculations performed by Igumenshchev *et al.*^{88,89} indicate that frequency shifts of $\Delta\lambda \gtrsim 5 \text{ \AA}$ (at $3\omega_0$) can have a mitigating effect. Very large bandwidths are required to mitigate multibeam TPD,¹⁹ but there is no fundamental reason why future laser systems cannot be constructed with this in mind.¹⁷⁸

Multibeam gain can be reduced by increasing the plasma temperature (since gains are usually inversely proportional to the plasma temperature)³ or by reducing the plasma density. This increase can be brought about by increasing absorption, through the use of higher- Z hohlraum fill gases,¹⁷⁹ high- Z ablators, or ablators with high- Z layers.^{29,89,180} Other more-exotic means, such as magnetizing thermal transport, may be

possible.¹⁸¹ For multibeam instabilities that share decay waves (**Three-Wave Interactions**, p. 61), the above observations still hold, except it may be possible to additionally reduce the level of cooperation between beams by making suitable choices of beam pointing or by moving regions of high gain away from regions where the beams overlap.³⁷

For instabilities that are not expected to be in the linearly convective regime, nonlinear models can provide insight into possible mitigation strategies. Figure 137.62 shows the results from 2-D quasilinear Zakharov calculations of TPD.¹⁴⁹ It can be seen that hot-electron production differs between plasmas of different effective ionization states for the same plasma parameters ($L_n = 330 \mu\text{m}$, $T_e = 2 \text{ keV}$). In these calculations,¹⁴⁹ the TPD was driven by two overlapping EM waves (as in Fig. 137.61). There are two contributing effects: The higher- Z plasma has a higher collisional damping rate ν_e for EPW’s, which modifies both the linear threshold and the nonlinear saturation.¹⁴⁹ Similar effects of EPW collisional damping on nonlinear saturation and hot-electron production were observed in PIC calculations

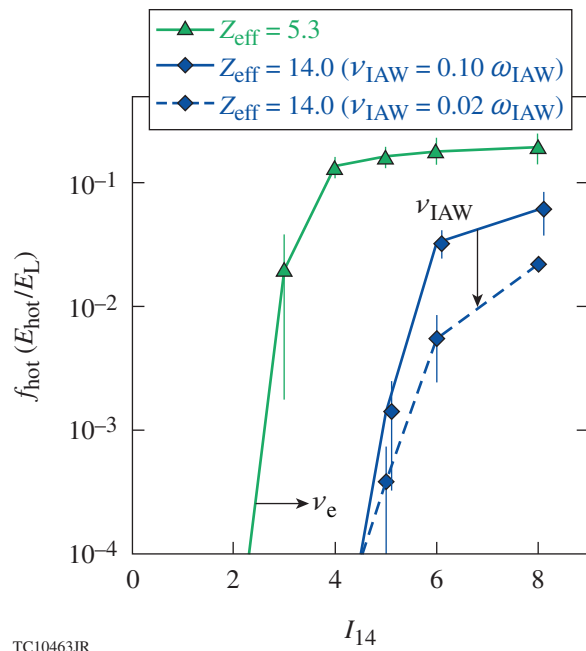


Figure 137.62

The simulated hot-electron fraction (energy in hot electrons normalized by laser energy) generated by TPD for three materials is shown as a function of overlapped laser intensity (in units of $1 \times 10^{14} \text{ W/cm}^2$). The green curve corresponds to a CH plasma with $Z_{\text{eff}} = 5.3$ and a normalized ion-acoustic damping rate $\nu_{\text{IAW}}/\omega_{\text{IAW}} = 0.1$. The blue solid (dashed) curves correspond to a material of higher effective Z ($Z_{\text{eff}} = 14$) with $\nu_{\text{IAW}}/\omega_{\text{IAW}} = 0.1$ (0.02). In all cases, $L_n = 330 \mu\text{m}$ and $T_e = 2 \text{ keV}$. These results have been taken from Ref. 149.

of TPD.¹⁵⁹ Lower hot-electron production in higher-Z ablators has been observed experimentally.¹⁸² A reduction in the ion-acoustic damping rate ν_{IAW} is shown to lead to a reduction in hot-electron production. This is a nonlinear effect that arises because of the role played by IAW's in the saturation of TPD.¹⁴⁹ Note that a similar effect has been observed experimentally for SRS in the small $k\lambda_{De}$ regime.^{64,183}

In practice, it might be necessary to use some combination of all of these effects to limit the deleterious effects of multi-beam interactions.

Summary and Discussion

A description of both the direct- and indirect-drive approaches to ICF has been presented, with an emphasis placed on the differences in conditions between the two and the resulting impact on laser-plasma instabilities involving multiple beams. The ability of different laser beams to become cooperatively unstable has been discussed in the context of three-wave interactions.

This article has reviewed the experimental evidence for three-wave multibeam LPI's of relevance to laser-driven inertial confinement fusion at the ignition scale. The instabilities described are cross-beam energy transfer, multibeam stimulated Raman scattering, and multibeam two-plasmon decay. Cross-beam energy transfer is seen to be common to both ICF approaches, and the similarities and differences were described, together with the different routes taken to numerically compute the effect. Multibeam SRS appears to be unique to indirect drive, while TPD is of more importance to direct drive.

Calculations of multibeam SRS that involve sharing a common EM wave were presented. These *pF3D* calculations involved the combination of three different numerical codes and highlight one of the problems with LPI's in ICF—the scale mixing. The experimental evidence for multibeam TPD was discussed in some detail since it has recently become a very active area of experimental research. Similarly, advances in the theoretical understanding (both linear and nonlinear) were also presented. The linear theory of multibeam TPD was shown to be complicated by the presence of absolute instability, which necessitates the use of nonlinear models. The effect of nonlinearity on the EPW spectrum was shown, taking results from extended Zakharov models.

This article concluded with a discussion of the general principles by which multibeam instabilities can be either avoided or mitigated. The final implication is that LPI's in ICF should

be viewed from a description based on multibeam rather than single-beam concepts.

ACKNOWLEDGMENT

The authors are grateful for the contributions from H. X. Vu (University of California, San Diego) and D. A. Russell and D. F. Dubois (Lodestar Research Corporation). This material is based upon work supported by the Department of Energy National Nuclear Security Administration under Award Number DE-NA0001944, the University of Rochester, and the New York State Energy Research and Development Authority. The support of DOE does not constitute an endorsement by DOE of the views expressed in this article.

REFERENCES

1. J. Nuckolls *et al.*, *Nature* **239**, 139 (1972).
2. J. D. Lindl, *Inertial Confinement Fusion: The Quest for Ignition and Energy Gain Using Indirect Drive* (Springer-Verlag, New York, 1998).
3. W. L. Kruer, in *The Physics of Laser Plasma Interactions*, *Frontiers in Physics*, Vol. 73, edited by D. Pines (Addison-Wesley, Redwood City, CA, 1988).
4. S. H. Glenzer *et al.*, *Science* **327**, 1228 (2010).
5. P. A. Norreys, *Science* **327**, 1208 (2010).
6. R. L. McCrory, R. Betti, T. R. Boehly, D. T. Casey, T. J. B. Collins, R. S. Craxton, J. A. Delettrez, D. H. Edgell, R. Epstein, J. A. Frenje, D. H. Froula, M. Gatu-Johnson, V. Yu. Glebov, V. N. Goncharov, D. R. Harding, M. Hohenberger, S. X. Hu, I. V. Igumenshchev, T. J. Kessler, J. P. Knauer, C. K. Li, J. A. Marozas, F. J. Marshall, P. W. McKenty, D. D. Meyerhofer, D. T. Michel, J. F. Myatt, P. M. Nilson, S. J. Padalino, R. D. Petrasso, P. B. Radha, S. P. Regan, T. C. Sangster, F. H. Séguin, W. Seka, R. W. Short, A. Shvydky, S. Skupsky, J. M. Soures, C. Stoeckl, W. Theobald, B. Yaakobi, and J. D. Zuegel, *Nucl. Fusion* **53**, 113021 (2013).
7. J. D. Lindl *et al.*, *Phys. Plasmas* **11**, 339 (2004).
8. G. B. Zimmerman and W. L. Kruer, *Comments Plasma Phys. Control. Fusion* **2**, 51 (1975).
9. P. B. Radha, T. J. B. Collins, J. A. Delettrez, Y. Elbaz, R. Epstein, V. Yu. Glebov, V. N. Goncharov, R. L. Keck, J. P. Knauer, J. A. Marozas, F. J. Marshall, R. L. McCrory, P. W. McKenty, D. D. Meyerhofer, S. P. Regan, T. C. Sangster, W. Seka, D. Shvarts, S. Skupsky, Y. Srebro, and C. Stoeckl, *Phys. Plasmas* **12**, 056307 (2005).
10. D. H. Froula, D. T. Michel, I. V. Igumenshchev, S. X. Hu, B. Yaakobi, J. F. Myatt, D. H. Edgell, R. Follett, V. Yu. Glebov, V. N. Goncharov, T. J. Kessler, A. V. Maximov, P. B. Radha, T. C. Sangster, W. Seka, R. W. Short, A. A. Solodov, C. Sorce, and C. Stoeckl, *Plasma Phys. Control. Fusion* **54**, 124016 (2012).
11. J. D. Moody *et al.*, *Nat. Phys.* **8**, 344 (2012).
12. J. M. Dawson, *Rev. Mod. Phys.* **55**, 403 (1983).
13. C. K. Birdsall and A. B. Langdon, *Plasma Physics via Computer Simulation* (McGraw-Hill, New York, 1985).

14. R. A. Fonseca *et al.*, *Lect. Notes Comput. Sci.* **2331**, 342 (2002).
15. K. J. Bowers *et al.*, *Phys. Plasmas* **15**, 055703 (2008); K. L. Bowers *et al.*, in the *Proceedings of the 2008 ACM/IEEE Conference on Supercomputing* (IEEE Press, Piscataway, NJ, 2008); K. J. Bowers *et al.*, *J. Phys.: Conf. Ser.* **180**, 012055 (2009).
16. D. Pesme, S. Hüller, J. Myatt, C. Riconda, A. Maximov, V. T. Tikhonchuk, C. Labaune, J. Fuchs, S. Depierreux, and H. A. Baldis, *Plasma Phys. Control. Fusion* **44**, B53 (2002).
17. R. L. Berger *et al.*, *Phys. Plasmas* **5**, 4337 (1998); C. H. Still *et al.*, *Phys. Plasmas* **7**, 2023 (2000).
18. S. Hüller *et al.*, *Phys. Plasmas* **13**, 022703 (2006).
19. J. Zhang, J. F. Myatt, R. W. Short, A. V. Maximov, H. X. Vu, D. F. DuBois, and D. A. Russell, "Multibeam Two-Plasmon Decay from Linear Threshold to Nonlinear Saturations," to be published in *Physical Review Letters*.
20. H. X. Vu, D. F. DuBois, D. A. Russell, J. F. Myatt, and J. Zhang, "Non-linear Development of the Two-Plasmon-Decay Instability in Three Dimensions," submitted to *Physics of Plasmas*.
21. J. D. Lindl, *Phys. Plasmas* **2**, 3933 (1995).
22. M. J. Edwards, P. K. Patel, J. D. Lindl, L. J. Atherton, S. H. Glenzer, S. W. Haan, J. D. Kilkenny, O. L. Landen, E. I. Moses, A. Nikroo, R. Petrasso, T. C. Sangster, P. T. Springer, S. Batha, R. Benedetti, L. Bernstein, R. Betti, D. L. Bleuel, T. R. Boehly, D. K. Bradley, J. A. Caggiano, D. A. Callahan, P. M. Celliers, C. J. Cerjan, K. C. Chen, D. S. Clark, G. W. Collins, E. L. Dewald, L. Divol, S. Dixit, T. Doeppner, D. H. Edgell, J. E. Fair, M. Farrell, R. J. Fortner, J. Frenje, M. G. Gatu Johnson, E. Giraldez, V. Yu. Glebov, G. Grim, B. A. Hammel, A. V. Hamza, D. R. Harding, S. P. Hatchett, N. Hein, H. W. Herrmann, D. Hicks, D. E. Hinkel, M. Hoppe, W. W. Hsing, N. Izumi, B. Jacoby, O. S. Jones, D. Kalantar, R. Kauffman, J. L. Kline, J. P. Knauer, J. A. Koch, B. J. Koziolowski, G. Kyrala, K. N. LaFortune, S. Le Pape, R. J. Leeper, R. Lerche, T. Ma, B. J. MacGowan, A. J. MacKinnon, A. Macphee, E. R. Mapoles, M. M. Marinak, M. Mauldin, P. W. McKenty, M. Meezan, P. A. Michel, J. Milovich, J. D. Moody, M. Moran, D. H. Munro, C. L. Olson, K. Opachich, A. E. Pak, T. Parham, H.-S. Park, J. E. Ralph, S. P. Regan, B. Remington, H. Rinderknecht, H. F. Robey, M. Rosen, S. Ross, J. D. Salmonson, J. Sater, D. H. Schneider, F. H. Séguin, S. M. Sepke, D. A. Shaughnessy, V. A. Smalyuk, B. K. Spears, C. Stoeckl, W. Stoeffl, L. Suter, C. A. Thomas, R. Tommasini, R. P. Town, S. V. Weber, P. J. Wegner, K. Widman, M. Wilke, D. C. Wilson, C. B. Yeamans, and A. Zylstra, *Phys. Plasmas* **20**, 070501 (2013).
23. S. W. Haan, J. D. Lindl, D. A. Callahan, D. S. Clark, J. D. Salmonson, B. A. Hammel, L. J. Atherton, R. C. Cook, M. J. Edwards, S. Glenzer, A. V. Hamza, S. P. Hatchett, M. C. Herrmann, D. E. Hinkel, D. D. Ho, H. Huang, O. S. Jones, J. Kline, G. Kyrala, O. L. Landen, B. J. MacGowan, M. M. Marinak, D. D. Meyerhofer, J. L. Milovich, K. A. Moreno, E. I. Moses, D. H. Munro, A. Nikroo, R. E. Olson, K. Peterson, S. M. Pollaine, J. E. Ralph, H. F. Robey, B. K. Spears, P. T. Springer, L. J. Suter, C. A. Thomas, R. P. Town, R. Vesey, S. V. Weber, H. L. Wilkens, and D. C. Wilson, *Phys. Plasmas* **18**, 051001 (2011); M. J. Edwards, J. D. Lindl, B. K. Spears, S. V. Weber, L. J. Atherton, D. L. Bleuel, D. K. Bradley, D. A. Callahan, C. J. Cerjan, D. Clark, G. W. Collins, J. E. Fair, R. J. Fortner, S. H. Glenzer, S. W. Haan, B. A. Hammel, A. V. Hamza, S. P. Hatchett, N. Izumi, B. Jacoby, O. S. Jones, J. A. Koch, B. J. Koziolowski, O. L. Landen, R. Lerche, B. J. MacGowan, A. J. MacKinnon, E. R. Mapoles, M. M. Marinak, M. Moran, E. I. Moses, D. H. Munro, D. H. Schneider, S. M. Sepke, D. A. Shaughnessy, P. T. Springer, R. Tommasini, L. Bernstein, W. Stoeffl, R. Betti, T. R. Boehly, T. C. Sangster, V. Yu. Glebov, P. W. McKenty, S. P. Regan, D. H. Edgell, J. P. Knauer, C. Stoeckl, D. R. Harding, S. Batha, G. Grim, H. W. Herrmann, G. Kyrala, M. Wilke, D. C. Wilson, J. Frenje, R. Petrasso, K. Moreno, H. Huang, K. C. Chen, E. Giraldez, J. D. Kilkenny, M. Mauldin, N. Hein, M. Hoppe, A. Nikroo, and R. J. Leeper, *Phys. Plasmas* **18**, 051003 (2011); O. L. Landen, J. Edwards, S. W. Haan, H. F. Robey, J. Milovich, B. K. Spears, S. V. Weber, D. S. Clark, J. D. Lindl, B. J. MacGowan, E. I. Moses, J. Atherton, P. A. Amendt, T. R. Boehly, D. K. Bradley, D. G. Braun, D. A. Callahan, P. M. Celliers, G. W. Collins, E. L. Dewald, L. Divol, J. A. Frenje, S. H. Glenzer, A. Hamza, B. A. Hammel, D. G. Hicks, N. Hoffman, N. Izumi, O. S. Jones, J. D. Kilkenny, R. K. Kirkwood, J. L. Kline, G. A. Kyrala, M. M. Marinak, N. Meezan, D. D. Meyerhofer, P. Michel, D. H. Munro, R. E. Olson, A. Nikroo, S. P. Regan, L. J. Suter, C. A. Thomas, and D. C. Wilson, *Phys. Plasmas* **18**, 051002 (2011).
24. E. I. Moses *et al.*, *Phys. Plasmas* **16**, 041006 (2009); E. I. Moses, *Fusion Sci. Technol.* **54**, 361 (2008); W. J. Hogan, E. I. Moses, B. E. Warner, M. S. Sorem, and J. M. Soures, *Nucl. Fusion* **41**, 567 (2001); J. A. Paisner, E. M. Campbell, and W. J. Hogan, *Fusion Technol.* **26**, 755 (1994).
25. S. Skupsky, J. A. Marozas, R. S. Craxton, R. Betti, T. J. B. Collins, J. A. Delettrez, V. N. Goncharov, P. W. McKenty, P. B. Radha, T. R. Boehly, J. P. Knauer, F. J. Marshall, D. R. Harding, J. D. Kilkenny, D. D. Meyerhofer, T. C. Sangster, and R. L. McCrory, *Phys. Plasmas* **11**, 2763 (2004).
26. T. R. Boehly, D. L. Brown, R. S. Craxton, R. L. Keck, J. P. Knauer, J. H. Kelly, T. J. Kessler, S. A. Kumpan, S. J. Loucks, S. A. Letzring, F. J. Marshall, R. L. McCrory, S. F. B. Morse, W. Seka, J. M. Soures, and C. P. Verdon, *Opt. Commun.* **133**, 495 (1997).
27. L. J. Waxer, D. N. Maywar, J. H. Kelly, T. J. Kessler, B. E. Kruschwitz, S. J. Loucks, R. L. McCrory, D. D. Meyerhofer, S. F. B. Morse, C. Stoeckl, and J. D. Zuegel, *Opt. Photonics News* **16**, 30 (2005).
28. D. N. Maywar, J. H. Kelly, L. J. Waxer, S. F. B. Morse, I. A. Begishev, J. Bromage, C. Dorner, J. L. Edwards, L. Folsbee, M. J. Guardalben, S. D. Jacobs, R. Jungquist, T. J. Kessler, R. W. Kidder, B. E. Kruschwitz, S. J. Loucks, J. R. Marcianti, R. L. McCrory, D. D. Meyerhofer, A. V. Okishev, J. B. Oliver, G. Pien, J. Qiao, J. Puth, A. L. Rigatti, A. W. Schmid, M. J. Shoup III, C. Stoeckl, K. A. Thorp, and J. D. Zuegel, *J. Phys., Conf. Ser.* **112**, 032007 (2008).
29. V. N. Goncharov, T. C. Sangster, R. Betti, T. R. Boehly, T. J. B. Collins, R. S. Craxton, J. A. Delettrez, D. H. Edgell, R. Epstein, R. Follet, C. J. Forrest, D. H. Froula, V. Y. Glebov, D. R. Harding, R. Henchen, S. X. Hu, I. V. Igumenshchev, R. Janezic, J. H. Kelly, T. J. Kessler, T. Z. Kosc, S. J. Loucks, J. A. Marozas, F. J. Marshall, A. V. Maximov, R. L. McCrory, P. W. McKenty, D. D. Meyerhofer, D. T. Michel, J. F. Myatt, R. Nora, P. B. Radha, S. P. Regan, W. Seka, W. T. Shmayda, R. W. Short, A. Shvydky, S. Skupsky, C. Stoeckl, B. Yaakobi, J. A. Frenje, M. Gatu-Johnson, R. D. Petrasso, and D. T. Casey, "Improving the Hot-Spot Pressure and Demonstrating Ignition Hydrodynamic Equivalence in Cryogenic DT Implosions on OMEGA," to be published in *Physics of Plasmas*.

30. T. J. B. Collins, J. A. Marozas, and P. W. McKenty, *Bull. Am. Phys. Soc.* **57**, 155 (2012); T. J. B. Collins, J. A. Marozas, K. S. Anderson, R. Betti, R. S. Craxton, J. A. Delettrez, V. N. Goncharov, D. R. Harding, F. J. Marshall, R. L. McCrory, D. D. Meyerhofer, P. W. McKenty, P. B. Radha, A. Shvydky, S. Skupsky, and J. D. Zuegel, *Phys. Plasmas* **19**, 056308 (2012).
31. S. W. Haan *et al.*, *Phys. Plasmas* **2**, 2480 (1995).
32. P. Michel *et al.*, *Phys. Rev. E* **83**, 046409 (2011).
33. R. L. McCrory, D. D. Meyerhofer, R. Betti, R. S. Craxton, J. A. Delettrez, D. H. Edgell, V. Yu Glebov, V. N. Goncharov, D. R. Harding, D. W. Jacobs-Perkins, J. P. Knauer, F. J. Marshall, P. W. McKenty, P. B. Radha, S. P. Regan, T. C. Sangster, W. Seka, R. W. Short, S. Skupsky, V. A. Smalyuk, J. M. Soures, C. Stoeckl, B. Yaakobi, D. Shvarts, J. A. Frenje, C. K. Li, R. D. Petrasso, and F. H. Séguin, *Phys. Plasmas* **15**, 055503 (2008).
34. E. A. Williams, B. I. Cohen, L. Divol, M. R. Dorr, J. A. Hittinger, D. E. Hinkel, A. B. Langdon, R. K. Kirkwood, D. H. Froula, and S. H. Glenzer, *Phys. Plasmas* **11**, 231 (2004).
35. D. J. Strozzi, E. A. Williams, D. E. Hinkel, D. H. Froula, R. A. London, and D. A. Callahan, *Phys. Plasmas* **15**, 102703 (2008).
36. S. Laffite and P. Loiseau, *Phys. Plasmas* **17**, 102704 (2010).
37. D. E. Hinkel *et al.*, *Phys. Plasmas* **18**, 056312 (2011).
38. H. Motz, *The Physics of Laser Fusion* (Academic Press, London, 1979).
39. R. C. Davidson, *Methods in Nonlinear Plasma Theory* (Academic Press, New York, 1972).
40. D. Pesme, in *L'Interaction Laser-Matière, Part I*, edited by L. Bergé *et al.*, La Fusion Thermonucléaire Inertielle par Laser, Collection du Commissariat à l'énergie Atomique, edited by R. Dautray and J.-P. Watteau (Eyrolles, Paris, 1993), Vol. 1, Chap. 2, Sec. IV.3, pp. 306–350.
41. R. J. Briggs, *Electron-Stream Interaction with Plasmas* (MIT Press, Cambridge, MA, 1964).
42. A. Bers, in *Physique des Plasmas: Université de Grenoble, Summer School of Theoretical Physics, Les Houches 1972*, edited by C. DeWitt and J. Peyraud (Gordon and Breach, New York, 1975).
43. M. N. Rosenbluth, *Phys. Rev. Lett.* **29**, 565 (1972).
44. D. F. DuBois, B. Bezzerides, and H. A. Rose, *Phys. Fluids B* **4**, 241 (1992).
45. W. L. Kruer *et al.*, *Phys. Plasmas* **3**, 382 (1996).
46. R. K. Kirkwood, P. Michel, R. London, J. D. Moody, E. Dewald, L. Yin, J. Kline, D. Hinkel, D. Callahan, N. Meezan, E. Williams, L. Divol, B. L. Albright, K. J. Bowers, E. Bond, H. Rose, Y. Ping, T. L. Wang, C. Joshi, W. Seka, N. J. Fisch, D. Turnbull, S. Suckewer, J. S. Wurtele, S. Glenzer, L. Suter, C. Haynam, O. Landen, and B. J. Macgowan, *Phys. Plasmas* **18**, 056311 (2011).
47. H. A. Rose and D. F. DuBois, *Phys. Fluids B* **4**, 252 (1992).
48. J. S. Li *et al.*, *Bull. Am. Phys. Soc.* **39**, 1584 (1994).
49. H. A. Rose, *Phys. Plasmas* **3**, 1709 (1996).
50. D. E. Hinkel, E. A. Williams, and C. H. Still, *Phys. Rev. Lett.* **77**, 1298 (1996).
51. J. D. Moody *et al.*, *Phys. Rev. Lett.* **77**, 1294 (1996).
52. N. M. Kroll, A. Ron, and N. Rostoker, *Phys. Rev. Lett.* **13**, 83 (1964); B. L. Stansfield, R. Nodwell, and J. Meyer, *Phys. Rev. Lett.* **26**, 1219 (1971).
53. C. J. Pawley, H. E. Huey, and N. C. Luhmann, Jr., *Phys. Rev. Lett.* **49**, 877 (1982); C. W. Domier and N. C. Luhmann, Jr., *Phys. Rev. Lett.* **69**, 3499 (1992); D. M. Villeneuve, H. A. Baldis, and J. E. Bernard, *Phys. Rev. Lett.* **59**, 1585 (1987).
54. E. A. Williams, D. M. Lininger, and M. V. Goldman, *Phys. Fluids B* **1**, 1561 (1989).
55. V. M. Malkin, G. Shvets, and N. J. Fisch, *Phys. Rev. Lett.* **82**, 4448 (1999); Y. Ping *et al.*, *Phys. Plasmas* **16**, 123113 (2009).
56. R. M. G. M. Trines *et al.*, *Nat. Phys.* **7**, 87 (2010).
57. D. S. Clark and N. J. Fisch, *Phys. Plasmas* **10**, 3363 (2003).
58. R. K. Kirkwood *et al.*, *Plasma Phys. Control. Fusion* **55**, 103001 (2013).
59. V. V. Eliseev *et al.*, *Phys. Plasmas* **3**, 2215 (1996).
60. C. J. McKinstrie *et al.*, *Phys. Plasmas* **3**, 2686 (1996).
61. H. A. Rose and S. Ghosal, *Phys. Plasmas* **5**, 1461 (1998).
62. B. I. Cohen *et al.*, *Phys. Plasmas* **5**, 3408 (1998).
63. J. A. F. Hittinger *et al.*, *J. Comput. Phys.* **209**, 695 (2005).
64. R. K. Kirkwood *et al.*, *Phys. Rev. Lett.* **77**, 2706 (1996).
65. H. A. Baldis *et al.*, *Phys. Rev. Lett.* **77**, 2957 (1996).
66. A. K. Lal *et al.*, *Phys. Rev. Lett.* **78**, 670 (1997).
67. J. C. Fernández *et al.*, *Phys. Rev. Lett.* **81**, 2252 (1998).
68. K. B. Wharton *et al.*, *Phys. Rev. Lett.* **81**, 2248 (1998).
69. K. B. Wharton *et al.*, *Phys. Plasmas* **6**, 2144 (1999).
70. C. Labaune *et al.*, *Phys. Plasmas* **6**, 2048 (1999).
71. C. Labaune *et al.*, *Phys. Rev. Lett.* **85**, 1658 (2000).
72. R. K. Kirkwood, J. D. Moody, A. B. Langdon, B. I. Cohen, E. A. Williams, M. R. Dorr, J. A. Hittinger, R. Berger, P. E. Young, L. J. Suter, L. Divol, S. H. Glenzer, O. L. Landen, and W. Seka, *Phys. Rev. Lett.* **89**, 215003 (2002).
73. R. K. Kirkwood *et al.*, *Phys. Rev. Lett.* **76**, 2065 (1996).
74. K. Marsh, C. Joshi, and C. McKinstrie, *Bull. Am. Phys. Soc.* **39**, 1585 (1994).

75. C. Labaune *et al.*, Phys. Rev. Lett. **82**, 3613 (1999).
76. P. Michel *et al.*, Phys. Rev. Lett. **102**, 025004 (2009).
77. P. Michel *et al.*, Phys. Plasmas **16**, 042702 (2009).
78. C. J. Randall, J. J. Thomson, and K. G. Estabrook, Phys. Rev. Lett. **43**, 924 (1979); C. J. Randall, J. R. Albritton, and J. J. Thomson, Phys. Fluids **24**, 1474 (1981).
79. W. Seka, H. A. Baldis, J. Fuchs, S. P. Regan, D. D. Meyerhofer, C. Stoeckl, B. Yaakobi, R. S. Craxton, and R. W. Short, Phys. Rev. Lett. **89**, 175002 (2002).
80. J. Myatt, A. V. Maximov, W. Seka, R. S. Craxton, and R. W. Short, Phys. Plasmas **11**, 3394 (2004).
81. A. V. Maximov, J. Myatt, W. Seka, R. W. Short, and R. S. Craxton, Phys. Plasmas **11**, 2994 (2004).
82. T. Dewandre, J. R. Albritton, and E. A. Williams, Phys. Fluids **24**, 528 (1981).
83. J. Delettrez, R. Epstein, M. C. Richardson, P. A. Jaanimagi, and B. L. Henke, Phys. Rev. A **36**, 3926 (1987).
84. D. H. Edgell, W. Seka, J. A. Delettrez, R. S. Craxton, V. N. Goncharov, I. V. Igumenshchev, J. Myatt, A. V. Maximov, R. W. Short, T. C. Sangster, and R. E. Bahr, Bull. Am. Phys. Soc. **52**, 195 (2007).
85. D. H. Edgell, W. Seka, J. A. Delettrez, R. S. Craxton, V. N. Goncharov, I. V. Igumenshchev, J. F. Myatt, A. V. Maximov, R. W. Short, T. C. Sangster, and R. E. Bahr, Bull. Am. Phys. Soc. **54**, 145 (2009).
86. D. H. Edgell, W. Seka, J. A. Delettrez, R. S. Craxton, V. N. Goncharov, I. V. Igumenshchev, J. F. Myatt, A. V. Maximov, R. W. Short, T. C. Sangster, and R. E. Bahr, Bull. Am. Phys. Soc. **53**, 168 (2008).
87. W. Seka, D. H. Edgell, J. P. Knauer, J. F. Myatt, A. V. Maximov, R. W. Short, T. C. Sangster, C. Stoeckl, R. E. Bahr, R. S. Craxton, J. A. Delettrez, V. N. Goncharov, I. V. Igumenshchev, and D. Shvarts, Phys. Plasmas **15**, 056312 (2008).
88. I. V. Igumenshchev, D. H. Edgell, V. N. Goncharov, J. A. Delettrez, A. V. Maximov, J. F. Myatt, W. Seka, A. Shvydky, S. Skupsky, and C. Stoeckl, Phys. Plasmas **17**, 122708 (2010).
89. I. V. Igumenshchev, W. Seka, D. H. Edgell, D. T. Michel, D. H. Froula, V. N. Goncharov, R. S. Craxton, L. Divol, R. Epstein, R. Follett, J. H. Kelly, T. Z. Kosc, A. V. Maximov, R. L. McCrory, D. D. Meyerhofer, P. Michel, J. F. Myatt, T. C. Sangster, A. Shvydky, S. Skupsky, and C. Stoeckl, Phys. Plasmas **19**, 056314 (2012).
90. I. V. Igumenshchev, D. H. Edgell, V. N. Goncharov, J. A. Delettrez, A. V. Maximov, J. F. Myatt, W. Seka, and A. Shvydky, Bull. Am. Phys. Soc. **54**, 145 (2009).
91. V. N. Goncharov, O. V. Gotchev, E. Vianello, T. R. Boehly, J. P. Knauer, P. W. McKenty, P. B. Radha, S. P. Regan, T. C. Sangster, S. Skupsky, V. A. Smalyuk, R. Betti, R. L. McCrory, D. D. Meyerhofer, and C. Cherfils-Clérouin, Phys. Plasmas **13**, 012702 (2006).
92. D. T. Michel, C. Sorce, R. Epstein, N. Whiting, I. V. Igumenshchev, R. Jungquist, and D. H. Froula, Rev. Sci. Instrum. **83**, 10E530 (2012).
93. D. H. Froula, I. V. Igumenshchev, D. T. Michel, D. H. Edgell, R. Follett, V. Yu. Glebov, V. N. Goncharov, J. Kwiatkowski, F. J. Marshall, P. B. Radha, W. Seka, C. Sorce, S. Stagnitto, C. Stoeckl, and T. C. Sangster, Phys. Rev. Lett. **108**, 125003 (2012).
94. G. A. Kyrala *et al.*, Phys. Plasmas **18**, 072703 (2011).
95. N. B. Meezan *et al.*, Phys. Plasmas **17**, 056304 (2010).
96. P. Michel *et al.*, Phys. Plasmas **17**, 056305 (2010).
97. M. M. Marinak *et al.*, Phys. Plasmas **8**, 2275 (2001).
98. P. Michel *et al.*, Phys. Rev. Lett. **109**, 195004 (2012).
99. P. Michel *et al.*, Phys. Plasmas **20**, 056308 (2013).
100. D. E. Hinkel, M. J. Edwards, P. A. Amendt, R. Benedetti, L. Berzak Hopkins, D. Bleuel, T. R. Boehly, D. K. Bradley, J. A. Caggiano, D. A. Callahan, P. M. Celliers, C. J. Cerjan, D. Clark, G. W. Collins, E. L. Dewald, T. R. Dittrich, L. Divol, S. N. Dixit, T. Doepfner, D. Edgell, J. Eggert, D. Farley, J. A. Frenje, V. Glebov, S. M. Glenn, S. W. Haan, A. Hamza, B. A. Hammel, C. A. Haynam, J. H. Hammer, R. F. Heeter, H. W. Herrmann, D. Ho, O. Hurricane, N. Izumi, M. Gatun Johnson, O. S. Jones, D. H. Kalantar, R. L. Kauffman, J. D. Kilkenny, J. L. Kline, J. P. Knauer, J. A. Koch, A. Kritcher, G. A. Kyrala, K. LaFortune, O. L. Landen, B. F. Lasinski, T. Ma, A. J. Mackinnon, A. J. Macphee, E. Mapoles, J. L. Milovich, J. D. Moody, D. Meeker, N. B. Meezan, P. Michel, A. S. Moore, D. H. Munro, A. Nikroo, R. E. Olson, K. Opachich, A. Pak, T. Parham, P. Patel, H.-S. Park, R. D. Petrasso, J. Ralph, S. P. Regan, B. A. Remington, H. G. Rinderknecht, H. F. Robey, M. D. Rosen, J. S. Ross, R. Rygg, J. D. Salmonson, T. C. Sangster, M. B. Schneider, V. Smalyuk, B. K. Spears, P. T. Springer, E. Storm, D. J. Strozzi, L. J. Suter, C. A. Thomas, R. P. J. Town, E. A. Williams, S. V. Weber, P. J. Wegner, D. C. Wilson, K. Widmann, C. Yeamans, A. Zylstra, J. D. Lindl, L. J. Atherton, W. W. Hsing, B. J. MacGowan, B. M. Van Wousterghem, and E. I. Moses, Plasma Phys. Control. Fusion **55**, 124015 (2013).
101. D. E. Hinkel, presented at the HEDP Summer School, Columbus, OH, 15–19 July 2013.
102. D. E. Hinkel *et al.*, Phys. Plasmas **15**, 056314 (2008).
103. D. H. Froula, Phys. Rev. Lett. **103**, 045006 (2009).
104. D. H. Froula, L. Divol, R. A. London, R. L. Berger, T. Döppner, N. B. Meezan, J. Ralph, J. S. Ross, L. J. Suter, and S. H. Glenzer, Phys. Plasmas **17**, 056302 (2010).
105. J. D. Moody *et al.*, Phys. Rev. Lett. **111**, 025001 (2013).
106. R. P. J. Town *et al.*, Phys. Plasmas **18**, 056302 (2011).
107. M. D. Rosen *et al.*, High Energy Density Phys. **7**, 180 (2011).
108. T. Chapman *et al.*, Phys. Rev. Lett. **108**, 145003 (2012).
109. L. Yin *et al.*, Phys. Rev. Lett. **108**, 245004 (2012).
110. L. Yin *et al.*, Phys. Plasmas **19**, 056304 (2012).
111. L. Yin *et al.*, Phys. Plasmas **20**, 012702 (2013).

112. S. P. Regan, N. B. Meezan, L. J. Suter, D. J. Strozzi, W. L. Kruer, D. Meeker, S. H. Glenzer, W. Seka, C. Stoeckl, V. Yu. Glebov, T. C. Sangster, D. D. Meyerhofer, R. L. McCrory, E. A. Williams, O. S. Jones, D. A. Callahan, M. D. Rosen, O. L. Landen, C. Sorce, and B. J. MacGowan, *Phys. Plasmas* **17**, 020703 (2010).
113. W. Seka, D. H. Edgell, J. F. Myatt, A. V. Maximov, R. W. Short, V. N. Goncharov, and H. A. Baldis, *Phys. Plasmas* **16**, 052701 (2009).
114. N. A. Ebrahim *et al.*, *Phys. Rev. Lett.* **45**, 1179 (1980).
115. H. A. Baldis and C. J. Walsh, *Phys. Rev. Lett.* **47**, 1658 (1981).
116. D. M. Villeneuve, R. L. Keck, B. B. Afeyan, W. Seka, and E. A. Williams, *Phys. Fluids* **27**, 721 (1984).
117. C. Rousseaux *et al.*, *Phys. Fluids B* **4**, 2589 (1992).
118. B. Yaakobi, P.-Y. Chang, A. A. Solodov, C. Stoeckl, D. H. Edgell, R. S. Craxton, S. X. Hu, J. F. Myatt, F. J. Marshall, W. Seka, and D. H. Froula, *Phys. Plasmas* **19**, 012704 (2012).
119. M. V. Goldman, *Ann. Phys.* **38**, 117 (1966).
120. Y. C. Lee and P. K. Kaw, *Phys. Rev. Lett.* **32**, 135 (1974).
121. V. P. Silin and A. N. Starodub, *Sov. Phys.-JETP* **39**, 82 (1974).
122. A. B. Langdon, B. F. Lasinski, and W. L. Kruer, *Phys. Rev. Lett.* **43**, 133 (1979).
123. A. Simon, R. W. Short, E. A. Williams, and T. Dewandre, *Phys. Fluids* **26**, 3107 (1983).
124. H. X. Vu, D. F. DuBois, D. A. Russell, and J. F. Myatt, *Phys. Plasmas* **17**, 072701 (2010).
125. C. S. Liu and M. N. Rosenbluth, *Phys. Fluids* **19**, 967 (1976).
126. B. B. Afeyan and E. A. Williams, *Phys. Rev. Lett.* **75**, 4218 (1995).
127. D. T. Michel, A. V. Maximov, R. W. Short, S. X. Hu, J. F. Myatt, W. Seka, A. A. Solodov, B. Yaakobi, and D. H. Froula, *Phys. Rev. Lett.* **109**, 155007 (2012).
128. R. Yan, A. V. Maximov, and C. Ren, *Phys. Plasmas* **17**, 052701 (2010).
129. C. S. Liu, in *Advances in Plasma Physics*, edited by A. Simon and W. B. Thompson (Wiley-Interscience, New York, 1976), Vol. 6, pp. 167–174.
130. D. F. DuBois, D. A. Russell, and H. A. Rose, *Phys. Rev. Lett.* **74**, 3983 (1995).
131. D. T. Michel, A. V. Maximov, R. W. Short, J. A. Delettrez, D. Edgell, S. X. Hu, I. V. Igumenshchev, J. F. Myatt, A. A. Solodov, C. Stoeckl, B. Yaakobi, and D. H. Froula, *Phys. Plasmas* **20**, 055703 (2013).
132. J. Zhang, J. F. Myatt, A. V. Maximov, R. W. Short, D. F. DuBois, D. A. Russell, and H. X. Vu, *Bull. Am. Phys. Soc.* **57**, 299 (2012).
133. R. W. Short, J. F. Myatt, and J. Zhang, *Bull. Am. Phys. Soc.* **58**, 27 (2013).
134. H. Derblom *et al.*, *J. Geophys. Res., A, Space Phys.* **94**, 10111 (1989).
135. D. W. Phillion *et al.*, *Phys. Rev. Lett.* **49**, 1405 (1982).
136. W. Seka, R. E. Bahr, R. W. Short, A. Simon, R. S. Craxton, D. S. Montgomery, and A. E. Rubenchik, *Phys. Fluids B* **4**, 2232 (1992).
137. D. A. Russell and D. F. DuBois, *Phys. Rev. Lett.* **86**, 428 (2001).
138. R. E. Turner *et al.*, *Phys. Fluids* **27**, 511 (1984).
139. J. Meyer and Y. Zhu, *Phys. Rev. Lett.* **71**, 2915 (1993).
140. R. L. Berger and L. V. Powers, *Phys. Fluids* **28**, 2895 (1985).
141. L. V. Powers and R. J. Schroeder, *Phys. Rev. A* **29**, 2298 (1984).
142. A. N. Starodub and M. V. Filippov, *Sov. J. Plasma Phys.* **5**, 610 (1979).
143. V. Yu. Bychenkov, V. P. Silin, and V. T. Tikhonchuk, *Sov. J. Plasma Phys.* **3**, 730 (1977).
144. A. I. Avrov *et al.*, *Sov. Phys.-JETP* **45**, 507 (1977).
145. R. L. Keck, L. M. Goldman, M. C. Richardson, W. Seka, and K. Tanaka, *Phys. Fluids* **27**, 2762 (1984).
146. B. Yaakobi, I. Pelah, and J. Hoose, *Phys. Rev. Lett.* **37**, 836 (1976).
147. J. D. Hares *et al.*, *Phys. Rev. Lett.* **42**, 1216 (1979).
148. C. Stoeckl, R. E. Bahr, B. Yaakobi, W. Seka, S. P. Regan, R. S. Craxton, J. A. Delettrez, R. W. Short, J. Myatt, A. V. Maximov, and H. Baldis, *Phys. Rev. Lett.* **90**, 235002 (2003).
149. J. F. Myatt, H. X. Vu, D. F. DuBois, D. A. Russell, J. Zhang, R. W. Short, and A. V. Maximov, *Phys. Plasmas* **20**, 052705 (2013).
150. D. H. Froula, B. Yaakobi, S. X. Hu, P.-Y. Chang, R. S. Craxton, D. H. Edgell, R. Follett, D. T. Michel, J. F. Myatt, W. Seka, R. W. Short, A. Solodov, and C. Stoeckl, *Phys. Rev. Lett.* **108**, 165003 (2012).
151. W. Seka, D. H. Edgell, D. H. Froula, J. Katz, J. F. Myatt, J. Zhang, R. W. Short, D. T. Michel, A. V. Maximov, and V. N. Goncharov, *Bull. Am. Phys. Soc.* **57**, 299 (2012).
152. J. J. Schuss, T. K. Chu, and L. C. Johnson, *Phys. Rev. Lett.* **40**, 27 (1978).
153. H. A. Baldis, J. C. Samson, and P. B. Corkum, *Phys. Rev. Lett.* **41**, 1719 (1978).
154. R. K. Follett, D. T. Michel, S. X. Hu, J. F. Myatt, R. J. Henchen, J. Katz, and D. H. Froula, *Bull. Am. Phys. Soc.* **58**, 27 (2013).
155. V. N. Goncharov, T. C. Sangster, T. R. Boehly, S. X. Hu, I. V. Igumenshchev, F. J. Marshall, R. L. McCrory, D. D. Meyerhofer, P. B. Radha, W. Seka, S. Skupsky, C. Stoeckl, D. T. Casey, J. A. Frenje, and R. D. Petrasso, *Phys. Rev. Lett.* **104**, 165001 (2010).
156. J. F. Myatt, J. Zhang, J. A. Delettrez, A. V. Maximov, R. W. Short, W. Seka, D. H. Edgell, D. F. DuBois, D. A. Russell, and H. X. Vu, *Phys. Plasmas* **19**, 022707 (2012).
157. B. Yaakobi, A. A. Solodov, J. F. Myatt, J. A. Delettrez, C. Stoeckl, and D. H. Froula, *Phys. Plasmas* **20**, 092706 (2013).

158. R. Yan, A. V. Maximov, C. Ren, and F. S. Tsung, *Phys. Rev. Lett.* **103**, 175002 (2009).
159. R. Yan, C. Ren, J. Li, A. V. Maximov, W. B. Mori, Z.-M. Sheng, and F. S. Tsung, *Phys. Rev. Lett.* **108**, 175002 (2012).
160. C. Riconda *et al.*, *Phys. Plasmas* **18**, 092701 (2011).
161. S. Weber *et al.*, *Phys. Rev. E* **85**, 016403 (2012).
162. H. X. Vu, D. F. DuBois, J. F. Myatt, and D. A. Russell, *Phys. Plasmas* **19**, 102703 (2012).
163. H. X. Vu, D. F. DuBois, D. A. Russell, and J. F. Myatt, *Phys. Plasmas* **19**, 102708 (2012).
164. F. S. Tsung *et al.*, *Bull. Am. Phys. Soc.* **45**, 357 (2000); F. S. Tsung, B. B. Afeyan, and W. B. Mori, *Bull. Am. Phys. Soc.* **46**, 282 (2001); *ibid.* **48**, 45 (2003); *ibid.* **49**, 277 (2004); *ibid.* **50**, 120 (2005); *ibid.* **51**, 288 (2006); *ibid.* **52**, 43 (2007); *ibid.* **53**, 232 (2008); *ibid.* **54**, 210 (2009); *ibid.* **55**, 232 (2010); *ibid.* **56**, 329 (2011); *ibid.* **57**, 99 (2012).
165. P. A. Robinson, *Rev. Mod. Phys.* **69**, 507 (1997).
166. M. V. Goldman, *Rev. Mod. Phys.* **56**, 709 (1984).
167. D. A. Russell, D. F. DuBois, and H. X. Vu, presented at the Workshop on the Nonlinear Saturation of Stimulated Raman and Brillouin Instabilities for Plasma and Laser Parameters of Interest to Inertial Fusion Confinement and High Energy Density Science, Livermore, CA, 3–5 April 2002.
168. K. Y. Sanbonmatsu *et al.*, *Phys. Plasmas* **7**, 2824 (2000).
169. J. Zhang, J. F. Myatt, A. V. Maximov, R. W. Short, D. F. DuBois, D. A. Russell, and H. X. Vu, *Bull. Am. Phys. Soc.* **58**, 27 (2013).
170. E. Z. Gusakov, *Sov. J. Plasma Phys.* **8**, 324 (1982).
171. E. A. Williams, J. R. Albritton, and M. N. Rosenbluth, *Phys. Fluids* **22**, 139 (1979).
172. G. Laval, R. Pellat, and D. Pesme, *Phys. Rev. Lett.* **36**, 192 (1976).
173. D. R. Nicholson and A. N. Kaufman, *Phys. Rev. Lett.* **33**, 1207 (1974).
174. P. W. McKenty, R. S. Craxton, A. Shvydky, F. J. Marshall, J. A. Marozas, S. Skupsky, D. D. Meyerhofer, and R. L. McCrory, *Bull. Am. Phys. Soc.* **56**, 241 (2011).
175. I. V. Igumenshchev, D. H. Froula, D. H. Edgell, V. N. Goncharov, T. J. Kessler, F. J. Marshall, R. L. McCrory, P. W. McKenty, D. D. Meyerhofer, D. T. Michel, T. C. Sangster, W. Seka, and S. Skupsky, *Phys. Rev. Lett.* **110**, 145001 (2013).
176. P. Michel, *Physics* **6**, 37 (2013).
177. D. H. Froula, T. J. Kessler, I. V. Igumenshchev, R. Betti, V. N. Goncharov, H. Huang, S. X. Hu, E. Hill, J. H. Kelly, D. D. Meyerhofer, A. Shvydky, and J. D. Zuegel, *Phys. Plasmas* **20**, 082704 (2013).
178. D. Eimerl, E. M. Campbell, W. F. Krupke, J. Zweiback, W. L. Kruer, J. Zuegel, J. Myatt, J. Kelly, D. Froula, and R. L. McCrory, “StarDriver: A Flexible Laser Driver for Inertial Confinement Fusion and High Energy Density Physics,” submitted to the *Journal of Fusion Energy*.
179. D. J. Strozzi *et al.*, *Bull. Am. Phys. Soc.* **58**, 324 (2013).
180. M. Lafon, R. Betti, R. Nora, K. S. Anderson, T. J. B. Collins, and P. W. McKenty, *Bull. Am. Phys. Soc.* **58**, 324 (2013).
181. D. S. Montgomery, B. J. Albright, J. L. Kline, L. Yin, P. Y. Chang, J. R. Davies, G. Fiksel, D. H. Froula, R. Betti, and M. J. MacDonald, *Bull. Am. Phys. Soc.* **58**, 27 (2013).
182. V. A. Smalyuk, R. Betti, J. A. Delettrez, V. Yu. Glebov, D. D. Meyerhofer, P. B. Radha, S. P. Regan, T. C. Sangster, J. Sanz, W. Seka, C. Stoeckl, B. Yaakobi, J. A. Frenje, C. K. Li, R. D. Petrasso, and F. H. Séguin, *Phys. Rev. Lett.* **104**, 165002 (2010).
183. J. C. Fernández *et al.*, *Phys. Rev. Lett.* **77**, 2702 (1996).

First-Principles Thermal Conductivity of Deuterium for Inertial Confinement Fusion Applications

Introduction

As a grand challenge to harvest the “ultimate” energy source in a controlled fashion, inertial confinement fusion (ICF)¹ has been actively pursued for decades using both indirect-drive^{2,3} and direct-drive^{4–6} configurations. Understanding and designing ICF capsule implosions rely on simulations using multi-physics radiation–hydrodynamics codes, in which each piece of the physics models must be accurate. According to the ICF ignition criterion,^{7,8} the minimum laser energy required for ignition scales as

$$E_L(\text{kJ}) \simeq 590 \times \alpha^{1.9} \times \left(\frac{3 \times 10^7}{V_{\text{imp}}} \right)^{6.6} \times \left(\frac{P_a}{100 \text{ Mbar}} \right)^{-0.8}, \quad (1)$$

where the implosion velocity V_{imp} is in cm/s, P_a is the ablation pressure in Mbar, and the DT shell’s adiabat α is conventionally defined as $\alpha = P/P_F$, the ratio of plasma pressure to the Fermi-degeneracy pressure (P_F). This scaling law indicates that the lower the shell adiabat, the less energy needed for ignition. For lower- α implosions, however, the DT shell is in the regime in which strong coupling and degeneracy plasma effects are important and must be taken into account for meaningful implosion modeling.

The determination of accurate plasma properties is also very important for understanding low-adiabat ($\alpha \leq 2$) ICF implosions. Precise knowledge of the static and dynamic properties of ICF target materials, including ablaters and the deuterium–tritium (DT) fuel, is required under high-energy-density conditions. For instance, the equation of state (EOS) of the target materials determines how much compression can be attained under external pressures generated by x-ray/laser ablations.⁹ For this exact reason, state-of-the-art EOS experiments and calculations have been performed for ICF-relevant materials^{10–16} over the past few years. The theoretical approaches have employed first-principles methods such as the path-integral Monte Carlo (PIMC),¹⁷ coupled electron–ion Monte Carlo (CEIMC),¹⁸ and quantum molecular dynamics

(QMD)¹⁹ based on the finite-temperature density-functional theory. Besides static EOS information, the dynamic transport properties of relevant materials are in high demand for accurate ICF simulations. Transport and optical properties (thermal and electrical conductivities) of DT and ablaters not only affect the thermal conduction, but also determine the radiation transport in the imploding shell.

Soon after the introduction of the ICF concept¹ in 1972, studies followed to determine the most-appropriate models for thermal conductivity of strongly coupled and degenerate plasmas in the high-density, low-temperature regime.²⁰ The Spitzer model²¹ of thermal conductivity κ , formulated in the 1950s for ideal plasmas, breaks down in this regime since the Coulomb logarithm^{22–26} for electron–ion collisions becomes negative. Brysk *et al.*²⁰ suggested in the 1970s that the Hubbard model²⁷ of degenerate plasma be “bridged” with the Spitzer model.²¹ In the 1980s, Lee and More²⁸ applied Krook’s model to the Boltzmann equation and derived a set of transport coefficients, including κ . Meanwhile, Ichimaru and colleagues²⁹ developed the so-called “Ichimaru model” of thermal conductivity for fully ionized plasmas using the linear response theory. In addition, the average-atom model³⁰ and its improved versions have been used to numerically calculate κ for materials of interest to ICF and astrophysics, with tools such as the PURGATORIO package³¹ and the SCAALP model.³² As a result of recent progress in the *first-principles* method of quantum molecular dynamics,^{33–37} these various thermal-conductivity models of hydrogen/DT have been tested against QMD calculations.^{38–43} For ICF stagnation plasma conditions near peak compression, the pioneering QMD calculations by Recoules *et al.*³⁸ have shown an orders-of-magnitude increase in κ for the coupled and degenerate regimes when compared with the extensively used Lee–More model²⁸ for a corresponding deuterium density of $\rho_D \simeq 160 \text{ g/cm}^3$.

These recent studies have motivated us to investigate how the more-accurate results of thermal conductivity κ derived from QMD calculations could affect the hydrodynamic pre-

dictions of ICF implosions. Apparently, the change in κ for ablator materials⁴⁰ (CH, Be, or C) can enhance heat flow into the cold shell from the hot coronal plasma. This may modify the mass ablation rate, thereby altering the implosion velocity. Data over a wide range of density and temperature conditions do not currently exist from QMD calculations of κ for ICF ablator materials. The effects of updated ablator thermal conductivities on ICF target performance are left for future studies. Here, we focus on how the QMD-calculated κ of DT fuel might affect ICF simulations. Recently, Lambert *et al.*³⁹ extended their original QMD calculations of κ_{DT} for three different densities of $\rho_{\text{DT}} = 25, 200, \text{ and } 400 \text{ g/cm}^3$. They argued that the variation of κ_{DT} can change the thermodynamical path to ignition by modifying the ablation process at the boundary between the hot core and the dense cold shell. Under similar circumstances, Wang *et al.*⁴³ also computed κ_{DT} for several other high-density points of $\rho_{\text{DT}} = 200 \text{ to } 600 \text{ g/cm}^3$, using the QMD simulation package *ABINIT*.⁴⁴ They briefly discussed the effect of κ variations on hydrodynamic simulations based solely on their high-density QMD results.

As we have shown previously,⁴⁵ an imploding DT shell undergoes a wide range of densities from $\rho_{\text{DT}} \simeq 1.0 \text{ g/cm}^3$ at the shock transit stage and $\rho_{\text{DT}} \simeq 5.0 \text{ to } 10.0 \text{ g/cm}^3$ during in-flight shell acceleration, up to $\rho_{\text{DT}} \geq 300 \text{ g/cm}^3$ at stagnation (i.e., at peak compression). To cover all the relevant density points in ICF, we have performed QMD calculations of the thermal conductivity κ through the usual Kubo–Greenwood formulation⁴⁶ by spanning deuterium densities from $\rho \simeq 1.0 \text{ g/cm}^3$ to $\rho \simeq 673.5 \text{ g/cm}^3$ at temperatures varying from $T = 5000 \text{ K}$ to $T = 8,000,000 \text{ K}$. We have compared the calculated κ_{QMD} with the following “hybrid” thermal-conductivity model currently used in our hydrocode *LILAC*.⁴⁷

$$\kappa_{\text{LILAC}} = \frac{20 \times (2/\pi)^{3/2} k_{\text{B}}^{7/2} T^{5/2}}{\sqrt{m_{\text{e}}} Z_{\text{eff}} e^4} \times \frac{0.095 \times (Z_{\text{eff}} + 0.24)}{1 + 0.24 Z_{\text{eff}}} \times \frac{1}{[\ln \Lambda]_{\text{LM}}} \times f_{\text{LM}}(\rho, T). \quad (2)$$

In this hybrid model of κ_{LILAC} , the Spitzer prefactor is used in combination with the replacement of the Spitzer Coulomb logarithm by that of Lee and More, $[\ln \Lambda]_{\text{LM}}$. In addition, the Lee–More degeneracy correction function $f_{\text{LM}}(\rho, T)$ has been adopted in the following form:

$$f_{\text{LM}}(\rho, T) = 1 + \frac{3\pi^5}{51,200} \times \left(\frac{T_{\text{F}}}{T} \right)^3 \times \left[\frac{1 + 0.24 Z_{\text{eff}}}{0.095 \times (Z_{\text{eff}} + 0.24)} \right]^2, \quad (3)$$

where $T_{\text{F}} = (\hbar^2/2m_{\text{e}}k_{\text{B}})(3\pi^2n_{\text{e}})^{2/3}$ is the Fermi temperature of the electrons in a fully ionized plasma, k_{B} is the Boltzmann constant, and m_{e} and n_{e} are the mass and number density of electrons. The effective charge of ions is defined as $Z_{\text{eff}} = \langle Z^2 \rangle / \langle Z \rangle$ averaging over the species ($Z_{\text{eff}} = 1$ for fully ionized DT plasmas). In general, our QMD results showed a factor-of-3 to 10 enhancement in κ_{QMD} over κ_{LILAC} within the ICF-relevant density and temperature ranges.

To test the effects of κ_{QMD} on ICF implosions, we have fitted the calculated κ_{QMD} with a fifth-order polynomial function of the coupling parameter $\Gamma = 1/(r_{\text{S}}k_{\text{B}}T)$ and the degeneracy parameter $\theta = T/T_{\text{F}}$. The Wigner–Seitz radius r_{S} is related to the electron number density $n_{\text{e}} = 3/(4\pi r_{\text{S}}^3)$. The fitted formula of κ_{QMD} is then applied in *LILAC* to simulate a variety of cryogenic DT implosions on OMEGA as well as direct-drive designs at the National Ignition Facility (NIF). Compared with simulations using κ_{LILAC} , we found variations of up to ~20% in the target-performance predictions using the more-accurate κ_{QMD} . The lower the adiabat of imploding shells, the stronger the coupling and degeneracy effects of κ_{QMD} .

This article is organized as follows: The QMD method is described briefly in the next section, which also examines other methods and experiments on deuterium plasma properties; the calculated κ_{QMD} of deuterium for a wide range of density and temperature points is presented and compared with κ_{LILAC} ; the κ_{QMD} effects on ICF implosion dynamics are discussed in detail, followed, in the final section, by the summary.

The Quantum Molecular Dynamics Method

We have used the QMD method for simulating warm, dense deuterium plasmas. Since the QMD procedures have been well documented elsewhere,^{34,48–50} we present only a brief description of its basics. The Vienna *ab-initio* Simulation Package (VASP)^{51,52} has been employed within the isokinetic ensemble (number of particles, volume, and temperature constant). VASP is based on the finite-temperature density-functional theory (FTDFT). Specifically, the electrons are treated quantum mechanically by plane-wave FTDFT calculations using the

Perdew-Burke-Ernzerhof generalized gradient approximation (GGA) for the exchange-correlation term. The electron-ion interaction was modeled by either a projector argumented wave (PAW) pseudopotential⁵³ or the pure Coulombic potential. The system was assumed to be in local thermodynamic equilibrium with equal electron and ion temperatures ($T_e = T_i$). The ion temperature was kept constant by simple velocity scaling.

A periodically replicated cubic cell was used with equal numbers of electrons and deuterium ions. The plasma density and the number of D atoms determined the volume of the cell. For the present simulations of densities below $\rho_D = 15.7 \text{ g/cm}^3$, we employed 128 atoms and the PAW pseudopotential. For high densities ($\rho_D \geq 15.7 \text{ g/cm}^3$), a varying number of atoms ($N = 216$ to 1000) were used and incorporated with the pure Coulombic potential.⁵⁴ For each molecular dynamics (MD) step, a set of electronic state functions for each k point was self-consistently determined for an ionic configuration. Then, the ions were moved classically with a velocity Verlet algorithm according to the combined ionic and electronic forces. Repeating the two steps propagated the system in time, resulting in a set of self-consistent ion trajectories and electronic state functions. These trajectories provide a consistent set of static, dynamical, and optical properties of the deuterium plasmas.

All of our QMD calculations employed only a Γ -point ($\mathbf{k} = 0$) sampling of the first Brillouin zone in the cubic cell; such a sampling has been shown to produce properties of sufficient accuracy in this regime.^{39,43} For low-density points, a tight PAW pseudopotential was used with a maximum energy cutoff of $E_{\text{max}} = 700 \text{ eV}$ to avoid core overlap. The Coulombic potential for high-density points had a cutoff energy varying from $E_{\text{max}} = 1000 \text{ eV}$ to $E_{\text{max}} = 8000 \text{ eV}$. A large number of energy bands N_b (up to 3500) were included to ensure high accuracy (the lowest population down to a level of 10^{-5}). To benchmark our current QMD calculations, we first compare the EOS results with previous PIMC calculations¹¹ for a deuterium density of $\rho_D = 5.4 \text{ g/cm}^3$. Both the QMD calculation using PAW pseudopotential and the PIMC simulation used 128 atoms in the cell. The total pressure is a sum of the electronic pressure (averaging over the MD times) and the classical ionic pressure; the internal energy is referenced to the ground-state energy ($E_0 = -15.9 \text{ eV}$) of a D_2 molecule. The EOS results shown in Fig. 137.63 demonstrated excellent agreement within the overlapping temperature range where both methods are valid. In addition, we have also performed convergence tests of QMD calculations by using the Coulombic potential and more atoms ($N = 343$) for this density. The results are plotted

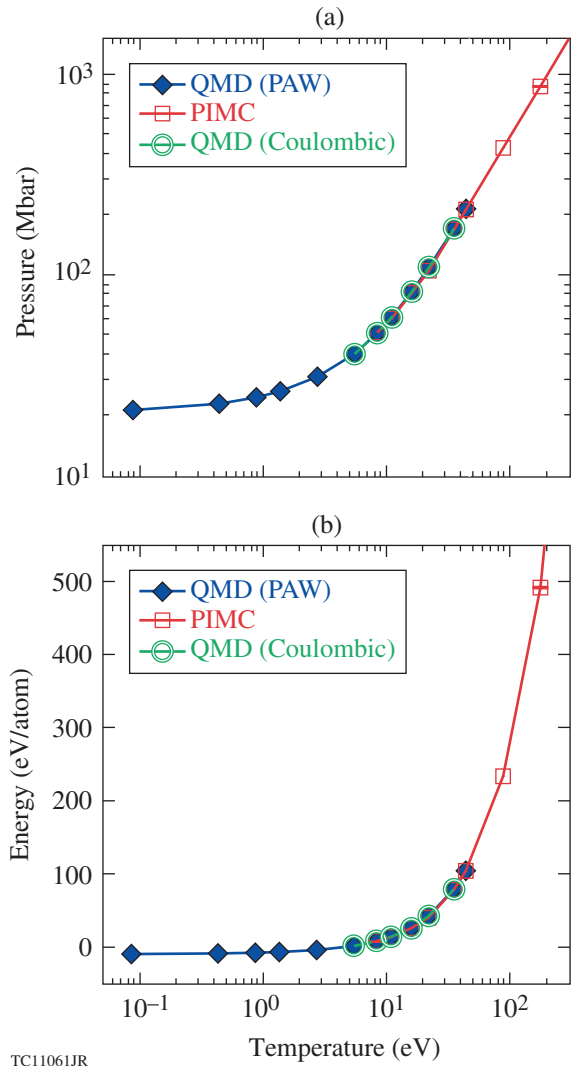


Figure 137.63

The equation-of-state comparison between quantum molecular dynamics (QMD) and path-integral Monte Carlo (PIMC) calculations for deuterium density at $\rho = 5.4 \text{ g/cm}^3$: (a) pressure versus temperature and (b) internal energy versus temperature. PAW: projector-argumented wave.

by green open circles in Fig. 137.63, which are almost identical to the PAW calculations.

To calculate the electron thermal conductivity of a plasma, we consider the linear response of the plasma to an electric field \mathbf{E} and a temperature gradient ∇T , which induce the electric current \mathbf{j}_e and the heat flux \mathbf{j}_q :

$$\mathbf{j}_e = \left(eL_{11}\mathbf{E} - \frac{L_{12}\nabla T}{T} \right) / e, \quad (4)$$

$$\mathbf{j}_q = \left(eL_{21}\mathbf{E} - \frac{L_{22}\nabla T}{T} \right) / e. \quad (5)$$

For plasmas having no electric current ($\mathbf{j}_e = 0$), the above equations in combination with the definition of $\mathbf{j}_q = -\kappa\nabla T$ give the thermal conductivity

$$\kappa = \frac{1}{T} \left(L_{22} - \frac{L_{12}^2}{L_{11}} \right) \quad (6)$$

with the Onsager coefficients given by L_{ij} . In the absence of temperature gradient ($\nabla T = 0$), Eq. (4) reduces to Ohm's law with the electrical conductivity of $\sigma = L_{11}$. The frequency-dependent Onsager coefficients can be calculated using the Kubo–Greenwood formalism:⁴⁶

$$L_{ij}(\omega) = \frac{2\pi(-e)^{4-i-j}}{3Vm_e^2\omega} \sum_{m,n} F_{mn} |D_{mn}|^2 \times \left(\frac{E_m + E_n}{2} - H \right)^{i+j-2} \delta(E_m - E_n - \hbar\omega), \quad (7)$$

where V is the atomic volume, $E_m(E_n)$ is the energy of the m th (n th) state, and H is the enthalpy (per atom) of the system. The quantity of F_{mn} is the difference between the Fermi–Dirac distributions for the involved states m and n at temperature T . The velocity dipole matrix elements D_{mn} can be computed from the VASP wave functions. In practical calculations, the

δ function in Eq. (7) is approximated by a Gaussian function of width ΔE ($\simeq 0.1$ to 0.5 eV). In addition, $L_{ij} \equiv L_{ij}(0)$ is used in Eq. (6). The resulting κ was averaged over at least ten snapshots of uncorrelated configurations along the MD trajectories. The determination of κ required, for convergence, a much larger number of energy bands ($\sim 3\times$) than for the MD simulation.

Since no direct measurements exist for the thermal conductivity in deuterium plasmas, we compared our QMD calculations to a related optical property, the reflectivity, which has been determined along the principal Hugoniot in shock-timing experiments^{55–58} using the velocity interferometer system for any reflector (VISAR). The reflectivity is determined by

$$R(\omega) = \frac{[1 - n(\omega)]^2 + k(\omega)^2}{[1 + n(\omega)]^2 + k(\omega)^2}, \quad (8)$$

with the real and imaginary parts of refraction indices $[n(\omega), k(\omega)]$ that can be computed from the dielectric function of $\epsilon(\omega) = \epsilon_1(\omega) + i\epsilon_2(\omega)$. The dielectric functions are obtained from the real electric conductivity $\sigma_1(\omega) = L_{11}(\omega)$ and its imaginary part $\sigma_2(\omega)$ determined by a principal-value integral of $\sigma_1(\omega)$. In Fig. 137.64, the calculated reflectivities of deuterium as a function of shock speed for different VISAR wavelengths are compared with both Nova⁵⁵ and recent OMEGA measurements along the principal Hugoniot. The OMEGA experiments were taken from a decayed shock in deuterium over many shots. This experimental confirmation, together with agreement with

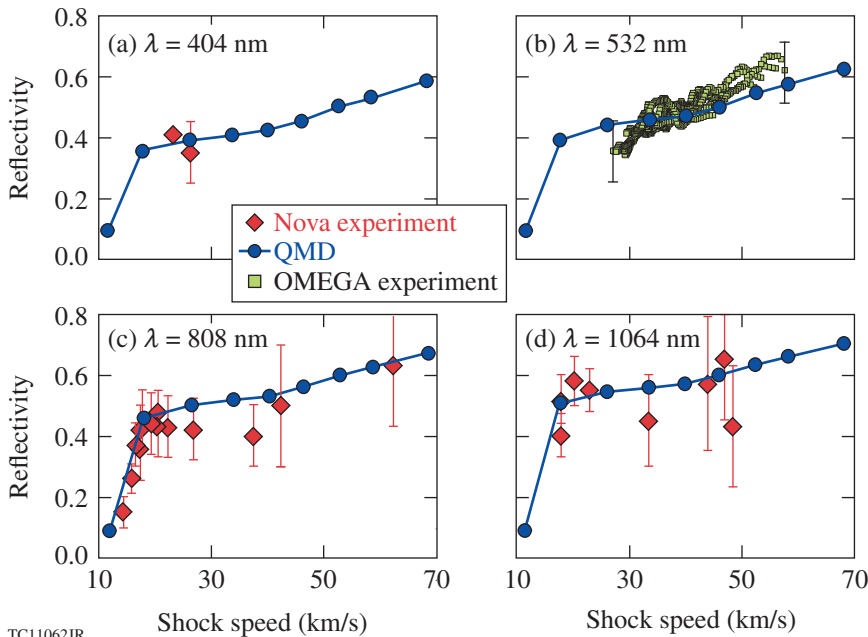


Figure 137.64

The QMD-calculated reflectivity of deuterium shock as a function of shock speed along the principal Hugoniot, which is compared to both a previous Nova measurement⁵⁵ and a recent OMEGA experiment for different VISAR wavelengths: (a) $\lambda = 404$ nm, (b) $\lambda = 532$ nm, (c) $\lambda = 808$ nm, and (d) $\lambda = 1064$ nm.

TC11062JR

other first-principle results,⁵⁹ lends credence to the L_{11} coefficients produced in this study and, in turn, to the other similarly calculated Onsager coefficients that determine κ .

Thermal Conductivity of Deuterium for a Wide Range of Densities and Temperatures

The QMD calculations of deuterium thermal conductivity have been performed for a wide range of densities [$\rho = 1.0$ to 673.5 g/cm^3], at temperatures varying from $T = 5000 \text{ K}$ to $T = 8,000,000 \text{ K}$. For each density point, the κ_{QMD} calculations have been performed to the highest temperature approaching $T \simeq T_F$. (Tabulated results of κ_{QMD} are found in the **Supplementary Material**, p. 92.) To test the effects of κ_{QMD} on ICF implosions, we have fitted the κ_{QMD} results to the following function (in a similar format of κ_{LILAC}):

$$\kappa_{\text{QMD}} = \frac{20 \times (2/\pi)^{3/2} k_B^{7/2} T^{5/2}}{\sqrt{m_e} Z_{\text{eff}} e^4} \times \frac{0.095 \times (Z_{\text{eff}} + 0.24)}{1 + 0.24 Z_{\text{eff}}} \times \frac{1}{(\ln \Lambda)_{\text{QMD}}}, \quad (9)$$

with the same Spitzer prefactor as used in κ_{LILAC} and $Z_{\text{eff}} = 1$. The generalized QMD Coulomb logarithm has the following form:

$$(\ln \Lambda)_{\text{QMD}} = \exp \left\{ \alpha_0 + \sum_{i=1}^5 \left[\alpha_i (\ln \Gamma)^i + \beta_i (\ln \theta)^i \right] \right\}. \quad (10)$$

This fifth-order polynomial function of coupling and degeneracy parameters (Γ, θ) has been fitted to the κ_{QMD} data using multivariable least-squares fitting. To make κ_{QMD} converge to κ_{LILAC} at the ideal plasma conditions ($\Gamma \ll 1$ and $\theta \gg 1$), we have added the high-temperature points of κ_{LILAC} into the data set for the global fitting. The resulting fitting parameters are:

$$\begin{aligned} \alpha_0 &= -0.74015 \\ \alpha_1 &= -0.18146 \\ \alpha_2 &= +6.39644 E-004 \\ \alpha_3 &= +1.47954 E-003 \\ \alpha_4 &= -1.23362 E-004 \\ \alpha_5 &= -2.58107 E-005 \\ \beta_1 &= +0.86155 \\ \beta_2 &= -0.10570 \\ \beta_3 &= -6.75783 E-003 \\ \beta_4 &= -1.69007 E-004 \\ \beta_5 &= +3.49201 E-004 \end{aligned} \quad (11)$$

The fit results of $(\ln \Lambda)_{\text{QMD}}$ are plotted in Figs. 137.65(a) and 137.65(b) as a function of $\ln(\Gamma)$ and $\ln(\theta)$, respectively. Overall,

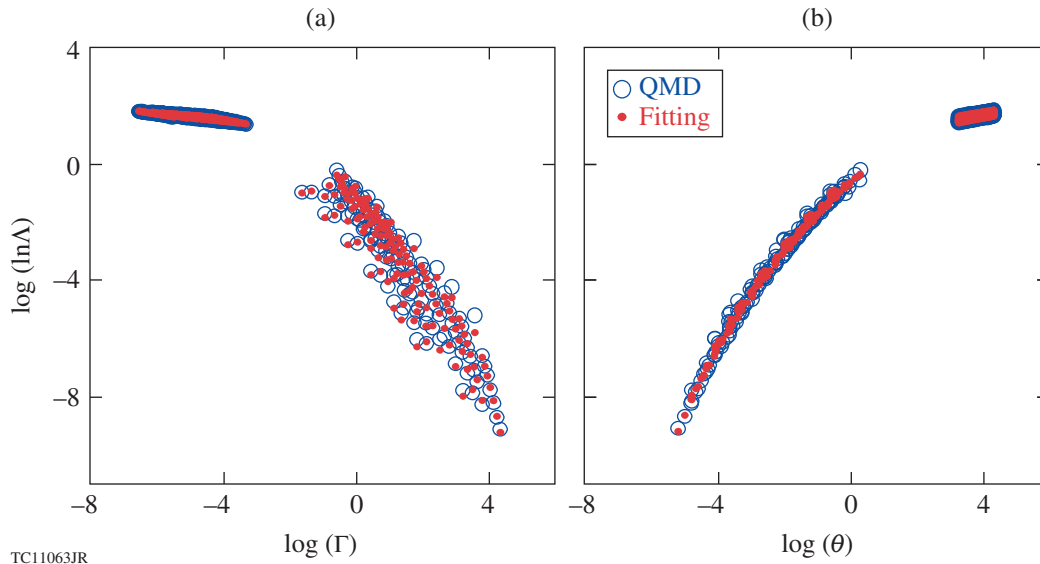


Figure 137.65 The generalized Coulomb logarithm, derived from QMD-calculated thermal conductivities for different densities and temperatures, is fitted with the polynomial function [Eq. (10)] of (a) the coupling parameter (Γ) and (b) the degeneracy parameter (θ). The values of $\ln \Lambda$ at high temperatures [i.e., $\log(\ln \Lambda) > 0$] are converged to the standard $LILAC$ values.

the global fitting with the above parameters gives only a small error of $\sim 5\%$.

Comparisons of κ_{QMD} with κ_{LILAC} are plotted in Figs. 137.66 and 137.67 for deuterium densities of $\rho = 2.5, 10.0, 43.1,$ and 199.6 g/cm^3 . The green dashed lines represent the thermal con-

ductivity currently used in our hydrocode *LILAC*, while the blue solid triangles represent the QMD results. The red solid line is the QMD fit discussed above. We observe that κ_{QMD} is higher than κ_{LILAC} by a factor of 3 to 10 in the coupled and degenerate regimes ($\Gamma > 1, \theta < 1$). The QMD-fit line merges into κ_{LILAC} at a high- T regime ($T > 10 T_F$), as expected.

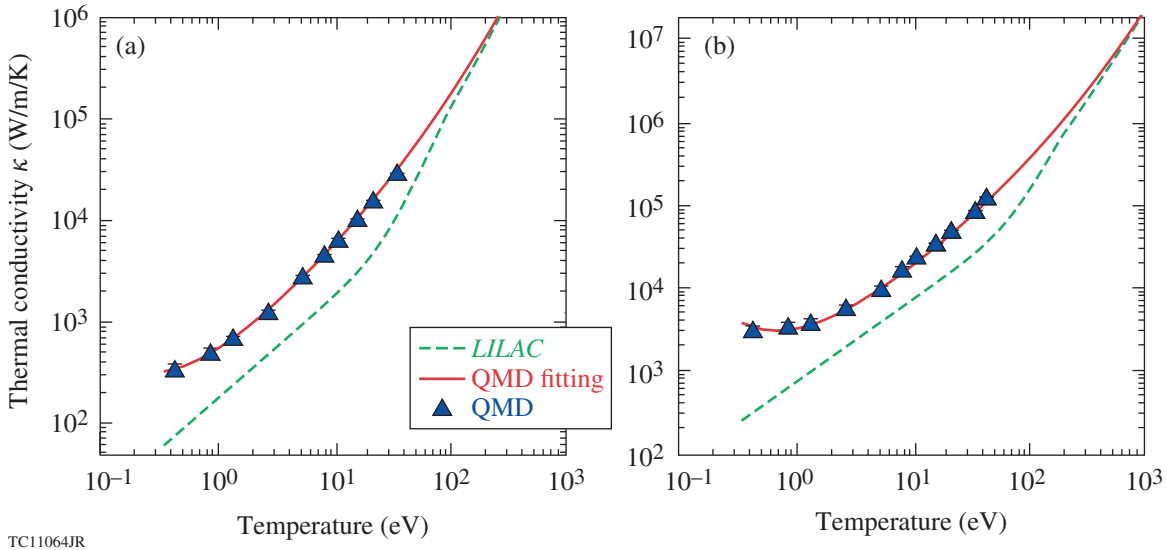


Figure 137.66

The thermal conductivities from first-principles QMD calculations, the QMD-fitting formula [Eq. (10)], and the hybrid model used in *LILAC* are plotted as a function of temperature for deuterium densities of (a) $\rho = 2.5 \text{ g/cm}^2$ and (b) $\rho = 10.0 \text{ g/cm}^2$.

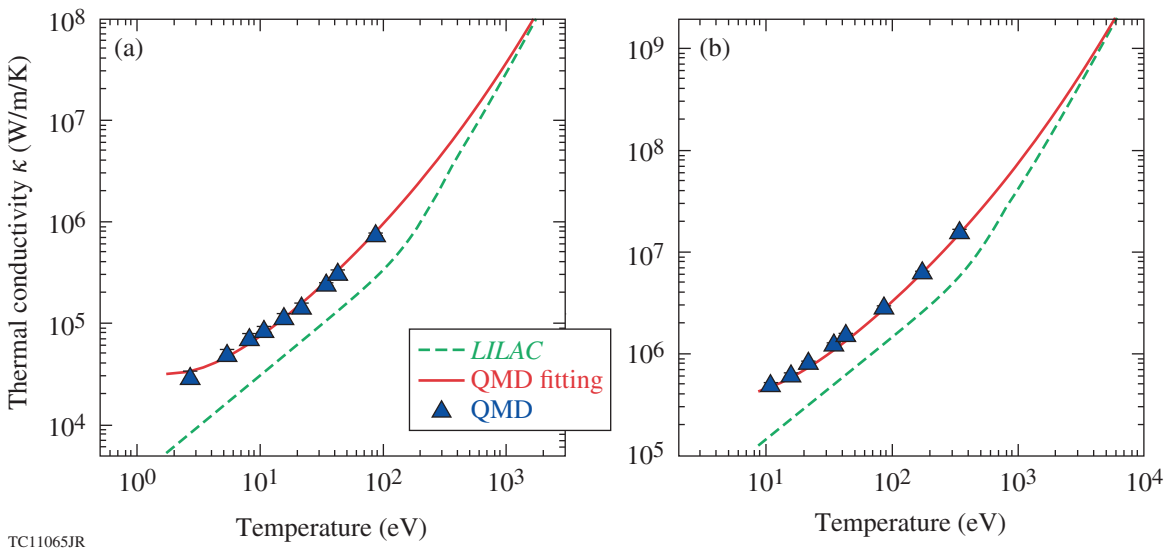


Figure 137.67

The thermal conductivities from first-principles QMD calculations, the QMD-fitting formula [Eq. (10)], and the hybrid model used in *LILAC* are plotted as a function of temperature for deuterium densities of (a) $\rho = 43.1 \text{ g/cm}^2$ and (b) $\rho = 199.6 \text{ g/cm}^2$.

Effects of κ_{QMD} on ICF Implosions

To test how the QMD-predicted thermal conductivity of DT affects ICF implosions, we have incorporated the κ_{QMD} fit into our one-dimensional (1-D) radiation–hydrocode *LILAC*. The hydrodynamic simulations employed the flux-limited thermal conduction model^{60–63} with a flux limiter of $f=0.06$. Two cryogenic DT target implosions on OMEGA and three NIF direct-drive designs have been examined. These ICF implosions span a wide range of implosion velocities and adiabats. The adiabat (α) characterizes the plasma degeneracy degree of the imploding DT shell: the lower the adiabat, the more degenerate the DT plasma.

First, we show simulations of two cryogenic DT implosions on OMEGA in Figs. 137.68 and 137.69. A typical OMEGA cryogenic DT target has a diameter of $\sim 860 \mu\text{m}$, which consists of a plastic ablator with a thickness of 8 to $11 \mu\text{m}$ and a layer of 45 to $65 \mu\text{m}$ of DT ice. In Fig. 137.68(a), the laser pulse has a relatively high first picket, which sets up the DT shell in a high adiabat of $\alpha \simeq 4$. The density and ion temperature profiles at the peak compression are plotted in Fig. 137.68(b). The blue dashed line represents the case of using standard κ_{LILAC} in the simulation, while the red solid line represents the κ_{QMD} simulation. Figure 137.68(b) shows that there is little change in the target performance for this high-adiabat implosion. In the end, the neutron yields are predicted to be 3.32×10^{14} (κ_{LILAC}) and 3.24×10^{14} (κ_{QMD}) for the two cases.

Predictions for the low-adiabat ($\alpha \simeq 2.2$) implosion are shown in Fig. 137.69. Figure 137.69(a) plots the laser pulse used for this OMEGA implosion. The in-flight plasma conditions are illustrated in Fig. 137.69(b) at $t = 2.7 \text{ ns}$, just before stagnation, in which the mass density and electron temperature are drawn as a function of the target radius. Noticeable differences in electron-temperature profiles are seen for the two cases using κ_{QMD} and κ_{LILAC} ; the peak density changed slightly when κ_{QMD} was used. These differences can affect the target performance at stagnation ($t = 2.84 \text{ ns}$), as shown by Fig. 137.69(c). Finally, Fig. 137.69(d) indicates that the neutron yield is $\sim 6\%$ lower in the κ_{QMD} simulation than for κ_{LILAC} . Table 137.VI summarizes the comparison of other quantities for the two simulations. The neutron-averaged compression ρR and T_i are hardly changed, but the peak density and neutron yield vary by $\sim 6\%$.

Table 137.VI: Comparison of an OMEGA implosion ($\alpha \simeq 2.2$) predicted using κ_{LILAC} versus κ_{QMD} .

	κ_{LILAC}	κ_{QMD}
$\langle \rho R \rangle_n$	298 mg/cm ²	296 mg/cm ²
$\langle T_i \rangle_n$	4.66 keV	4.64 keV
$\langle P \rangle_n$	197 Gbar	194 Gbar
$\langle \rho \rangle_{\text{peak}}$	380.8 g/cm ³	361.7 g/cm ³
Yield	5.34×10^{14}	5.05×10^{14}

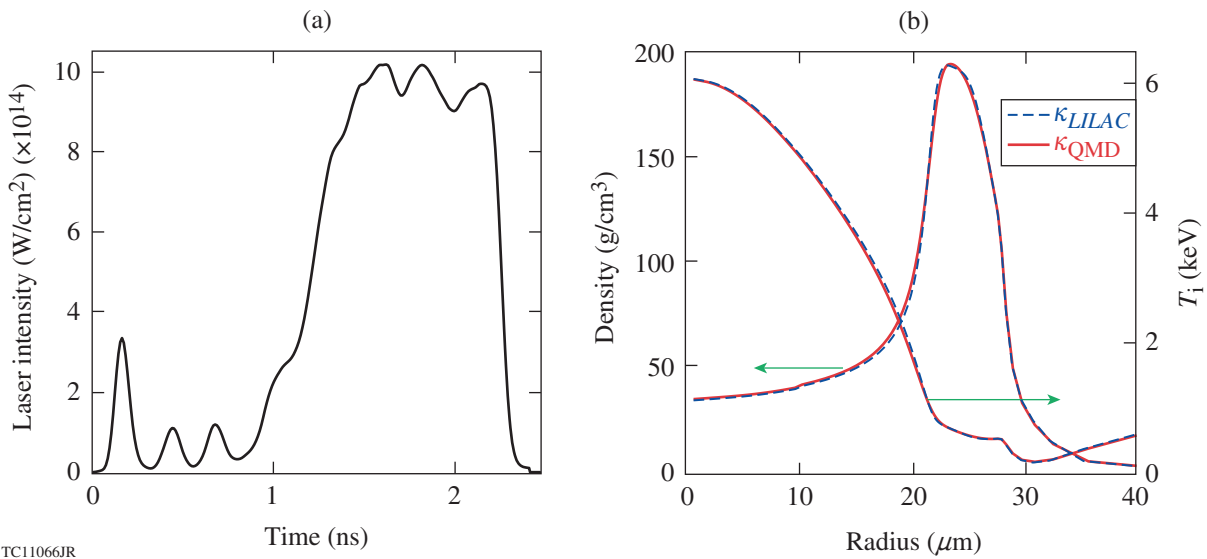


Figure 137.68

(a) The laser pulse shape used for a high-adiabat ($\alpha = 4$) cryogenic DT implosion on OMEGA (the $\phi = 868.8\text{-}\mu\text{m}$ capsule consists of $47 \mu\text{m}$ of DT ice with an $8.4\text{-}\mu\text{m}$ -thick plastic ablator); (b) comparisons of the density and ion-temperature profiles at peak compression for the two hydrodynamic runs using κ_{LILAC} (blue dashed lines) and κ_{QMD} (red solid lines), respectively. Very little difference is seen in target performance for the two thermal-conductivity models used for such a high-adiabat implosion. Green arrows indicate the vertical axis that applies to each curve.

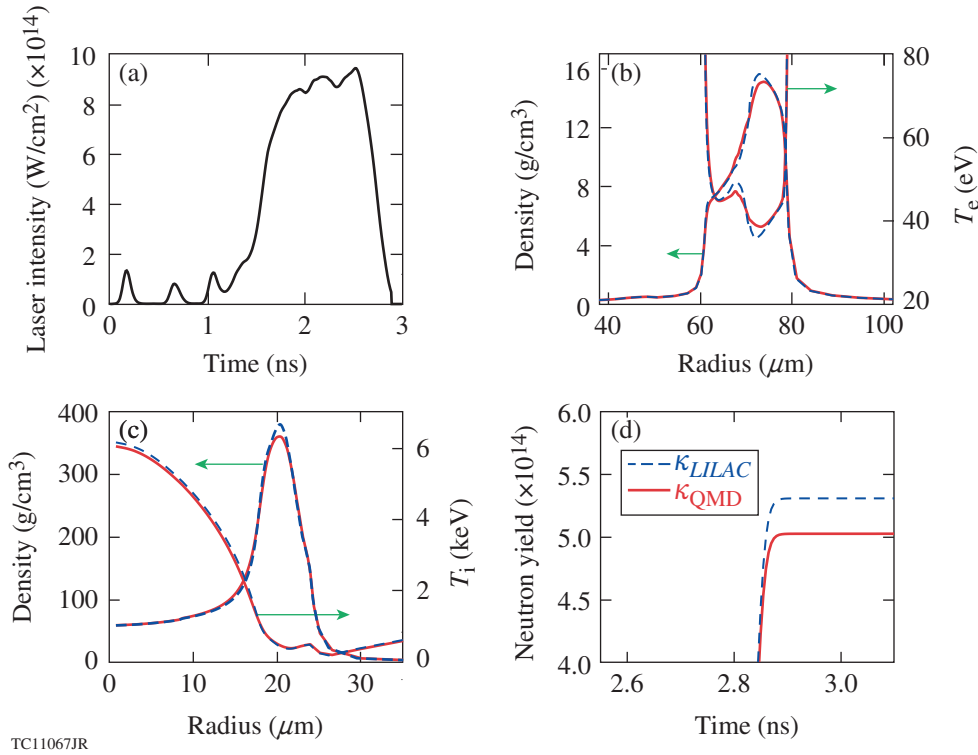


Figure 137.69

(a) The laser pulse shape used for a low-adiabat ($\alpha = 2.2$) cryogenic DT implosion on OMEGA (the $\phi = 860.6\text{-}\mu\text{m}$ capsule consists of $49\ \mu\text{m}$ of DT ice with an $8.3\text{-}\mu\text{m}$ -thick plastic ablator). [(b),(c)] Comparisons of the density and temperature profiles at the beginning of the deceleration phase and at peak compression, respectively, for the two hydrodynamic simulations using κ_{LILAC} (blue dashed lines) and κ_{QMD} (red solid lines). (d) The neutron yields as a function of time are plotted for the two cases. A modest variation ($\sim 6\%$) in target performance is seen in such low-adiabat OMEGA implosions, when κ_{QMD} is compared to the hybrid *LILAC* model.

Next we discuss the κ_{QMD} effects on three different direct-drive-ignition designs for the NIF. These NIF designs have slightly different target sizes varying from $\phi = 3294\ \mu\text{m}$ to $\phi = 3460\ \mu\text{m}$. The thickness of the DT-ice layer changes from $d = 125\ \mu\text{m}$ to $d = 220\ \mu\text{m}$; all targets have a plastic ablator at somewhat different thicknesses of 22 to $30\ \mu\text{m}$. We discuss the κ_{QMD} effects on the performance of three NIF designs from a mid-adiabat ($\alpha = 3.2$) implosion to a very low adiabat ($\alpha = 1.7$) design. Figure 137.70 shows first the mid-adiabat ($\alpha = 3.2$) design: (a) the triple-picket pulse shape (total energy of $1.5\ \text{MJ}$) and (b) the density and ion-temperature profiles at the bang time ($t = 13.78\ \text{ns}$, i.e., the time for peak neutron production). Similar to what was seen in Fig. 137.68, only small differences between κ_{QMD} and κ_{LILAC} simulations are observed for this mid-adiabat NIF design. The comparison of target performance is summarized in Table 137.VII, in which the differences in neutron-averaged ρR , T_i , pressure $\langle P \rangle_n$, hot-spot radius R_{hs} , hot-spot convergence ratio C_{hs} , neutron yield, and gain are all within $\sim 2\%$.

Figure 137.71 illustrates the simulation results for a slightly lower adiabat ($\alpha \simeq 2.5$), high-convergence NIF design. Similar to Fig. 137.69 for the $\alpha = 2.2$ OMEGA implosion, Figs. 137.71(a)–137.71(d) plot (a) the pulse shape (total energy of $1.6\ \text{MJ}$),

 Table 137.VII: Comparison of a mid-adiabat ($\alpha = 3.2$) NIF design simulated with κ_{LILAC} versus κ_{QMD} .

	κ_{LILAC}	κ_{QMD}
$\langle \rho R \rangle_n$	$0.654\ \text{g}/\text{cm}^2$	$0.655\ \text{g}/\text{cm}^2$
$\langle T_i \rangle_n$	$12.2\ \text{keV}$	$12.1\ \text{keV}$
$\langle P \rangle_n$	$250\ \text{Gbar}$	$248\ \text{Gbar}$
$\langle \rho \rangle_{\text{peak}}$	$337.4\ \text{g}/\text{cm}^3$	$331.8\ \text{g}/\text{cm}^3$
R_{hs}	$91.4\ \mu\text{m}$	$91.3\ \mu\text{m}$
C_{hs}	18.9	18.9
Yield	6.45×10^{18}	6.33×10^{18}
Gain	12.1	11.8

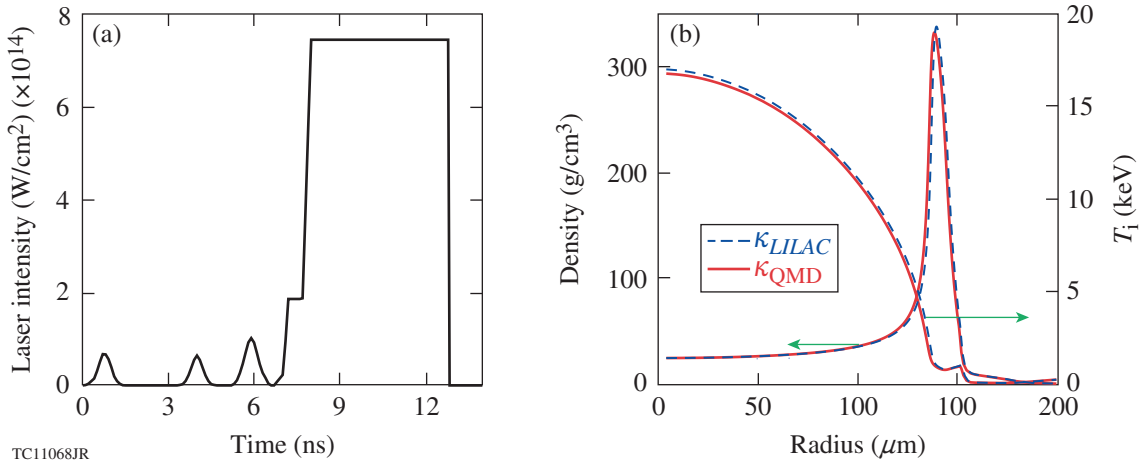


Figure 137.70 Similar to Fig. 137.68 but for a NIF-scale implosion: (a) The laser pulse shape for a mid-adiabat ($\alpha = 3.2$), 1.5-MJ direct-drive NIF design (the $\phi = 3460\text{-}\mu\text{m}$ capsule consists of $220\ \mu\text{m}$ of DT ice with a $30\text{-}\mu\text{m}$ -thick plastic ablator); (b) comparisons of the density and ion-temperature profiles at the peak compression for the two hydrodynamic runs using κ_{LILAC} (blue dashed lines) and κ_{QMD} (red solid lines), respectively. The effects of using different κ are small for such mid-adiabat designs.

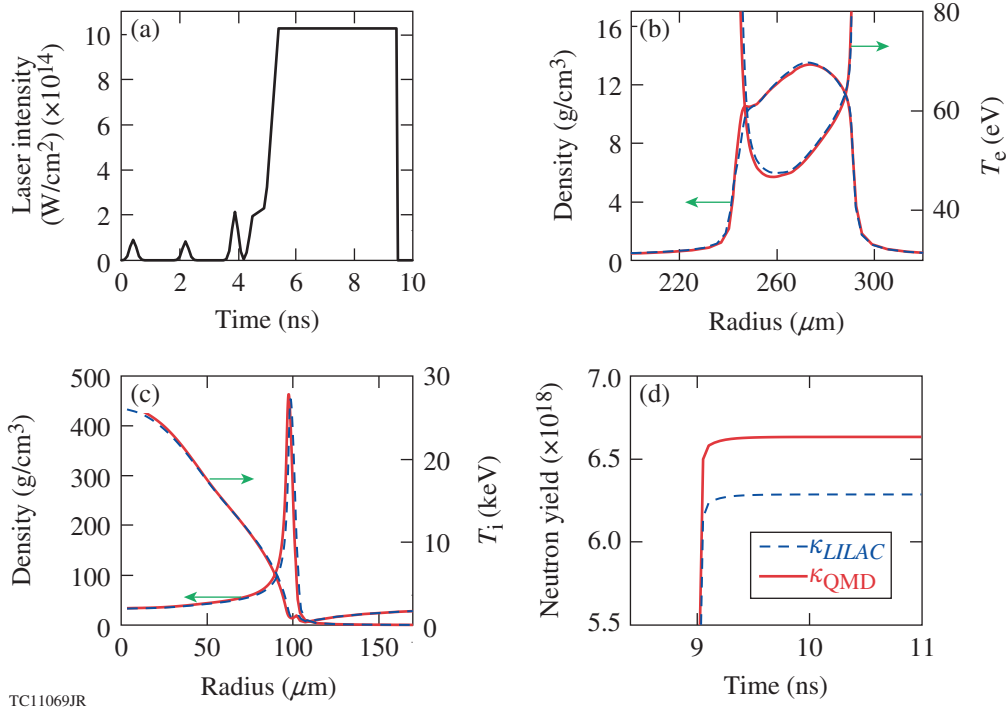


Figure 137.71 Tests on a high-implosion-velocity NIF design: (a) The laser pulse shape ($\alpha = 2.5$) has a total energy of 1.6 MJ (the $\phi = 3294\text{-}\mu\text{m}$ capsule consists of $125\ \mu\text{m}$ of DT ice with a $22\text{-}\mu\text{m}$ -thick plastic ablator). Panels (b) and (c) compare the density and temperature profiles at the beginning of the deceleration phase and at peak compression, respectively, for the two hydrodynamic simulations using κ_{LILAC} (blue dashed lines) and κ_{QMD} (red solid lines). The neutron yields as a function of time are plotted in panel (d) for the two cases. The use of κ_{QMD} modestly changes the 1-D prediction of implosion performance ($\sim 6\%$).

(b) the in-flight density and electron-temperature profiles at $t = 8.6$ ns, (c) the bang-time density and ion-temperature profiles at $t = 8.91$ ns, and (d) the final neutron yield. Again, some slight differences in the electron temperature at the back surface of the shell can be seen in Fig. 137.71(b). The observables predicted by the two hydrodynamic simulations using κ_{QMD} in contrast to κ_{LILAC} are summarized in Table 137.VIII. Overall, a level of $\sim 6\%$ increase in target performance is seen in the κ_{QMD} simulation when compared to the standard κ_{LILAC} case.

Table 137.VIII: Comparison of a low-adiabat ($\alpha = 2.5$) NIF design simulated with κ_{LILAC} versus κ_{QMD} .

	κ_{LILAC}	κ_{QMD}
$\langle \rho R \rangle_n$	0.646 g/cm ²	0.661 g/cm ²
$\langle T_i \rangle_n$	20.8 keV	21.5 keV
$\langle P \rangle_n$	715 Gbar	763 Gbar
$\langle \rho \rangle_{\text{peak}}$	456.8 g/cm ³	466.9 g/cm ³
R_{hs}	56.2 μm	53.8 μm
C_{hs}	29.3	30.6
Yield	6.3×10^{18}	6.7×10^{18}
Gain	11.1	11.7

We further analyze the implosion dynamics of the NIF design shown in Fig. 137.71. The noticeable ρ/T_e differences at the back of the shell illustrated by Fig. 137.71(b) must come from the different shock dynamics in early stages of the implosion. To further explore the differences, in Fig. 137.72 we have plotted the DT plasma conditions at the shock transit stage. In Fig. 137.72(a), the density and temperature profiles are displayed for a snapshot at $t = 4.0$ ns. To clearly see the differences, we have plotted these profiles as a function of the simulation Lagrangian cell number. At this snapshot, the first shock [dashed circle in Fig. 137.63(a)] has propagated to near the back surface (at the 150th cell) of the DT ice layer. An interesting difference between two simulations can be clearly seen at the first shock front (near the 165th cell), in which the temperature front (at the 175th cell) predicted by the κ_{LILAC} simulation does *not* follow the density front of the shock. This occurs because the standard κ_{LILAC} significantly underestimates the thermal conductivity by an order of magnitude, for the shocked-DT plasma condition of $\rho_{\text{DT}} \simeq 1$ g/cm³ and $T_e \simeq 1$ to 2 eV. The reduced thermal conductivity in κ_{LILAC} decreases the heat flow behind the shock front. On the contrary, the κ_{QMD} simulation (red solid lines) indicates the same shock-front location for both density and temperature, as expected. Differences in both density and temperature are also seen after the second

shock [near the 260th cell shown in Fig. 137.72(a)]. The κ_{LILAC} simulation predicts more “artificial” fluctuations in density and temperature after the second shock. Figure 137.72(b) shows another snapshot at $t = 4.8$ ns, when the first shock breaks out at the back of the DT ice layer into the DT gas. A large difference in electron-temperature profile is observed for the two simulations: the instant heat conduction in the κ_{QMD} case results in

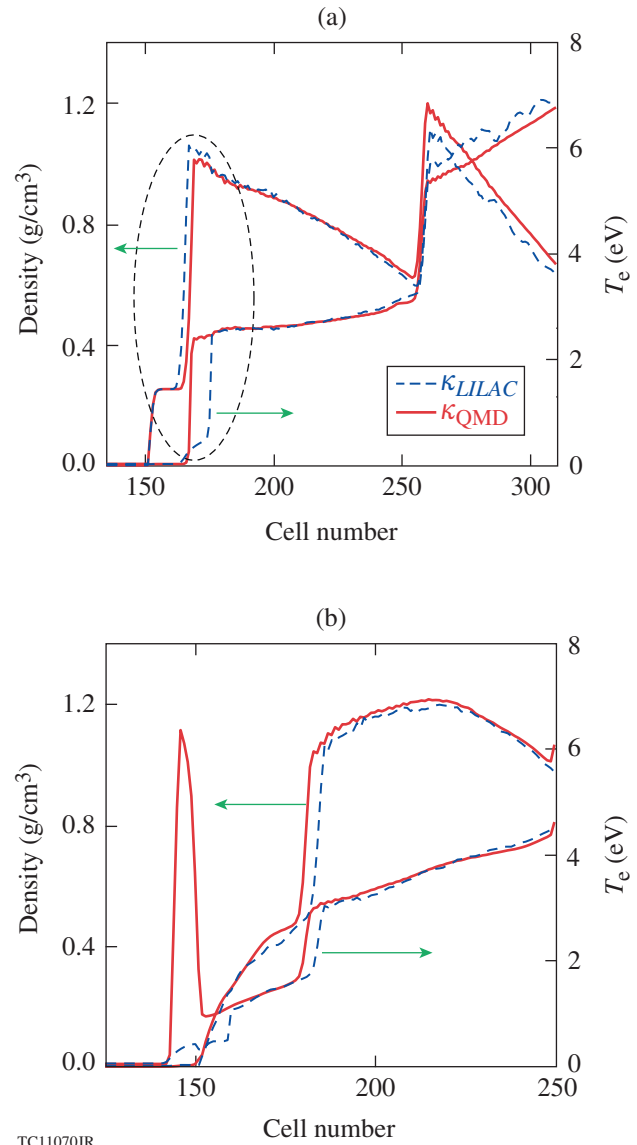


Figure 137.72

The predicted shock conditions during the shock transit stage in the DT ice, for the NIF design plotted in Fig. 137.71. The density and electron temperature are plotted as a function of the Lagrangian cell numbers for times at (a) $t = 4.0$ ns and (b) $t = 4.8$ ns. Again, the two cases of using κ_{LILAC} (blue dashed lines) and κ_{QMD} (red solid lines) are compared. The dashed circle highlights the first shock.

the immediate heating up of the releasing back surface, which is in contrast to the delayed heating in the κ_{LILAC} simulation. These different shock dynamics at the early stage of implosion cause the observable density–temperature variations late in the implosion, plotted in Fig. 137.71(b). This is the major contribution responsible for the final difference in target performance, which is discussed below.

Finally, the very low adiabat ($\alpha \simeq 1.7$) NIF design is examined in Fig. 137.73 and Table 137.IX. The implosion is designed to be driven by a 1.2-MJ pulse shape shown in Fig. 137.73(a), which has a ramping and low-intensity main pulse to avoid possible preheat from two-plasmon-decay–induced hot electrons.^{64,65} The implosion velocity for this design is about 3.3×10^7 cm/s. Since the adiabat is so low that the DT-plasma conditions for the in-flight shell lie deeply within the more-degenerate and coupled regime, where κ_{QMD} is much higher than κ_{LILAC} , the effects of using κ_{QMD} are dramatically increased when compared to the higher-adiabat implosions discussed above. From Table 137.IX and Fig. 137.73, an $\sim 20\%$ variation in target performance (yield and gain) is observed in

the predictions of the two cases. Figure 137.73(b) shows that the simulation using κ_{QMD} predicts a lower electron-temperature profile for the back of the shell ($R \simeq 420 \mu\text{m}$). This results in a larger peak density of the shell and higher T_i at the bang time for the κ_{QMD} case, illustrated by Fig. 137.73(c), thereby leading to more neutron yields and gain.

Table 137.IX: Comparison of a very low adiabat ($\alpha = 1.7$) NIF design simulated with κ_{LILAC} versus κ_{QMD} .

	κ_{LILAC}	κ_{QMD}
$\langle \rho R \rangle_n$	0.679 g/cm ²	0.69 g/cm ²
$\langle T_i \rangle_n$	13.1 keV	14.1 keV
$\langle P \rangle_n$	299 Gbar	335 Gbar
$\langle \rho \rangle_{\text{peak}}$	475.7 g/cm ³	495.1 g/cm ³
R_{hs}	80.9 μm	79.3 μm
C_{hs}	21.1	21.6
Yield	7.07×10^{18}	8.41×10^{18}
Gain	16.6	19.7

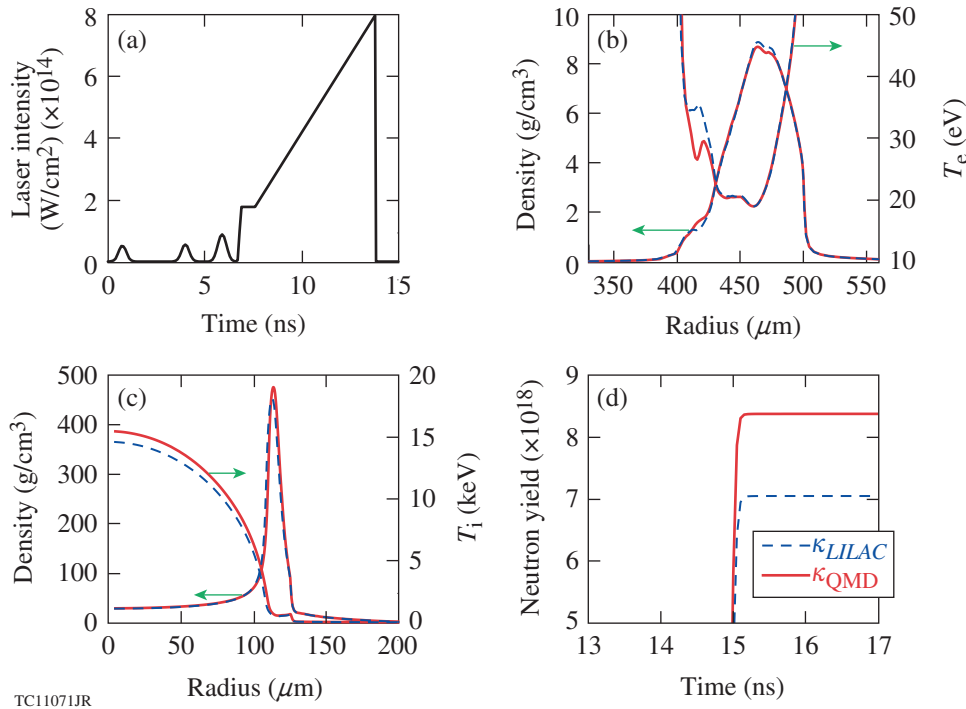


Figure 137.73 Similar to Fig. 137.71 but for a relatively lower adiabat ($\alpha = 1.7$) and lower implosion velocity ($V_{\text{imp}} = 3.3 \times 10^7$ cm/s) NIF design: (a) The laser pulse shape has a total energy of 1.2 MJ and the $\phi = 3420\text{-}\mu\text{m}$ capsule consists of 180 μm of DT ice with a 30- μm -thick plastic ablator. [(b),(c)] Comparison of the density and temperature profiles at the beginning of the deceleration phase and at the peak compression, respectively. (d) Comparison of the neutron yields for the two cases, which shows an $\sim 20\%$ variation in the 1-D predictions of target performance using κ_{LILAC} and κ_{QMD} .

To test the conventional speculation that κ_{QMD} affects mainly the hot-spot formation, we performed a “hybrid” simulation for this design by switching κ_{QMD} to the standard κ_{LILAC} during the target deceleration phase and burn ($t > 13.6$ ns). This hybrid simulation gives a total neutron yield of 9.29×10^{18} and a gain of 21.8. Comparing with the full κ_{QMD} simulation results ($Y = 8.41 \times 10^{18}$ and $G = 19.7$), the variation is modest with respect to the change from the full κ_{LILAC} simulation to the full κ_{QMD} case. This indicates that the major part of the κ_{QMD} effects on target performance comes from the shock dynamics during the early stage of the implosion, although the use of κ_{QMD} moderately decreases the target performance during the hot-spot formation.

Summary

For inertial confinement fusion applications, we have performed first-principles calculations of deuterium thermal conductivity in a wide range of densities and temperatures, using the quantum molecular dynamics method. For the density and temperature conditions in an imploding DT shell, the QMD-calculated thermal conductivity κ_{QMD} is higher by a factor of 3 to 10 than the hybrid Spitzer–Lee–More model κ_{LILAC} currently adopted in our hydrocodes. To test its effects on ICF implosions, we have fitted κ_{QMD} to a fifth-order polynomial function of Γ and θ and incorporated this fit into our hydrocodes. The hydrodynamic simulations of both OMEGA cryogenic DT implosions and direct-drive NIF designs have been performed using κ_{QMD} . Compared with the standard simulation results using κ_{LILAC} , we found the ICF implosion performance predicted by κ_{QMD} could vary by as much as $\sim 20\%$. The lower the adiabat of the DT shell, the more the effects of κ_{QMD} are observed. Analyses of the implosion dynamics have identified that the shock-dynamic differences at an early stage of the implosion, predicted differently by κ_{QMD} versus κ_{LILAC} , predominantly contribute to the final variations of implosion performance (neutron yield and target gain). This is in contrast to the previous speculation that κ_{QMD} might affect ICF mainly during the hot-spot formation. The thermal conductivities of deuterium reported here, together with the established FPEOS tables^{11,45} and opacity tables (future work) from such first-principles calculations, could provide complete physical information of fusion fuel at high-energy-density conditions for accurate ICF hydrodynamic simulations. The same strategy also applies for building self-consistent tables of ICF-relevant ablator materials. These efforts could increase the predictive capability of hydrodynamic modeling of ICF implosions.

Supplementary Material

Table 137.X: The thermal-conductivity (κ_{QMD}) table of deuterium for a wide range of densities.

Temperature T (K)	κ_{QMD} (W/m/K)
$\rho = 1.000 \text{ g/cm}^3$	$(r_S = 1.753 \text{ bohr})$
5,000	59.87 ± 4.93
10,000	127.3 ± 10.3
15,625	202.1 ± 13.2
31,250	451.6 ± 18.7
62,500	1199.6 ± 49.6
95,250	2227.5 ± 90.3
125,000	3281.4 ± 139.0
181,825	6041.6 ± 144.3
250,000	10491.2 ± 203.1
$\rho = 1.963 \text{ g/cm}^3$	$(r_S = 1.4 \text{ bohr})$
5,000	239.77 ± 21.7
10,000	374.07 ± 34.46
15,625	492.57 ± 43.67
31,250	$(1.00 \pm 0.04) \times 10^3$
62,500	$(2.17 \pm 0.09) \times 10^3$
95,250	$(3.68 \pm 0.21) \times 10^3$
125,000	$(5.17 \pm 0.25) \times 10^3$
181,825	$(8.41 \pm 0.37) \times 10^3$
250,000	$(1.30 \pm 0.02) \times 10^4$
400,000	$(2.32 \pm 0.02) \times 10^4$
$\rho = 2.452 \text{ g/cm}^3$	$(r_S = 1.3 \text{ bohr})$
5,000	345.5 ± 39.5
10,000	499.2 ± 47.6
15,625	676.5 ± 41.6
31,250	$(1.21 \pm 0.08) \times 10^3$
62,500	$(2.74 \pm 0.11) \times 10^3$
95,250	$(4.38 \pm 0.18) \times 10^3$
125,000	$(6.26 \pm 0.29) \times 10^3$
181,825	$(1.00 \pm 0.04) \times 10^4$
250,000	$(1.53 \pm 0.04) \times 10^4$
400,000	$(2.79 \pm 0.05) \times 10^4$

Table 137.X (continued).

Temperature T (K)	κ_{QMD} (W/m/K)
$\rho = 3.118 \text{ g/cm}^3$	
$(r_S = 1.2 \text{ bohr})$	
5,000	472.5±54.6
10,000	745.7±76.2
15,625	953.7±72.2
31,250	$(1.61 \pm 0.10) \times 10^3$
62,500	$(3.55 \pm 0.20) \times 10^3$
95,250	$(5.53 \pm 0.25) \times 10^3$
125,000	$(7.61 \pm 0.30) \times 10^3$
181,825	$(1.24 \pm 0.04) \times 10^4$
250,000	$(1.85 \pm 0.05) \times 10^4$
400,000	$(3.47 \pm 0.08) \times 10^4$
$\rho = 4.048 \text{ g/cm}^3$	
$(r_S = 1.1 \text{ bohr})$	
5,000	778.8±83.3
10,000	$(1.03 \pm 0.08) \times 10^3$
15,625	$(1.36 \pm 0.12) \times 10^3$
31,250	$(2.12 \pm 0.05) \times 10^3$
62,500	$(4.48 \pm 0.22) \times 10^3$
95,250	$(7.17 \pm 0.28) \times 10^3$
125,000	$(9.75 \pm 0.52) \times 10^3$
181,825	$(1.51 \pm 0.06) \times 10^4$
250,000	$(2.32 \pm 0.08) \times 10^4$
400,000	$(4.36 \pm 0.12) \times 10^4$
$\rho = 5.388 \text{ g/cm}^3$	
$(r_S = 1.0 \text{ bohr})$	
5,000	$(1.19 \pm 0.17) \times 10^3$
10,000	$(1.41 \pm 0.15) \times 10^3$
15,625	$(1.84 \pm 0.27) \times 10^3$
31,250	$(2.76 \pm 0.32) \times 10^3$
62,500	$(5.60 \pm 0.25) \times 10^3$
95,250	$(9.33 \pm 0.42) \times 10^3$
125,000	$(1.27 \pm 0.06) \times 10^4$
181,825	$(2.01 \pm 0.06) \times 10^4$
250,000	$(2.91 \pm 0.11) \times 10^4$
400,000	$(5.53 \pm 0.17) \times 10^4$
500,000	$(9.48 \pm 0.13) \times 10^4$

Table 137.X (continued).

Temperature T (K)	κ_{QMD} (W/m/K)
$\rho = 7.391 \text{ g/cm}^3$	
$(r_S = 0.9 \text{ bohr})$	
5,000	$(2.00 \pm 0.37) \times 10^3$
10,000	$(2.24 \pm 0.21) \times 10^3$
15,625	$(2.67 \pm 0.28) \times 10^3$
31,250	$(4.14 \pm 0.33) \times 10^3$
62,500	$(7.59 \pm 0.59) \times 10^3$
95,250	$(1.30 \pm 0.07) \times 10^4$
125,000	$(1.75 \pm 0.10) \times 10^4$
181,825	$(2.61 \pm 0.08) \times 10^4$
250,000	$(3.80 \pm 0.17) \times 10^4$
400,000	$(6.94 \pm 0.23) \times 10^4$
500,000	$(9.52 \pm 0.33) \times 10^4$
$\rho = 10.000 \text{ g/cm}^3$	
$(r_S = 0.814 \text{ bohr})$	
5,000	$(3.01 \pm 0.48) \times 10^3$
10,000	$(3.34 \pm 0.55) \times 10^3$
15,625	$(3.77 \pm 0.43) \times 10^3$
31,250	$(5.74 \pm 0.46) \times 10^3$
62,500	$(9.65 \pm 0.69) \times 10^3$
95,250	$(1.66 \pm 0.12) \times 10^4$
125,000	$(2.32 \pm 0.13) \times 10^4$
181,825	$(3.40 \pm 0.19) \times 10^4$
250,000	$(4.78 \pm 0.29) \times 10^4$
400,000	$(8.37 \pm 0.32) \times 10^4$
500,000	$(1.24 \pm 0.04) \times 10^5$
$\rho = 15.709 \text{ g/cm}^3$	
$(r_S = 0.8 \text{ bohr})$	
10,000	$(7.29 \pm 0.70) \times 10^3$
15,625	$(7.57 \pm 0.80) \times 10^3$
31,250	$(1.20 \pm 0.09) \times 10^4$
62,500	$(1.99 \pm 0.11) \times 10^4$
95,250	$(2.78 \pm 0.17) \times 10^4$
125,000	$(3.50 \pm 0.17) \times 10^4$
181,825	$(5.24 \pm 0.21) \times 10^4$
250,000	$(7.50 \pm 0.33) \times 10^4$
400,000	$(1.34 \pm 0.05) \times 10^5$
500,000	$(1.80 \pm 0.04) \times 10^5$
1,000,000	$(3.79 \pm 0.11) \times 10^5$

Table 137.X (continued).

Temperature T (K)	κ_{QMD} (W/m/K)
$\rho = 24.945 \text{ g/cm}^3$	$(r_S = 0.6 \text{ bohr})$
15,625	$(1.49 \pm 0.15) \times 10^4$
31,250	$(1.71 \pm 0.13) \times 10^4$
62,500	$(3.18 \pm 0.21) \times 10^4$
95,250	$(4.24 \pm 0.27) \times 10^4$
125,000	$(5.31 \pm 0.27) \times 10^4$
181,825	$(7.06 \pm 0.49) \times 10^4$
250,000	$(9.95 \pm 0.35) \times 10^4$
400,000	$(1.68 \pm 0.07) \times 10^5$
500,000	$(2.19 \pm 0.11) \times 10^5$
1000,000	$(5.63 \pm 0.21) \times 10^5$
$\rho = 43.105 \text{ g/cm}^3$	$(r_S = 0.5 \text{ bohr})$
31,250	$(3.09 \pm 0.33) \times 10^4$
62,500	$(5.14 \pm 0.40) \times 10^4$
95,250	$(7.36 \pm 0.78) \times 10^4$
125,000	$(8.82 \pm 0.64) \times 10^4$
181,825	$(1.17 \pm 0.08) \times 10^5$
250,000	$(1.44 \pm 0.15) \times 10^5$
400,000	$(2.46 \pm 0.08) \times 10^5$
500,000	$(3.14 \pm 0.24) \times 10^5$
1,000,000	$(7.62 \pm 0.28) \times 10^5$
$\rho = 84.190 \text{ g/cm}^3$	$(r_S = 0.4 \text{ bohr})$
31,250	$(7.72 \pm 0.98) \times 10^4$
62,500	$(7.52 \pm 0.64) \times 10^4$
95,250	$(1.21 \pm 0.15) \times 10^5$
125,000	$(1.64 \pm 0.17) \times 10^5$
181,825	$(2.03 \pm 0.27) \times 10^5$
250,000	$(2.65 \pm 0.33) \times 10^5$
400,000	$(3.74 \pm 0.35) \times 10^5$
500,000	$(4.66 \pm 0.24) \times 10^5$
1,000,000	$(1.15 \pm 0.06) \times 10^6$
2,000,000	$(3.12 \pm 0.05) \times 10^6$

Table 137.X (continued).

Temperature T (K)	κ_{QMD} (W/m/K)
$\rho = 199.561 \text{ g/cm}^3$	$(r_S = 0.3 \text{ bohr})$
125,000	$(4.93 \pm 0.21) \times 10^5$
181,825	$(6.18 \pm 0.24) \times 10^5$
250,000	$(8.19 \pm 0.20) \times 10^5$
400,000	$(1.25 \pm 0.05) \times 10^6$
500,000	$(1.52 \pm 0.06) \times 10^6$
1,000,000	$(2.86 \pm 0.09) \times 10^6$
2,000,000	$(6.38 \pm 0.09) \times 10^6$
4,000,000	$(1.57 \pm 0.10) \times 10^7$
$\rho = 673.518 \text{ g/cm}^3$	$(r_S = 0.2 \text{ bohr})$
250,000	$(2.43 \pm 0.17) \times 10^6$
400,000	$(3.18 \pm 0.24) \times 10^6$
500,000	$(3.76 \pm 0.26) \times 10^6$
1,000,000	$(7.34 \pm 0.35) \times 10^6$
2,000,000	$(1.44 \pm 0.07) \times 10^7$
4,000,000	$(3.33 \pm 0.06) \times 10^7$
8,000,000	$(8.92 \pm 0.08) \times 10^7$

ACKNOWLEDGMENT

This material is based on work supported by the Department of Energy National Nuclear Security Administration under Award Number DE-NA0001944, the University of Rochester, and the New York State Energy Research and Development Authority. This work was also supported by Scientific Campaign 10 at the Los Alamos National Laboratory, operated by Los Alamos National Security, LLC for the National Nuclear Security Administration of the U.S. Department of Energy under Contract No. DE-AC52-06NA25396. The support of DOE does not constitute an endorsement by DOE of the views expressed in this article. SXH acknowledges the advice from Prof. G. Kresse on the Coulombic potential for high-density VASP simulations.

REFERENCES

1. J. Nuckolls *et al.*, *Nature* **239**, 139 (1972); S. Atzeni and J. Meyer-ter-Vehn, *The Physics of Inertial Fusion: Beam Plasma Interaction, Hydrodynamics, Hot Dense Matter*, International Series of Monographs on Physics (Clarendon Press, Oxford, 2004).
2. J. D. Lindl, *Phys. Plasmas* **2**, 3933 (1995).
3. C. Cherfils-Cl  rouin *et al.*, *J. Phys.: Conf. Ser.* **244**, 022009 (2010).

4. R. L. McCrory, R. Betti, T. R. Boehly, D. T. Casey, T. J. B. Collins, R. S. Craxton, J. A. Delettrez, D. H. Edgell, R. Epstein, J.A. Frenje, D. H. Froula, M. Gatu-Johnson, V. Yu. Glebov, V. N. Goncharov, D. R. Harding, M. Hohenberger, S. X. Hu, I. V. Igumenshchev, T. J. Kessler, J. P. Knauer, C.K. Li, J. A. Marozas, F. J. Marshall, P. W. McKenty, D. D. Meyerhofer, D. T. Michel, J. F. Myatt, P. M. Nilson, S. J. Padalino, R.D. Petrasso, P. B. Radha, S. P. Regan, T. C. Sangster, F. H. Séguin, W. Seka, R. W. Short, A. Shvydky, S. Skupsky, J. M. Soures, C. Stoeckl, W. Theobald, B. Yaakobi, and J. D. Zuegel, *Nucl. Fusion* **53**, 113021 (2013).
5. D. D. Meyerhofer, R. L. McCrory, R. Betti, T. R. Boehly, D. T. Casey, T. J. B. Collins, R. S. Craxton, J. A. Delettrez, D. H. Edgell, R. Epstein, K. A. Fletcher, J. A. Frenje, Y. Yu. Glebov, V. N. Goncharov, D. R. Harding, S. X. Hu, I. V. Igumenshchev, J. P. Knauer, C. K. Li, J. A. Marozas, F. J. Marshall, P. W. McKenty, P. M. Nilson, S. P. Padalino, R. D. Petrasso, P. B. Radha, S. P. Regan, T. C. Sangster, F. H. Séguin, W. Seka, R. W. Short, D. Shvarts, S. Skupsky, J. M. Soures, C. Stoeckl, W. Theobald, and B. Yaakobi, *Nucl. Fusion* **51**, 053010 (2011).
6. V. N. Goncharov, T. C. Sangster, T. R. Boehly, S. X. Hu, I. V. Igumenshchev, F. J. Marshall, R. L. McCrory, D. D. Meyerhofer, P. B. Radha, W. Seka, S. Skupsky, C. Stoeckl, D. T. Casey, J. A. Frenje, and R. D. Petrasso, *Phys. Rev. Lett.* **104**, 165001 (2010).
7. M. C. Herrmann, M. Tabak, and J. D. Lindl, *Nucl. Fusion* **41**, 99 (2001).
8. C. D. Zhou and R. Betti, *Phys. Plasmas* **15**, 102707 (2008).
9. S. X. Hu, V. A. Smalyuk, V. N. Goncharov, J. P. Knauer, P. B. Radha, I. V. Igumenshchev, J. A. Marozas, C. Stoeckl, B. Yaakobi, D. Shvarts, T. C. Sangster, P. W. McKenty, D. D. Meyerhofer, S. Skupsky, and R. L. McCrory, *Phys. Rev. Lett.* **100**, 185003 (2008).
10. J. Clérouin and J.-F. Dufrière, *Phys. Rev. E* **64**, 066406 (2001); L. Caillabet, S. Mazevet, and P. Loubeyre, *Phys. Rev. B* **83**, 094101 (2011).
11. S. X. Hu, B. Militzer, V. N. Goncharov, and S. Skupsky, *Phys. Rev. B* **84**, 224109 (2011).
12. M. A. Morales *et al.*, *High Energy Density Phys.* **8**, 5 (2012).
13. S. Hamel, L. X. Benedict, P. M. Celliers, M. A. Barrios, T. R. Boehly, G. W. Collins, T. Döppner, J. H. Eggert, D. R. Farley, D. G. Hicks, J. L. Kline, A. Lazicki, S. LePape, A. J. Mackinnon, J. D. Moody, H. F. Robey, E. Schwegler, and P. A. Sterne, *Phys. Rev. B* **86**, 094113 (2012); P. Loubeyre, S. Brygoo, J. Eggert, P. M. Celliers, D. K. Spaulding, J. R. Rygg, T. R. Boehly, G. W. Collins, and R. Jeanloz, *Phys. Rev. B* **86**, 144115 (2012).
14. J. Vorberger, D. O. Gericke, and W. D. Kraeft, *High Energy Density Phys.* **9**, 448 (2013).
15. C. Wang and P. Zhang, *Phys. Plasmas* **20**, 092703 (2013).
16. V. V. Karasiev *et al.*, *Phys. Rev. B* **88**, 161108 (2013).
17. B. Militzer and D. M. Ceperley, *Phys. Rev. Lett.* **85**, 1890 (2000); B. Militzer *et al.*, *Phys. Rev. Lett.* **87**, 275502 (2001).
18. J. M. McMahon *et al.*, *Rev. Mod. Phys.* **84**, 1607 (2012).
19. L. Collins *et al.*, *Phys. Rev. E* **52**, 6202 (1995).
20. H. Brysk, P. M. Campbell, and P. Hammerling, *Plasma Phys.* **17**, 473 (1975).
21. L. Spitzer, Jr. and R. Härm, *Phys. Rev.* **89**, 977 (1953).
22. J. Daligault and G. Dimonte, *Phys. Rev. E* **79**, 056403 (2009).
23. L. X. Benedict *et al.*, *Phys. Rev. Lett.* **102**, 205004 (2009).
24. B. Xu and S. X. Hu, *Phys. Rev. E* **84**, 016408 (2011).
25. L. X. Benedict *et al.*, *Phys. Rev. E* **86**, 046406 (2012).
26. C. Blancard, J. Clérouin, and G. Faussurier, *High Energy Density Phys.* **9**, 247 (2013).
27. W. B. Hubbard, *Astrophys. J.* **146**, 858 (1966).
28. Y. T. Lee and R. M. More, *Phys. Fluids* **27**, 1273 (1984).
29. S. Ichimaru and S. Tanaka, *Phys. Rev. A* **32**, 1790 (1985); H. Kitamura and S. Ichimaru, *Phys. Rev. E* **51**, 6004 (1995).
30. D. A. Liberman, *Phys. Rev. B* **20**, 4981 (1979).
31. B. Wilson *et al.*, *J. Quant. Spectrosc. Radiat. Transf.* **99**, 658 (2006).
32. G. Faussurier *et al.*, *Phys. Plasmas* **17**, 052707 (2010); J. Clérouin *et al.*, *Phys. Rev. E* **82**, 046402 (2010).
33. J. G. Clérouin and S. Bernard, *Phys. Rev. E* **56**, 3534 (1997).
34. L. A. Collins *et al.*, *Phys. Rev. B* **63**, 184110 (2001).
35. M. P. Desjarlais, *Phys. Rev. B* **68**, 064204 (2003).
36. S. A. Bonev, B. Militzer, and G. Galli, *Phys. Rev. B* **69**, 014101 (2004).
37. J. D. Kress *et al.*, *Phys. Rev. E* **82**, 036404 (2010).
38. V. Recoules *et al.*, *Phys. Rev. Lett.* **102**, 075002 (2009).
39. F. Lambert *et al.*, *Phys. Plasmas* **18**, 056306 (2011).
40. D. E. Hanson *et al.*, *Phys. Plasmas* **18**, 082704 (2011).
41. B. Holst, M. French, and R. Redmer, *Phys. Rev. B* **83**, 235120 (2011).
42. C. E. Starrett *et al.*, *Phys. Plasmas* **19**, 102709 (2012).
43. C. Wang *et al.*, *Phys. Rev. E* **88**, 013106 (2013).
44. For details of the *ABINIT* code, please refer to <http://www.abinit.org/>.
45. S. X. Hu, B. Militzer, V. N. Goncharov, and S. Skupsky, *Phys. Rev. Lett.* **104**, 235003 (2010).

46. R. Kubo, *J. Phys. Soc. Jpn.* **12**, 570 (1957); D. A. Greenwood, *Proc. Phys. Soc. Lond.* **71**, 585 (1958).
47. J. Delettrez, R. Epstein, M. C. Richardson, P. A. Jaanimagi, and B. L. Henke, *Phys. Rev. A* **36**, 3926 (1987).
48. I. Kwon, J. D. Kress, and L. A. Collins, *Phys. Rev. B* **50**, 9118 (1994).
49. M. P. Desjarlais, J. D. Kress, and L. A. Collins, *Phys. Rev. E* **66**, 025401 (2002).
50. B. Holst, R. Redmer, and M. P. Desjarlais, *Phys. Rev. B* **77**, 184201 (2008).
51. G. Kresse and J. Hafner, *Phys. Rev. B* **47**, 558 (1993).
52. G. Kresse and J. Hafner, *Phys. Rev. B* **49**, 14,251 (1994); G. Kresse and J. Furthmüller, *Phys. Rev. B* **54**, 11,169 (1996).
53. G. Kresse and D. Joubert, *Phys. Rev. B* **59**, 1758 (1999).
54. G. Kresse, University of Vienna, private communication (2013).
55. P. M. Celliers *et al.*, *Phys. Rev. Lett.* **84**, 5564 (2000).
56. T. R. Boehly, D. H. Munro, P. M. Celliers, R. E. Olson, D. G. Hicks, V. N. Goncharov, G. W. Collins, H. F. Robey, S. X. Hu, J. A. Marozas, T. C. Sangster, O. L. Landen, and D. D. Meyerhofer, *Phys. Plasmas* **16**, 056302 (2009).
57. T. R. Boehly, V. N. Goncharov, W. Seka, S. X. Hu, J. A. Marozas, D. D. Meyerhofer, P. M. Celliers, D. G. Hicks, M. A. Barrios, D. Fratanduono, and G. W. Collins, *Phys. Plasmas* **18**, 092706 (2011).
58. T. R. Boehly, V. N. Goncharov, W. Seka, M. A. Barrios, P. M. Celliers, D. G. Hicks, G. W. Collins, S. X. Hu, J. A. Marozas, and D. D. Meyerhofer, *Phys. Rev. Lett.* **106**, 195005 (2011).
59. L. A. Collins, J. D. Kress, and D. E. Hanson, *Phys. Rev. B* **85**, 233101 (2012).
60. R. C. Malone, R. L. McCrory, and R. L. Morse, *Phys. Rev. Lett.* **34**, 721 (1975).
61. S. X. Hu, V. Smalyuk, V. N. Goncharov, S. Skupsky, T. C. Sangster, D. D. Meyerhofer, and D. Shvarts, *Phys. Rev. Lett.* **101**, 055002 (2008).
62. S. X. Hu, P. B. Radha, J. A. Marozas, R. Betti, T. J. B. Collins, R. S. Craxton, J. A. Delettrez, D. H. Edgell, R. Epstein, V. N. Goncharov, I. V. Igumenshev, F. J. Marshall, R. L. McCrory, D. D. Meyerhofer, S. P. Regan, T. C. Sangster, S. Skupsky, V. A. Smalyuk, Y. Elbaz, and D. Shvarts, *Phys. Plasmas* **16**, 112706 (2009).
63. S. X. Hu, V. N. Goncharov, P. B. Radha, J. A. Marozas, S. Skupsky, T. R. Boehly, T. C. Sangster, D. D. Meyerhofer, and R. L. McCrory, *Phys. Plasmas* **17**, 102706 (2010).
64. D. H. Froula, B. Yaakobi, S. X. Hu, P.-Y. Chang, R. S. Craxton, D. H. Edgell, R. Follett, D. T. Michel, J. F. Myatt, W. Seka, R. W. Short, A. Solodov, and C. Stoeckl, *Phys. Rev. Lett.* **108**, 165003 (2012).
65. S. X. Hu, D. T. Michel, D. H. Edgell, D. H. Froula, R. K. Follett, V. N. Goncharov, J. F. Myatt, S. Skupsky, and B. Yaakobi, *Phys. Plasmas* **20**, 032704 (2013).

Self-Phase Modulation Compensation in a Regenerative Amplifier Using Cascaded Second-Order Nonlinearities

Laser systems delivering short optical pulses are commonly built using chirped-pulse amplification (CPA).¹ CPA decreases the intensity of the pulse being amplified below the damage threshold of optical components and reduces the accumulated intensity-dependent nonlinearity. With or without CPA, an optical pulse propagating in a laser system can accumulate significant amounts of phase via self-phase modulation (SPM), i.e., a phase $\varphi(\vec{r}, t) = \Gamma I(\vec{r}, t)$, at intensities well below the damage threshold. SPM is a concern because it leads to spatial self-focusing and spectral broadening that can disrupt the amplification process. CPA is often space consuming because of the footprint of grating-based stretchers and compressors. It is difficult to implement on low-bandwidth pulses because of the large dispersion required to significantly stretch these pulses. SPM compensation methods are attractive for amplifying picosecond pulses at intensities below the damage threshold without CPA.

In fiber-based systems² temporal phase modulators can be used to compensate for SPM, but this compensation is limited to particular operating conditions. For a pulse propagating in free space, a phase that is negatively proportional to the intensity can be induced by propagation at a specific wavelength in a semiconductor wafer^{3,4} or in a cesium vapor,⁵ but these processes have limited wavelength and nonlinearity tunability. Cascaded nonlinearities obtained by propagation in a nonlinear crystal detuned from phase matching introduce an intensity-

dependent phase.⁶ SPM compensation using a cascaded nonlinearity with a negative n_2 is simple to implement, relies on commercially available nonlinear crystals that can be procured with high quality, has a small footprint, is usable at a wide range of optical wavelengths, and provides nonlinearity tunability. The accumulated intensity-dependent phase is a linear function of the intensity only up to ~ 1 rad. This compensation strategy is not suitable for large, accumulated nonlinear phase shifts, but it is well suited for iterative compensation of the small nonlinear phase shifts from multiple passes in a regenerative amplifier cavity, even if these phase shifts add up to a large phase shift in the absence of compensation. Intracavity nonlinearity compensation has been used to compensate for the pump-pulse time-dependent phase shift that decreases the enhancement factor of a cavity-enhanced optical parametric chirped-pulse-amplification system;⁷ to control low-power continuous-wave light via optical bistability;⁸ and to mode-lock a continuous-wave (cw)-pumped laser;⁹ however, it has not been studied or demonstrated to control the properties of a pulse amplified by a laser amplifier.

Simulations have been conducted to understand the origin of SPM in the Nd:YLF regenerative amplifier schematized in Fig. 137.74. This regenerative amplifier architecture is used to amplify nanosecond pulses at 1053 nm suitable to seed large-scale Nd:glass laser systems¹⁰ and for amplification with pulse durations limited by gain narrowing in the Nd:YLF (~ 12 ps),

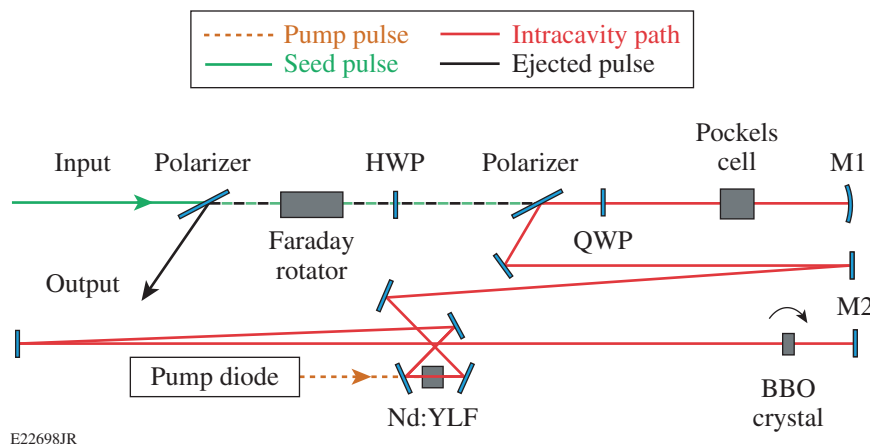


Figure 137.74
Regenerative amplifier layout. HWP = half-wave plate; QWP = quarter-wave plate; BBO: beta-barium borate.

E22698JR

e.g., to generate short UV pulses after fourth-harmonic generation¹¹ and optical-parametric-amplifier pump pulses after second-harmonic generation (SHG).¹² The amplifier has a near-hemispherical cavity with an end-cavity plane mirror and an end-cavity spherical mirror ($R = 5$ m). The propagation simulations in the paraxial approximation are implemented with *MATLAB*¹³ in cylindrical coordinates, i.e., the field is a function of the radius r and time t . Nonlinearity in the deuterated potassium dihydrogen phosphate (DKDP) Pockels cell (PC), the Nd:YLF crystal, air, and the Faraday isolator is taken into account. The PC is the largest SPM contributor. An intracavity pulse train measured behind one of the cavity mirrors is used to scale the pulse energy after each pass in the Nd:YLF crystal. The simulations show that the amplified pulse accumulates temporal phase (leading to spectral broadening) but no spatial phase (which could lead to self-focusing). The intracavity spectral broadening is uniform across the beam at the output of the regenerative amplifier but is slightly spatially varying after the isolator. The uniform intracavity spectral broadening and absence of a significant spatially varying wavefront are explained by the large number of passes in the cavity that constrain the spatial phase at the two end mirrors and constrain the beam to the highest-gain cavity eigenmode.

Without SPM compensation, amplification to 0.5 mJ after 124 round-trips leads to ~ 1.8 rad of accumulated phase, including ~ 1.1 rad from propagation in the intracavity PC and ~ 0.4 rad from the extracavity Faraday isolator. The intracavity beam remains approximately Gaussian with a flat spatial phase at mirror M2, but the waist size decreases by $\sim 5\%$ when the intracavity energy reaches 0.5 mJ. Propagation in the PC at the last pass induces a nonlinear phase smaller than 0.1 rad. In this regime, the spatiotemporal phase induced by the cascaded nonlinearity is proportional to the intensity for an adequately detuned crystal. Simulations show that a compensating element with nonlinear coefficient $\Gamma = -3 \times 10^{-15}$ m²/W located close to mirror M2 provides minimal spectral broadening at output energies up to ~ 2 mJ (Fig. 137.75). The polarization at M2 is linear for all passes, as required for the operation of the cascaded nonlinearities, and this location is convenient to access. Compensation closer to the PC—the main contributor to intracavity nonlinearity—operates over a larger range of energies, but it was not experimentally attempted because of layout issues.

When a nonlinear crystal (nonlinear coefficient d_{eff} and refractive indices n_{ω} and $n_{2\omega}$ at the fundamental frequency ω and upconverted frequency 2ω) is significantly detuned out of phase matching ($\Delta k(\Delta kL \gg 1)$), cascaded nonlinearities lead

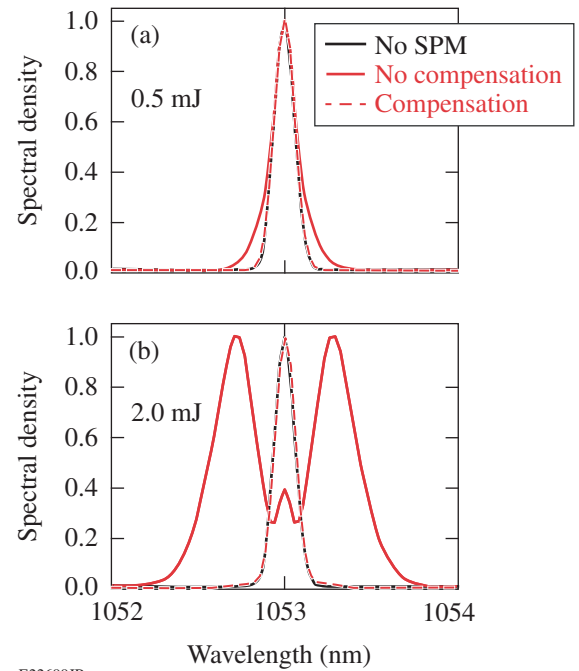


Figure 137.75

Simulated optical spectra without self-phase modulation (SPM) in the cavity (black line), with SPM and no compensation (solid red line), and with SPM and compensation (dashed red line) at output energies of (a) 0.5 mJ and (b) 2.0 mJ.

to an effective nonlinear index on the field at the fundamental wavelength λ (Ref. 6) given by

$$n_2^{\text{eff}} = -\frac{4\pi d_{\text{eff}}^2}{c\epsilon_0 \lambda n_{2\omega} n_{\omega}^2 \Delta k}. \quad (1)$$

Operating at large Δk allows one to precisely tune the nonlinearity by tuning the phase-matching angle. A 5-mm beta-barium–borate (BBO) crystal antireflection coated at 1053 nm and 526.5 nm was placed in the cavity close to mirror M2, with phase matching around a vertical axis.

Experimental results were obtained on two regenerative amplifiers seen in the layout in Fig. 137.74. These systems amplify the pump pulse for the optical parametric amplifier in the front end of the Multi-Terawatt Laser Facility^{12,14} and in the ultra-broadband front end.¹⁵ They are both seeded by ~ 6 -nm optical pulses centered at 1053 nm originating from mode-locked lasers. The output energy decreased by $\sim 15\%$ when the compensation crystal was introduced, most likely because of reflection losses. The optimal SPM compensation was determined by measuring the output spectrum after the Faraday isolator for various detuning angles. The narrowest spectrum

has a full width at half maximum (FWHM) equal to 0.14 nm and is similar to the fluorescence spectrum of the unseeded amplifier. Figure 137.76 shows the optical spectra measured at output energies of ~ 0.5 mJ and ~ 0.8 mJ without and with nonlinearity compensation. Operation at higher energy was obtained by increasing the pump-diode current and decreasing the number of round-trips in the cavity to eject the pulse at the peak of the buildup. Very good SPM compensation was obtained at the higher energy without retuning the intracavity BBO crystal. SPM compensation was performed on a second regenerative amplifier that operated with a larger number of round-trips at an output energy of 0.8 mJ. Excellent compensation of the larger spectral broadening was also obtained.

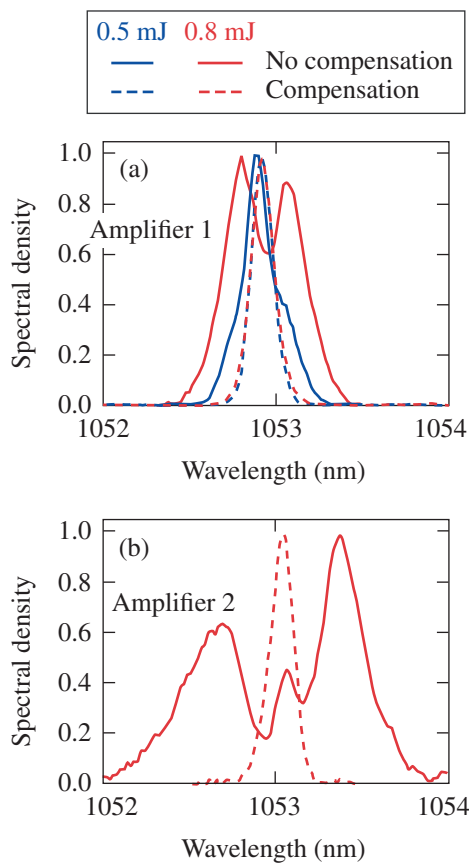


Figure 137.76 Optical spectra without compensation (solid lines) and with compensation (dashed line) for output energies of 0.5 mJ and 0.8 mJ, respectively. The data were measured on two different regenerative amplifiers.

Optimal compensation was obtained for these two amplifiers when the internal angular detuning was $\sim 0.9^\circ$ from phase matching ($\Delta kL \sim 90$), corresponding to a nonlinear index -1.7×10^{-15} cm²/W and nonlinearity $\Gamma = -5.1 \times 10^{-15}$ m²/W. The

magnitude of the nonlinearity is larger than what has been identified by simulations, but the Kerr nonlinearity of the intracavity BBO crystal ($n_2 = 5 \times 10^{-16}$ cm²/W) (Ref. 16) reduces the compensating nonlinearity by $\sim 30\%$. The simulations ignore propagation in various short optical components such as wave plates and polarizers. Considering the uncertainties on the nonlinear index of DKDP and BBO,^{16,17} the detuning experimentally required for SPM compensation is in good agreement with expectations.

The output energy at 1053 nm and intracavity-generated energy at 526.5 nm were characterized when finely tuning the compensating crystal. The SHG energy was measured behind the end mirror M2 (transmission $\sim 85\%$ at 526.5 nm) and was not temporally resolved, i.e., the reported value corresponds to the total SHG energy reaching the energy meter during amplification for all round-trips. Anticorrelated variations of these energies are observed (Fig. 137.77) because intracavity SHG is a loss mechanism for the pulse being amplified. The period of these variations is consistent with phase matching in a 5-mm BBO crystal, where the efficiency of the SHG process is proportional to $[\text{sinc}(\Delta kL/2)]^2$. Because of the $\sim 10\%$ variation of the output energy, the crystal detuning angle must be controlled to $\sim 0.01^\circ$ to maximize the output energy.

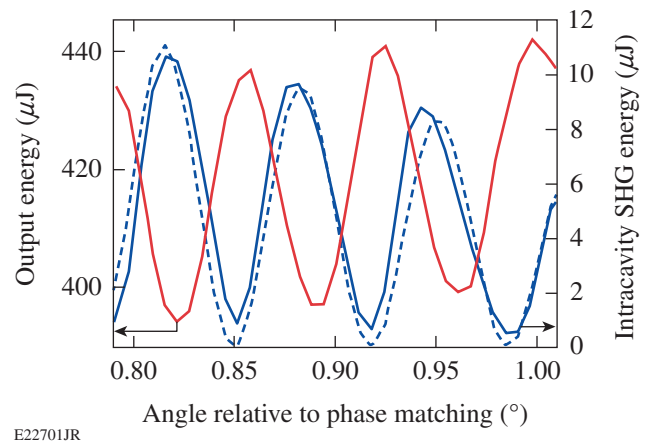
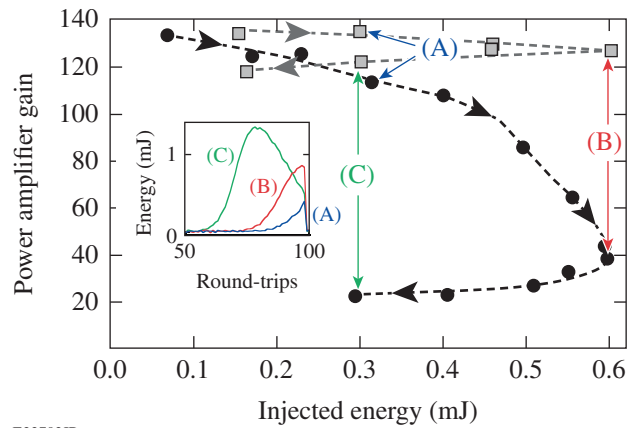


Figure 137.77 Regenerative amplifier output energy (red line) and intracavity second-harmonic-regeneration (SHG) energy generated in the BBO crystal leaking through mirror M2 (solid blue line) compared to arbitrarily scaled SHG efficiency $[\text{sinc}(\Delta kL/2)]^2$ (dashed blue line).

Another experiment was performed to highlight the advantage of SPM compensation in a laser system composed of multiple amplifiers based on the same laser material. The highest efficiency for an amplifier, particularly in the unsaturated regime, is obtained when the amplifier gain is high over the

entire spectral density of the seed pulse. Without compensation, SPM in the regenerative amplifier broadens the spectrum of the pulse seeded in a custom-built flash-lamp-pumped power amplifier based on three Nd:YLF rods (total length = 265 mm). For this experiment, the regenerative amplifier output pulse energy was throttled down by 25% independently of the energy, to avoid damage at high energy; e.g., the input energy to the power amplifier is 0.6 mJ at the nominal regenerative-amplifier energy of 0.8 mJ. The power amplifier's spectral gain was not measured, but by comparing its small signal gain to the gain of the regenerative amplifier [$\sim 10^2$ and $\sim 10^8 = (10^2)^4$, respectively], we estimated its FWHM to be twice the FWHM of the regenerative-amplifier gain; i.e., 0.28 nm, assuming Gaussian gain functions. This FWHM was significantly smaller than the width of the optical spectra observed in the absence of SPM compensation.

The regenerative amplifier's pump-diode current was scanned to vary the accumulated intracavity nonlinearity of the output pulse and the energy injected into the power amplifier without modifying the ejection timing (examples shown in the inset of Fig. 137.78). Nominal operation corresponds to ejection at the peak of the intracavity buildup [(B) in Fig. 137.78]. Under the simplifying assumption that the accumulated nonlinear phase is proportional to the sum of the energy of all the pulses in the measured pulse train, the low-current and high-current configurations [(A) and (C) in Fig. 137.78] correspond to 32% and 308%, respectively, of the nominal nonlinear phase for the same injected energy of 0.3 mJ. The power-amplifier gain for a small amount of SPM is ~ 135 . Without compensation, the gain decreases steadily when the regenerative amplifier's intracavity nonlinearity increases, reaching ~ 40 at the maximal regenerative amplifier output energy [pumping condition (B)] and ~ 20 for higher intracavity nonlinearity [pumping condition (C)]. Without compensation, the highest output energy, ~ 40 mJ, is obtained when the injected energy is ~ 0.4 mJ. Large spectral broadening of the regenerative amplifier's output pulse was observed as the current was increased because of intracavity SPM. When the latter was compensated without retuning the cascaded nonlinearity, the regenerative amplifier's pump-current increase did not induce a significant decrease in the power amplifier's efficiency. In particular, the energy gain remained higher than 120 in the three pumping conditions shown in Fig. 137.78. The highest output energy, ~ 75 mJ, was obtained for the highest injected energy, 0.6 mJ, demonstrating a gain of 125. These experimental results confirm that intracavity SPM compensation is suitable for SPM compensation over a large range of operating conditions, making efficient amplification possible in later amplification stages.



E22702JR

Figure 137.78

Power-amplifier gain versus injected energy without (solid black circles) and with (solid gray squares) SPM compensation in the regenerative amplifier. Examples of regenerative-amplifier buildup pulse train envelopes are shown in the inset: (A), (B), and (C) correspond to regenerative-amplifier output energies of 0.4 mJ, 0.8 mJ, and 0.4 mJ, respectively; i.e., injected energies of 0.3 mJ, 0.6 mJ, and 0.3 mJ after throttling down by 25%.

Intracavity nonlinearity compensation in a regenerative amplifier has been studied via simulations and experiments in the context of short-pulse amplification in Nd:YLF. DKDP Pockels-cell Kerr nonlinearity is the main contributor to the overall nonlinearity. Self-phase modulation leads mostly to spectral broadening because the large number of round-trips in the cavity constrains the beam profile to the spatial mode of the cavity having the smallest overall losses. Intracavity compensation of SPM with cascaded nonlinearities is a powerful strategy to compensate for the small nonlinear phase shifts accumulated in optical components at each round-trip. Experimental results obtained with a BBO crystal in two Nd:YLF regenerative amplifiers confirm the validity of this approach. Significant reduction of spectral broadening allows for high-efficiency amplification of the generated pulses in two Nd:YLF power amplifier.

This work can be extended in different directions: First, it is interesting to theoretically and experimentally test the limit of this approach, e.g., in terms of per-round-trip nonlinear phase shift and relative location of elements inducing nonlinearities. Applications to amplifiers with broader spectral gain capable of generating subpicosecond pulses are of practical interest, following the demonstration that cascaded nonlinearities can be used at these shorter pulse durations.¹⁸ Cascaded nonlinearities can be precisely tuned to increase the spectral content of the amplified optical pulse and allow for pulse recompression, as demonstrated with intracavity nonlinear propagation in a Nd:glass amplifier,¹⁹ or seeding of another amplifier with gain centered at a different wavelength.

ACKNOWLEDGMENT

This material is based upon work supported by the Department of Energy National Nuclear Security Administration under Award Number DE-NA0001944, the University of Rochester, and the New York State Energy Research and Development Authority. The support of DOE does not constitute an endorsement by DOE of the views expressed in this article.

REFERENCES

1. D. Strickland and G. Mourou, *Opt. Commun.* **56**, 219 (1985).
2. J. van Howe, G. Zhu, and C. Xu, *Opt. Lett.* **31**, 1756 (2006).
3. M. Sheik-Bahae *et al.*, *IEEE J. Quantum Electron.* **27**, 1296 (1991).
4. O. A. Konoplev and D. D. Meyerhofer, *IEEE J. Sel. Top. Quantum Electron.* **4**, 459 (1998).
5. R. H. Lehberg, J. Reintjes, and R. C. Eckardt, *Appl. Phys. Lett.* **30**, 487 (1977).
6. G. I. Stegeman, D. J. Hagan, and L. Torner, *Opt. Quantum Electron.* **28**, 1691 (1996).
7. F. Ö. Ilday and F. X. Kärtner, *Opt. Lett.* **31**, 637 (2006).
8. A. G. White, J. Mlynek, and S. Schiller, *Europhys. Lett.* **35**, 425 (1996).
9. M. Zavelani-Rossi, G. Cerullo, and V. Magni, *IEEE J. Quantum Electron.* **34**, 61 (1998).
10. A. V. Okishev and J. D. Zuegel, *Appl. Opt.* **43**, 6180 (2004).
11. C. Dorrer, I. A. Begishev, A. V. Okishev, and J. D. Zuegel, *Opt. Lett.* **32**, 2143 (2007).
12. D. H. Froula, R. Boni, M. Bedzyk, R. S. Craxton, F. Ehrne, S. Ivancic, R. Jungquist, M. J. Shoup, W. Theobald, D. Weiner, N. L. Kugland, and M. C. Rushford, *Rev. Sci. Instrum.* **83**, 10E523 (2012).
13. MATLAB® The MathWorks, Inc., Natick, MA 01760-2098 (<http://www.mathworks.com>).
14. V. Bagnoud, I. A. Begishev, M. J. Guardalben, J. Puth, and J. D. Zuegel, *Opt. Lett.* **30**, 1843 (2005).
15. J. Bromage, C. Dorrer, M. Millicchia, J. Bunkenburg, R. Jungquist, and J. D. Zuegel, in *Conference on Lasers and Electro-Optics 2012*, OSA Technical Digest (online) (Optical Society of America, 2012), Paper CTh1N.7.
16. M. Bache *et al.*, *Opt. Mater. Express* **3**, 357 (2013).
17. I. A. Kulagin *et al.*, *J. Opt. Soc. Am. B* **23**, 75 (2006).
18. F. Wise, L. Qian, and X. Liu, *J. Nonlinear Opt. Phys. Mater.* **11**, 317 (2002).
19. L. Yan, Y.-Q. Liu, and C. H. Lee, *IEEE J. Quantum Electron.* **39**, 2194 (1994).

Publications and Conference Presentations

Publications

C. Dorrer, R. Roides, R. Cuffney, A. V. Okishev, W. A. Bittle, G. Balonek, A. Consentino, E. Hill, and J. D. Zuegel, "Fiber Front End With Multiple Phase Modulations and High-Bandwidth Pulse Shaping for High-Energy Laser-Beam Smoothing," *IEEE J. Sel. Top. Quantum Electron.* **19**, 3500112 (2013).

W. Fox, G. Fiksel, A. Bhattacharjee, P.-Y. Chang, K. Germaschewski, S. X. Hu, and P. M. Nilson, "Filamentation Instability of Counterstreaming Laser-Driven Plasmas," *Phys. Rev. Lett.* **111**, 225002 (2013).

M. Hohenberger, N. E. Palmer, G. LaCaille, E. L. Dewald, L. Divol, E. J. Bond, T. Döppner, J. J. Lee, R. L. Kauffman, J. D. Salmonson, C. A. Thomas, D. K. Bradley, C. Stoeckl, and T. C. Sangster, "Measuring the Hot-Electron Population Using Time-Resolved, Hard X-Ray Detectors on the NIF," in *Target Diagnostics Physics and Engineering for Inertial Confinement Fusion II*, edited by P. M. Bell and G. P. Grim (SPIE, Bellingham, WA, 2013), Vol. 8850, Paper 88500F.

J. Katz, J. S. Ross, C. Sorce, and D. H. Froula, "A Reflective Image-Rotating Periscope for Spatially Resolved Thomson-Scattering Experiments on OMEGA," *J. Inst.* **8**, C12009 (2013).

H. P. H. Liddell, K. Mehrotra, J. C. Lambropoulos, and S. D. Jacobs, "Fracture Mechanics of Delamination Defects in Multilayer Dielectric Coatings," *Appl. Opt.* **52**, 7689 (2013).

K. L. Marshall, D. Saulnier, H. Xianyu, S. Serak, and N. Tabiryan, "Liquid Crystal Near-IR Laser Beam Shapers Employing Photoaddressable Alignment Layers for High-Peak-Power Applications," in *Liquid Crystals XVII*, edited by I. C. Khoo (SPIE, Bellingham, WA, 2013), Vol. 8828, Paper 88280N.

R. L. McCrory, D. D. Meyerhofer, R. Betti, T. R. Boehly, T. J. B. Collins, R. S. Craxton, J. A. Delettrez, D. H. Edgell, R. Epstein, D. H. Froula, V. Yu. Glebov, V. N. Goncharov, D. R. Harding, S. X. Hu, I. V. Igumenshchev, J. P. Knauer, S. J. Loucks, J. A. Marozas, F. J. Marshall, P. W. McKenty, T. Michel, P. M.

Nilson, P. B. Radha, S. P. Regan, T. C. Sangster, W. Seka, W. T. Shmayda, R. W. Short, D. Shvarts, S. Skupsky, J. M. Soures, C. Stoeckl, W. Theobald, B. Yaakobi, J. A. Frenje, D. T. Casey, C. K. Li, R. D. Petrasso, F. H. Séguin, S. J. Padalino, K. A. Fletcher, P. M. Celliers, G. W. Collins, and H. F. Robey, "Progress in Direct-Drive Inertial Confinement Fusion," *EPJ Web of Conferences* **59**, 01004 (2013).

P. W. McKenty, T. J. B. Collins, J. A. Marozas, T. J. Kessler, J. D. Zuegel, M. J. Shoup, R. S. Craxton, F. J. Marshall, A. Shvydky, S. Skupsky, V. N. Goncharov, P. B. Radha, R. Epstein, T. C. Sangster, D. D. Meyerhofer, R. L. McCrory, J. D. Kilkenny, A. Nikroo, M. L. Hoppe, A. J. MacKinnon, S. LePape, M. M. Marinak, M. J. Schmitt, P. A. Bradley, N. S. Krasheninnikova, G. R. Magelssen, and T. J. Murphy, "Preparing for Polar-Drive Ignition on the National Ignition Facility," *EPJ Web of Conferences* **59**, 02014 (2013).

D. T. Michel, V. N. Goncharov, I. V. Igumenshchev, R. Epstein, and D. H. Froula, "Demonstration of the Improved Rocket Efficiency in Direct-Drive Implosions Using Different Ablator Materials," *Phys. Rev. Lett.* **111**, 245005 (2013).

P. B. Radha, F. J. Marshall, T. R. Boehly, T. J. B. Collins, R. S. Craxton, D. Edgell, R. Epstein, J. Frenje, V. N. Goncharov, J. A. Marozas, R. L. McCrory, P. W. McKenty, D. D. Meyerhofer, R. D. Petrasso, T. C. Sangster, A. Shvydky, and S. Skupsky, "Polar Drive on OMEGA," *EPJ Web of Conferences* **59**, 02013 (2013).

S. Salzman, H. J. Romanofsky, Y. I. Clara, L. J. Giannechini, G. West, J. C. Lambropoulos, and S. D. Jacobs, "Magnetorheological Finishing with Chemically Modified Fluids for Studying Material Removal of Single-Crystal ZnS," in *Optifab 2013*, edited by J. L. Bentley and M. Pfaff, (SPIE, Bellingham, WA, 2013), Vol. 8884, Paper 888407.

D. Saulnier, B. Taylor, K. L. Marshall, T. J. Kessler, and S. D. Jacobs, "Liquid Crystal Chiroptical Polarization Rotators for

the Near-UV Region: Theory, Materials, and Device Applications,” in *Liquid Crystals XVII*, edited by I. C. Khoo (SPIE, Bellingham, WA, 2013), Vol. 8828, Paper 882807.

M. Storm, B. Eichman, Z. Zhong, W. Theobald, P. Schiebel, C. Mileham, C. Stoeckl, I. A. Begishev, G. Fiksel, R. B. Stephens, R. R. Freeman, and K. U. Akli, “Note: Characterization of a High-Photon-Energy X-Ray Imager,” *Rev. Sci. Instrum.* **84**, 106103 (2013).

W. Theobald, A. Casner, R. Nora, X. Ribeyre, M. Lafon, K. S. Anderson, R. Betti, R. S. Craxton, J. A. Delettrez, J. A. Frenje, V. Yu. Glebov, O. V. Gotchev, M. Hohenberger, S. X. Hu, F. J. Marshall, R. L. McCrory, D. D. Meyerhofer, L. J. Perkins, T. C. Sangster, G. Schurtz, W. Seka, V. A. Smalyuk, C. Stoeckl, and B. Yaakobi, “Progress in the Shock-Ignition Inertial Confinement Fusion Concept,” *EPJ Web of Conferences* **59**, 03001 (2013).

Forthcoming Publications

H.-M. P. Chen and S. H. Chen, “Glassy Liquid Crystals as Self-Organized Solid Films for Opto-electronics,” to be published in *Nanoscience with Liquid Crystals: From Organized Nanostructures to Applications*.

C. Dorrer, “Spectral and Temporal Properties of Optical Signals with Multiple Sinusoidal Phase Modulations,” to be published in *Applied Optics*.

D. Haberberger, S. Ivancic, S. X. Hu, R. Boni, M. Barczys, R. S. Craxton, and D. H. Froula, “Measurements of the Electron Density Profiles Using an Angular Filter Refractometer,” to be published in *Physics of Plasmas*.

M. Hohenberger, W. Theobald, S. X. Hu, K. S. Anderson, R. Betti, T. R. Boehly, A. Casner, D. E. Fratanduono, M. Lafon, D. D. Meyerhofer, R. Nora, X. Ribeyre, T. C. Sangster, G. Schurtz, W. Seka, C. Stoeckl, and B. Yaakobi, “Shock-Ignition—Relevant Experiments with Planar Targets on OMEGA,” to be published in *Physics of Plasmas*.

M. Mikulics, H. Hardtdegen, R. Adam, D. Grützmacher, D. Gregušová, J. Novák, P. Kordoš, Z. Sofer, J. Serafini,

J. Zhang, R. Sobolewski, and M. Marso, “Impact of Thermal Annealing on Nonequilibrium Carrier Dynamics in Single-Crystal, Free-Standing GaAs Mesostructures,” to be published in *Semiconductor Science and Technology*.

J. B. Oliver, J. Bromage, C. Smith, D. Sadowski, C. Dorrer, and A. L. Rigatti, “Plasma-Ion—Assisted Coatings for 15-fs Laser Systems,” to be published in *Applied Optics*.

H. F. Robey, P. M. Celliers, J. D. Moody, J. Sater, T. Parham, B. Koziowski, R. Dylla-Spears, J. S. Ross, S. LePape, J. E. Ralph, M. Hohenberger, E. L. Dewald, L. Berzak Hopkins, J. J. Kroll, B. E. Yoxall, A. V. Hamza, T. R. Boehly, A. Nikroo, O. L. Landen, and M. J. Edwards, “Shock-Timing Measurements and Analysis in Deuterium—Tritium Ice-Layered Capsule Implosions on the NIF,” to be published in *Physics of Plasmas*.

J. E. Schoenly, W. Seka, and P. Rechmann, “Pulsed-Laser Ablation of Dental Calculus in the Near-Ultraviolet,” to be published in the *Journal of Biomedical Optics*.

Conference Presentations

The following presentations were made at the SLAC High-Power Laser Workshop, Menlo Park, CA, 1–2 October 2013:

D. H. Froula, “Direct-Drive Fusion and High-Energy-Density Research at the Laboratory for Laser Energetics.”

R. J. Henchen, R. K. Follett, D. H. Edgell, V. N. Goncharov, J. S. Ross, J. Katz, C. Sorce, and D. H. Froula, “Collective Ultraviolet Thomson Scattering from High-Power Laser-Produced Plasmas.”

P. W. McKenty, "Current Status of NIF Polar-Drive-Ignition Designs," ICF Burning Plasma Platforms, Livermore, CA, 2–3 October 2013.

R. Epstein, S. P. Regan, B. A. Hammel, L. J. Suter, H. A. Scott, M. A. Barrios, D. K. Bradley, D. A. Callahan, C. Cerjan, G. W. Collins, S. N. Dixit, T. Döppner, M. J. Edwards, D. R. Farley, K. B. Fournier, S. Glenn, S. H. Glenzer, I. E. Golovkin, A. Hamza, D. G. Hicks, N. Izumi, O. S. Jones, M. H. Key, J. D. Kilkenny, J. L. Kline, G. A. Kyrala, O. L. Landen, T. Ma, J. J. MacFarlane, A. J. Mackinnon, R. C. Mancini, R. L. McCrory, D. D. Meyerhofer, N. B. Meezan, A. Nikroo, H.-S. Park, P. K. Patel, J. E. Ralph, B. A. Remington, T. C. Sangster, V. A. Smalyuk, P. T. Springer, R. P. J. Town, and J. L. Tucker, "Applications and Results of X-Ray Spectroscopy in Implosion Experiments on the National Ignition Facility," 18th Annual International Conference on Atomic Processes in Plasmas, Auburn, AL, 7–10 October 2013 (invited).

S. Salzman, H. J. Romanofsky, Y. I. Clara, L. J. Giannechini, G. West, J. C. Lambropoulos, and S. D. Jacobs, "Magneto-rheological Finishing with Chemically Modified Fluids for Studying Material Removal of Single Crystal ZnS," Optifab 2013, Rochester, NY, 14–17 October 2013.

The following presentations were made at the Sixth International Symposium on Ultrafast Photonics Technologies, Rochester, NY, 21–22 October 2013:

J. Bromage, R. G. Roides, S.-W. Bahk, J. B. Oliver, C. Mileham, C. Dorrer, and J. D. Zuegel, "Noncollinear Optical Parametric Amplifiers for Ultra-Intense Lasers."

D. D. Meyerhofer, "The University of Rochester is a Pioneer in Laser Fusion."

W. T. Shmayda and N. Redden, "New Tritium Facilities at the University of Rochester's Laboratory for Laser Energetics," 10th International Conference on Tritium Science and Technology, Nice, France, 21–25 October 2013.

The following presentations were made at the 55th Annual Meeting of the APS Division of Plasma Physics, Denver, CO, 11–15 November 2013:

K. S. Anderson, P. W. McKenty, T. J. B. Collins, J. A. Marozas, and R. Betti, "An Implosion-Velocity Survey for Shock Ignition on the NIF."

D. H. Barnak, P.-Y. Chang, G. Fiksel, R. Betti, and C. Taylor, "Increasing the Magnetic-Field Capability of MIFEDS Using an Inductively Coupled Coil."

R. Betti, K. S. Anderson, M. Lafon, R. Nora, W. Theobald, J. A. Delettrez, A. Solodov, J. R. Davies, C. Stoeckl, R. Yan, J. Li, and C. Ren, "Electron Shock Ignition."

A. Bose, R. Betti, R. Nora, K. Woo, P.-Y. Chang, J. R. Davies, A. Christopherson, J. A. Delettrez, and K. S. Anderson, "Hydrodynamic Scaling of the Deceleration-Phase Rayleigh-Taylor Instability."

P.-Y. Chang, G. Fiksel, D. Barnak, J. R. Davies, and R. Betti, "Neutron Yield Enhancement by Magnetizing Implosions on OMEGA."

T. J. B. Collins, J. A. Marozas, J. A. Delettrez, P. W. McKenty, K. S. Anderson, A. Shvydky, F. J. Marshall, D. Cao, J. Chenhall, A. Prochaska, and G. Moses, "Optimization of the NIF Polar-Drive-Ignition Point Design."

R. S. Craxton, P. B. Radha, A. K. Davis, D. H. Froula, M. Hohenberger, P. W. McKenty, D. T. Michel, P. A. Olson, T. C. Sangster, S. LePape, T. Ma, and A. J. Mackinnon, "Optimization of Azimuthal Uniformity in NIF Polar-Drive Implosions."

A. K. Davis, D. T. Michel, R. S. Craxton, R. Epstein, M. Hohenberger, T. C. Sangster, P. B. Radha, T. Mo, and D. H. Froula, "Three-Dimensional Modeling of X-Ray Self-Emission Images on NIF Polar-Drive Implosions."

J. A. Delettrez, T. J. B. Collins, P. W. McKenty, P. B. Radha, S. X. Hu, S. Skupsky, F. J. Marshall, S. To, A. Shvydky, D. Cao, A. Prochaska, J. Chenhall, and G. Moses, "Effect of Nonlocal Thermal-Electron Transport on the Symmetry of Polar-Drive Experiments."

D. F. DuBois, D. A. Russell, H. X. Vu, J. F. Myatt, and W. Seka, "Half-Harmonic Radiation from Turbulence Driven by the Two-Plasmon-Decay Instability."

D. H. Edgell, D. Haberberger, S. X. Hu, D. T. Michel, J. F. Myatt, C. Stoeckl, B. Yaakobi, and D. H. Froula, "Measurements of the Two-Plasmon–Decay Generated Hot-Electron Fraction as a Function of the Quarter-Critical Density Scale Length."

R. Epstein, F. J. Marshall, V. N. Goncharov, R. Betti, A. R. Christopherson, R. Nora, I. E. Golovkin, and J. J. MacFarlane, "A Pressure Diagnostic Based on X-Ray Continuum Images of Compressed Isobaric Hydrogen Implosion Cores."

G. Fiksel, D. Barnak, P.-Y. Chang, S. X. Hu, P. M. Nilson, R. Betti, W. Fox, A. Bhattacharjee, and K. Germaschewski, "Magnetic Reconnection of an Externally Applied Magnetic Field in a High-Energy-Density Plasma."

R. K. Follett, D. H. Edgell, R. Henchen, S. X. Hu, D. T. Michel, J. F. Myatt, and D. H. Froula, "Observation of Two-Plasmon–Decay Electron Plasma Waves Driven by Multiple Beams Using UV Thomson Scattering."

C. J. Forrest, V. Yu. Glebov, V. N. Goncharov, S. X. Hu, D. D. Meyerhofer, P. B. Radha, T. C. Sangster, C. Stoeckl, J. A. Frenje, and M. Gatu Johnson, "Diagnosing Cryogenic DT Implosion Performance Using Neutron Spectroscopy on OMEGA."

D. H. Froula, T. J. Kessler, I. V. Igumenshchev, V. N. Goncharov, H. Huang, S. X. Hu, E. Hill, J. H. Kelly, D. T. Michel, D. D. Meyerhofer, A. Shvydky, J. D. Zuegel, and R. Epstein, "Mitigation of Cross-Beam Energy Transfer in Direct-Drive Implosions on OMEGA."

V. Yu. Glebov, C. J. Forrest, K. L. Marshall, A. Pruyne, M. Romanofsky, T. C. Sangster, M. J. Shoup III, and C. Stoeckl, "A New Neutron Time-of-Flight Detector for Areal Density Measurements on OMEGA."

V. N. Goncharov, T. C. Sangster, R. Betti, T. R. Boehly, T. J. B. Collins, R. S. Craxton, J. A. Delettrez, D. H. Edgell, R. Epstein, C. J. Forrest, D. H. Froula, V. Yu. Glebov, D. R. Harding, S. X. Hu, I. V. Igumenshchev, R. Janezic, J. H. Kelly, T. J. Kessler, T. Z. Kosc, S. J. Loucks, J. A. Marozas, F. J. Marshall, A. V. Maximov, R. L. McCrory, P. W. McKenty, D. D. Meyerhofer, D. T. Michel, J. F. Myatt, R. Nora, P. B. Radha, S. P. Regan, W. Seka, W. T. Shmayda, R. W. Short, A. Shvydky, S. Skupsky, C. Sorce, C. Stoeckl, B. Yaakobi, J. A. Frenje, M. Gatu Johnson, R. D. Petrasso, and D. T. Casey, "Demonstrating Ignition Hydrodynamic Equivalence in Cryogenic DT Implosions on OMEGA" (invited).

M. C. Gregor, R. Boni, A. Sorce, C. A. McCoy, M. Millot, J. H. Eggert, P. M. Celliers, T. R. Boehly, and D. D. Meyerhofer, "The Absolute Calibration of the Streaked Optical Pyrometer at the Omega Laser Facility."

D. Haberberger, D. H. Edgell, S. X. Hu, S. Ivancic, B. Yaakobi, R. Boni, and D. H. Froula, "Coronal Plasma Density Characterization in Long-Scale-Length High-Energy-Density Plasmas" (invited).

R. J. Henchen, V. N. Goncharov, D. T. Michel, R. K. Follett, J. Katz, and D. H. Froula, "Ultraviolet Thomson Scattering from Direct-Drive Coronal Plasmas."

M. Hohenberger, A. Shvydky, J. A. Marozas, T. J. B. Collins, D. Canning, M. J. Bonino, G. Fiksel, T. J. Kessler, P. W. McKenty, D. D. Meyerhofer, J. D. Zuegel, and T. C. Sangster, "Measurement of 1-D Multi-FM SSD Smoothing Performance on OMEGA EP."

S. X. Hu, P. B. Radha, V. N. Goncharov, R. Betti, R. Epstein, F. J. Marshall, R. L. McCrory, D. D. Meyerhofer, T. C. Sangster, and S. Skupsky, "Integrated Two-Dimensional DRACO Simulations of Cryogenic DT Target Performance on OMEGA."

I. V. Igumenshchev, P. M. Nilson, V. N. Goncharov, A. B. Zylstra, C. K. Li, and R. D. Petrasso, "Investigation of Electric and Self-Generated Magnetic Fields in Implosion Experiments on OMEGA."

S. Ivancic, W. Theobald, D. Haberberger, D. H. Froula, C. Stoeckl, K. S. Anderson, D. D. Meyerhofer, K. Tanaka, H. Habara, and T. Iwawaki, "Optical-Probe Measurements of a Plasma Channel for Fast Ignition."

J. P. Knauer, J. A. Caggiano, R. Hatarik, J. M. McNaney, B. K. Spears, M. Gatu Johnson, J. A. Frenje, and J. D. Kilkenny, "Bulk Fluid Velocity Construction from NIF Neutron Spectral Diagnostics."

M. Lafon, R. Betti, K. S. Anderson, T. J. B. Collins, J. Li, R. Nora, C. Ren, and P. W. McKenty, "Direct-Drive–Ignition Designs with Moderate-Z Ablators."

J. Li, C. Ren, X. Kong, M. C. Huang, and W. B. Mori, "Adapting a Collision Package in Particle-in-Cell Simulations on a GPU."

J. A. Marozas, T. J. B. Collins, J. A. Delettrez, P. B. Radha, P. W. McKenty, I. V. Igumenshchev, D. H. Edgell, D. H.

Froula, M. Hohenberger, F. J. Marshall, D. T. Michel, W. Seka, A. J. Mackinnon, S. LePape, T. Ma, D. Cao, A. Prochaska, J. Chenhall, and G. Moses, "Comparison of 2-D *DRACO* Cross-Beam Energy Transfer (CBET) Simulations with OMEGA and NIF Experiments."

F. J. Marshall, P. B. Radha, M. J. Bonino, D. R. Harding, J. A. Delettrez, R. Epstein, and E. Giraldez, "Improved Polar-Driven Implosion Performance Obtained with Contoured Shells."

A. V. Maximov, J. F. Myatt, R. W. Short, I. V. Igumenshchev, and W. Seka, "Laser-Plasma Interaction Model for Cross-Beam Energy Transfer."

P. W. McKenty, J. A. Marozas, F. J. Marshall, J. A. Delettrez, R. S. Craxton, M. Hohenberger, D. H. Froula, D. T. Michel, P. A. Olson, S. To, D. D. Meyerhofer, R. L. McCrory, D. Cao, G. Moses, S. Laffite, L. Videau, S. LePape, T. Ma, and A. J. Mackinnon, "Evaluation of Cross-Beam Energy Transfer in NIF Polar-Drive Exploding-Pusher Experiments."

D. D. Meyerhofer, R. S. Craxton, D. H. Froula, M. Hohenberger, P. W. McKenty, D. T. Michel, F. J. Marshall, J. F. Myatt, P. B. Radha, T. C. Sangster, W. Seka, S. LePape, K. N. LaFortune, B. J. MacGowan, A. J. Mackinnon, J. D. Moody, and C. Widmayer, "Initial Polar-Drive Implosions on the NIF."

D. T. Michel, V. N. Goncharov, I. V. Igumenshchev, P. B. Radha, R. J. Henchen, S. X. Hu, and D. H. Froula, "Comparison of Implosion Velocities for Be, C, and CH Ablators Measured in Direct-Drive Implosions."

J. F. Myatt, R. W. Short, A. V. Maximov, A. A. Solodov, J. Zhang, R. S. Craxton, C. Ren, R. Yan, I. V. Igumenshchev, S. X. Hu, V. N. Goncharov, W. Seka, D. H. Edgell, D. H. Froula, B. Yaakobi, D. T. Michel, D. F. DuBois, D. A. Russell, D. E. Hinkel, P. Michel, and H. X. Vu, "Multibeam Laser-Plasma Interactions in Inertial Confinement Fusion" (invited).

P. M. Nilson, C. Stillman, A. Shvydky, A. A. Solodov, R. Betti, D. H. Froula, and D. D. Meyerhofer, "Material Release at High-Energy Densities."

R. Nora, R. Betti, K. S. Anderson, A. Shvydky, A. Bose, K. M. Woo, A. R. Christopherson, J. A. Marozas, T. J. B. Collins, P. B. Radha, S. X. Hu, R. Epstein, F. J. Marshall, T. C. Sangster, and D. D. Meyerhofer, "Theory of Hydro-Equivalent Ignition for Inertial Fusion and Its Applications to OMEGA and the NIF" (invited).

P. B. Radha, M. Hohenberger, R. S. Craxton, J. A. Marozas, F. J. Marshall, D. H. Edgell, R. Epstein, D. T. Michel, D. H. Froula, V. N. Goncharov, R. L. McCrory, P. W. McKenty, D. D. Meyerhofer, T. C. Sangster, A. Shvydky, S. Skupsky, T. Ma, A. J. Mackinnon, and S. Le Pape, "Polar-Drive Implosions on the NIF."

S. P. Regan, R. Epstein, T. C. Sangster, D. D. Meyerhofer, C. A. Iglesias, B. G. Wilson, H.-S. Park, L. J. Suter, H. Scott, O. S. Jones, J. D. Kilkenny, B. A. Hammel, M. A. Barrios, V. A. Smalyuk, B. Remington, G. A. Kyrala, T. J. Murphy, J. Kline, P. A. Bradley, N. S. Krasheninnikova, and R. J. Kanzleiter, "Plasma Conditions of the Compressed Ablator at Stagnation in NIF Implosions."

T. C. Sangster, V. N. Goncharov, P. B. Radha, R. Betti, T. R. Boehly, C. J. Forrest, D. H. Froula, V. Yu. Glebov, S. X. Hu, I. V. Igumenshchev, J. Kwiatkowski, F. J. Marshall, R. L. McCrory, P. W. McKenty, D. D. Meyerhofer, D. T. Michel, J. F. Myatt, W. Seka, C. Stoeckl, J. A. Frenje, and M. Gatu Johnson, "Status of Ignition Hydro-Equivalent Implosion Performance on OMEGA."

W. Seka, J. F. Myatt, J. Zhang, R. W. Short, D. H. Froula, A. V. Maximov, V. N. Goncharov, and I. V. Igumenshchev, "Non-linearity of the Two-Plasmon-Decay Instability in Imploding Direct-Drive Targets."

R. W. Short, J. F. Myatt, and J. Zhang, "The Effects of Beam Geometry and Polarization on Two-Plasmon Decay Driven by Multiple Laser Beams."

A. Shvydky, M. Hohenberger, J. A. Marozas, M. J. Bonino, D. Canning, T. J. B. Collins, T. J. Kessler, B. E. Kruschwitz, P. W. McKenty, D. D. Meyerhofer, T. C. Sangster, and J. D. Zuegel, "Two-Dimensional Numerical Evaluation of 1-D Multi-FM SSD Experiments on OMEGA EP."

A. A. Solodov, W. Theobald, K. S. Anderson, A. Shvydky, R. Epstein, R. Betti, J. F. Myatt, C. Stoeckl, L. C. Jarrott, C. McGuffey, B. Qiao, F. N. Beg, M. S. Wei, and R. B. Stephens, "Simulations of Fuel Assembly and Fast-Electron Transport in Integrated Fast-Ignition Experiments on OMEGA."

C. Stoeckl, R. Epstein, G. Fiksel, D. Guy, V. N. Goncharov, D. W. Jacobs-Perkins, R. K. Jungquist, C. Mileham, P. M. Nilson, T. C. Sangster, M. J. Shoup III, and W. Theobald, "Soft X-Ray Backlighting of Cryogenic Implosions Using a Narrowband Crystal Imaging System."

B. R. Talbot, V. V. Ivanov, I. A. Begishev, A. L. Astanovitskiy, V. Nalajala, and O. Dmitriev, "Development of the Diagnostic Laser for Deep UV Probing of the Dense Z-Pinch."

W. Theobald, R. Nora, M. Lafon, K. S. Anderson, J. R. Davies, M. Hohenberger, T. C. Sangster, W. Seka, A. A. Solodov, C. Stoeckl, B. Yaakobi, R. Betti, A. Casner, C. Reverdin, X. Ribeyre, and A. Vallet, "Demonstration of 200-Mbar Ablation Pressure for Shock Ignition."

H. Wen, A. V. Maximov, R. Yan, C. Ren, J. F. Myatt, and W. B. Mori, "Three-Dimensional Modeling of the Two-Plasmon-Decay Instability and Stimulated Raman Scattering Near the Quarter-Critical Density in Plasmas."

J. Zhang, J. F. Myatt, R. W. Short, A. V. Maximov, H. X. Vu, D. A. Russell, and D. F. DuBois, "Two-Plasmon Decay Driven by Multiple Incoherent Laser Beams."

D. R. Harding, H. Goodrich, A. Caveglia, and M. Anthamatten, "Properties and Fracture Behavior of Nanoliter Size Volumes of Acrylate Adhesives at Cryogenic Temperatures," 2013 Materials Research Society Fall Meeting, Boston, MA, 1-6 December 2013.

The following presentations were made at the Fusion Power Associates 34th Annual Meeting, Washington, DC, 11 December 2013:

R. Betti and D. D. Meyerhofer, "Near-Term Issues for Inertial Confinement Fusion."

R. L. McCrory, "Perspectives on Inertial Fusion Energy."